

University of Windsor

Scholarship at UWindor

Electronic Theses and Dissertations

Theses, Dissertations, and Major Papers

2-1-2022

Analysis Guidelines and Functionalities of the CATIA Native FEA Solver for Composite Materials

Mohamed Edrisy
University of Windsor

Follow this and additional works at: <https://scholar.uwindsor.ca/etd>



Part of the [Aerospace Engineering Commons](#), and the [Mechanical Engineering Commons](#)

Recommended Citation

Edrisy, Mohamed, "Analysis Guidelines and Functionalities of the CATIA Native FEA Solver for Composite Materials" (2022). *Electronic Theses and Dissertations*. 8794.

<https://scholar.uwindsor.ca/etd/8794>

This online database contains the full-text of PhD dissertations and Masters' theses of University of Windsor students from 1954 forward. These documents are made available for personal study and research purposes only, in accordance with the Canadian Copyright Act and the Creative Commons license—CC BY-NC-ND (Attribution, Non-Commercial, No Derivative Works). Under this license, works must always be attributed to the copyright holder (original author), cannot be used for any commercial purposes, and may not be altered. Any other use would require the permission of the copyright holder. Students may inquire about withdrawing their dissertation and/or thesis from this database. For additional inquiries, please contact the repository administrator via email (scholarship@uwindsor.ca) or by telephone at 519-253-3000ext. 3208.

Analysis Guidelines and Functionalities of the CATIA Native FEA Solver for Composite Materials

By

Mohamad Edrisy

A Thesis

Submitted to the Faculty of Graduate Studies
through the Department of Mechanical, Automotive, and Materials Engineering
in Partial Fulfillment of the Requirements for
the Degree of Master of Applied Science
at the University of Windsor

Windsor, Ontario, Canada

© 2022 Mohamad Edrisy

Analysis Guidelines and Functionalities of the CATIA Native FEA Solver for Composite Materials

by
Mohamad Edrisy

APPROVED BY:

S. Das
Department of Civil and Environmental Engineering

J. Johrendt
Department of Mechanical, Automotive, and Materials Engineering

N. Zamani, Advisor
Department of Mechanical, Automotive, and Materials Engineering

February 03, 2022

DECLARATION OF ORIGINALITY

I hereby certify that I am the sole author of this Thesis and that no part of this Thesis has been published or submitted for publication.

I certify that, to the best of my knowledge, my Thesis does not infringe upon anyone's copyright nor violate any proprietary rights and that any ideas, techniques, quotations, or any other material from the work of other people included in my Thesis, published or otherwise, are fully acknowledged in accordance with the standard referencing practices. Furthermore, to the extent that I have included copyrighted material that surpasses the bounds of fair dealing within the meaning of the Canada Copyright Act, I certify that I have obtained a written permission from the copyright owner(s) to include such material(s) in my Thesis and have included copies of such copyright clearances to my appendix.

I declare that this is a true copy of my Thesis, including any final revisions, as approved by my Thesis committee and the Graduate Studies office, and that this Thesis has not been submitted for a higher degree to any other University or Institution.

ABSTRACT

The emergence of commercial FEA solvers was a significant breakthrough that boosted the accuracy and complexity of engineering design. While composite materials are special materials, their mechanical properties can be custom made by considering the needs and requirements of the design problem. Given the rapidly expanding global consumption of composite materials, access to FEA solvers capable of assigning these materials is an absolute requirement.

The CATIA software is a platform for designing, analyzing, and manufacturing of parts. However, there is no meaningful documentation in the public domain exploring the finite element functionalities of CATIA software for composite materials. Isotropic materials are used in numerous references investigating the CATIA FEA solver; however, the extension to composite materials has been lacking. The present study investigates two phenomena: (1) the procedure to import composite material properties into the Generative Structural Analysis workbench, and (2) the pre-processing and the post-processing toolbars and functionalities pertaining to this matter. The thesis does not address the CAD modelling aspects of the composites per se since there are many references available concentrating on such issues in the CATIA public literature.

The composite models are selected from different scenarios labeled as benchmark problems. The results generated by CATIA's native FEA solver for the static, dynamic, and buckling cases are compared with other tools available to the engineering community. These tools encompass the Classical Lamination Theory and two commercial CAE codes, known as ABAQUS and ANSYS.

DEDICATION

To my daughter,

ACKNOWLEDGEMENTS

I would like to express my most sincere gratitude and profound appreciation to Dr. N. Zamani for his supervision, guidance and support. His knowledge and expertise have been of immeasurable assistance throughout my graduate studies and research. I appreciate all his contributions to make my experience productive and stimulating at the University of Windsor. The joy and enthusiasm he has for this research were contagious and motivational for me throughout my graduate degree. This work could not have been achieved without his help and support.

I would like to take this opportunity to also thank my committee members, Dr. S. Das and Dr. J. Johrendt for helping me throughout this thesis. Your suggestions brought in threads of thought that made my research so much richer and my dissertation something I can be proud of having written. You've also inspired me with your own body of research and the gift of helping me visualize a similar trajectory for myself.

Lastly, I offer my regards and blessings to my family, friends, colleagues, and all of those who supported me in any respect during the completion of this thesis.

TABLE OF CONTENTS

DECLARATION OF ORIGINALITY	iii
ABSTRACT	iv
DEDICATION	v
ACKNOWLEDGEMENTS	vi
LIST OF TABLES	xi
LIST OF FIGURES	xii
LIST OF APPENDICES	xvi
LIST OF ABBREVIATIONS/SYMBOLS	xvii
NOMENCLATURE.....	xx
1. INTRODUCTION	1
2. BASIC CONCEPTS	7
2.1 CATIA FEA Solver	7
2.2 ASTM Code.....	9
2.3 Classical Hand Calculations	10
2.4 Other FEA Solvers Used for Verifications in the Thesis:	11
2.4.1 ANSYS	12
2.4.2 ABAQUS.....	12
3. COMPOSITE MATERIALS, REVIEW	13
3.1 Material Properties.....	13
3.1.1 Lamina’s Engineering Constants	14
3.1.2 Laminate Engineering Constants	17
3.2 Loads’ Conditions.....	19
3.2.1 General load conditions for a flat element.....	19
3.3 Stacking Sequence (Special characteristics).....	23
3.3.1 Quasi-isotropic laminate	23
3.4 Strength Criteria.....	24
3.4.1 First-order theory	25
4. COMPOSITE MATERIALS, CATIA CAD	27
4.1 Base Laminate Surface Design	27

4.2	Material Library.....	27
4.3	Composite Parameters	28
4.3.1	List of materials	28
4.3.2	Direction/Orientation properties of plies	29
4.3.3	Rosettes.....	29
4.4	Laminate Design.....	30
4.4.1	Draping (the stacking sequence).....	30
4.4.2	Manual ply creation	30
4.4.3	Modifying the plies by using Excel	31
4.4.4	Modifying the plies by Stacking Management:.....	31
5.	COMPOSITE MATERIALS, CATIA FEA	33
5.1	Meshing of the Part (Shell elements).....	33
5.1.1	Join, Normal to Shell, and local CS directions	33
5.1.2	Draping direction	34
5.2	Imported Properties	35
5.2.1	Geometries consisting of different Composite Parameters.....	36
5.3	Imposing Loads and Restraints.....	37
5.3.1	Defining the location of applied load (symmetrical or un-symmetrical loading condition).....	37
5.4	Visualizing the Results	38
5.4.1	Generating the CATIA results and reports	38
6.	BASIC BENCHMARKS (BMP1 to BMP11)	40
6.1	Introduction:	40
6.1.1	General comments on benchmark problems' status	40
6.1.2	RCT (General framework).....	45
6.2	BMP1 (Tensile loading condition)	47
6.2.1	Problem statement	47
6.2.2	Results and Discussion	48
6.3	BMP2 (Bending loading condition).....	51
6.3.1	Problem statement	51
6.3.2	Results and discussion	52
6.4	BMP3 (Shearing loading condition).....	54

6.4.1	Problem statement	54
6.4.2	Results and discussion	55
6.5	BMP4 (Twisting loading conditions)	58
6.5.1	Problem statement	58
6.5.2	Results and discussion	59
6.6	BMP5 (Temperature effect in unidirectional composites)	62
6.6.1	Problem statement	62
6.6.2	Results and discussion	63
6.7	BMP6 (Temperature effect in woven fabric composites).....	66
6.7.1	Problem statement	66
6.7.2	Results and discussion	66
6.8	BMP7 (Superposition load in unidirectional composites).....	69
6.8.1	Problem statement	69
6.8.2	Results and discussion	70
6.9	BMP8 (Superposition load in woven fabric composites).....	74
6.9.1	Problem statement	74
6.9.2	Results and discussion	74
6.10	BMP9 (Draping in the "+Z" vs. "-Z" directions).....	77
6.10.1	Problem statement (Draping in the "+Z" and "-Z" directions)	77
6.10.2	Results and discussion	80
6.11	BMP10 (Torsion of a cylinder).....	83
6.11.1	Problem statement	83
6.11.2	Results and discussion	85
6.12	BMP11 (Externally applied pressure on a sphere)	87
6.12.1	Problem statement	87
6.12.2	Results and discussion	89
7.	INTERMEDIATE BENCHMARKS (BMP12 to BMP14)	92
7.1	Introduction:	92
7.2	BMP12 (Drop-off condition).....	93
7.2.1	Problem statement	93
7.2.2	Different methods to stack up the laminate	94

7.2.3	ABAQUS simulation for compiling the needed data	96
7.2.4	Results and discussion	97
7.2.5	The symmetry plane presumed by the original reference.....	100
7.3	BMP13 (The dynamic response of a composite plate).....	101
7.3.1	Basics of modal superposition	101
7.3.1	Case I	102
7.3.2	Case II.....	105
7.3.3	Case III.....	106
7.3.4	Natural frequency validation	107
7.4	BMP14 (Thermal buckling of a sandwich panel).....	108
7.4.1	Thermal buckling analysis.....	108
7.4.2	Problem statement	109
7.4.3	Results and discussion	111
8.	PRACTICAL ANALYTICAL MODELS.....	113
8.1	Introduction:	113
8.2	BMP15 (Buckling of a stiffened panel).....	114
8.2.1	Problem statement	114
8.2.2	Results and discussion	115
8.3	BMP16 (An idealized propeller blade).....	120
8.3.1	Modelling the geometry and the composite parameters	121
8.3.2	Imposing loads and restraints	127
8.3.3	Results and discussion	128
8.4	BMP17 (Loading acting on an Aircraft Wing in Pull up Maneuver).....	132
8.4.1	Modelling the geometry and the composite parameters	132
8.4.2	Imposing loads and restraints	136
8.4.3	Results and discussion	137
9.	CONCLUSIONS and DISCUSSION	140
	REFERENCES/BIBLIOGRAPHY.....	143
	APPENDICES	149
	VITA AUCTORIS	157

LIST OF TABLES

Table 1: The topics and comments for Benchmark Problems	5
Table 2: ASTM composite standards classifications	9
Table 3: Structural performance ranking of conventional materials [29].....	13
Table 4 : Number of independent elastic constants for various types of materials	14
Table 5: Effective mechanical properties of a symmetric laminate.....	19
Table 6: Quasi-isotropic material, Fibre orientation when “n” is 3 to7.....	24
Table 7: The stages before using Elfini Solver	27
Table 8: The Pre-processing, solveing, and Post-procesing stages	33
Table 9: Available images and reports using CATIA FEA Solver.....	39
Table 10: Lamina properties used in Chapter Six (extracted from [29]).....	41
Table 11: Summary on the basic examples using CATIA Solver BMP1 to BMP11	42
Table 12: All the mesh sizes and loading conditions for BMP1 to BMP11	44
Table 13: Engineering shear strain is half of the shear strain (results from the BMP3).....	56
Table 14: BMP7 mid-plane surface strain computation	71
Table 15: BMP8 mid-plane surface strain computation	75
Table 16: BMP9 mid-plane surface strain computation	81
Table 17: CFRP lamina properties (extracted from [57]).....	94
Table 18: Validate the new repeated ABAQUS simulation	96
Table 19: CFRP lamina properties (extracted from [59]).....	103
Table 20: The various natural frequencies modes, ω ,.....	107
Table 21: Parameters involved in problem cases for BMP14	110
Table 22: Lamina and core properties (extracted from [65]).....	110
Table 23: Critical Temperature (T_{cr}) values reported from CATIA FEA Solver corresponding each Case # and the computed Thermal stability parameter ($\lambda_T \times 100$).....	112
Table 24: Lamina and Core properties (extracted from [67]).....	115
Table 25: Different stiffener height and location used in BMP15.....	119
Table 26: Boundary conditions and their LSS.....	123
Table 27: RSF values for lamina 1-20	129
Table 28: The guide points used to model the “Spar.1”	133
Table 29: the “Point.A” and “Point.B” for all the spars	133
Table 30: Lamina and Core properties (extracted from [69]).....	134
Table 31: Benchmark problems validation BMP1 to BMP11	141

LIST OF FIGURES

Figure 1: Map of the study.....	2
Figure 2: Benchmark problems' workflow for modeling, analysis, and validation	4
Figure 3: The challenges and questions answered in this study	6
Figure 4: CATIA modules mavailable for the designers.....	8
Figure 5: Some Workbenches Used Concerning Composite Materials	9
Figure 6: Open-Hole compressive strength composite test machine [17].....	9
Figure 7: Boeing 787 Wing Flex Test [18].....	10
Figure 8: Stress-Strain Computation Flow Chart of a Laminate	11
Figure 9: Different mesh used in ABAQUS [24]	12
Figure 10: Planes of symmetry for a unidirectional orthotropic material.....	15
Figure 11: Lamina stress and strain in the global and local coordinate systems	17
Figure 12: Ply coordinates in the “z” direction, numbered from the bottom.....	18
Figure 13: In-plane forces and moments on a laminate.....	20
Figure 14: Strain, layer moduli and stress variations through the thickness [29].....	20
Figure 15: Torsion load imposed a thin tube	21
Figure 16: Feathering, Z-Spiking to prevent delamination[4].....	23
Figure 17: Typical Tsai-Hill failure criteria, different biaxial and shear stresses [48].....	25
Figure 18: Section of a laminate normal to the y-axis before and after the deformation	26
Figure 19: Properties of the material in CATIA software	28
Figure 20: Composite Parameters toolbar	28
Figure 21: Assigning materials to the design.....	29
Figure 22: Direction properties of plies.....	29
Figure 23: Rosettes Definition toolbar	30
Figure 24: Manual ply creation.....	31
Figure 25: Exported information using Ply Table tools	31
Figure 26: Laminate Design (Stacking preview).....	32
Figure 27: Some of the features in the Meshing Tools.....	34
Figure 28: Deformation curve for solid profiles with 45°, 0°, 90° presenting corresponding laminate.....	35
Figure 29: Comparison between different Drapings: True (left) and False (right).....	35
Figure 30: 2D properties interactive window	36
Figure 31: Mesh and Boundaries depiction	36
Figure 32: "Add/Remove Constraint" tools to define the Boundaries.....	37

Figure 33: loads & restraints when the Symmetrical option in the Imported Properties is checked or unchecked.....	37
Figure 34: Simple illustration of problem status BMP1	47
Figure 35: BMP1's Report Card Test (Pure Tensile loads).....	50
Figure 36: Simple illustration of the BMP2 problem status	51
Figure 37: BMP2's Report Card Test (Pure Bending Load)	53
Figure 38: Simple illustration of the BMP3 problem case	54
Figure 39: BMP3's Report Card Test (Pure Shearing Loads).....	57
Figure 40: Simple illustration of the BMP4 problem case	59
Figure 41: BMP4's Report Card Test (Pure Twisting Load on a Plate).....	61
Figure 42: Simple illustration of the BMP5, MP6 problem case.....	62
Figure 43: BMP5's Report Card Test (Temperature Effect using unidirectional lamina)	65
Figure 44: BMP6's Report Card Test (Temperature Effect using Woven Fabric).....	68
Figure 45: Simple illustration of the BMP7, MP8 problem case.....	69
Figure 46: BMP7's Report Card Test (Unidirectional plies (3D vs. 2D properties)).....	73
Figure 47: BMP8's Report Card Test (Woven Fabric (3D vs. 2D properties)).....	76
Figure 48: Simple illustration of the BMP9 (Draping in the "+Z" directions)	79
Figure 49: Simple illustration of the BMP9 (Draping in the "-Z" directions)	79
Figure 50: BMP9's Report Card Test (Draping in the "+Z" vs. "-Z" directions).....	82
Figure 51: Simple illustration of the BMP10 problem case; (a) BLS, (b) Reference Surface	84
Figure 52: BMP10's Report Card Test (Torsion on a Cylinder)	86
Figure 53: Simple illustration of the BMP11—half of the sphere is shown—problem case; (a) BLS, (b) Reference Surface.....	88
Figure 54: BMP11's Report Card Test (Pressure on the outside surface of a Sphere).....	91
Figure 55: Simple illustration of the BMP12.....	94
Figure 56: Some methods to stack up the laminate in CATIA software; (a) the Grid method, (b) the manual ply creation when all the BLSs are joined, (c) the Zone method, and (d) the manual ply creation when the BLSs are joined separately.....	95
Figure 57: BMP12's Report Card Test (Unsymmetrical Loading conditions).....	99
Figure 58: The deformed shapes when considering or not considering the symmetric condition, respectively	100
Figure 59: Single degree of freedom, Mass-Spring-Damper System	101
Figure 60: Simple illustration of the BMP13 (Case I).....	103
Figure 61: transient responses of the center node deflection (Case I).....	104

Figure 62: Simple illustration of the BMP13 (Case II)	105
Figure 63: transient responses of the center node deflection (Case II).....	105
Figure 64: Simple illustration of the BMP13 (Case III)	106
Figure 65: transient responses of the center node deflection (Case III)	106
Figure 66: Simple illustration of the BMP14.....	110
Figure 67: Effects of thickness ratio (h_f/h) and fibre orientation angle (θ) on the Thermal stability parameter(λ_T) of square sandwich panels; Left: $a/h=20$, right: $a/h=10$	112
Figure 68: Simple illustration of the BMP15.....	115
Figure 69: First mode shape and values for various “h,” when the stiffener is located at half of the plate’s width.....	116
Figure 70: Varied buckling loads with stiffener height. The stiffener is located in the middle of the plate’s width.....	117
Figure 68: First mode shape and values for various “h,” when the stiffener is located at one-quarter of the plate’s width	118
Figure 72: Varied buckling loads with stiffener height. The stiffener is located at a quarter of the plate’s width.....	119
Figure 73: The base design of the propeller extracted from [49]	120
Figure 74: The reference problem case, failed elements (IRF>1)	121
Figure 75: main Base Laminate Surfaces	121
Figure 76: the Sub_BLSs inside the main BLSs.....	122
Figure 77: Isometric view (top) and the right view (bottom) of the 2D stacking sequences.....	124
Figure 78: Top view of the 2D stacking sequences on the XY plane.....	125
Figure 79: (a) Rosettes for the Base and Ring, (b) rosette for the Front and Back, (c) the composite angle symbol for plies with 90°	126
Figure 80: the element meshes and loading conditions in different Bboundaries	127
Figure 81: Mesh types used om BMP16: TR6 and QD8.....	128
Figure 79: Tsai-Hill criterion discontinuous color map report for the elements in Lamina1 (top) and Lamina 20 (bottom)	130
Figure 80: Tsai-Hill criterion discontinuous color map report for the elements in Lamina10 (top) and Lamina 17 (bottom)	131
Figure 84: Airfoil Wing’s compartments	132
Figure 85: the guide points, Top Curve, Bottom Curve, and LCS for “Spar.1”.....	133
Figure 86: The location of different ribs, stiffeners and Airfoil shells in "Spar.1"	134

Figure 87: (a) Rosettes for the Bars, Spars, Top Curve and the Bottom Curve (b) the composite angle symbol for plies with 90°	135
Figure 88: the element meshes and loading conditions in different Boundaries	136
Figure 89: Edit Simplification tools used for eliminating the extra edges	137
Figure 90: Using different tools to modify one sample of unsatisfactory elements, stages from bottom left to right	138
Figure 91: A sample of the nodes at the edges and corners located in different components	138
Figure 92: Quality Report for BMP17	139
Figure 93: the deflection of the aircraft wing	139

LIST OF APPENDICES

APPENDICES	149
Appendix A Stacking Sequence Classification:	149
Appendix B Licenses needed to perform the indicated scenarios [73].	154
Appendix C Figures	156

LIST OF APPENDICES FIGURES

Appendices Figure A: Mid-fuselage structure of Space Shuttle Orbiter showing boron-aluminum tubes (photo courtesy of U.S. Air Force/NASA)	156
Appendices Figure B: Two-dimensional geometric deformation of an infinitesimal material element [74]	156

LIST OF APPENDICES TABLES

Appendices Table A: Summary of different laminate characterization	150
Appendices Table B: [ABD] Couplings drawbacks investigation	152

LIST OF ABBREVIATIONS/SYMBOLS

L, W, Thk.	length, width, and thickness
(x, y, z) / (X, Y, Z)	local / global coordinate system
[] or { }	matrix
S#	state#
IEEE	Institute of Electrical and Electronics Engineers
NASA	National Aeronautics and Space Administration
ASTM	American Society for Testing and Materials
CAD	Computer-Aided Design
CAE	Computer-Aided Engineering
ACP (Pre/Post)	ANSYS Composite Prep/Post Processing component system
GUI	Graphic User Interface
.iges	Initial Graphics Exchange Specifications file
MSC	MacNeal-Schwendler Corporation
UMAT, VUMAT	User Material, Vectorized User Material
VCCT	Virtual Crack Closure Technique
N _x , N _y / N _{xy}	Axial load / shear load (N _{mm}) in the "xy" plane
LFD	Line Force Density (N _{mm})
M	Moment applied on the Edge in CATIA (N.mm)
C11, C22, C12	Tensor Component
U _x =0	User-defined Translation1 is Restrained
U _y =0	User-defined Translation2 is Restrained
U _z =0	User-defined Translation3 is Restrained
GPS	Single parts analysis
GAS	hybrid assembly analysis
GDY	dynamic response analysis
EST	pre/post-processing and solving
FMS	surface meshing
FMD	solid meshing
N _{mm}	Newton per Millimeter
r	radius
r _m	mean radius of the shaft
rpm	revolutions per minute
t or Thk.	thickness
DOF	degrees of freedom
IRF	inverse reserve factor
ρ	density
β ₁₁ , β ₂₂	The Coefficient of moisture expansion along with principal ply directions
α ₁₁ , α ₂₂	The Coefficient of thermal expansion along with principal ply directions
[A]	Extensional stiffness matrix for the laminate
[D]	Bending stiffness matrix for the laminate
[B]	Coupling stiffness matrix for the laminate
D ₁₆ , D ₂₆	Bending-Twisting Coupling

A_{16}, A_{26}	Shear-Extension Coupling
η	Shear-Extension Coupling coefficient
μ	Shear-Shear Coupling coefficient
CFRP	carbon fiber-reinforced plastic
NCF	Non-Crimp fabric
E	Young's modulus (with the appropriate subscript in different directions)
ν	Poisson's ratio (with the appropriate subscript in different directions)
G	Shear Young's modulus (with the appropriate subscript in different directions)
E_1	longitudinal Young's modulus
E_2, E_3	Transverse Young's modulus
F_{1t}	Longitudinal Tensile Strength
F_{2t}, F_{3t}	Transverse and Out-of-plane Tensile Strength
F_{1c}	Longitudinal Compressive Strength
F_{2c}, F_{3c}	Transverse and Out-of-plane Compressive Strength
F_4, F_5	Out-of-Plane Shear Strength
F_6	In-Plane Shear Strength
D	Compartment Law which is a function of Poisson Ratio and Young's Modulus
Θ	The angle of fibres within lamina of interest relative to "x" axis of laminate in "xy" plane
LSS	Laminate Stacking Sequence
TL / SS	Stacking Sequence / Thickness law
Top Reference Plane	The orders of plies in the laminate: [Ply1/ PLY2/ Ply3/ ...]
\	backslash is used instead of a bar over (while printing the LSS)
:	colon is used instead of subscript information, such as number or symmetry (while printing the LSS)
Mid_S	mid-plane surface
R	rosette
$[M^T]$	Thermal moment resultant matrix
$[N^T]$	Thermal stress resultant matrix
[S]	Stiffness matrix
$[C]=[S]^{-1}$	Compliance matrix
[Q]	Lamina (ply) stiffness matrix within 1-2-3 local coordinate system
$[Q(\Theta)]$	The compliance matrices in different angles
[T]	Transformation matrix
[ϵ]	Strain matrix
Kappa_xy or κ_{xy}	Curvature matrix
[N]	Force matrix (the unit is N_mm)
[M]	Moment matrix
Mx, My, Mxy	Bending and twisting load (the unit is Newton)
P	internal gage pressure
ΔT	the uniform change in Moisture
ΔM	the uniform change in temperature
T	torque load
FSDT	first-order shear deformation

GDQ	generalized differential quadrature technique
HSDT	higher-order shear deformation theories
CHC	Classical Hand Calculation
CLT	Classical Laminate Theory
U_x, U_y, U_z	Displacement in three directions of the coordinate system
QD8 /QD4	two-dimensional quadrangle parabolic/ linear mesh
TR6	two-dimensional triangle parabolic mesh
$P_{APPLIED}$	applied load
P_{cr}	buckling load
IRF	Inverse Reverse Factor
$\Delta T_{APPLIED}$	The specified rise or drop of temperature
ΔT_{cr}	The critical temperature rises from the T_0 (temperature of the environment)
λ	load multiplier
λ_T	Thermal stability parameter
γ_{xy}	engineering shear strain
$\varepsilon_x, \varepsilon_y / \gamma_{xy}$	Axial strain / shear strain in the "xy" plane
$\sigma_x, \sigma_y / \tau_{xz}$	Axial stress / shear stress in the "xy" plane
⊗	"No comparison has been conducted" sign
○	"Partially in compliance" sign
✓	"In compliance mostly" sign
☑	"Totally in compliance" sign

NOMENCLATURE

BMP	Benchmark Problem
GCS	General Coordinate System
LCS	Local Coordinate System
RAS	Repeated ABAQUS Simulation
L# / R#	The address in the RCT showing the left/right sides on row#
{1, 2, 3} rule	The minimum number of restraints which is imposed to avoid rigid body motion and avoid unnecessary stresses in the part
STN / STS	Strains / Stress
BLS	Base Laminate Surface
RCT	Report Card Test
V	The Vertex to apply Restraints

CHAPTER ONE: INTRODUCTION

Due to the increasing worldwide consumption of composite materials, many CATIA users dealing with composites find it necessary to analyze their models using the Finite Element Method. However, for all practical purposes, there is a dearth of documentation about CATIA v5 on this subject [1]. To confirm this, the question was posed to the experts' community, and the answer confirmed that no comprehensive documentation regarding this topic has been released [2]. This study's goal is twofold. First, it aims to fill the gap by presenting guidelines and methodologies that can be used to solve several Benchmark Problems. Also, it seeks to illustrate the procedure to conduct the preliminary analysis of composite materials using CATIA's native FEA solver.

The increasing demand for special materials with unique properties—such as high specific strength and specific stiffness, superiority to metal alloys, ceramics, or polymers—has led to the development of composite materials [3]. In that case, designers can manipulate the engineering constants of the raw materials to reach desired properties. Comprehensively considering all the loads and constraints of an engineering problem allows one to simulate fully optimized composite material for each specific condition.

In 1977, the CATIA software was first released by French aircraft manufacturer Avions Marcel Dassault [4] and has since been one of the top computer software tools in the engineering community [5]. As of 2021, over 50,000 multinational companies—including Boeing, Tesla Motors, Gulfstream Aerospace, Bell Helicopter, Fisker Automotive, and Magna—use CATIA as one of their tools [6], from the design to the manufacture of final products [5].

CATIA is a Product Lifecycle Management (PLM) software that manages the product during its development. All CAD, CAE, CAM features are used to file, revise, modify, and finalize each part of the entire product. The CATIA platform is also used for designing, analyzing, and manufacturing a product [5].

Apart from professional engineers, many engineering students learn and use CATIA software during their studies [1]. It assists the students to design a product for educational purposes (the correlation between load, constraint, and material) and challenges them to use creativity and knowledge to formulate, analyze, and solve complex engineering problems to reach substantiated conclusions.

This includes students in the University of Windsor's Department of Mechanical, Automotive, and Materials Engineering. They learn the basic steps during their sophomore year and apply them to their capstone project in the final year.

Composite materials are among the materials that future engineers need to learn how to model and analyze, especially in the aviation industry [7].

Organization of the thesis:

Figure 1 illustrates the relationships between different chapters in this study. Fundamental knowledge is presented in Chapter Two through Chapter Four, which is essential for solving more realistic models outlined beginning in Chapter Five and continuing through to Chapter Eight. Validation and verification are conducted in Chapter Six through to Chapter Eight. The thesis ends with Chapter Nine, which contains the conclusions and recommendations.

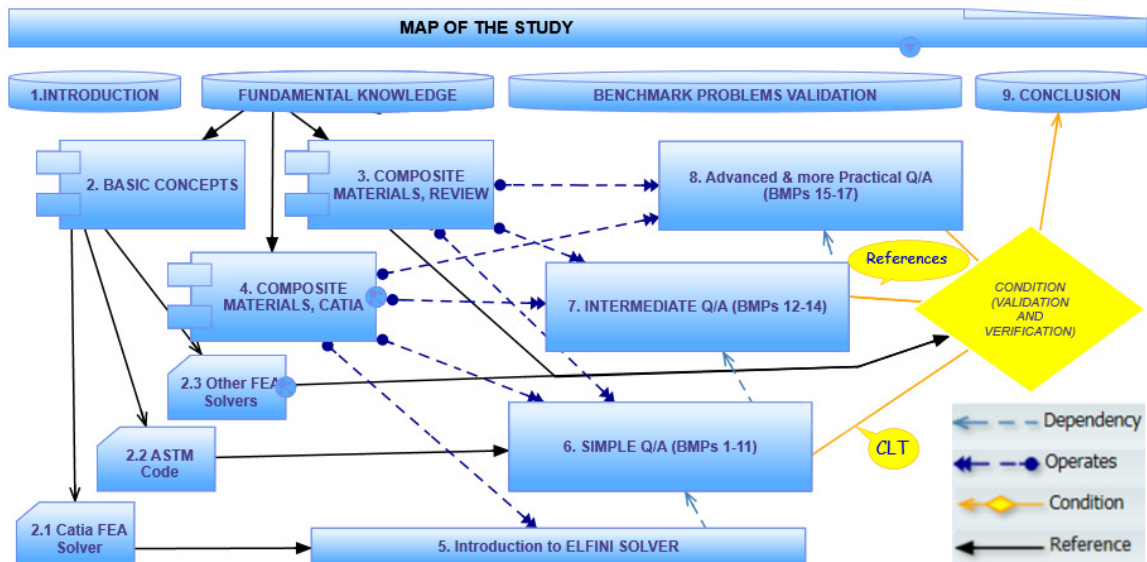


Figure 1: Map of the study

In Chapter Two, some general but relevant topics essential for this study are discussed. For example, the general features and capabilities of CATIA’s FEA workbench are listed, ASTM standards are briefly introduced, and the reasons for issuing different methods to test composite materials are stated. Other methods to validate the results from CATIA software are also presented. The relevance of the thesis content to the Capstone Project is discussed.

Chapter Three contains some fundamental topics related to analyzing composite materials. This is vital for a designer to predetermine the results from FEA software. In addition, the governing equations for different load conditions and properties of the materials used in this study are clarified.

Chapter Four explains the modelling of composite material in the CATIA software. There are some limited references on these topics; however, they provide the model for manufacturing purposes. Here, the point of view is to use them as much as possible to prepare a model for computational analysis purposes. Accordingly, the modelling tools

and the instructions introduced in this chapter are only used for CAD purposes and not the Finite Element aspects.

Information on the Elfini solver (CATIA's Native FEA Solver) is introduced in Chapter Five. The Elfini solver is not widely documented in the public domain; therefore, some examples are included to explain the steps or characteristics of GUI tools used for modelling the part. For instance, the chapter explains topics such as importing composite properties and the loading position, the importance of Join, Draping direction, Generating Images, and visualization of reports.

The verification manual of the Elfini program is extremely restricted in the modelling of composite materials [8]. Accordingly, in Chapter Six through to Chapter Nine, several reference benchmark problems are explored to test the reliability of CATIA FEA Solver corresponding composite materials (Validation). In addition, its graphic user interfaces (GUI) are evaluated for the imposed conditions (Verification). The method is based on IEEE Standard 1012, which suggests methods to certify different systems, software, and hardware [9].

Chapter Six investigates the general methods to model some simple benchmark problems comprising a discerning selection of loads, constraints, geometries, stacking sequences, and types of composite materials. These are analyzed and validated using Classical Laminated Theory (CLT). In addition, ANSYS and ABAQUS software is alternatively used to verify the results.

Chapter Seven presents simulation of problems which are more complicated to be compared with the CLT method; therefore, the results are compared with the published references.

Chapter Eight involves practical engineering problems, mostly concentrating on the techniques to design the composite parameters and to interpret the final results. The thesis concludes with a discussion and review of the main points in Chapter Nine.

Figure 2 illustrates the general workflow to model, analyze, and validate problems employing CATIA software. In steps 1 to 6, the corresponding GUI workbenches, categories investigated, and the main comments are presented in the figure. Moreover, the benchmark problems (BMP) or the section of the thesis where these subjects are studied are mentioned in the rightmost column. Steps 1 to 3 are introduced in Chapter Four. Then in Chapter Five, they are developed while exploring steps 4 and 5. Step 6, validation, is outlined in Chapter Six through Chapter Nine after presenting and computing the Benchmark Problems.



Figure 2: Benchmark problems' workflow for modeling, analysis, and validation

Table 1 presents the topic and comment/remark for each BMP and the chapters in which they are discussed.

Table 1: The topics and comments for Benchmark Problems

Chap.	BMP#	Topic	Comment / remark regarding the CATIA software	
Six	BMP1	Pure Tensile Load:	1- Imposing Nx or Ny,	2- Strains in the mid plane surface of the laminate is not directly accessible.
	BMP2	Pure Bending Load:	1- Imposing Mx or My,	2- CATIA presents the engineering curvature.
	BMP3	Pure Shearing Load:	1- Imposing Nxy or Nyx,	2- CATIA presents the engineering shear strain.
	BMP4	Pure Twisting Load on the Plate:	1- Imposing Mxy or Myx,	2- Unsatisfying results from the FEA solvers specially ABAQUS.
	BMP5	Temperature Effect:	1- Unidirectional lamina,	2- Limited problem conditions can be solved: First, Small temperature gap.
	BMP6	Temperature Effect:	1- Woven Fabric,	Second, when the longitudinal thermal expansion coefficient is positive or small compared to the transverse thermal expansion coefficient.
	BMP7	3D vs. 2D orthotropic properties:	1- Unidirectional plies,	2- Superposition of loads,
	BMP8	3D vs. 2D orthotropic properties:	1- Woven Fabric,	3- The linear responses of the CATIA FEA Solver are investigated.
	BMP9	Draping in the "+Z" vs. "-Z" directions:	Two preconditions;	First, the rosette and draping should be aligned. Second, reversing the sign of Bending loads and shearing loads.
	BMP10	Axial Torsion on a Cylinder:	The thin symmetrical the CLT method.	laminates with small thicknesses compared to the radius are comparable with
	BMP11	Pressure load on the outside surface of a Sphere:	1- Limited due to Mfg. Mthd. ($0^\circ < \theta < 5^\circ$).	The thin symmetrical laminates with small thicknesses compared to the radius are comparable with the CLT method.
Seven	BMP12	Drop-off condition:	1- Meshing the complex geometries	2- The option to import the properties as "Symmetrical" is unchecked 3- Multiple methods to define the Laminates are investigated
	BMP13	Transient Responses	1-Natural frequency validation	2- Three Cases with different geometries and stacking sequences under dynamic loading conditions are suggested and validated.
	BMP14	Thermal Buckling	1- HoneyComb mechanical properties	2- The first buckling modes of a sandwich panel are validated
Eight	BMP15	Buckling in a stiffened panel	1- Meshing the complex geometries	2-The buckling modes of the stiffened plate with different width and stiffener height under uniaxial compressive load are validated
	BMP16	Propeller	1- Meshing the complex geometries	2- The "Tsai Hill" failure criterion is employed to predict the failure of the elements on a propeller, and IRF<1 is concluded by adding layers in different
	BMP17	Aircarf Wing	1- Meshing the complex geometries	2- Loading acting on an Aircraft Wing in Pull up Maneuver

Benchmark Problems are considered with different geometries (cross-sections), such as plate, cylindrical, spherical, curved geometry and "T" shape, and various loads, boundary conditions are implemented to ascertain the sensitivity of the FEA solver. In addition, parametric studies are investigated for each Benchmark Problem, and the harshest critical conditions are applied to validate the proposed problems. For example, the rectangular shape was selected to proceed with a stronger argument.

Designing composite materials has some unique challenges in comparison to isotropic materials. As a result, 24 different cases are selected and studied, showing a comprehensive collection of stacking sequences, detailed in Appendix A.

Figure 3 illustrates the challenges and objectives of each step, from designing the geometry and laminate to preparation for FEA analysis and post-processing validations. The figure consists of two sections. The top box introduces the material available from different literature. Sometimes these references are unclear for the reader. For instance, the literature does not state the relation between load conditions and the Symmetrical check box in the importing properties interactive window. The reason is that these references' viewpoint does not cover FEA analysis. The same condition exists for the references covering the FEA analysis employing isotropic materials, and they do not cover composite aspects in the numerical computations.

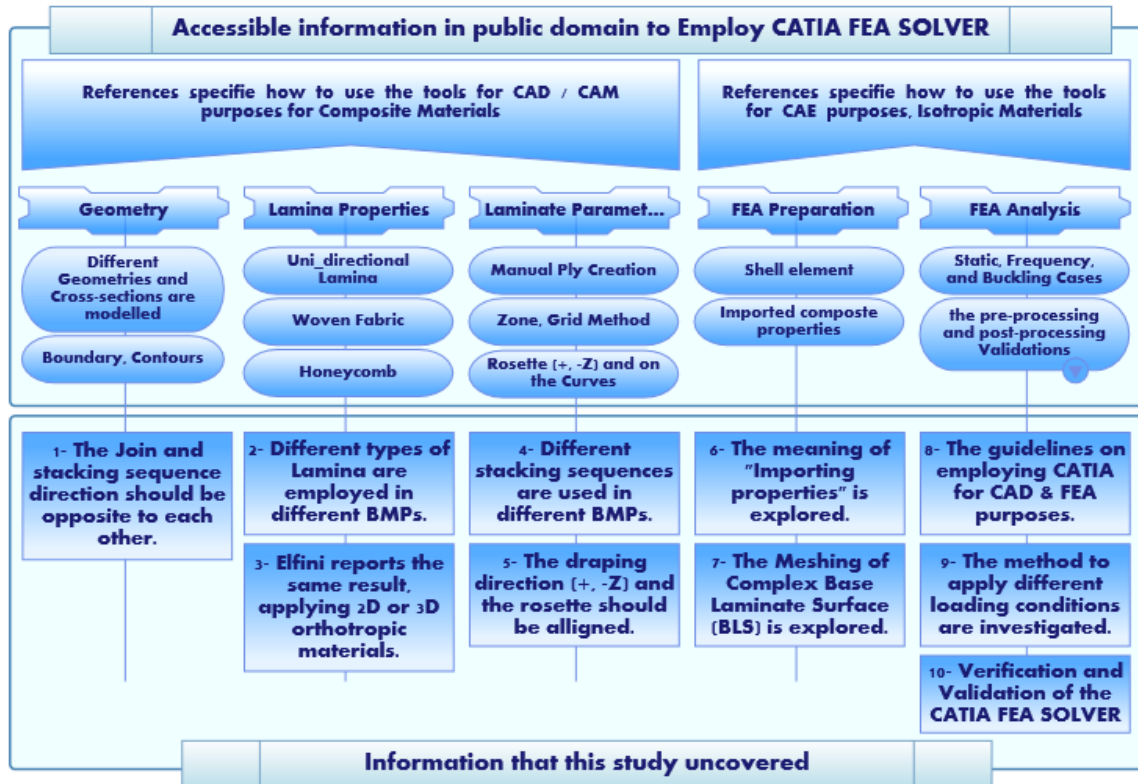


Figure 3: The challenges and questions answered in this study

The findings presented in this study are highly influenced by the exploratory work carried out in [10]. The current study aims to develop the original problems proposed in the indicated reference with more complex laminate parameters, geometries, and loading conditions (BMP1, 5, 6, 7, 8, 9, 13 and 16). While developments in [10] are used as the general guidelines; however, for some BMPs, new approaches to model the laminate parameters in part or in total are used such as BMP 10, 12 and 14. Furthermore, some BMPs in this thesis introduce standalone new topics (BMP2, 3, 4, 11, 14, 15, and 17).

Objective statement to this thesis:

In summary, since no comprehensive documentation regarding analyzing composite material has been released from the CATIA developers, this study tries to accumulate and tabulate report card tests for some discerning selected Benchmark Problems (BMPs). This study specifies how to use CATIA FEA SOLVER and the type of problems it can address. The verifications of these problems are sought through Classical Laminate Theory (CLT), other established FEA commercial software when needed and/or published references.

CHAPTER TWO:

BASIC CONCEPTS

To conduct an FEA analysis, one first needs to correctly understand the fundamentals, then model the geometry, material properties, loads, and boundary conditions. Interpretation of the results is the final step.

2.1 CATIA FEA Solver

CATIA Software can formulate limited types of engineering problems to conduct an FEA analysis. The Hooke's Law ($F = K \cdot \Delta X$) shows the relation between force and displacement for a simple axial spring, is also the fundamental assumption for FEA analysis in this software.

The CATIA solver uses the generalized Hooke's law described by the constitutive matrix (D), Strain vector (ϵ), and the Stress vector (σ) through equation (1). The matrix D is a function of Poisson Ratio and Young's Modulus [11].

$$\sigma = D * \epsilon \quad 1$$

Considering the stress-strain relationship in the linear elastic region, the CATIA solver provides accurate results. Beyond the linear elastic region, further analysis can be conducted with more advanced commercial solvers [12]. Moreover, visualizing the pre-processing specifications directly on the mesh—such as mesh visualization, Local axis symbol, Thickness fringe—and generating images and reports are some embedded capabilities of the FEA Solver [13]. In addition, some of the FEA's capabilities of CATIA include Static structural analysis, Linear Buckling, Thermal Stresses Analysis, Linear Dynamic Analysis.

CATIA has a simple, comprehensive and user-friendly environment that allows engineers to design and analyze their parts efficiently. Single parts analysis (GPS), hybrid assembly analysis (GAS), and dynamic response analysis (GDY) are some basic modules that CATIA offers at the preliminary design level. Users have additional options, such as pre/post-processing and solving (EST), surface meshing (FMS), and solid meshing (FMD) [14].

GPS module applies to single small to medium size models (parts), with automatic meshing for Structural Analysis. The GAS module provides structural analysis for several purposes, most notably hybrid assemblies (products), assembly analysis, and a full set of mechanical interaction tools for simulation purposes. GDY module or Generative Dynamic Structural Analysis is used for frequency and time response, as well as excitation through modulation of loads or imposed displacements in time or frequency domains. CATIA Elfini Structural Analysis consists of advanced linear structural analysis

and composite materials properties available in the EST module. Finally, the FMS module provides Advanced Surface Meshing tools for complicated surfaces [14]. These modules are all seamlessly integrated within the CATIA program [15].

Figure 4 presents the mentioned modules in more detail. The areas pertinent to this Thesis are specified in bold black colour.

Row	A	B	C	D	E
	Properties	Meshing	Pre-processing	Solving	Post-processing
1	Solid (properties)	Octree Solid mesher	Standard loading	Static Analysis	Standard post-processing
2	Shell properties	Octree Surface mesher	Pressure	Frequency Analysis	Displacements
3	Beam (standard)	Beam Mesher	Densities	Single case management	Von misses criteria
4	Isometric materials	Virtual parts mesher	Forces	Adaptivity computation	Principal stress
5	Smooth and rigid properties on virtual parts	Connection mesh	Accelerations	Contact Analysis	Local Error
6	connection properties	Remote connection	Imposed Displacements	Bolt tightening Analysis	Standard Visualization
7	rigid	Incompatible mesh connection	Standard Restraints	Pressure Fitting Analysis	Deformed shape
8	smooth	Weld-point connection mesh	Standard Additional Mass definition	Frequency response analysis	Animation
9	contact	seam weld connection mesh	Time and Frequency modulation definition	Time response analysis	Cutting Plane
10	sliding connections	Adhesive weld connection mesh	Import of excel or txt files	Multi case management	Contour Plot
11	beams	Point to point connections	White noise definition	Advanced cases	Global Sensors
12	springs	Advanced beam meshing	Load excitation combination	Buckling Analysis	Maximum Stress
13	Bolt-tightening	Compatible with existing mesh	Imposed Displacement Excitation	Solution combination	Frequencies
14	MPC	Advanced parameters	Damping Definition	Static constrained modes	Global Error
15	Etc.	Advanced Surface mesher	Advanced loading	Advanced Frequency	Standard Reporting
16	Advanced Properties	Compatible with existing mesh	Bearing loads	Frequency shifting	Sensor follow-up
17	Advanced beam properties	Based on geometry simplification	Therm o-mechanical loading	load stiffening	time of frequency domain
18	Bars	Local mesh parameters definition	Grid based Force import	Large Model Analysis	FE Visualization
19	Membrane , shear panel	Various types mesh algorithm	Data mapping	64 bits on AIX (V5R14)	time of frequency domain
20	Data-Mapping	Mesh local Edition	Inertia definition	Lanczos model solver	Advanced post-processing
21	Orthotropic materials	Smoothing based on mesh quality criteria	Pre-processing	Parallel processing	Strains
22	Composites	Mesh by transformation	Visualization on FE		Reactions
23	Transfer from design definition	1D extrusion	Grouping		Contact pressure and output
24	Composite properties	Rotation, Symmetry Translation	Import of V4 Pre-processing		Local & Advanced Sensored
25	Import of V4 FE model	Offsetting			FE Image customization
26		Mesh Analysis tools	LEGEND: The CELLS are COLOURED based on the modules that they belong to.	GPS	Advanced visualization
27		Mesh Quality Analysis		GAS	Advanced Reporting
28		Mesh interference checking		GDY	Report Customization
29		Cutting plane Analysis		EST	Cases combination
30		Compatible mesh connection generation		FMS	Envelope cases

Figure 4: CATIA modules available for the designers

The graphic user interface (GUI) of CATIA presents different workbenches using the modules mentioned above. Figure 5 illustrates some workbenches which can be employed for CAD/CAE purposes dealing with composite materials. In Chapters Four through to Chapter Nine, some of these modules are used extensively.

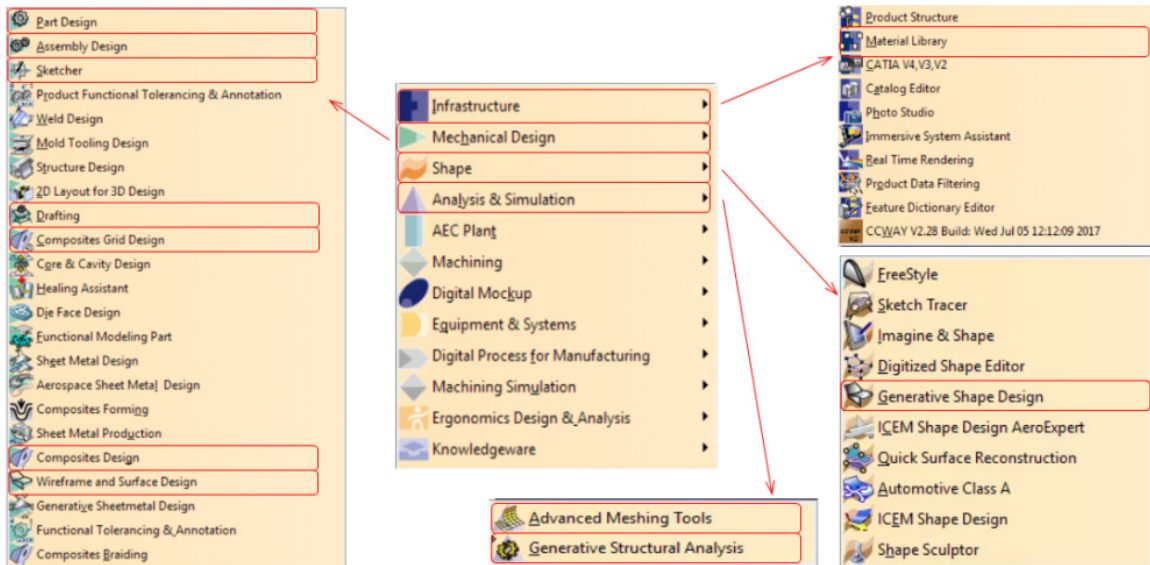


Figure 5: Some Workbenches Used Concerning Composite Materials

2.2 ASTM Code

The ASTM international composite standards are designed to evaluate and determine different composite materials' shear, tensile, flexural, and compressive properties [16]. Table 2 shows the number of standards in each classified group.

Table 2: ASTM composite standards classifications

	Classification title	The number of relative standards
1	Composites for Civil Structures	12
2	Constituent/Precursor Properties	10
3	Editorial and Resource Standards	4
4	Interlaminar Properties	6
5	Lamina and Laminate Test Methods	20
6	Sandwich Construction	23
7	Structural Test Methods	14

Except for the third row, almost all the nearly 80 standards focus on providing procedures on how to conduct different tests. Note that, composites respond differently, depending on the operational mode and the nature of the constraints and loads.

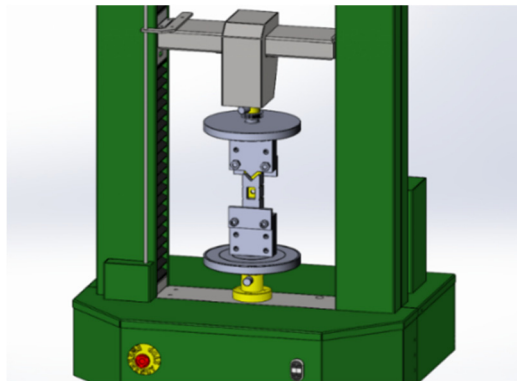


Figure 6: Open-Hole compressive strength composite test machine [17]

For instance, according to ASTM D6484, the test machine for open-hole compressive strength of a multidirectional balanced symmetric composite contains continuous fibre or discontinuous fibres (tape or fabric) are presented in Figure 6. The standard ASTM D6484/D648M-14 topic is the Standard Test Method for Open-Hole Compressive Strength of Polymer Matrix Composite Laminates.

Released testing methods issued by ASTM are just general ones, and for more specific problems, the manufacturer should design some practical situations to test the final product. For nearly every type of question, a unique testing method is needed, which is a challenge for designers. For example, Figure 7 illustrates the static test of the ultimate-load wing-up bending test. The test aircraft basically never flies. This test is a part of the certification process, which is 150% of the most expected extreme forces [18].



Figure 7: Boeing 787 Wing Flex Test [18]

Considering the number of Benchmark Problems conducted in this study, it was not feasible to compare them with experimental data. Therefore, Classical Hand Calculation (CHC) and other FEA Solvers are employed to validate the results.

In addition, the dimensions for the geometries assigned for the simple Benchmark Problems were extracted from ASTM standards. Similarly, applied loads must impose a secure elastic strain during the deformation that is less than 0.002 for strain (ϵ) [19], [20].

2.3 Classical Hand Calculations

CHC (based on the Classical Lamination Theory) is a valuable tool that engineers can use to predict the expected deformation before simulating the model using a commercial FEA Solver. Predicting the layers containing higher stresses, stress concentration location, and deformed shape are essential to check if one correctly modelled the part [3]. Otherwise, one may end up with meaningless unrealistic patterns of deformation and results.

Before conducting a Finite Element Analysis, it is essential to have a thorough understanding of five considerations: the composite material lamina and laminate, Classical Lamination Theory, rule of mixture, the importance of constituent properties for each type of composite material such as woven, unidirectional, or honeycomb core. The architecture of the composite has a major influence on the stiffness and compliance properties, and on the principal and transformed directions defining the relation between stress and strain in the mid-plane surface.

The method to compute the stiffness matrix for a single element or through CLT for a laminate is presented in Figure 8. The final equation is simple: The external loads are equal to stiffness matrix multiplied by displacements. The relationship between in-plane load and strain and out of plane moment and curvature for a plate geometry, detailed in Chapter Three, is computed as follows.

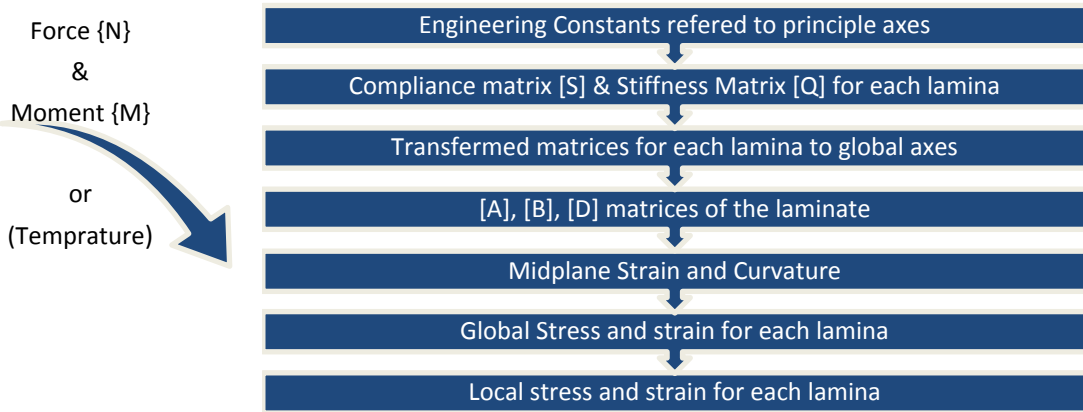


Figure 8: Stress-Strain Computation Flow Chart of a Laminate

2.4 Other FEA Solvers Used for Verifications in the Thesis:

Though tedious, it is possible to compute 15 unknown components entities, six stresses (σ_{ij}), six strains (ϵ_{ij}), and three displacements (u, v, w) using hand calculations for geometries resembling a single element. However, for other geometries, finite element analysis must be employed [21].

FEA leads to approximate results from a finite number of 1D, 2D, and 3D elements (first or second order) used to define geometry connected via nodes. However, as previously noted modelling by the correct type of elements gives an uncertain result and should be verified using simple models to create physical understanding and results [21]. When the geometry of the composite part to be analyzed becomes complicated, the potential of using hand calculations based on CLT is not available. At that point, one must resort to Finite Element Analysis to arrive at numerical predictions.

Here, for some cases, the results generated by CATIA are validated using other software, such as ANSYS and ABAQUS. A brief description of these two well known software are give below.

2.4.1 ANSYS

The primary reason for using other FEA Solvers in this study was the complexity of the calculations when analyzing complicated geometries. ANSYS is well-known commercial FEA software that features ACP pre/post-processing, which can be used to analyze different phenomena, from micro scale fibres/matrix to the macro-scale of laminate [22].

ANSYS provides a range of shell and solid elements, linear or non-linear analyses, and other possibilities. The ANSYS workbench is designed for relatively simple geometries, parts or layups. For example, ACP Preprocessing and ACP Post-Processing component systems are integrated with the ANSYS software and intuitively define layup. The modelling process regarding the manufacturing process and post-processing allows detailed failure analysis (ply-by-ply). Fibre directions and draping analysis are extended, and the visualization of rosette, fibre and layup directions is provided using section cut, sampling point toolbars [23].

2.4.2 ABAQUS

Another well-known FEA Solver used in this study is ABAQUS. It contains different methods to model composite materials using various shell elements, continuum-shell, and solid mesh with various restraints and load conditions (Figure 9 illustrates three different meshes).

Micro, macro, and mixed reinforcement modelling and sub-modelling are techniques used based on the purpose of the analysis in ABAQUS. In addition, ABAQUS can model progressive damage and failure interfaces using Hashin criteria, UMAT, VUMAT, VCCT, and Cohesive element and contact [24].

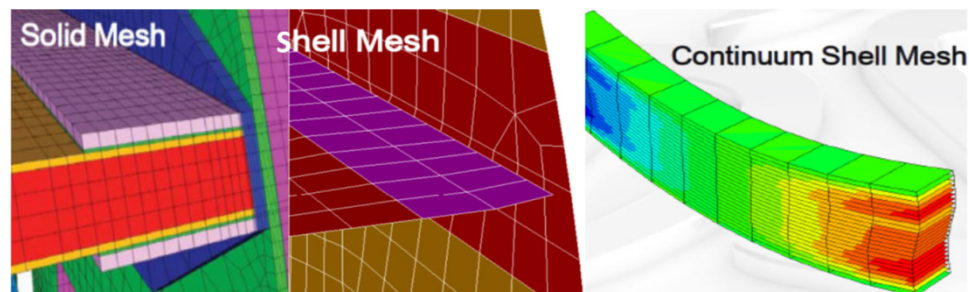


Figure 9: Different mesh used in ABAQUS [24]

In addition, ABAQUS can be coupled with other software—including Isight, Tosca, and Fe-Safe—to solve some complex problems, such as non-linear constitutive laws, optimization, and fatigue analysis, respectively [25].

CHAPTER THREE:

COMPOSITE MATERIALS, REVIEW

3.1 Material Properties

ASTM standard defines composite materials as combined insolvable, comprising several different constituents that form functional engineering materials [26]. Composites' functionality depends on being incredibly strong, light, corrosion-resistant, and non-conductive [27]. However, they are expensive to design, manufacture, inspect, and repair. [28] In contrast, it can be argued that long-term cost savings typically offset the high initial costs. Table 3 offers a ranked comparison of the advantage or desirability of metals, bulk ceramic and fibres ceramic, and polymers.

Table 3: Structural performance ranking of conventional materials [29]

Row	Properties	Metals	Ceramics		Polymers
			Bulk	Fibres	
1	Tensile strength	+	-	++	v
2	Stiffness	++	v	++	-
3	Fracture toughness	+	-	v	+
4	Impact strength	+	-	v	+
5	Fatigue endurance	+	v	+	+
6	Creep	v	v	++	-
7	Hardness	+	+	+	-
8	Density	-	+	+	++
9	Dimensional stability	+	v	+	-
10	Thermal stability parameter	v	+	++	-
11	Hygroscopic sensitivity	++	v	+	v
12	Weather ability	v	v	v	+
13	Erosion resistance	+	+	+	-
14	Corrosion resistance	-	v	v	+

Legend: (v) variable, ++ Superior, +Good, -Poor.

Based on the data outlined in Table 3, if one wants to secure the advantages for a given application, it would be highly desirable to combine materials to utilize each constituent's best in a synergistic way. For example, ceramic fibres in a polymeric matrix would serve as a complementary combination [29].

The fibre-reinforced metal matrix composites are used in the space shuttles, automobiles, bicycles, golf clubs, electronic substrates, and many other consumer products. They have several characteristics that make them advantageous, including low coefficient of thermal expansion and high special stiffness, strength, and thermal conductivity. During the 1940s, boron aluminum tubular struts were used for the first time in the mid-fuselage section as the frame and rib truss members. This led to a 45% reduced weight compared with the baseline aluminum design (Appendices Figure A: Mid-fuselage structure of Space Shuttle Orbiter showing boron-aluminum tubes (photo courtesy of U.S. Air Force/NASA) [30]).

3.1.1 Lamina's Engineering Constants

3.1.1.1 General composite materials

There are a large number of possibilities that can be used to design composite materials to achieve properties, as outlined in Table 3. However, the accuracy of the table depends on a reliable database of material properties, standardized methods, models, and material processing techniques. Composite materials' design and analysis process are more complex due to the numerous options available [29], [31].

In other words, analyzing engineering problems depends on the value of a material's mechanical properties. Conventional isotropic materials with only two independent properties can sufficiently analyze some problems. In contrast, composite materials need complex proof tests that measure an excessive number of independent elastic constants [29].

Table 4 classifies composite materials based on the number of independent elastic constants. General anisotropic materials have no plane of symmetry; therefore, the mechanical properties are different at each point and in each direction. Furthermore, when considering the symmetry of stress and strain tensors ($\sigma_{ij} = \sigma_{ji}$, $\epsilon_{ij} = \epsilon_{ji}$), it becomes evident that anisotropic materials have 36 independent elastic constants.

Table 4 : Number of independent elastic constants for various types of materials

Row	Material	Quantity
1	General anisotropic material	81
2	Anisotropic material considering the symmetry of stress and strain tensors	36
3	Anisotropic material with elastic energy considerations	21
4	General orthotropic material	9
5	Orthotropic material with transverse isotropy	5
6	Isotropic material	2

The lamina has several mechanical properties, such as Young's Modulus (E), Poisson's ratio (ν), Shear modulus (G), and analytically measured constants. These constants include shear-extension coupling coefficients (η) and shear-shear coupling coefficients (μ). All of these properties can be physically measured through specimen testing. It is crucial to follow the test procedures introduced in 2.2; otherwise, the sample will deform and twist in multiple directions due to significant coupling between the applied stresses.

The stress-strain relation (constitutive law) for anisotropic material with symmetry of components about its diagonal is presented in equation (2) [32]. In addition, the types of different coupling are illustrated immediately below [32], [33].

$$\begin{matrix} \text{Extension} \\ \left[\begin{matrix} \epsilon_{11} \\ \epsilon_{22} \\ \epsilon_{33} \\ \gamma_{23} \\ \gamma_{13} \\ \gamma_{12} \end{matrix} \right] \end{matrix} = \begin{matrix} \text{Extension-Extension Coupling} \\ \left[\begin{matrix} \frac{1}{E_1} & -\frac{\nu_{21}}{E_2} & -\frac{\nu_{31}}{E_3} \\ -\frac{\nu_{12}}{E_1} & \frac{1}{E_2} & -\frac{\nu_{32}}{E_3} \\ -\frac{\nu_{13}}{E_1} & -\frac{\nu_{23}}{E_2} & \frac{1}{E_3} \end{matrix} \right] \end{matrix} \begin{matrix} \text{Shear-Extension Coupling} \\ \left[\begin{matrix} \eta_{41} & \eta_{51} & \eta_{61} \\ \eta_{42} & \eta_{52} & \eta_{62} \\ \eta_{43} & \eta_{53} & \eta_{63} \end{matrix} \right] \end{matrix} \begin{matrix} \text{Shear-Shear Coupling} \\ \left[\begin{matrix} \frac{1}{G_4} & \frac{\mu_{54}}{G_5} & \frac{\mu_{64}}{G_6} \\ \frac{\mu_{45}}{G_4} & \frac{1}{G_5} & \frac{\mu_{65}}{G_6} \\ \frac{\mu_{46}}{G_4} & \frac{\mu_{56}}{G_5} & \frac{1}{G_6} \end{matrix} \right] \end{matrix} \begin{matrix} \text{Shear} \\ \left[\begin{matrix} \sigma_{11} \\ \sigma_{22} \\ \sigma_{33} \\ \sigma_{23} \\ \sigma_{13} \\ \sigma_{12} \end{matrix} \right] \end{matrix}$$

The primary objective of using composite material is to maximize the useful mechanical properties needed for a design and reduce the effects of the three couplings. Focusing on more realistic practical cases, only three bottom composite materials stated in Table 4 are investigated in this study.

3.1.1.2 Orthotropic materials (lamina stiffness)

The isotropic materials have an infinite number of planes of symmetry [29]. In contrast, general orthotropic materials have three planes of symmetry. Figure 10 illustrates the three planes of symmetry for a unidirectional orthotropic material, as well as the principal material axes perpendicular to each plane. In this context, it is important to note that E_1, E_2, E_3 for isotropic materials are identical.

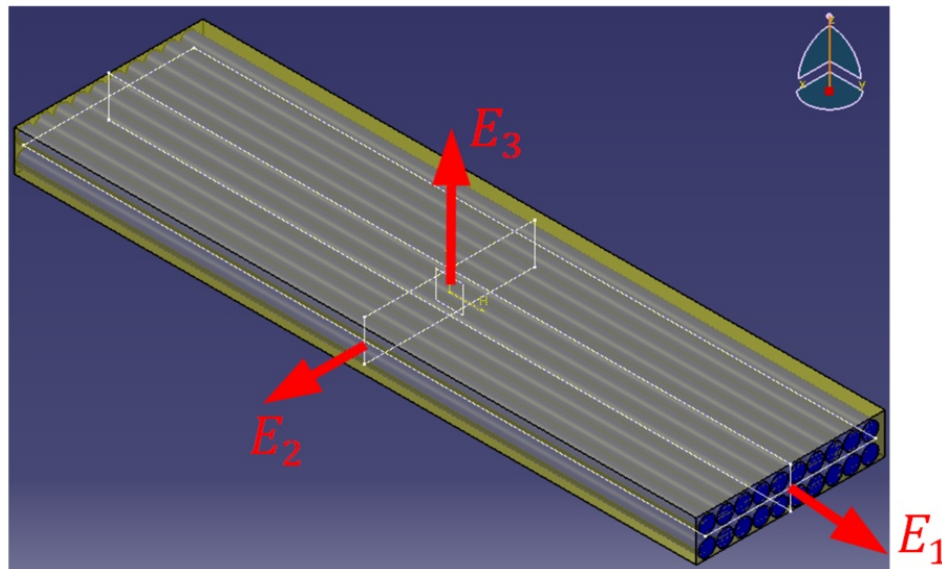


Figure 10: Planes of symmetry for a unidirectional orthotropic material

A 3D unidirectional lamina has nine independent elastic mechanical properties: E_1, E_2, E_3 , (Young's modulus), G_{12}, G_{23}, G_{13} (shear modulus), and $\nu_{12}, \nu_{23}, \nu_{13}$ (Poisson's ratios) [29]. Three principal directions—1, 2, 3—are perpendicular to three planes of symmetry.

Therefore, Extension- Extension Coupling, Shear-Shear Coupling (μ), and Shear-Extension Coupling (η) are zero. The final symmetric compliance matrix based on Hooke's law are modified in equation (3), which [29] presents as

$$\begin{bmatrix} \varepsilon_1 \\ \varepsilon_2 \\ \varepsilon_3 \\ \gamma_4 \\ \gamma_5 \\ \gamma_6 \end{bmatrix} = \begin{bmatrix} \frac{1}{E_1} & \frac{-\nu_{21}}{E_2} & \frac{-\nu_{31}}{E_3} & 0 & 0 & 0 \\ \frac{-\nu_{12}}{E_1} & \frac{1}{E_2} & \frac{-\nu_{32}}{E_3} & 0 & 0 & 0 \\ \frac{-\nu_{13}}{E_1} & \frac{-\nu_{23}}{E_2} & \frac{1}{E_3} & 0 & 0 & 0 \\ 0 & 0 & 0 & \frac{1}{G_{23}} & 0 & 0 \\ 0 & 0 & 0 & 0 & \frac{1}{G_{13}} & 0 \\ 0 & 0 & 0 & 0 & 0 & \frac{1}{G_{12}} \end{bmatrix} * \begin{bmatrix} \sigma_1 \\ \sigma_2 \\ \sigma_3 \\ \tau_4 \\ \tau_5 \\ \tau_6 \end{bmatrix} \quad 3.$$

According to the Kirchhoff-Love assumptions, the Classical Laminate Theory (CLT) directly extends classical plate theory for the homogeneous isotropic material [34], [35]. Regarding the Plane Stress assumption, the number of independent parameters is reduced to only strains in the “x,” “y” directions and the in-plane shear strain. It should be noted that the strain in the thickness direction is nonzero. However, it is related to the in-plane stresses through the following equation:

$$\begin{aligned} \sigma_3 = 0, \quad \tau_4 = \sigma_{13} = 0, \quad \tau_5 = \sigma_{23} = 0, \quad \gamma_4 = \varepsilon_{13} = 0, \quad \gamma_5 = \varepsilon_{23} = 0 \\ \varepsilon_3 = \frac{-\nu_{12}}{E_1} * \sigma_1 + \frac{-\nu_{21}}{E_2} * \sigma_2 \end{aligned} \quad 4.$$

The number of independent elastic constants for 3D orthotropic material with transverse isotropy is five ($E_1, E_2, G_{12}, G_{23}, \nu_{12}$):

$$E_2 = E_3, \quad G_{12} = G_{13}, \quad \nu_{12} = \nu_{13}, \quad \text{and } \nu_{21} = \nu_{12} * \left(\frac{E_2}{E_1}\right) \quad 5$$

Accordingly, four independent elastic parameters are sufficient to determine a 2D orthotropic layer's mechanical properties under plane stress ($E_1, E_2, G_{12}, \nu_{12}$). As suggested in [23], the simplified equation (6) of the compliance matrix representing the relation between stress and strain is

$$\begin{bmatrix} \varepsilon_1 \\ \varepsilon_2 \\ \gamma_6 \end{bmatrix} = \begin{bmatrix} S_{11} & S_{12} & 0 \\ S_{21} & S_{22} & 0 \\ 0 & 0 & S_{66} \end{bmatrix} * \begin{bmatrix} \sigma_1 \\ \sigma_2 \\ \tau_6 \end{bmatrix} = \begin{bmatrix} \frac{1}{E_1} & \frac{-\nu_{21}}{E_2} & 0 \\ \frac{-\nu_{12}}{E_1} & \frac{1}{E_2} & 0 \\ 0 & 0 & \frac{1}{G_{12}} \end{bmatrix} * \begin{bmatrix} \sigma_1 \\ \sigma_2 \\ \tau_6 \end{bmatrix} \quad 6.$$

3.1.2 Laminate Engineering Constants

3.1.2.1 Transformation of stress and strain (two-dimensional)

Figure 11 illustrates the direction (θ) of the sample lamina from the laminate global coordinate system. The figure also shows the corresponding stresses and strains in the local coordinate system and laminate global coordinate system. The engineering constants of each lamina in the local coordinate system should be transformed to the laminate global coordinate system (CS). After computing the global CS strain, it should be converted back to the lamina local CS to present the maximum stresses.

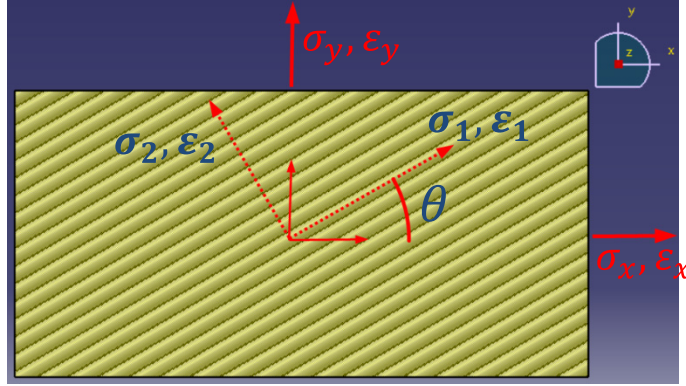


Figure 11: Lamina stress and strain in the global and local coordinate systems

$$\begin{bmatrix} \sigma_1 \\ \sigma_2 \\ \tau_6 \end{bmatrix} = [T] \begin{bmatrix} \sigma_x \\ \sigma_y \\ \tau_s \end{bmatrix} \quad \text{or} \quad \begin{bmatrix} \epsilon_1 \\ \epsilon_2 \\ \frac{1}{2}\gamma_6 \end{bmatrix} = [T] \begin{bmatrix} \epsilon_x \\ \epsilon_y \\ \frac{1}{2}\gamma_s \end{bmatrix} \quad (\text{transformation matrix } [T])$$

$$[\sigma] = \{[Q]\} * [\epsilon] \Rightarrow \begin{bmatrix} \sigma_1 \\ \sigma_2 \\ \tau_6 \end{bmatrix} = \begin{bmatrix} Q_{11} & Q_{12} & 0 \\ Q_{21} & Q_{22} & 0 \\ 0 & 0 & Q_{66} \end{bmatrix} * \begin{bmatrix} \epsilon_1 \\ \epsilon_2 \\ \frac{1}{2}\gamma_6 = \epsilon_{12} \end{bmatrix}$$

The transformed stiffness matrix ($[T]^{-1} * [S] * [T]$) leads to the equation (7), which in [36] illustrates the transformed compliance matrix as a function of principal lamina compliances in the general coordinate system as follows:

$$\begin{bmatrix} Q_{xx}(\theta) \\ Q_{xy}(\theta) \\ Q_{yy}(\theta) \\ Q_{xs}(\theta) \\ Q_{ys}(\theta) \\ Q_{ss}(\theta) \end{bmatrix} = \begin{bmatrix} c^4 & 2c^2s^2 & s^4 & 4s^2c^2 \\ c^2s^2 & c^4 + s^4 & c^2s^2 & -4s^2c^2 \\ s^4 & 2c^2s^2 & c^4 & 4s^2c^2 \\ c^3s & -cs(c^2 - s^2) & -cs^3 & -2cs(c^2 - s^2) \\ cs^3 & cs(c^2 - s^2) & -c^3s & 2cs(c^2 - s^2) \\ c^2s^2 & -2c^2s^2 & c^2s^2 & (c^2 - s^2)^2 \end{bmatrix} * \begin{bmatrix} C_{11} \\ C_{12} \\ C_{22} \\ C_{66} \end{bmatrix} \Rightarrow$$

$$\Rightarrow [Q(\theta)] = \begin{bmatrix} Q_{xx}(\theta) & Q_{xy}(\theta) & Q_{xs}(\theta) \\ Q_{yx}(\theta) & Q_{yy}(\theta) & Q_{ys}(\theta) \\ Q_{sx}(\theta) & Q_{sy}(\theta) & Q_{ss}(\theta) \end{bmatrix} \Rightarrow \begin{bmatrix} \sigma_x \\ \sigma_y \\ \tau_{xy} \end{bmatrix} = [Q(\theta)] \begin{bmatrix} \epsilon_x \\ \epsilon_y \\ \gamma_{xy} \end{bmatrix} \quad 7$$

In this context, it is important to note that $c: \cos(\theta)$, $s: \sin(\theta)$).

3.1.2.2 ABD matrices

The compliance matrices in different angles $Q(\theta)$ for each lamina are calculated in the laminate coordinate system. Likewise, the coefficients of the [A], [B], and [D] matrices are calculated from equations (8), (9), and (10). The h_k and h_{k-1} represent the ply “k” position from the geometric mid-plane illustrated in Figure 12 [37]. Equation (11) shows these matrices for the sample laminate. In addition, the couplings governing the responses of the laminate in different loading conditions are presented.

$$A_{ij} = \sum_{k=1}^n Q_{ij}(\theta)(h_k - h_{k-1}) = \sum_{k=1}^n Q_{ij}(\theta)(t_k) \quad , i, j = x, y, s \quad 8$$

$$B_{ij} = \sum_{k=1}^n Q_{ij}(\theta) \frac{(h_k^2 - h_{k-1}^2)}{2} = \sum_{k=1}^n Q_{ij}(\theta)(t_k * \bar{z}_k) \quad , \bar{z}_k = \frac{z_k + z_{k-1}}{2} \quad , i, j = x, y, s \quad 9$$

$$D_{ij} = \sum_{k=1}^n Q_{ij}(\theta) \frac{(h_k^3 - h_{k-1}^3)}{3} = \sum_{k=1}^n Q_{ij}(\theta)(t_k * \bar{z}_k^2 + \frac{t_k^3}{12}) \quad , i, j = x, y, s \quad 10$$

From Above:

$$\begin{bmatrix} A_{xx} & A_{xy} & A_{xs} & B_{xx} & B_{xy} & B_{xs} \\ A_{xy} & A_{yy} & A_{ys} & B_{xy} & B_{yy} & B_{ys} \\ A_{xs} & A_{ys} & A_{ss} & B_{xs} & B_{ys} & B_{ss} \\ B_{xx} & B_{xy} & B_{xs} & D_{xx} & D_{xy} & D_{xs} \\ B_{xy} & B_{yy} & B_{ys} & D_{xy} & D_{yy} & D_{ys} \\ B_{xs} & B_{ys} & B_{ss} & D_{xs} & D_{ys} & D_{ss} \end{bmatrix} \quad 11$$

Shear-extension coupling (points to A_{xs}, A_{ys})
Bend-extension coupling (points to B_{xs}, B_{ys})
Bend-Twist coupling (points to D_{xs}, D_{ys})

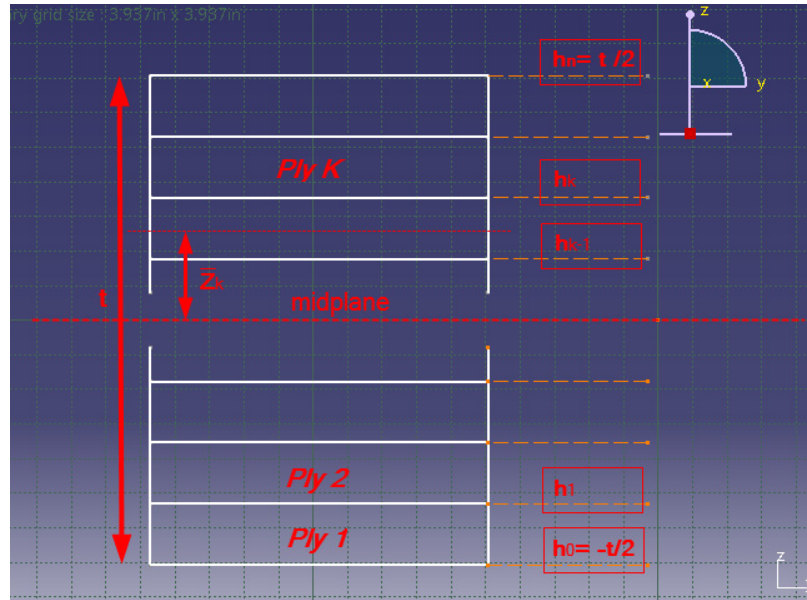


Figure 12: Ply coordinates in the “z” direction, numbered from the bottom

The Young's modulus in the "X" direction is based on equation (12), in which A_{11}, A_{12}, A_{22} are coefficients for [A] matrix, and "t" is the thickness of the composite plate [38].

$$E_x = \frac{1}{t} * (A_{11} - \frac{A_{12}^2}{A_{22}}) \quad 12$$

In addition, effective mechanical properties of symmetrical laminate are computable from equations in Table 5 below [29]:

Table 5: Effective mechanical properties of a symmetric laminate

Effective mechanical properties	Resulted from ([A] ⁻¹ Inverted Matrix)	Resulted from ([C] Compliance matrix)
E _{xx} (Pa)	(1/thickness)*A ₁₁	1/S ₁₁
E _{yy} (Pa)	(1/Thickness)*A ₂₂	1/S ₂₂
v _{xy}	A ₁₂ / A ₁₁	S ₁₂ / S ₁₁
v _{yx}	A ₁₂ / A ₂₂	S ₁₁ / S ₂₂
G _{xy} (Pa)	(1/Thickness)*A ₆₆	1/S ₆₆

3.2 Loads' Conditions

3.2.1 General load conditions for a flat element

General loading conditions imposed on a flat element consist of Tensile, Shear, Moment, and twisting loading conditions. These are illustrated in Figure 13 (directions refer to [39]). Equation (13) shows the relation between Force matrix[N], the Moment matrix [M], Strain matrix[ε], and the Curvature matrix[κ] using the coefficients of [A], [B], and [D] matrices [37].

$$\begin{bmatrix} N_x \\ N_y \\ N_s = N_{xy} \\ M_x \\ M_y \\ M_s = M_{xy} \end{bmatrix} = \begin{bmatrix} A_{xx} & A_{xy} & A_{xs} & B_{xx} & B_{xy} & B_{xs} \\ A_{xy} & A_{yy} & A_{ys} & B_{xy} & B_{yy} & B_{ys} \\ A_{xs} & A_{ys} & A_{ss} & B_{xs} & B_{ys} & B_{ss} \\ B_{xx} & B_{xy} & B_{xs} & D_{xx} & D_{xy} & D_{xs} \\ B_{xy} & B_{yy} & B_{ys} & D_{xy} & D_{yy} & D_{ys} \\ B_{xs} & B_{ys} & B_{ss} & D_{xs} & D_{ys} & D_{ss} \end{bmatrix} * \begin{bmatrix} \epsilon_x^0 \\ \epsilon_y^0 \\ \gamma_{xy}^0 \\ \kappa_x \\ \kappa_y \\ \kappa_{xy} \end{bmatrix} \quad 13$$

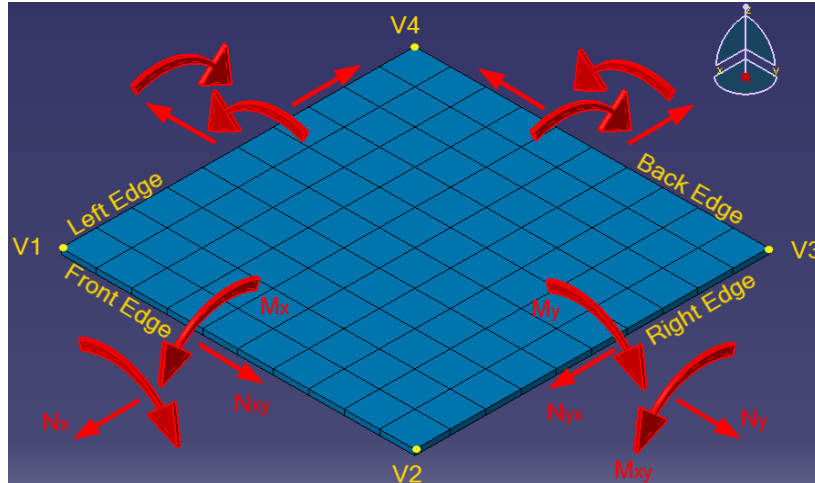


Figure 13: In-plane forces and moments on a laminate

The strain in the mid-plane surface is shown as (ϵ^0) in equation (13). In the Classical Laminate Theory, the strain component in the thickness direction is equal to zero (plane strain assumption: $\epsilon_z = 0$). The curvature matrix is constant at each node; therefore, corresponding strain and stress matrices are computable through the thickness. Figure 14 illustrates a laminate that consists of 4 laminas, as well as strain (ϵ_x) , relative layer moduli (E_x) , and stress (σ_x) respectively from left to right [3].

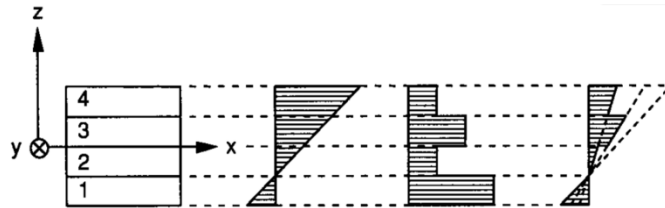


Figure 14: Strain, layer moduli and stress variations through the thickness ¹ [29]

3.2.1.1 Torsion load

The torsional stresses can be modelled using the general equation (14). In that case, " $N_{xy}=N_s$ " is computed from equation (13). In this context, it is important to note that imposing torque load (T) applied to a thin circular tube, shown in Figure 15, is equivalent to imposing " N_{xy} " to the tiny element on the surface of the cylinder, far from the loads, edges, and restraints [40].

$$N_{xy} = \frac{T}{2\pi r_m^2}, \quad r_m: \text{mean radius of the shaft (m)} \quad 14$$

¹ The figure reference number is (Fig.7.3)

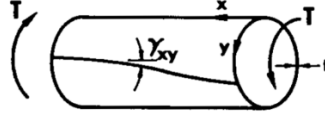


Figure 15: Torsion load imposed a thin tube

3.2.1.2 Pressure load

Circumferential stress (hoop stress) and longitudinal stress for thin-walled cylindrical pressure vessels are respectively obtained through equations (15) and (16). These two stresses for thin-walled spherical pressure vessels are obtained through equation (15) [40].

$$\sigma_x = \frac{Pr}{2t}, \quad N_x = \frac{Pr}{2} \quad 15$$

$$\sigma_y = \frac{Pr}{t}, \quad N_y = Pr \quad 16$$

P: internal gage pressure, psi or MPa

r: radius of the cylinder, in. or mm

t: the thickness of cylinder, in. or mm

3.2.1.3 Temperature and moisture effects:

The proof test to obtain the mechanical properties should be conducted in a predefined environment due to temperature and moisture influence [29], [16]. This is because the thermal cycle of the fabrication process may cause residual stresses and warpages. The reversible and irreversible deformations are computed from constitutive law. Equation (17) considers the uniform change in temperature (ΔT) and moisture (ΔM) for 2D orthotropic laminated composite [36]. The mechanical properties are assumed to remain the same during the changes in temperature (ΔT) and moisture (ΔM).

$$\begin{Bmatrix} \sigma_{11} \\ \sigma_{22} \\ \tau_{12} \end{Bmatrix} = \begin{bmatrix} Q_{11} & Q_{12} & 0 \\ Q_{12} & Q_{22} & 0 \\ 0 & 0 & Q_{66} \end{bmatrix} \begin{Bmatrix} \epsilon_{11} - \Delta T\alpha_{11} - \Delta M\beta_{11} \\ \epsilon_{22} - \Delta T\alpha_{22} - \Delta M\beta_{22} \\ \gamma_{12} \end{Bmatrix} \quad 17$$

$$\begin{Bmatrix} N \\ M \end{Bmatrix} = \begin{bmatrix} A & B \\ B & D \end{bmatrix} \begin{Bmatrix} \epsilon^o \\ \kappa \end{Bmatrix} - \begin{Bmatrix} N^T \\ M^T \end{Bmatrix}$$

α_{11}, α_{22} : The Coefficient of thermal expansion along with principal ply directions

β_{11}, β_{22} : The Coefficient of moisture expansion along with principal ply directions

N^T : Thermal stress resultant

M^T : Thermal moment resultant

3.2.1.4 Buckling load

A linear buckling analysis consists of finding the buckling mode, shapes, and the critical buckling factors corresponding to a specified load case applied to an elastic structure, which is considered in this thesis.

The laminated composite in fibre or laminate may experience instability caused by the compressive load [37]. The critical magnitude of this load leads to instability in the laminate level calculated from equation (18). In this equation, P_{cr} , λ , $P_{APPLIED}$ are respectively buckling load, load multiplier, and applied load [41].

$$P_{cr} = \lambda * P_{APPLIED} \quad 18$$

During the buckling of composite plates, the load multiplier is calculated from equation (19) [41]. In this equation, “a” and “b” are the dimensions of the plate in the “X” and “Y” directions, and “ N_x ” is the load per unit of length. The load multiplier resulting from different values of “n” and “m”, respectively representing the number of the half-waves in the “X” and “Y” direction. D_{11} , D_{12} , D_{66} , D_{22} are the coefficients of the [D] matrix.

$$\lambda = \left(\frac{\pi^2}{N_x} \right) \left(D_{11} * \left(\frac{m}{a} \right)^2 + 2 * (D_{12} + D_{66}) \left(\frac{n}{b} \right)^2 + D_{22} * \left(\frac{a}{m} \right)^2 \left(\frac{n}{b} \right)^4 \right) \quad 19$$

When studying the buckling modes, the first mode is the only mode with practical significance because instability will not have an opportunity to transfer to the second mode.

3.2.1.5 Drop-off Condition

The area named drop-off between the different thicknesses of layers is inevitable and may cause delamination. Thus, to stack up the stiffener and the skins, one should design the drop-off using Z-Spiking or “feathering at the ply drops methods [42]. Figure 16 contains related figures showing mentioned methods to design the drop-off.

In Figure 16, it is assumed that this area has non-linear characteristics because of the presence of the matrix. This is because CATIA software neglects the interactions forces inside the drop-off (step or ramp) area.

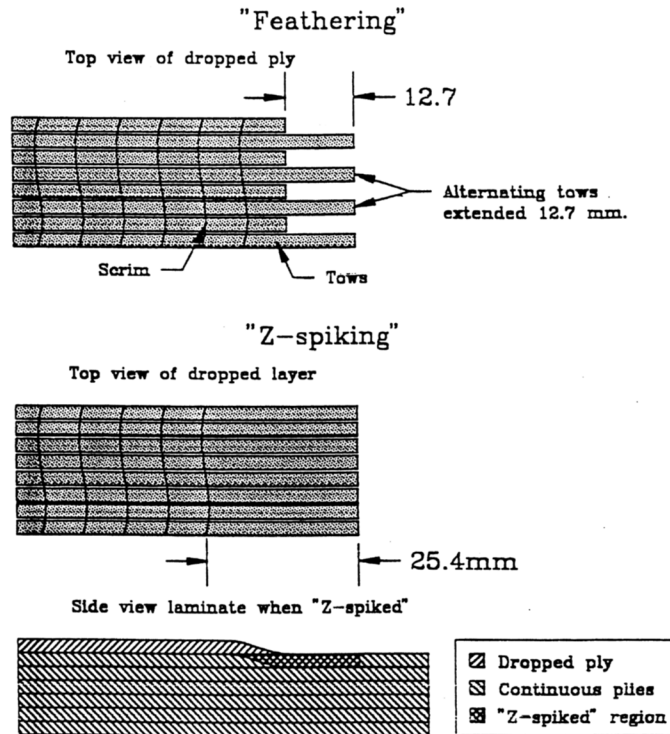


Figure 16: Feathering, Z-Spiking to prevent delamination[4]¹.

3.3 Stacking Sequence (Special characteristics)

The properties of general orthotropic materials rely on plies directions and distance from the mid-plane surface. The number of possibilities to build a laminate with different angles placed in individual distances (Figure 12) is enormously high. Hence, designers should pay attention to these issues.

In Appendix A some laminates (stacking sequences) are listed and the characteristics of each in comparison to each other are discussed. This list consists of General, Balanced, Symmetric, Cross-Ply, Angle-Ply, Asymmetric, Antisymmetric, Special Orthotropic, Quasi-Isotropic, and Carpet Plot gathered from [29], [40]. Each of these configurations has some drawbacks resulting from the three couplings based on components in the [ABD] matrices.

3.3.1 *Quasi-isotropic laminate*

In order to make a layup behave as a quasi-isotropic laminate, the number of plies should be more than three. All layers should consist of the same materials and thickness. The steps of the successive layers in a laminate group should be a multiplier of $(\frac{\pi}{n})$, in which "n" is equal to the number of different directions of layers [43]. Table 6 illustrates

¹ The figure reference number is (Fig.12)

$\Delta\theta$ relative to “n” for “n” varying between 3 and 7. The extensional stiffness matrix [A] of these materials behaves as a planar isotropic material presented in equation (20) [40]. Also, for this situation, it is known that $A_{11} = A_{22}$, $A_{16} = A_{26} = 0$, and $A_{66} = \frac{A_{11}-A_{22}}{2}$ [44].

Table 6: Quasi-isotropic material, Fibre orientation when “n” is 3 to 7

n	3	4	5	6	7
$\Delta\theta$	60	45	36	30	26

$$[A] = \begin{bmatrix} \frac{E}{1-\nu^2} & \frac{\nu E}{1-\nu^2} & 0 \\ \frac{\nu E}{1-\nu^2} & \frac{E}{1-\nu^2} & 0 \\ 0 & 0 & \frac{E}{2(1+\nu)} \end{bmatrix} * h \quad 20$$

Due to tetragonal characteristic ($A_{11} = A_{22}$), when the loads (N_x and or N_y) and the relative restraints are changed by 90° , the results considering the [A] matrix remains the same. It is important to note that, based on ASTM standard, D3878-19 quasi-isotropic materials should be balanced and symmetric [26].

3.4 Strength Criteria

Different references show that the fibres mainly influence the stiffness of orthotropic composites. The strength attributes are in general a microscopic phenomenon which cannot be modelled in the CATIA program. Here, it is assumed that the ultimate strength for a lamina is predetermined by experimental test methods.

In terms of the macroscopic scale, lamina failure theories can be classified into three categories: (1) non-interactive theories, such as maximum stress or maximum strain theories, (2) partially interactive theories, and (3) interactive theories, such as Tsai-Hill or Tsai-Wu theories. Originally, Hill’s theory was developed for homogeneous anisotropic ductile materials. Azzi and Tsai adapted it in 1965 to anisotropic heterogeneous and brittle composites, and it introduced the so-called Tsai-Hill theory [29].

Tsai-Hill failure criteria predict overall failure mode using equations involving all the components' stresses divided into fibre-dominated failure and matrix-dominated ones, and material with different strengths in tensile and compression [45]. This method can only predict the failure based on von Mises distortional energy yield criteria, but not the Failure Mode [46]. Equation (21) presents the Tsai-Hill failure criteria for in-plane loading in a 3D state of stress in CATIA documentation [47]:

$$\left(\frac{\sigma_x}{S_1}\right)^2 + \left(\frac{\sigma_y}{S_2}\right)^2 + \left(\frac{\tau_{xy}}{S_{12}}\right)^2 + \left(\frac{\tau_{xz}}{S_{13}}\right)^2 + \left(\frac{\tau_{yz}}{S_{23}}\right)^2 - \frac{\sigma_x \sigma_y}{S_1^2} \leq 1 \quad 21$$

$$S_1 = S_{1C} \text{ if } \sigma_x \leq 0, \quad S_1 = S_{1T} \text{ if } \sigma_x > 0$$

$$S_2 = S_{2c} \text{ if } \sigma_y \leq 0, \quad S_2 = S_{2t} \text{ if } \sigma_y > 0$$

For the $\frac{\sigma_x \sigma_y}{S_1^2}$ term; if $\sigma_x \sigma_y \geq 0$, $S_1 = S_{1T}$; otherwise $S_1 = S_{1C}$

Figure 17 illustrates the typical elliptical envelop of the Tsai-Hill Failure criteria. The magnitude of the shear strain affects the size of the ellipse [48]. Figure 17 highlights the difference between tensile and compressive strengths.

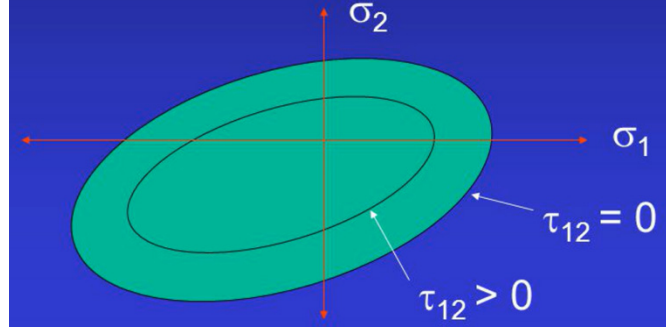


Figure 17: Typical Tsai-Hill failure criteria, different biaxial and shear stresses [48]

Using the Tsai-Hill criterion, sometimes the composite failure is described using inverse reserve factor (IRF). The IRF is the load value divided by the failure load [49]. CATIA software uses the IRF to demonstrate the failure criteria of a part. Thus, the composite is safe when the $IRF < 1$ and fails when $IRF > 1$.

The Tsai-Wu criteria is another interactive criteria in which the safety factor for given two-dimensional stress ($\sigma_1, \sigma_2, \tau_6$) is computed in equation (22):

$$\frac{\sigma_x^2}{S_{1T}S_{1C}} + \frac{\sigma_y^2}{S_{2T}S_{2C}} + \left(\frac{\tau_{xy}}{S_{12}}\right)^2 + \left(\frac{\tau_{xz}}{S_{13}}\right)^2 + \left(\frac{\tau_{yz}}{S_{23}}\right)^2 + \left(\frac{1}{S_{1T}} - \frac{1}{S_{1C}}\right)\sigma_x + \left(\frac{1}{S_{2T}} - \frac{1}{S_{2C}}\right)\sigma_y - \frac{\sigma_x \sigma_y}{(S_{1T}S_{1C}S_{2T}S_{2C})^{\frac{1}{2}}} \leq 1 \quad 22$$

$$S_1 = S_{1C} \text{ if } \sigma_x \leq 0, \quad S_1 = S_{1T} \text{ if } \sigma_x > 0$$

$$S_2 = S_{2C} \text{ if } \sigma_y \leq 0, \quad S_2 = S_{2T} \text{ if } \sigma_y > 0$$

For the $\frac{\sigma_x \sigma_y}{S_1^2}$ term; if $\sigma_x \sigma_y \geq 0$, $S_1 = S_{1T}$; otherwise $S_1 = S_{1C}$

As soon as one of the plies in the laminate exceeds the maximum given by the specific criteria, the laminate's total strength is decreased, and the whole laminate is analyzed again for the next ply to fail. When the imposed load causes the failure of all plies, the entire composite laminate is assumed to fail [37].

3.4.1 First-order theory

According to classical lamination theory, shear stresses, (τ_{xz}) and (τ_{yz}), and shear strains, (γ_{xz}) and (γ_{yz}) are respectively zero. However, if low-stiffness central plies and the laminate are thick, their components are not negligible. As a result, the assumption of normality of thickness axis to the deformed shape is no longer valid.

Consequently, this generates a new displacement equation $w(x, y, z)$ for any points off the mid-plane. Figure 18 illustrates the rotations of the cross-section, α_x and α_y , normal to the x-axes and y-axes [29]:

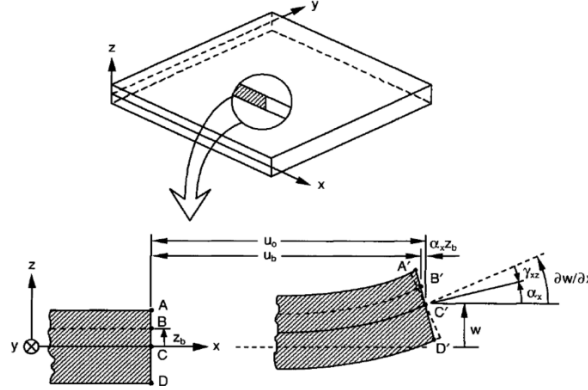


Figure 18: Section of a laminate normal to the y-axis before and after the deformation

The transverse shear resultant is defined by equation (23) [29].

$$\begin{bmatrix} V_q \\ V_{qr} \end{bmatrix} = \begin{bmatrix} A_{qq} & A_{qr} \\ A_{rq} & A_{rr} \end{bmatrix} \begin{bmatrix} \frac{\partial w}{\partial y} - \alpha_y \\ \frac{\partial w}{\partial x} - \alpha_x \end{bmatrix} \quad 23$$

where: Transvers shear stiffness $A_{ij} = \sum_{k=1}^n C_{ij}^k(t_k)$, $i, j = q, r$

Substituting the in-plane force and moment within the equation (13) and equation (24) presents the relation between load and displacement based on first-order shear theory [29]:

$$\begin{bmatrix} N_x \\ N_y \\ N_s \\ M_x \\ M_y \\ M_s \end{bmatrix} = \begin{bmatrix} A_{xx} & A_{xy} & A_{xs} & B_{xx} & B_{xy} & B_{xs} \\ A_{xy} & A_{yy} & A_{ys} & B_{xy} & B_{yy} & B_{ys} \\ A_{xs} & A_{ys} & A_{ss} & B_{xs} & B_{ys} & B_{ss} \\ B_{xx} & B_{xy} & B_{xs} & D_{xx} & D_{xy} & D_{xs} \\ B_{xy} & B_{yy} & B_{ys} & D_{xy} & D_{yy} & D_{ys} \\ B_{xs} & B_{ys} & B_{ss} & D_{xs} & D_{ys} & D_{ss} \end{bmatrix} * \begin{bmatrix} \varepsilon_x^0 \\ \varepsilon_y^0 \\ \gamma_{xy}^0 \\ \frac{-\partial \alpha_x}{\partial x} \\ \frac{-\partial \alpha_y}{\partial y} \\ \frac{-\partial \alpha_x}{\partial x} + \frac{-\partial \alpha_y}{\partial y} \end{bmatrix} \quad 24$$

In this chapter, the equations governing the final characteristics of composite laminated materials are briefly explained. As mentioned before, this is especially important since a designer should have a mindset about the expected results and deformation before conducting the FEA analysis. In Chapter Six, these characteristics will be discussed in the results and discussion sections for each benchmark.

CHAPTER FOUR: COMPOSITE MATERIALS, CATIA CAD

This chapter briefly explores the CATIA CAD platform, which consists of the main workbenches (shown in Figure 5) and the essential tools for defining composite parameters before employing the ELFINI solver. All the screenshots from the software were extracted from CATIA V5-6R 2018. The order of the mentioned stages (rows 1 to 5) that should be followed is listed in Table 7. Also, the section in the thesis exploring these sub-stages are shown in the rightmost column of the table.

Table 7: The stages before using Elfini Solver

Stages	Row	Sub-stage	Sec.
Model the Geometry	1	Use the Wireframe and surface design or Generative Shape Design workbenches to generate the Basic Laminate Surface (BLS).	4.1
Lamina Creation	2	Add new composite material defining the mechanical properties of the ply in the Material Library workbench.	4.2
Laminate Definition	3	Composite Parameters consists of the list of the Rosettes, Directions, and Materials are Defined.	4.3
	4	The stacking Sequence of the Laminate is established.	4.4
	5	The Parameters like Draping and Plies Direction are checked.	4.5

4.1 Base Laminate Surface Design

The Wireframe and surface design and Generative Shape Design are the only two workbenches needed to set up the surface, and they are required to create a Base Laminate Surface (BLS). The essential elements of the BLS are direction and edges. The direction is assigned as opposite to the predefined draping direction, and tools such as Boundary define the edges. The method employed to make the BLS surface is not the topic of this study. Two special workbenches were used to define composite parameters: Composite Design and Composite Grid Design. In this context, similar tools are provided to design contours and other wireframe geometry inside the boundaries [50].

4.2 Material Library

The Material Library workbench was designed to define new materials in CATIA V5. The path to reach the Material Library is illustrated in Figure 5. Isotropic material and other types of composite materials (Orthotropic 2D/3D, Fibre, Honeycomb, and Anisotropic), that can be defined in CATIA software are illustrated in Figure 19 under the Analysis tab. Also, some manufacturing properties are accessible through the Composites tab. The most important entry that the user should supply is the Cured Thickness box, which describes the thickness of the ply.

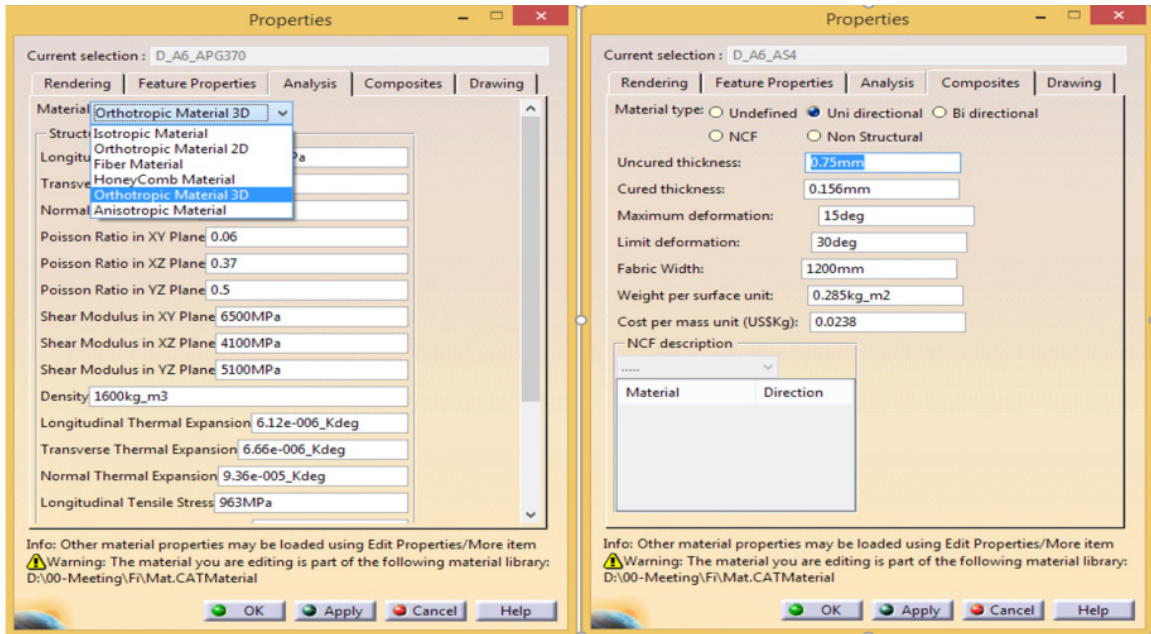


Figure 19: Properties of the material in CATIA software

4.3 Composite Parameters

The composite parameters should be predefined in the Composite Design or the Composite Grid Design workbenches. The main characteristics of a composite material consist of the complete catalogue of all the materials' ply orientations, while rosettes are determined using the window shown in Figure 20.

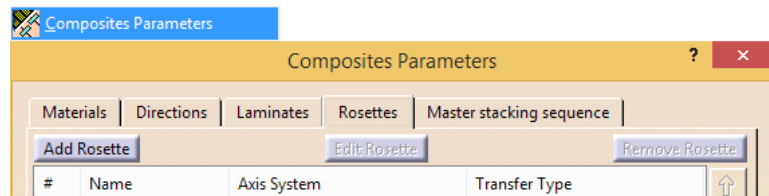


Figure 20: Composite Parameters toolbar

4.3.1 List of materials

In the Materials tab, the process of adding new material from the predefined material catalogue is illustrated in Figure 21.

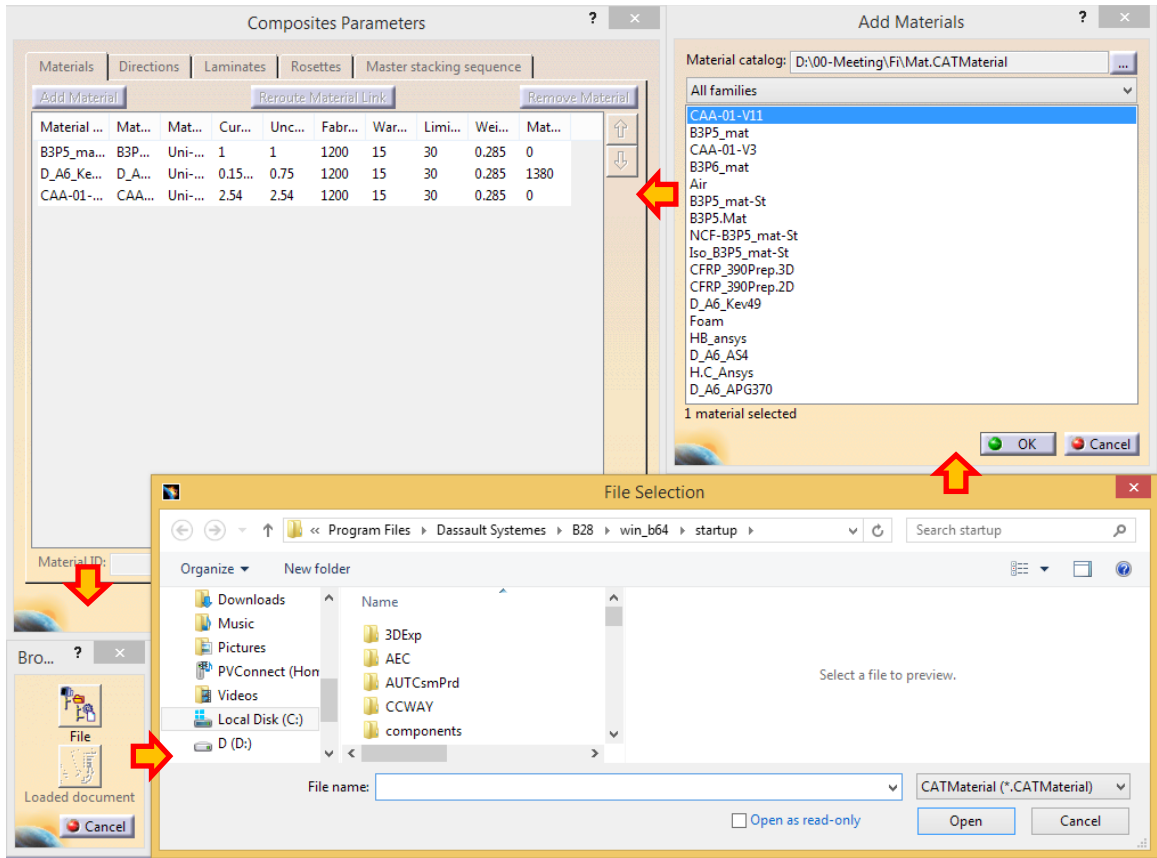


Figure 21: Assigning materials to the design

4.3.2 Direction/Orientation properties of plies

The list of default orientations is assigned for the whole design and is predefined in the Directions tab. With respect to the layer orientation, the Name and Value categories were set to -45_deg and -45, respectively, while the Colour was set to green (Figure 22).

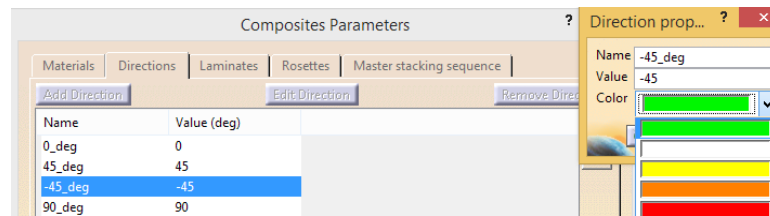


Figure 22: Direction properties of plies

4.3.3 Rosettes

The axis system of the ply directions at each point can be identified through Cartesian System or other options (Figure 23). The features that were used to create the Axis System and other options are provided in this window. One advantage is the capability to transfer the rosette directions along a curve. More information on this issue is presented in section 6.11 for a cylindrical shaped composite part.

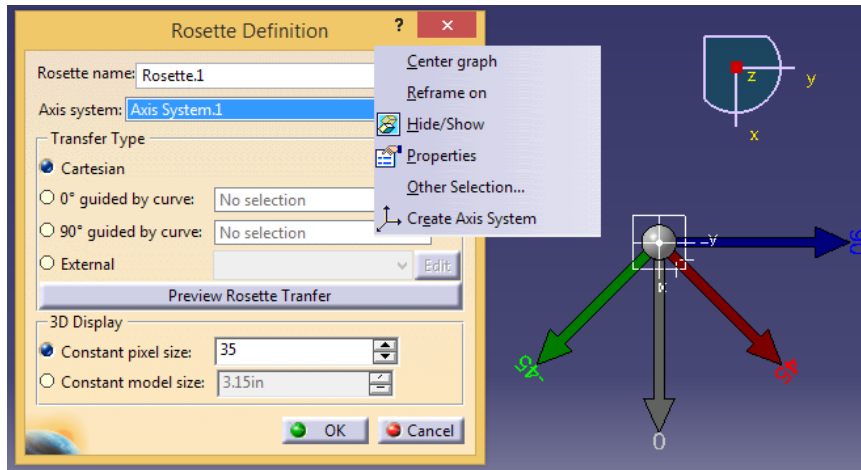


Figure 23: Rosettes Definition toolbar

4.4 Laminate Design

The Ply group, representing a group of plies created over the same surface, can be defined in the Composite Design or Composite Grid Design workbenches using different methods. Then laminates, which refer to the sequence of laminas, for different BLSs should be laid up in the Stacking (Engineering) branch of the CATIA tree. [50].

4.4.1 Draping (the stacking sequence)

The direction in which plies are stacked is the known as the draping direction. The Draping and Join directions should be opposite of each other. Different methods can be used to define the draping direction for a ply group. One of the simplest methods is defining it during manual ply creation.

4.4.2 Manual ply creation

The simplest way to define the plies is by creating them manually, one by one. This is efficient when the number of plies is limited. After modelling the BLS, the Plies group is defined by reversing the direction of Join for the draping direction and selecting the Rosette. Through the Ply Definition, the specific boundary and attribution of each ply are defined. Figure 24 shows the above information in the displayed windows. Notice the “Join.ABC” as a Base Laminate Surface and “Sketch_A” as the boundary for the “Sequence.A”. They are shown in the Ply Groups and Ply Definition windows, respectively. Using Ply Explorer tools, the “Rosette.+Z” and the plies’ orientations show the plies graphically by colour, as illustrated in the rosette 3D display on the right of Figure 24. The tree shows the entire laminate design attributes such as the ply groups, sequences, and plies.

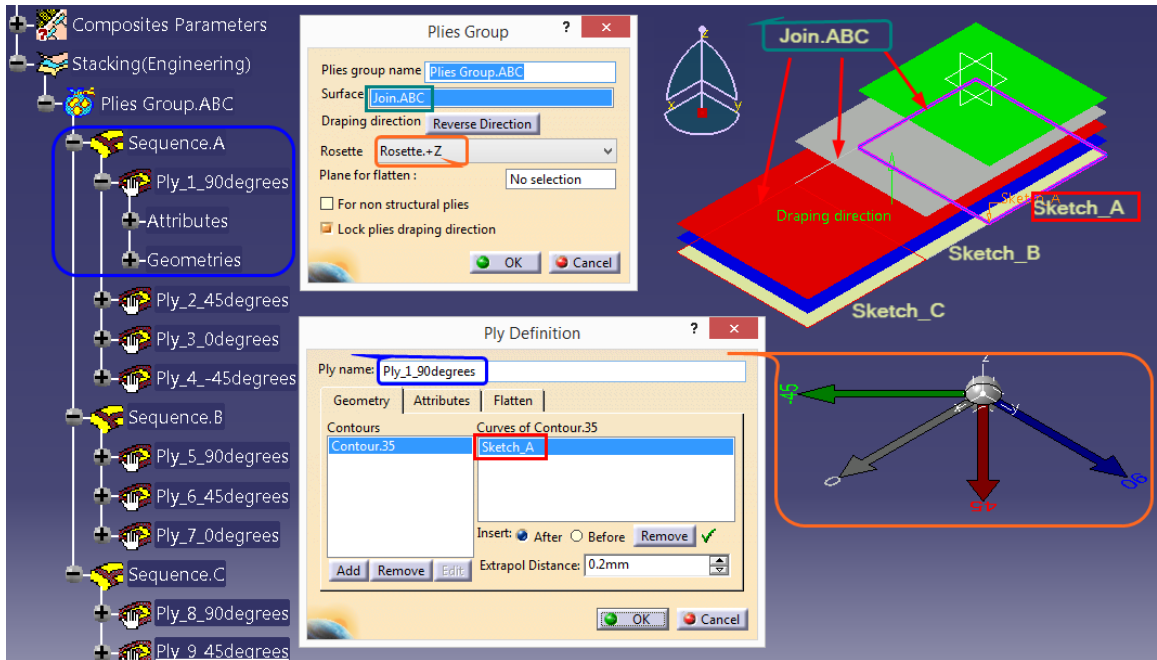


Figure 24: Manual ply creation

4.4.3 Modifying the plies by using Excel

Components of the Stacking (Engineering) information can be exported to an Excel file using Ply Table (Figure 25). Once this is done, the modification can be updated again to the CATIA using the Ply Table Import feature. When many layers are assigned to a large number of surfaces, it is more practical to use the capabilities of Excel software. Notice that only an update of the information is possible. As a result, it is easy to expand the laminate to the number of Plies Groups, Sequences, and Plies required using the Copy and Paste or Zone (TL or SS) method before updating the information and names using Excel file.

	A	B	C	D	E	F	G	H	I
1	PlyGroup	Sequence	Ply	Material	Direction	Rosette	Surface	Draping	Ply ID
2	Plies Group.ABC	Sequence.A	Ply_90deg.	B3P5_mat	90	Rosette.+Z	Join.ABC	F	1
3	Plies Group.ABC	Sequence.A	Ply_45deg.	B3P5_mat	45	Rosette.+Z	Join.ABC	F	2
4	Plies Group.ABC	Sequence.A	Ply_0deg.	B3P5_mat	0	Rosette.+Z	Join.ABC	F	3
5	Plies Group.ABC	Sequence.A	Ply_-45deg.	B3P5_mat	-45	Rosette.+Z	Join.ABC	F	4
6	Plies Group.ABC	Sequence.B	Ply_90deg.	B3P5_mat	90	Rosette.+Z	Join.ABC	F	5
7	Plies Group.ABC	Sequence.B	Ply_45deg.	B3P5_mat	45	Rosette.+Z	Join.ABC	F	6
8	Plies Group.ABC	Sequence.B	Ply_0deg.	B3P5_mat	0	Rosette.+Z	Join.ABC	F	7
9	Plies Group.ABC	Sequence.C	Ply_90deg.	B3P5_mat	90	Rosette.+Z	Join.ABC	F	8
10	Plies Group.ABC	Sequence.C	Ply_45deg.	B3P5_mat	45	Rosette.+Z	Join.ABC	F	9

Figure 25: Exported information using Ply Table tools

4.4.4 Modifying the plies by Stacking Management:

The Stacking Management icon located in the Analysis toolbar is another method that can be used to modify the information prepared in the Composite Design workbench. The Tools Palette is the special toolbar that displays each ply's exact direction, position, and size. Figure 26 shows Stacking Management in the top window. Its characteristics in the

sequence “Sequence_B” in “Plies Group_ABC” are shown. The Entity Preview window for “Ply_45deg” is depicted at the bottom of the figure.

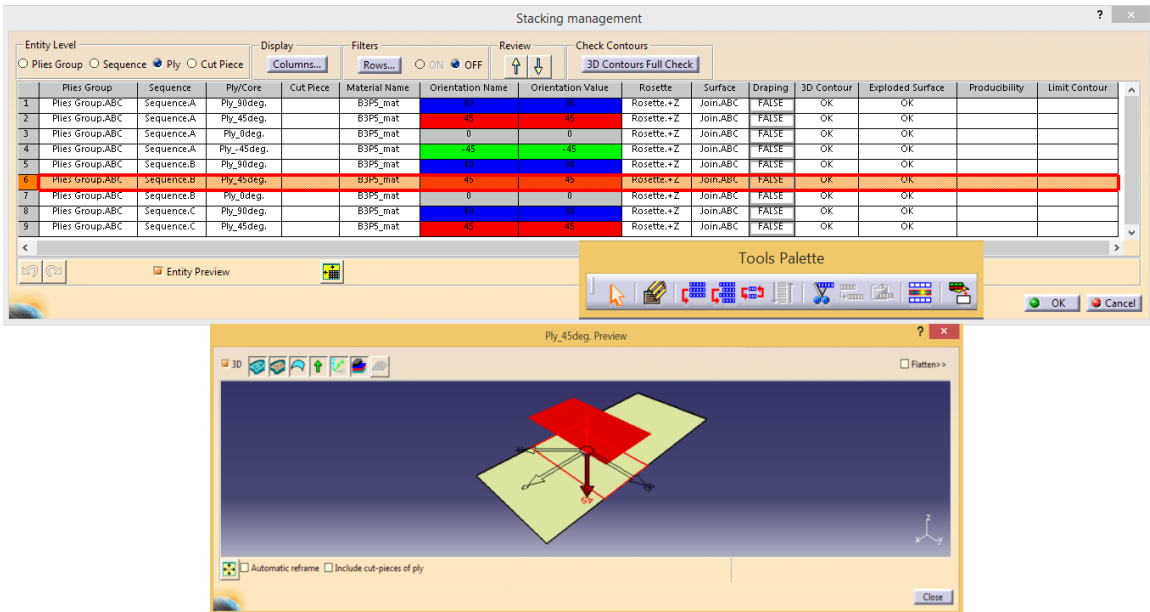


Figure 26: Laminate Design (Stacking preview)

Similar interactive windows such as Virtual Stacking Management employed in the Composite Grid Design and Multiple Core Sample that is provided while laying up Non-Crimp Fabric (NCF) materials [50] are not explored in this study.

CHAPTER FIVE:

COMPOSITE MATERIALS, CATIA FEA

This chapter discusses the CATIA FEA platform functionalities for pre-processing, solution, and post-processing stages. Some general aspects are outlined, and those that are specific to the composite materials are investigated in more detail. The order of the discussed stages (row 6 to 13) and the corresponding section are depicted in Table 7 of the previous chapter and are listed in Table 8 below. The eleven sub-stages (Row 1 to 11) explained in Chapter Four and Chapter Five are the required stages of conducting the finite element analysis of composite materials.

Table 8: The Pre-processing, solving, and Post-processing stages

Stages	Row	Sub-stage	Sec.
Pre-processing	6	Open the Generative Structural Analysis workbench, select the Analyze Type.	5.1
	7	Mesh the part through Generative Structural Analysis or Advanced Meshing Tools workbench.	
	8	Import the properties to the meshed surface.	5.2
	9	Impose the restraints and loads.	5.2.1
Solving	10	Compute the Analysis	0
Post-processing	11	Visualize the results.	5.4
	12	Interpret the results and Mesh Refinement iterations.	6,7,8,9
	13	Manage the results (Image Edition or Report Generation).	

5.1 Meshing of the Part (Shell elements)

After defining the materials properties, the part should be meshed. Here, shell elements are the only options for importing material properties to analyze the model in the CATIA FEA Solver. Therefore, the laminated composites can only be modeled with shell elements.

Octree Surface Mesher, Surface Mesher, and Advanced Surface Mesher are tools provided in Generative Structural Analysis and Advanced Meshing Tools workbenches. CATIA provides basic functionalities, such as local mesh refinement, as well as remote connection, mesh capture, and the ability to add or remove constraints (edge, curve, line or point) [51]. Figure 27 shows some of the tools, toolbars, and options that CATIA provides for meshing purposes. They are applicable to any type of material, composite or otherwise.

5.1.1 Join, Normal to Shell, and local CS directions

The Local Coordinate System (CS) consists of three perpendicular axes: two in the plane and one aligned with Shell's normal direction. As mentioned in 4.1, the normal orientation of the Base Laminate Surface (BLS), defined by the Join direction, is opposite the Shell and Local CS. It is recommended to use the Join command while modelling the BLS. That leads to better control over the shell direction and Local CS.

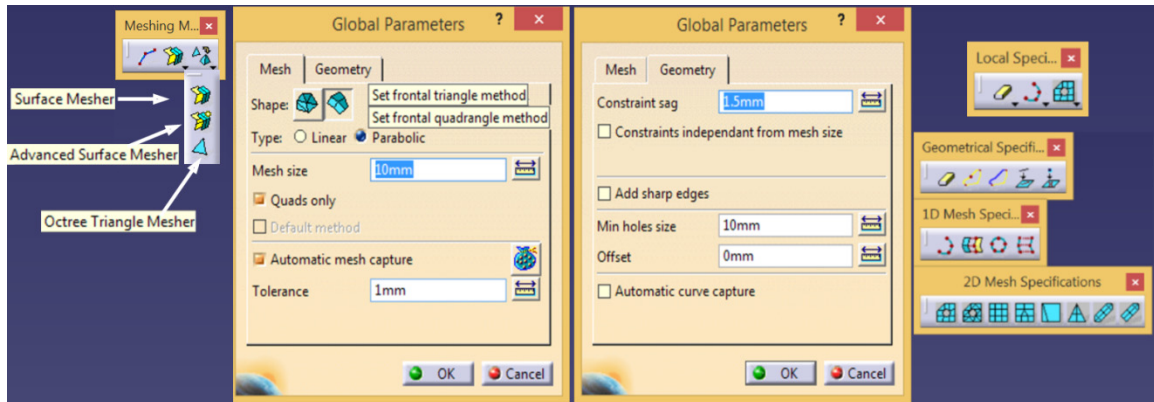


Figure 27: Some of the features in the Meshing Tools

5.1.2 Draping direction

The draping or stacking sequence follows the Local CS, which is aligned with the Normal to Shell direction. Ply number 1 is assigned to the minimum distance from the BLS plane in the shell direction. CATIA software can graphically display a laminate in the global coordinate system's positive or negative normal axis to BLS. However, the FEA solver considers the local coordinate system for the computation. As a result, Draping Up or Down is a matter of perspective as long as one models the constraints and loads in the correct directions.

The trial-and-error process easily demonstrate that the Draping direction should be opposite to the direction of the Join explained in 4.4.2. In the final stage of defining the laminate, the designer should verify that it is recorded as “False” through the stacking management table or other tools (4.4.4). If it is displaying “True”, it should be modified by importing to an excel file, and, after modifying and exporting again, it should be verified as False.

To confirm the above statement, an experiment was conducted as follows: The terms "True" and "False" respectively mean "draping" and "join" are in identical and opposite directions. A laminate consisting of plies with 90° , 0° , and 45° directions (zero in between two others) was considered under a pure tensile loading in the zero direction. The deformed shape is bent toward the layer that delivers the most resistance against the load, which here is the layer with 45° . In other words, since in the flat bar with the 90° orientation, there is little resistance against tensile loads, the deformed shape will bend in a way that the outer surface close to the layer with 90° will stretch. Therefore, the layer with 90° stretches due to the pure tensile loads, and the ply with 45° contracts. The middle of the ply with 0° is aligned with the load direction and remains neutral against the load. Figure 28 illustrates the above argument, which is modelled with isotropic material. In addition, there are solid steel bars under the pure tensile loads, which represent the corresponding laminate. Different profiles with 90° , 0° , and 45° are shown in three views, as well as the isometric view.

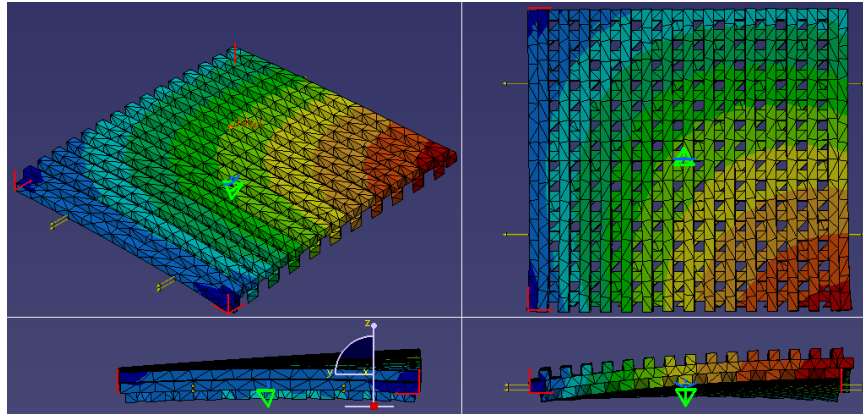


Figure 28: Deformation curve for solid profiles with 45°, 0°, 90° presenting corresponding laminate

Similarly, the correct curvature for the similar laminate with stacking sequence of [90/0/45] is expected. Therefore, similar draping directions and conditions are modelled, and the only difference is the draping direction: “True” or “False”. These two drapings were analyzed with CATIA FEA Solver and Classical Lamination Theory (CLT). The deformation, strain energy, and von Mises stresses were the same for both drapings, although the curvature signs were different.

Figure 29 illustrates the curvatures that resulted from the above analysis. It shows that the curvature for the False draping matches the isotropic model and is in compliance with CLT, which is different from the “True” draping.

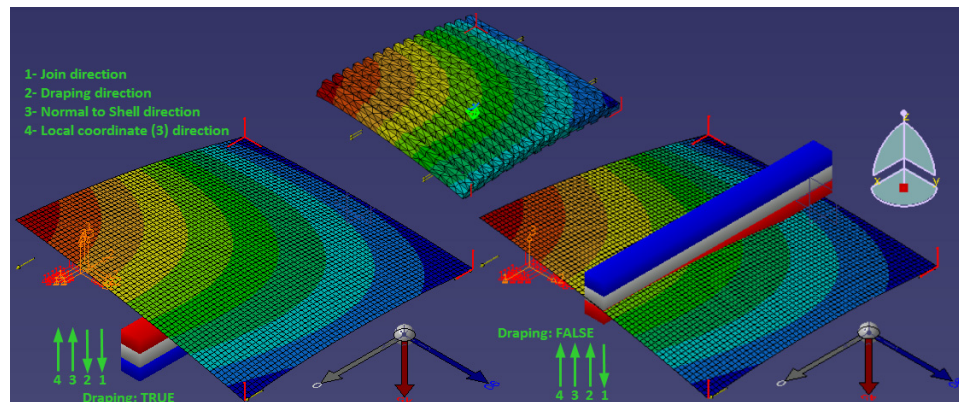


Figure 29: Comparison between different Drapings: True (left) and False (right)

5.2 Imported Properties

CATIA uses the 2D Properties tools to import composite parameters for the elements from composite workbench to the FEA module. Figure 30 shows where to find 2D properties tools and their interactive window in the Generative Structural Analysis workbench. After assigning the BLS as the Supports, it is important to note that only the “By ply” option in the Analysis drop-down menu leads to the correct definition of the laminate. Analyzing the By Zone option will change the stacking sequence internally according to the software internal instructions.

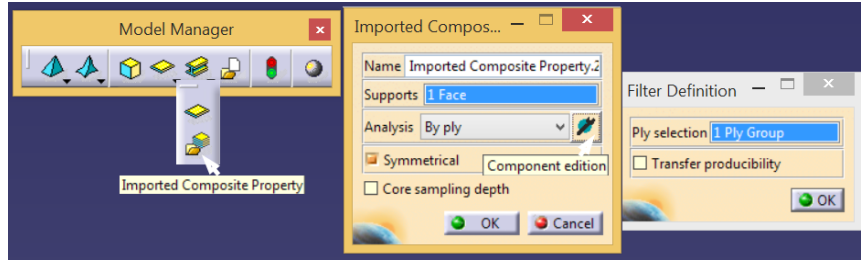


Figure 30: 2D properties interactive window

5.2.1 Geometries consisting of different Composite Parameters

In the event that the geometry consists of two or more basic laminate surfaces (BLS), each should be modelled, meshed, and assigned imported properties separately. The boundaries used while defining composite parameters should be employed again while meshing the elements. Figure 31 illustrates the boundary of each BLS with specific composite properties and the element meshes. In the ADD/Remove Constraints interactive window, the limits of three sequences are selected and shown in yellow; therefore, the mesh is constrained to them. The result from the left simulation is incorrect since the boundaries are in the middle of the elements shown in orange.

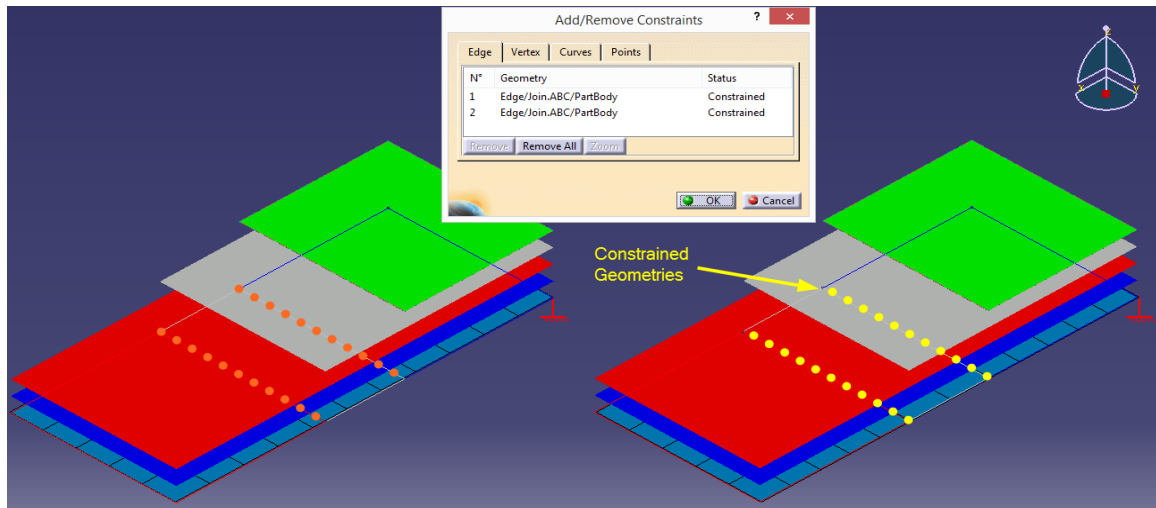


Figure 31: Mesh and Boundaries depiction

A straightforward option could be to join the different surfaces, define the composite properties, mesh the joined surface, and import properties one by one. Because the rosette is identical for all the regions, all the smaller parts can be organized under the same Ply Group in different sequences, as demonstrated by the tree in Figure 24. The element mesh should be defined in a way that accommodates the boundary between Base Laminate Surfaces. In such instances, one can use the advanced surface mesher tools and identify the boundaries through Add/Remove Constraint tools. Figure 32 illustrates the boundaries and the final mesh while using only one join and meshed the geometry all at once. The figure shows that the new element size in the middle BLS (section AB) adjusts to fit the new boundaries.

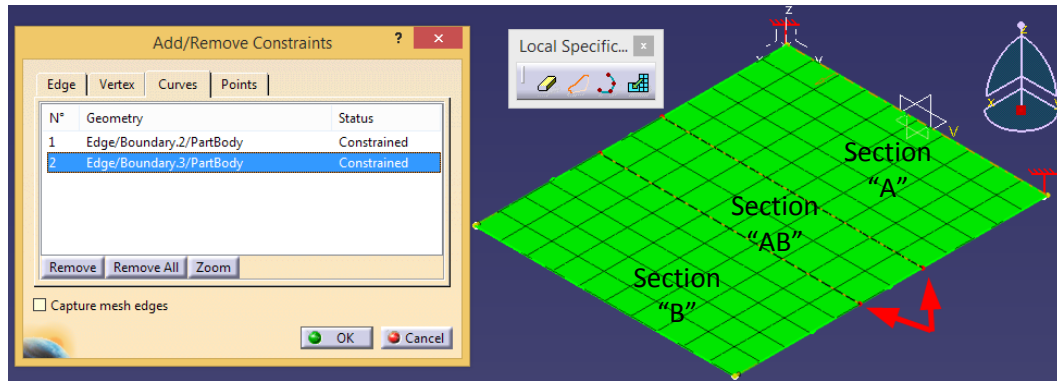


Figure 32: "Add/Remove Constraint" tools to define the Boundaries

5.3 Imposing Loads and Restraints

5.3.1 Defining the location of applied load (symmetrical or un-symmetrical loading condition)

The Symmetrical option is selected in the import composite material interactive window (Figure 30). Based on the Symmetrical option, Elfini treats the location of imposing loads and constraints differently on the assigned shell elements. Therefore, if the symmetrical option is selected, the loads and constraints are assigned to the mid-plane surface of the selected composite material.

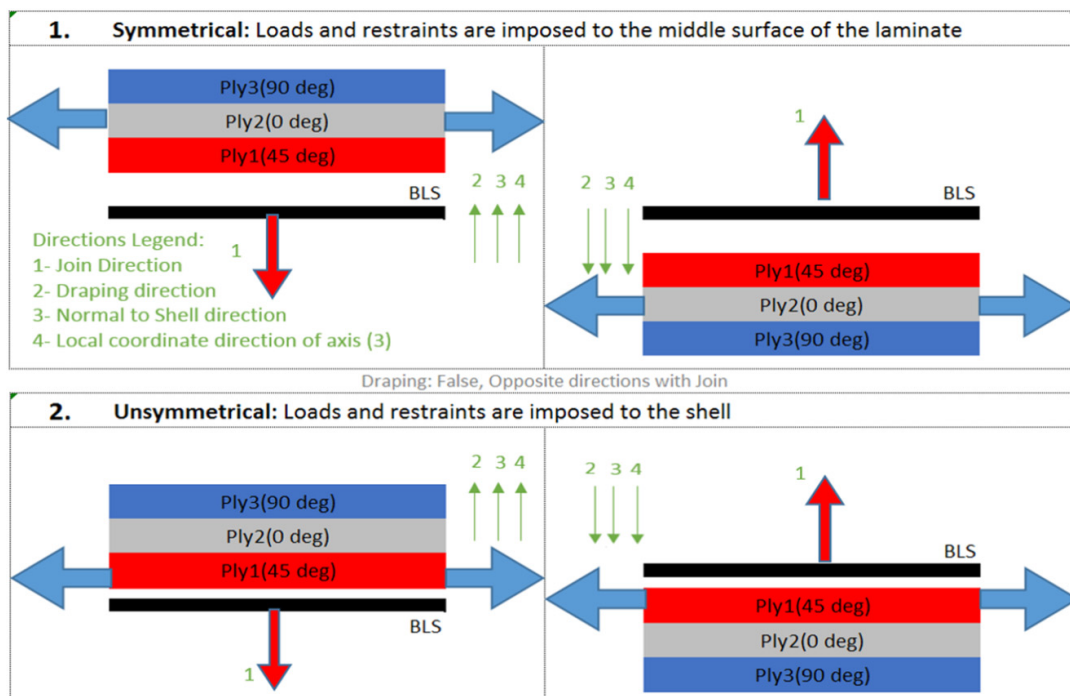


Figure 33: loads & restraints when the Symmetrical option in the Imported Properties is checked or unchecked

Figure 33 illustrates two possible load positions regarding the symmetrical or unsymmetrical condition of the importing properties to the shell elements. In each, the join, draping, normal to the shell, and local coordinate directions when the laminate is

stacked up on top or bottom of the BLS are shown respectively by numbers from 1 to 4, which were discussed in section 5.1.

5.4 Visualizing the Results

After completing the analysis, it is essential to visualize and interpret the results. To post process the results, there are different options embedded in the CATIA software. In addition, various tools can be used to generate reports, such as Deformed Shape, Animation, Cutting Plane, Contour Plot, Global Sensors, Maximum Stress, and Frequencies. However, the current study focuses exclusively on generating reports specific to the composite materials.

The deformations and the results should be in agreement with the laws of physics. It is common to make unintentional mistakes when modelling the geometry, material, and load conditions. That is why the designer should focus on the load condition and predict the deformed shape before conducting the analysis. Another critical point is to identify where and how one should look for the results. Generally, predicted values in the re-entrant corners or close to the loads and restraints may be misleading. If these locations are important to the user, one should utilize a much finer mesh in those areas.

Local mesh refinement may also be needed to improve the results. A Mesh convergence study is always to be conducted. If the results are changing, for example, by changing the size of the elements, the mesh is inadequate or coarse. For such a scenario, the analysis should be repeated until the solution converges.

5.4.1 *Generating the CATIA results and reports*


Through Generating Advanced Reports (), one can request the specific information to generate the desired output. Also, a wide range of reports and plots are available to generate. Different types of results, named “Image” in CATIA, can be generated. Some of them are interactive according to the magnitude, component, vector, and symbol. The ones used in this study are specified in Heavy black colour in Table 9.

Table 9: Available images and reports using CATIA FEA Solver

FE Tab	Physical Type		Image Name	Sub Type	
Restraints	3D Mechanical DOF	1	Derees Of Freedom Symbol		
Loads	Lineic Force Vector	2	Line Force Vector		
Nodes and Elements	3D Mechanical DOF	3	Degrees. Of Freedom Symbol		
	30 Coordinates	4	Element Centroid Symbol		
		5	Nodal Coordinates Symbol		
	Element Set	6	Elements Text		
		7	Mesh		
	Local Axis	8	Local Axis Symbol		
	Node Set	9	Nodes Text		
	Physical Type	10	Physical Type Fringe		
	User Number	11	User Elements Text		
		12	User Nodes Text		
Properties	Angle	13	Composite Angle Symbol		
	Number Of Laminates	14	Laminate Number Text		
	Element Material	15	Material Fringe		
	Ply ID	16	Ply Id Text		
	3D Shell Thickness	17	Thickness Fringe		
Static Case Solution	30 Rotation Vector	18	Local Singularity In Rotation	Singularity	
		19	Rotational Displacement Magnitude		
	30 Rotation Vector Strain	20	Rotational Displacement Vector		
	30 Translation Vector		21	Translational Displacement Component	
			22	Translational Displacement Magnitude	
			23	Translational Displacement Vector	
	Curvature	24	Curvature Text		
	Elastic Energy	25	Local Strain Energy		
		26	Local Strain Energy Symbol		
	Elastic Energy Density	27	Local Strain Energy Density		
	Element Set	28	Deformed Mesh		
	Estimated Error	29	Estimated Local Error		
	Failure Criterion		30	Hoffman Criterion Discontinuous Iso	Hoffman
			31	Maximum Failure Criterion Discontinuous Iso	Max Failure
			32	Tsai-Hill Criterion Discontinuous Iso	Tsai-Hill
			33	Tsai-Wu Criterion Discontinuous Iso	Tsai-Wu
	Force Flow	34	Force Flow 2D Text		
		35	Force Flow 3D Text	20	
	Mass Inertia	36	Mass Inertia (Text)		
	Mass Moment Of Inertia	37	Mass Moment Of Inertia (Text)		
	Moment Flow	38	Moment Flow Text		
	Point Force Vector	39	Free Bod Y Force Vector	3D	
		40	Point Force Vector		
	Point Mass	41	Point Mass Symbol		
		42	Point Mass Text		
	Point Moment Vector	43	Free Bod Y Moment Vector		
		44	Point Moment Vector		
	Strain		45	Strain Full Tensor Component (Nodal Values)	
		46	Strain Principal Tensor Component (Nodal Values)		
		47	Strain Principal Tensor Symbol		
		48	Transverse Shear Strain Text		
Stress		49	Stress Full Tensor Component (Element'S Nodes Values)		
		50	Stress Full Tensor Component (Nodal Values)		
		51	Stress Full Tensor Text		
		52	Stress Principal Tensor Component (Element'S Nodes Values)		
		53	Stress Principal Tensor Symbol		
		54	Transverse Shear Stress Text		
Buckling Case Solution	Element Set	55	Deformed Mesh		
	30 Rotation Vector	56	Rotationa L Displacement Magnitude		
		57	Rotationa L Displacement Vector		
	30 Translation Vector		58	Translational Displacement Component	
			59	Translational Displacement Magnitude	
			60	Translational Displacement Vector	

CHAPTER SIX:

BASIC BENCHMARKS (BMP1 to BMP11)

6.1 Introduction:

The CATIA FEA Solver is studied in the next three chapters, highlighting some of its main characteristics in dealing with composites. In this chapter, eleven basic benchmark problems (BMP1 to BMP11) are carefully selected to predict and visualize the results that could be compared with the Classical Laminate Theory (CLT). In addition, the results from ABAQUS and ANSYS software are presented as alternative sources, especially for comparing the deformed shape of the models and then comparing total strain energy and displacement values. The von Mises stress and the principal stresses (the maximum and the minimum) are selected as the main parameter to compare all the methods' outcomes.

Later in this chapter, all these eleven BMPs discussed in detail, and a Report Card Test (RCT) for each problem is generated to present the summary of the test condition, results, and BMPs' verification. The general organization of the RCT is explained in 6.1.2.

6.1.1 *General comments on benchmark problems' status*

As stated before, the BMPs are discerningly selected from a wide variety of applied loads, constraints, geometries, and composite parameters to check the solver's sensitivity against these influential parameters. The topics, geometries, and the composite parameters of BMPs explored in this chapter are summarized in Table 11, and the loading conditions are listed in Table 12. It is wise to outline the benchmark problems' status here to distinguish their differences and similarities before going through them one by one.

Table 11 summarises the main purpose of each BMP in the Topic and Comments/Remark columns. In BMP1 to BMP5, the method of applying different loading conditions—tensile, bending, shearing, twisting, and temperature effect—is indicated. The BMP7 and BMP9 are focused on other characteristics that need to be examined in more complicated situations. The load superposition is employed for the BMP7 and BMP9.

An important parameter is the shape of the base surface. Different shape features are investigated, including the flat bar (BMP1 to BMP3), thin rectangular plate (BMP4 to BMP9), and cylindrical and spherical geometry (respectively in BMP10 and BMP11).

The rectangular plate's length, width, and thickness ($L \times W \times \text{Thk.}$) for BMP1 were extracted from the tensile test sample conditions [19]. The preferred dimensions are based on the ASTM standards or as practical as possible when the dimensions according to standards are not possible. The circular cross-sections' laminate thicknesses in BMP10 and BMP11 are equivalent to 6 millimetres [52], whereas laminate thicknesses of the rectangular plates employed in BMP1 to BMP9 is equal to 2.5 mm [19].

Composite parameters are changed from one benchmark to another. The draping directions are in the “+Z” direction of the general coordinate system (CS) except for BMP9. Consequently, the rosette in the “-Z” direction is investigated in BMP9. All the eight different laminate types—see the Type No. defined in Appendices Table A—that was investigated in Appendix A are employed in BMP1 to BMP11. The relative specific orientations are also included using the top reference plane method [53] to write the embedded orientation codes. The orientation codes shown in the table are based on ASTM D6507¹. Unidirectional lamina and woven fabrics are both experimented with in this thesis. Woven fabrics are employed in BMP6 and BMP8, respectively; apart from the materials used, they are identical to BMP5 and BMP7. Table 10 presents the composite material properties consisting of elastic, strength, and thermal expansion properties for unidirectional lamina and woven fabrics used in this chapter [29].

Table 10: Lamina properties used in Chapter Six (extracted from [29])

Property (Unit)	Unidirectional	Woven Fabric
	AS4	APG370
Density (g.cm ⁻³)	1.6	1.6
Young's modulus E_1 (MPa)	147000	77000
Young's modulus E_2 and E_3 (MPa)	10300	75000, 13800
Poisson's Ratio ν_{23}	0.54	0.37
Poisson's Ratio ν_{12} and ν_{13}	0.27	0.06, 0.5
Shear Modulus G_{23} (MPa)	3700	4100
Shear Modulus G_{12} and G_{13} (MPa)	7000	6500, 5100
Orthotropic stress limits		
Longitudinal Tensile Strength F_{1t} (MPa)	2280	963
Transverse and Out-of-plane Tensile Strength F_{2t}, F_{3t} (MPa)	57	856, 60
Longitudinal Compressive Strength F_{1c} (MPa)	1725	900
Transverse and Out-of-plane Compressive Strength F_{2c}, F_{3c} (MPa)	228	900, 813
In-Plane Shear Strength F_6 (MPa)	76	71
Out-of-Plane Shear Strength F_4, F_5 (MPa)	--, --	65, 75
Thermal Expansion Coefficient		
Longitudinal Thermal Expansion Coefficient $\alpha_1, 10^{-6}/^{\circ}\text{F}$ ($10^{-6}/\text{K}$)	-0.5	1.9
Transverse and Out-of-plane Thermal Expansion Coefficient $\alpha_2, \alpha_3, 10^{-6}/^{\circ}\text{F}$ ($10^{-6}/\text{K}$)	15 (27)	2.1, 29 (3.78, 52.2)

¹ A colon (:) is used instead of subscript information, such as number and symmetry, and backslash (\) is used instead of a bar over. For example: [0/45/90]\:s is the same as [0/45/90/45/0] or [0/45/90]_s. Note that, in all the above examples, the ply with 0° is the first ply.

For all the BMP1 to BMP11 investigated in this chapter, loading conditions are applied symmetrically. It is enforced when the Symmetrical option in the imported composite materials interactive window shown in Figure 30, is selected. In this condition, the mid-surface coincides with the Reference Surface and therefore, loads and restraints are imposed symmetrically to the laminated composite.

Table 11: Summary on the basic examples using CATIA Solver BMP1 to BMP11

Benchmark Problem No.	Topic	Comment / remark	Base Surface			Composite Parameters					
			Shape Feature	Dimensions (mm): Length(L)×Width×Thickness (Thk.)	T.Thk. (mm)	Composite Type	Type No.	Employed orientation codes	No. of Layers	Ply Thk. (mm)	Ply [29]
BMP1	Pure Tensile Load	1-Imposing Nx or Ny	Flat Bar	300×25×2.5 [19]	2.5	Balanced Antisymmetric Crossply	5	[0/90]:8	16	0.156	AS4
BMP2	Pure Bending Load	1- Imposing Mx or My 2- CATIA presents the Engineering Curvature	Flat Bar	300×25×2.5	2.5	Balanced Carpet Plot	2	[(0):2/(±45):3]:s	16	0.156	AS4
BMP3	Pure Shearing Load	1-Imposing Nxy or Nyx 2-CATIA presents the Engineering Shear Strain	Flat Bar	300×25×2.5	2.5	Balanced Angle-Ply	6	[±45]:8	16	0.156	AS4
BMP4	Pure Twisting Load on the Plate	Imposing Mxy	Thin Plate	300×200×2.5	2.5	General Laminated Composite	8	[90/45/-30/(-45):2/0/45/(90):2/-45/0/(45):2/0/-45/90]	16	0.156	AS4
BMP5	Temperature Effect	Unidirectional lamina	Thin Plate	300×200×2.5	2.5	Quasi Isotropic	7	[90/45/0/-45]:4	16	0.156	AS4
BMP6	Temperature Effect	Woven Fabric	Thin Plate	300×200×2.5	2.5	Quasi Isotropic	7	[90/45/0/-45]:4	16	0.156	APG 370
BMP7	Unidirectional plies (3D vs. 2D properties)	1- Superposition of loads 2- The linear responses of the CATIA FEA Solver	Thin Plate	300×200×2.5	2.5	Balanced Modified Quasi Isotropic	1	[(90/45/0/-45):s/(90/-45/0/45):s]	16	0.156	AS4 (2D &3D)
BMP8	Woven Fabric (3D vs. 2D properties)	1- Superposition of loads 2- The linear responses of the CATIA FEA Solver	Thin Plate	300×200×2.5	2.5	Balanced Modified Quasi Isotropic	1	[(90/45/0/-45):s/(90/-45/0/45):s]	16	0.156	APG 370 (2D &3D)
BMP9	Draping in the "+Z" vs. "-Z" directions	How to apply the rosettes and the loads in the "+Z" and in the "-Z" directions.	Thin Plate	300×200×2.5	2.5	General Laminated Composite	8	[90/45/-30/(-45):2/0/45/(90):2/-45/0/(45):2/0/-45/90]	16	0.156	AS4
BMP10	Axial Torsion on a Cylinder	The CLT agrees only with symmetrical laminates.	Cylinder	L: 140 mm Diameter (D): 100 mm Thk.: 6mm [52]	6	Symmetric or Asymmetric	3	[+45/-45]:s:3	15	0.400	AS4
BMP11	Pressure on the outside surface of a Sphere	1- The CLT agrees only with symmetrical laminates. 2-Limited due to Mfg. Mthd. ($0^\circ < \Theta < 5^\circ$).	Sphere	D:300 Thk.:6	6	Symmetric	4	[2.5]:15 $\Theta=2.5^\circ$	15	0.4	AS4

Table 12 indicates the mesh sizes, directions, and the magnitudes of the loading conditions. The parabolic quads shell elements (see Figure 27) are assigned to the BMP1 to BMP10, while the mesh for BMP11 is Octree Triangle Mesh, shell elements. The

mesh sizes are selected so that the number of elements in the Reference Surface's in-plane directions is odd. This greatly simplifies the comparison of the CATIA results with the other software, when needed.

The depiction on the bottom right side of Table 12 defines the position and the directions of both the applied loads and restraints in the CATIA software. The vertices and the edges relative to the coordinate system are labelled and shown. The loading conditions are distinguished with similar colours to the assigned row in the table. The vertices are in light green in the figure and in the table. Likewise, tensile loads are illustrated in orange, twisting loads in yellow, bending loads in pink, and shearing loads in white. The loads' magnitudes are indicated by the symbols [N, M]. In Table 13, the negative magnitudes are recorded in red for a quick glance.

The minimum number of restraints should be imposed to avoid rigid body motion and avoid unnecessary stresses in the part. The {1, 2, 3} rule, also known as Isostatic in CATIA, is used.

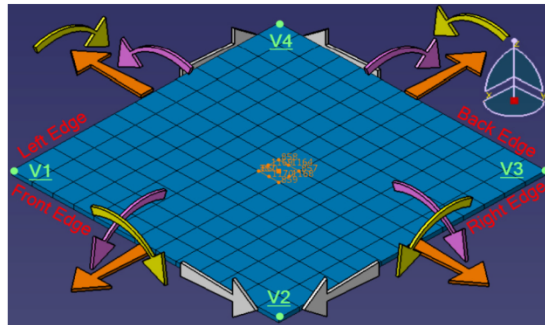
The manual imposition of the {1, 2, 3} rule requires the usage of the user-defined restraint. In Table 12, some different combinations of the {1, 2, 3} rule are applied on vertices (shown in light green) for different BMPs. There is no preference between these combinations, and every one of them is applicable to the part. At the same time, employing an identical combination is critical to compare some relative outcomes from different software, such as deformation magnitudes, the sign of the maximum and minimum principal stresses, and the sign of the curvature. The Abbreviation list is also included below the figure and explains the terms used in Table 12.

This study did not consider the finite element symmetry to reduce the computation time. In general, finite element symmetry is possible when the shape feature, boundary conditions, loads, and material properties are symmetric.

Table 12: All the mesh sizes and loading conditions for BMP1 to BMP11

Benchmark Problem		BMP1	BMP2	BMP3	BMP4	BMP5	BMP6	BMP7	BMP8	BMP9_R+z	BMP9_R-z		
Mesh size (mm)		4.92	4.92	4.92	5.26	5.26	5.26	5.26	5.26	5.26	5.26		
Load Conditions		Nx	Mx	Nxy	Mxy	[N,M] ^T	[N,M] ^T	[N,M]	[N,M]	[N,M]	[N,M]		
CLT	Loads	Nx	N_mm	100	0	0	-49.4	-80.9	100	100	100	100	
		Ny	N_mm	0	0	0	0	-49.4	-80.9	0	0	0	
		Nxy	N_mm	0	0	37.5	0	0	0	37.5	37.5	37.5	
		Mx	N	0	18.8	0	0	2.2	0.2	18.8	18.8	12.4	12.4
		My	N	0	0	0	0	-2.2	-0.2	0	0	6.2	6.2
		Mxy	N	0	0	0	18.8	-2.2	-0.2	18.8	18.8	18.8	18.8
CATIA SOFTWARE	Restraints	V1	Ux=Uy=Uz=0	Ux=Uz=0	Uy=Uz=0	Ux=Uy=Uz=0	Uz=0	Uz=0			Ux=Uz=0	Ux=Uz=0	
		User-defined Restraint V2	Ux=Uz=0	Ux=Uy=Uz=0	Uz=0	Ux=Uz=0	Uy=Uz=0	Uy=Uz=0	Uz=0	Uz=0	Ux=Uy=Uz=0	Ux=Uy=Uz=0	
		V3	Uz=0	Uz=0					Ux=Uz=0	Ux=Uz=0	Uz=0	Uz=0	
		V4			Ux=Uy=Uz=0	Uz=0	Ux=Uy=Uz=0	Ux=Uy=Uz=0	Ux=Uy=Uz=0	Ux=Uy=Uz=0			
		Other Option	Isostatic	Isostatic	Isostatic	Isostatic	Isostatic	Isostatic	Isostatic	Isostatic	Isostatic	Isostatic	
CATIA SOFTWARE	Loads	LFD(x)	N_mm	100					100	100	100	100	
		LFD(y)	N_mm			37.5			37.5	37.5	37.5	-37.5	
		M(x)	N.mm				-3760		-3760	-3760	-3760	-3760	
		M(y)	N.mm		470				3760	3760	2480	-2480	
		LFD(x)	N_mm			37.5			37.5	37.5	37.5	-37.5	
		LFD(y)	N_mm										
		M(x)	N.mm								-1860	1860	
		M(y)	N.mm				5640		5640	5640	5640	5640	
		LFD(x)	N_mm	-100					-100	-100	-100	-100	
		LFD(y)	N_mm			-37.5			-37.5	-37.5	-37.5	37.5	
		M(x)	N.mm				3760		3760	3760	3760	3760	
		M(y)	N.mm		-470				-3760	-3760	-2480	2480	
		LFD(x)	N_mm			-37.5			-37.5	-37.5	-37.5	37.5	
		LFD(y)	N_mm										
		M(x)	N.mm								1860	-1860	
		M(y)	N.mm				-5640		-5640	-5640	-5640	-5640	
		Envir. Temp.	Kelvin					70	70				
		Field Temp.	Kelvin					270	270				

Benchmark Problem		BMP10	BMP11		
Mesh size		3.491	10		
Load Conditions		Nxy	Nx,Ny		
CLT	Loads	Nx	N_mm	0	-750
		Ny	N_mm	0	-750
		Nxy	N_mm	63.67	0
		Mx	N	0	0
		My	N	0	0
		Mxy	N	0	0
CATIA SOFTWARE	Restraints	Left edge (XZ Plane)			
		Back edge (YZ Plane)	Clamped		
		Right edge			
		Front edge			
		Body		Isostatic	
CATIA SOFTWARE	Loads	Axial Torsion	Nmm	1.00E+06	
		Outward Pressure	MPa		10



The locations and the directions of different loads and Restraints [32]

Abbreviation List			
Nx, Ny, Nxy	Axial load and shear load (N_mm)	N.mm	Niotons millimeter
Mx, My, Mxy	Bending and twisting load (N)	V	The Vertex to apply Restraints
LFD	Line Force Density (N_mm)	Ux=0	User-defined Translation1 is Restrained
M	Moment applied on the Edge (N.mm)	Uy=0	User-defined Translation2 is Restrained
N mm	Niotons per millimeter	Uz=0	User-defined Translation3 is Restrained

6.1.2 RCT (General framework)

The RCTs (Report Card Test) summarize three categories of information shared amongst all the FEA commercial software (CATIA, ABAQUS, and or ANSYS) and CLT method regarding each BMP:

1. The identical conditions in terms of geometry and loading conditions problem are applied to all above tools.
2. The deformed shapes that are extracted from CATIA and other FEA analyses.
3. A comparison of four types of results generated by different tools:
 - a. The strain and curvature in the mid-plane surface.
 - b. The Mises stress and principal stresses values in the middle of all the layers.
 - c. The deformation magnitudes in the Norm and the individual components in millimetres.
 - d. The strain energy for which they are compared each BMP.

All the RCTs have similar format. In the following paragraphs, different components of the general RCT are explained (for instance, see the RCT framework issued for BMP1 in Figure 35). It consists of four rows and two columns. The rows are numbered “1” to “4”, and the columns are labeled as “L” and “R,” representing the left and the right side of the figure. For example, “L1” represents column “L” row “1” in the top left side of the figure.

The exact condition of the problem, given in the first row, consists of L1 and R1. In the left of row 1 (“L1”), the condition is explained. It includes these four main summaries:

1. The relative loading conditions—the [N] and [M] matrices and the restraints—that were used in the CLT method.
2. The Base Laminate Surface dimensions and the size and type of the mesh.
3. Laminate parameters: the lamina and laminate type, the orientation code, and the general characteristics of the [ABD] matrices.
4. The general comment on each BMP.

The information in L1 is displayed in a graphical way on the right. Let us recall that this column was labelled as “R1”. Accordingly, the illustration discloses three main elements:

1. The loads and the restraints in which the load directions are synchronized with the figure presented in Table 12 and the magnitudes that were entered into the CATIA GUI are presented in Table 12.
2. The geometry and mesh image generated from the CATIA software are shown.
3. Laminate parameters: the stacking sequence and the rosette in which illustrates the colour-coding of the plies’ direction.

In the second row, the ABAQUS deformed shape on the left (“L2”) and the CATIA deformed shape on the right (“R2”) are illustrated. Identical amplification magnitudes to the deformed shapes are applied, and the presented shapes are captured while the CATIA and ABAQUS software generates the displacement magnitude.

A table is embedded in the third row of the report which presents the Total Strain Energy, the Displacement, and the Strain and Curvature from the mid-surface of the laminate. These are calculated using the CLT method and extracted from the CATIA and other software.

In the fourth row, a graph is organized comparing von Mises and the principal stresses (plane stress) at the middle of the plies through the laminate thickness from the selected element. The selected element is located exactly in the middle of the geometry and far from the edges and the applied loads and restraints. In the presented graph, “solid line,” “square,” and “circle,” respectively represent ABAQUS, CLT, and CATIA results. The lines and symbols are selected in red, blue, and green respectively to represent the von Mises, the maximum principal stresses, and minimum principal stresses.

6.2 BMP1 (Tensile loading condition)

The three primary purposes explored in BMP1 are as follows:

1. The method to impose pure tensile load in CATIA software is investigated.
2. CATIA FEA Solver is validated for analyzing the tensile loading condition.
3. It is explained that the strains in the mid-plane surface are not accessible directly from the CATIA software.

6.2.1 Problem statement

Figure 34 is depicting the BMP1 problem status consisting of three features: geometry, laminate parameters, and the loading conditions. First, the geometry (BLS) is a thin flat bar with $300 \times 25 \times 2.5$ (in millimetres) extracted from the tensile test sample conditions ASTM D3039 [19].

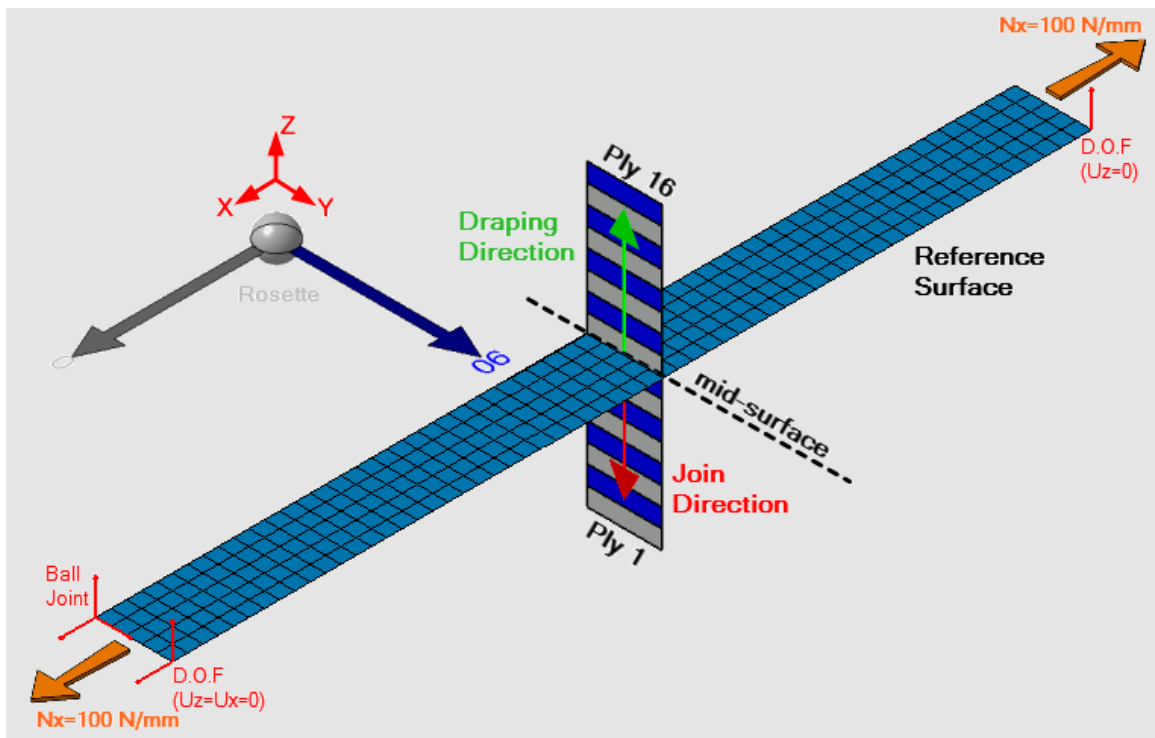


Figure 34: Simple illustration of problem status BMP1

Second, the laminate parameters consist of the rosette, the lamina, draping direction and mid-surface position as shown. The axes of the global coordinate system (shown in red) and the rosette are in the same direction. The rosette shows 0° and 90° respectively in grey and navy blue, and the 2D scaleless stacking sequence is illustrated in the figure. Sixteen layers of unidirectional AS4 (see Table 10) laminae coded as $[0/90]:8$ (Type5: see Appendices Table A) using the top reference plane method [53] are stacked on the BLS. The Reference Surface is exactly located in the middle of the laminate's thickness

(mid-surface). It is important to notice that the join and the stacking sequence directions are apposite, respectively shown in red and green.

Third, the loading conditions are as follows: a pair of opposing tensile loads equal to 100 (N/mm) align with the “X” direction and is applied on two ends of the Reference Surface (the meshed BLS located in the mid-surface). The laminate properties are imported while the symmetrical option is selected. The Base Laminate Surface (BLS) is meshed with Quads (4.92 mm size) Parabolic Shell Elements. Three vertices to restrain the base laminate support are shown in red.

6.2.2 Results and Discussion

The balanced anti-symmetric cross-ply laminate is selected for this problem (Type5: Appendices Table A); therefore, the laminate [ABD] matrices’ characteristics are as follows. Since " $A_{16} = A_{26} = 0, D_{16} = D_{26} = 0$ ", there is no shear-extension coupling and no bend-twist coupling. In addition, for the proposed problem status, since B_{11} and B_{22} are not zero, bend-extension coupling causes the sheet to bend about the “Y” axis apart from the stretch in the “X” axis and contraction along the “Y” axis.

Figure 35 shows the RCT for the BMP1. The problem status is summarized on the left side of row 1 (L1). In addition, a screenshot captured from the CATIA software is presented on the right side of row 1 (R1). In R1, the tensile loads are in orange, and the restraints in the vertices are shown in red (See Table 12 for the imported supports, directions, and magnitudes in CATIA software). Moreover, the rosette and laminate stacking sequence with the colour consistent in the same ply directions are illustrated.

In Figure 35, row 2, the deformed shapes for ABAQUS software on the left and CATIA software on the right are captured, showing the Norm displacement in the isometric view with the same deformation amplification magnitude. The Norm displacement is the resultant vector’s magnitude when the individual components are squared, added together, and reported in the CATIA software.

Row 3 shows the deformation magnitudes in the Norm and the individual components in millimetres, and the total strain energy magnitudes in millijoules. The discrepancies are roughly 2% comparing these magnitudes from the two GUIs (ABAQUS and CATIA software) and the CLT method.

Row 4 presents the Mises stresses, maximum and minimum principal stresses in the middle of each ply extracted from three methods, and again, the differences are less than 2%. To sum up, rows 2 to 4 show that the CATIA software, CLT, and other software results are all in compliance with each other and the errors are negligible.

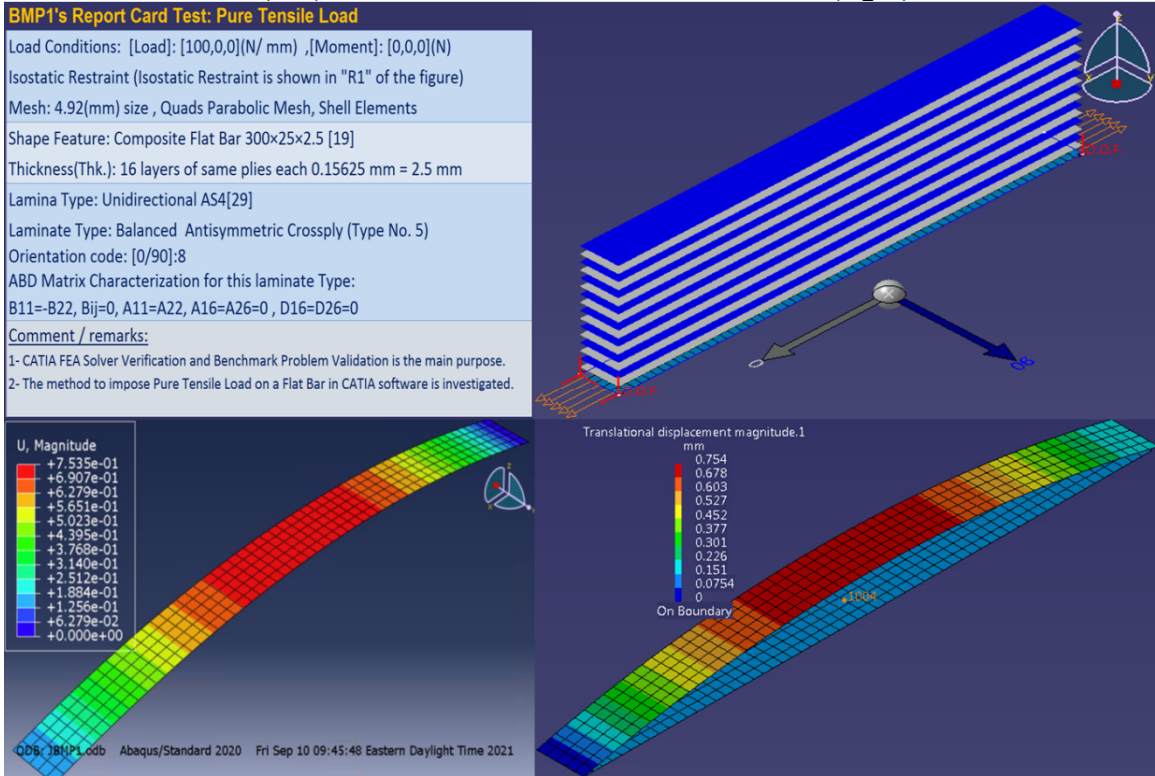
Considering the table embedded in the row 3 of the RCT, the CATIA software does not directly present the strains in the mid-plane surface. It is important to notice that the

stresses in each ply are resulted from the strains and curvature in the mid-plane surface. They are validated in the graph (in row 4); therefore, we can infer without computation that they are almost the same as the results mentioned in the table from ABAQUS software and the CLT method.

Nevertheless, one can calculate the strains in the mid-plane surface using the strains in the layers (see 2.3), which are directly accessible in CATIA software. The procedure for calculating these at the middle surface is described in BMP7.

L (left)

R (right)



Method	Total Strain Energy mJ	Norm mm	Max. Displacement			Strain Mid surface_x	Strain Mid surface_y	Strain Mid surface_xy	kappa_x 1/mm	kappa_y 1/mm	kappa_xy 1/mm
			Ux mm	Uy mm	Uz mm						
CLT	-		1.52E-01	-4.51E-04	-	5.12E-04	-1.81E-05	-4.21E-21	6.69E-05	-7.54E-10	-2.50E-21
CATIA	191.7	0.754	1.53E-01	-4.52E-04	7.50E-01	-	-	-	6.63E-05	1.99E-16	1.99E-12
ABAQUS	191.678	0.7535	1.53E-01	-4.53E-04	7.50E-01	5.10E-04	-1.80E-05	-1.30E-17	6.66E-05	5.80E-13	3.50E-17

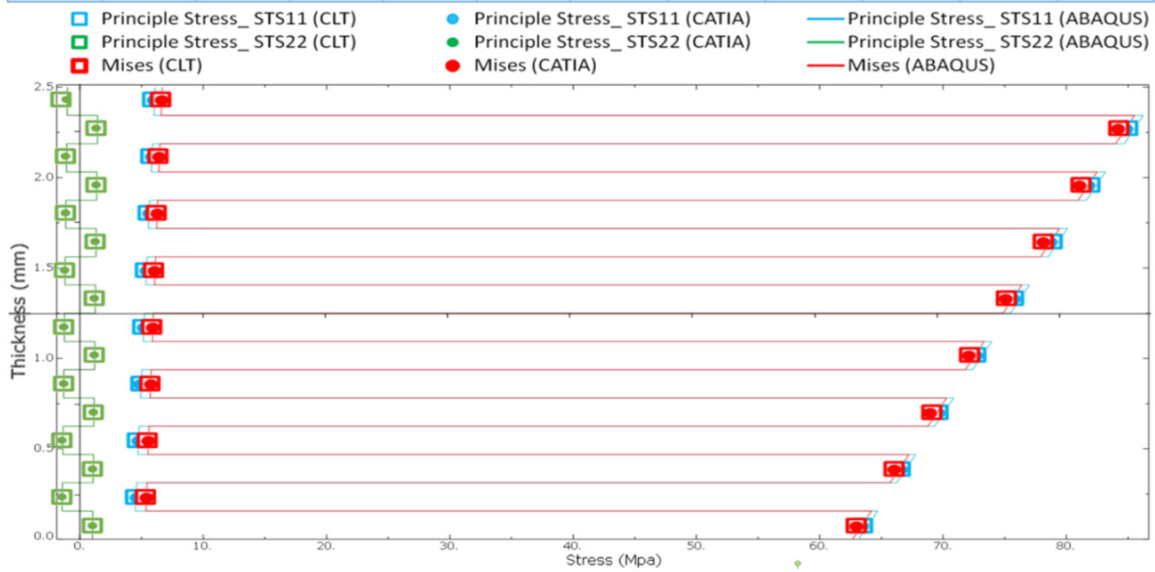


Figure 35: BMP1's Report Card Test (Pure Tensile loads)

6.3 BMP2 (Bending loading condition)

The three primary purposes investigated in BMP2 are as follows:

1. The method to impose pure bending loads in CATIA software is investigated.
2. CATIA FEA Solver is validated for the bending load condition.
3. A discussion on the CATIA output for the tensorial curvature Kappa_{xy} (κ_{xy}), which is half of the engineering curvature, resulting from the CLT or the other two FEA software.

6.3.1 Problem statement

Figure 36 is presented to explain the BMP2 problem status consisting of three features: geometry, laminate parameters, and the loading conditions. The stacking sequence, load's type, and restraints' position have changed compared to BMP1. The geometry (BLS) is the same, a thin flat bar with $300 \times 25 \times 2.5$ (in millimetres).

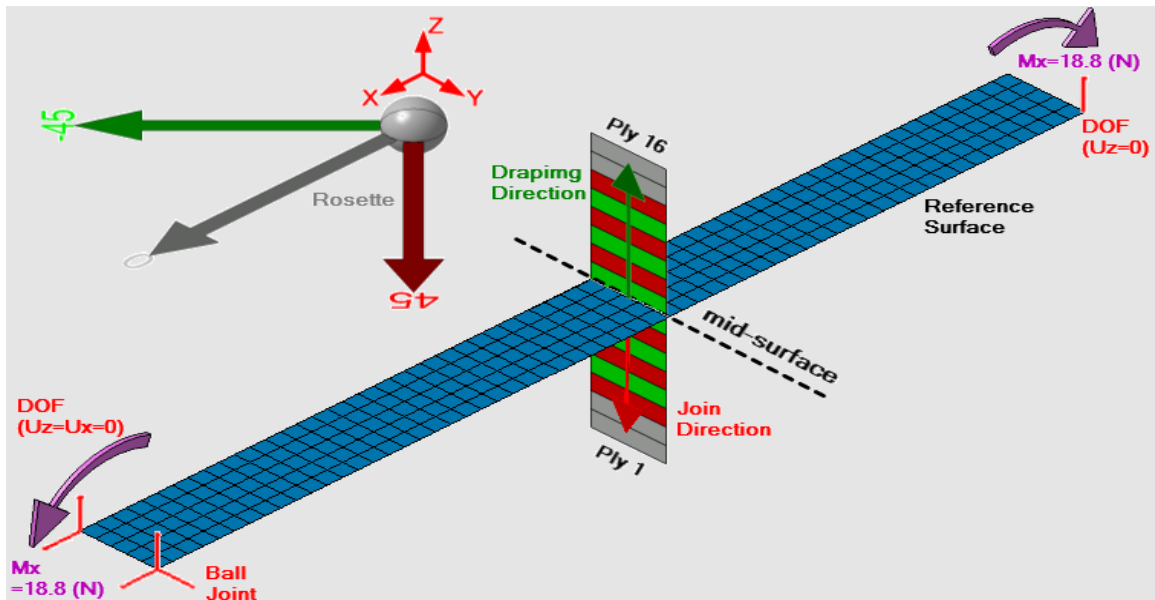


Figure 36: Simple illustration of the BMP2 problem status

The laminate parameters consist of the rosette, the lamina, draping direction, and mid-surface position, as shown in Figure 36. The axes of the global coordinate system (shown in red) and the rosette are in the same direction. The rosette presents -45° , 0° , and 45° respectively in light green, gray, and red; correspondingly, the 2D scaleless stacking sequence is illustrated in the figure. Sixteen layers of unidirectional AS4 plies are employed to stack up the laminate with the orientation code as $[(0):2/(\pm 45):3]:s$ (Type2: Appendices Table A) on the BLS. The join and the stacking sequence directions are opposite, respectively shown in red and dark green.

The loading conditions presented in Figure 36 are as follows: a pair of opposing bending loads about the y axis equal to 18.8 (N)—[Load]= $[0,0,0](\text{N}/\text{mm})$, [Moment]=

[18.8,0,0](N)—is applied on two ends of the Reference Surface (the meshed BLS located in the mid-surface). The symmetrical option was selected; therefore, the Reference Surface and the mid-plane surface are in the middle of the laminate’s thickness. The BLS is meshed with Quads Parabolic Shell Elements with 4.92 mm size. Three vertices are selected as “support” to restrain the base laminate are employed differently from the other BMPs, and shown in red.

6.3.2 Results and discussion

The Balanced laminate is selected for this problem (Type2: Appendices Table A); therefore, the characteristics of the [ABD] matrices for the laminate are as follows. Since " $A_{16} = A_{26} = 0$, $[B] = 0$ ", there is no shear-extension coupling and no bend-extension coupling. In addition, since D_{16} and D_{26} are not zero, bend-twist coupling causes the part to twist and bend for the proposed problem case.

Figure 37 shows the RCT for the BMP2. The problem status is summarized on the left side of row 1 (L1), as explained in 6.3.1. In addition, on the right side of row 1 (R1), the problem status is presented as captured from the CATIA software.

In R1, the bending loads are in pink, applied at the front and back edges, and the restraints in the vertices are shown in red (See Table 12 for the assigned supports, directions, and magnitudes in CATIA software). Moreover, the rosette and laminate stacking sequence with the colour consistent in the same ply directions are illustrated.

In Figure 37, row 2, the deformed shapes for ABAQUS software on the left and CATIA software on the right are captured while the isometric view with the same amplification magnitudes of deformations showing the Norm displacement are presented.

The embedded table in row 3 presents the following magnitudes resulting from different tools: the deformations—in the Norm and the individual—in millimetres, the total strain energy in millijoules, and the strains and curvatures in the mid-surface of the laminate. Similar to BMP1, the differences are around 2% comparing these magnitudes from the two GUIs (ABAQUS and CATIA software) and the CLT method.

Row 4 presents the Mises stresses, maximum and minimum principal stresses in the middle of each ply extracted from three methods, and again, the discrepancies are less than 2%. To sum up, rows 2 to 4 clarify that the CATIA software, CLT, and other software results are all in compliance with each other, and the errors are negligible.

Here another undocumented characteristic of CATIA FEA Solver is noticed: the CATIA software presents the tensorial curvature, which is half of the engineering curvature $Kappa_{xy}$ (κ_{xy}), resulting from the CLT or other two FEA software. To report the exact numbers, $Kappa_{xy}$ (κ_{xy}) resulted from the CATIA software is equal to $-5.45e-6$ (1/mm), which is half of the $-1.09e-5$ (1/mm) resulting from the CLT and ABAQUS software.

L (left)

R (right)

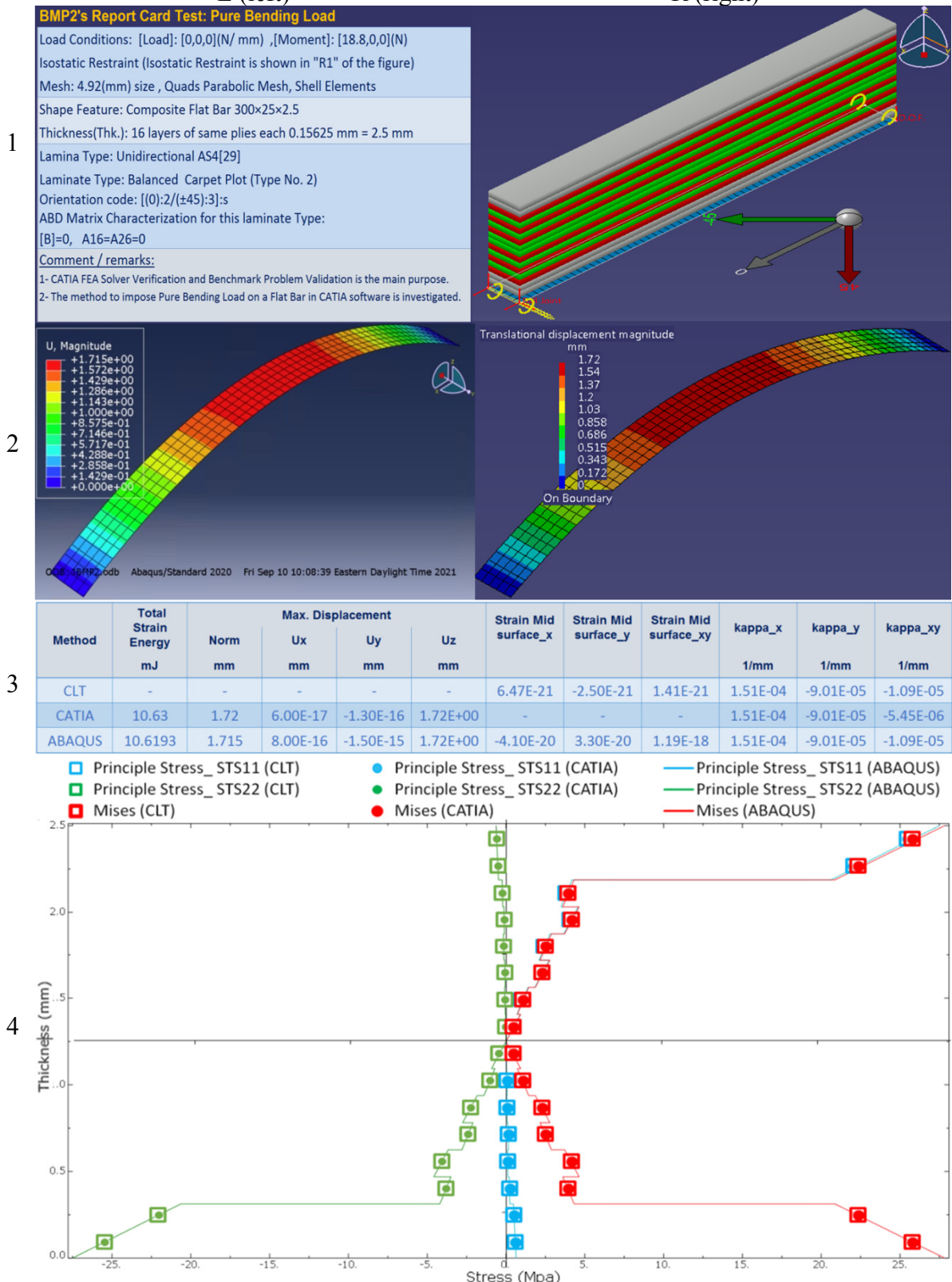


Figure 37: BMP2's Report Card Test (Pure Bending Load)

6.4 BMP3 (Shearing loading condition)

The three primary purposes studied in BMP3 are as follows:

1. The method to impose pure shearing loads in CATIA software is investigated.
2. CATIA FEA Solver is validated for the shearing load condition.
3. It is explained that the CATIA software presents the tensorial shear strain, which is half of the engineering shear strain “(γ_{xy})” resulting from the CLT or the other two FEA software.

6.4.1 Problem statement

Figure 38 is pieced together to illustrate the geometry, laminate parameters, and the loading conditions to explain the BMP3 problem case. The stacking sequence, load's type, and restraints' position have changed compared to BMP1 and BMP2. However, the geometry (BLS) is still the same, a thin flat bar with $300 \times 25 \times 2.5$ (in millimetres).

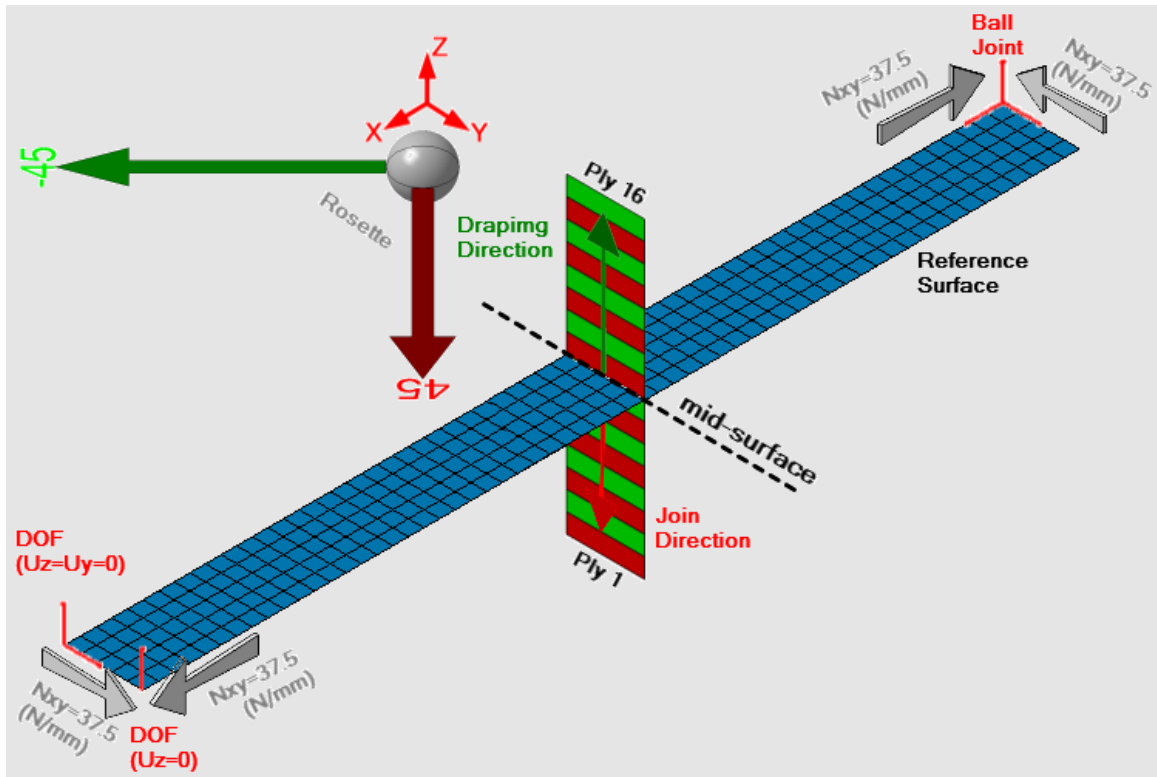


Figure 38: Simple illustration of the BMP3 problem case

The laminate parameters consist of the rosette, the lamina, draping direction, and mid-surface position, as demonstrated in Figure 38. The axes of the global coordinate system (shown in red) and the rosette are in the same direction. The rosette shows -45° and 45° in light green and red, indicating the plies' directions; moreover, the 2D scaleless stacking sequence is illustrated using similar colours in the figure. Sixteen layers of unidirectional AS4 plies (see Table 10) are employed to stack up the laminate with the

orientation code as $[\pm 45]:8$ (Type2: Appendices Table A) on the BLS. The join and the stacking sequence directions are opposite, respectively shown in red and dark green.

The loading conditions presented in Figure 38 are as follows: two pairs of opposing shearing loads in grey equal to 37.5 (N/mm)—[Load]= $[0, 37.5, 0]$ (N/mm), [Moment]= $[0, 0, 0]$ (N)—are applied on all four edges of the Reference Surface. As discussed in 5.3.1, the symmetrical option was selected; therefore, the Reference Surface and the mid-plane surface coincide. The BLS is meshed with Quads Parabolic Shell Elements with 4.92 mm size. Three vertices are selected as “support” to restrain the base laminate. This is done differently from the previous two BMPs, and shown in red.

6.4.2 Results and discussion

The balanced angle-ply laminate is selected for this problem (Type6: Appendices Table A); therefore, the characteristics of the $[ABD]$ matrices for the laminate are as follows. Since " $A_{16} = A_{26} = 0, D_{16} = D_{26} = 0$ ", there is no shear-extension coupling and no bend-twist coupling. In addition, since B_{16} and B_{26} are not zero, bend-extension coupling for this load condition causes the model to bend about the “X” and “Y” axis; meanwhile, the curvature in the “XY” direction is negligible.

Figure 39 shows the RCT for the BMP3. The problem case is summarized on the left side of row 1 (L1). In addition, on the right side of row 1 (R1), the problem status is shown as captured from the CATIA software.

In R1, the shearing loads are in white, placed in all four edges as “support,” and a new combination of user-defined restraints located in three vertices are shown in red. Moreover, the rosette and laminate stacking sequence with the colour consistent in the same ply directions are illustrated.

In Figure 39, row 2, the deformed shapes for ABAQUS software on the left and CATIA software on the right are captured, showing the Norm displacement in the isometric view with the same deformation amplification magnitude. Also, shearing loads and restraints are displayed.

The table in row 3 presents the magnitudes of the deformations—in the Norm and three main coordinate directions—in millimetres, the total strain energy magnitudes in millijoules, and the strains and curvatures in the mid surface. As in the previous two BMPs, the discrepancies are approximately 2% when compared with the ABAQUS software and the CLT method.

Row 4 presents the Mises stresses, maximum and minimum principal stresses in the middle of each ply extracted from three methods. Once again, the differences are less than 2%. To sum up, rows 2 to 4 confirm that the CATIA software, CLT, and other software outcomes agree with each other, and the differences are negligible.

Similar to the curvature κ_{xy} (κ_{xy}) discussed in BMP2, the tensorial shear strain is half of the engineering shear strain ($C12 = \gamma_{xy}$) when compared to the CLT and the other two FEA software.

Table 13 presents the strain tensor components— $C11 = \gamma_{xx}$, $C22 = \gamma_{yy}$, and $C12 = \gamma_{xy}$ —generated by CATIA and the computed values using the CLT method in different plies. For each of them, the Differences column is presented, and obviously for “C12,” it is essential to multiply the CATIA results by 2. The magnitudes in the Differences columns are almost zero.

Table 13: Engineering shear strain is half of the shear strain (results from the BMP3)

Ply	Tensor Component C11(strain)			Tensor Component C22(strain)			Tensor Component C12(strain)			
	CLT	CATIA	Differences	CLT	CATIA	Differences	CLT	CATIA	Multi. by 2	Differences
1	1.77E-04	1.77E-04	-4.82E-07	-1.06E-04	-1.06E-04	4.68E-07	1.28E-05	6.39E-06	1.28E-05	-5.87E-09
2	1.53E-04	1.53E-04	-1.76E-08	-9.15E-05	-9.10E-05	-4.61E-07	1.11E-05	5.54E-06	1.11E-05	-9.09E-09
3	1.29E-04	1.29E-04	4.47E-07	-7.74E-05	-7.74E-05	1.01E-08	9.37E-06	4.68E-06	9.36E-06	7.69E-09
4	1.06E-04	1.06E-04	-8.91E-08	-6.33E-05	-6.33E-05	-1.90E-08	7.66E-06	3.83E-06	7.66E-06	4.48E-09
5	8.24E-05	8.24E-05	-2.48E-08	-4.92E-05	-4.92E-05	-4.81E-08	5.96E-06	2.98E-06	5.96E-06	1.26E-09
6	5.88E-05	5.88E-05	3.94E-08	-3.52E-05	-3.52E-05	2.28E-08	4.26E-06	2.13E-06	4.26E-06	-1.96E-09
7	3.53E-05	3.53E-05	3.64E-09	-2.11E-05	-2.11E-05	-6.33E-09	2.55E-06	1.28E-06	2.56E-06	-5.17E-09
8	1.18E-05	1.18E-05	-3.21E-08	-7.04E-06	-7.04E-06	4.56E-09	8.52E-07	4.26E-07	8.52E-07	-3.92E-10
9	-1.18E-05	-1.18E-05	3.21E-08	7.04E-06	7.04E-06	-4.56E-09	-8.52E-07	-4.26E-07	-8.52E-07	3.92E-10
10	-3.53E-05	-3.53E-05	-3.64E-09	2.11E-05	2.11E-05	6.33E-09	-2.55E-06	-1.28E-06	-2.56E-06	5.17E-09
11	-5.88E-05	-5.88E-05	-3.94E-08	3.52E-05	3.52E-05	-2.28E-08	-4.26E-06	-2.13E-06	-4.26E-06	1.96E-09
12	-8.24E-05	-8.24E-05	2.48E-08	4.92E-05	4.92E-05	4.81E-08	-5.96E-06	-2.98E-06	-5.96E-06	-1.26E-09
13	-1.06E-04	-1.06E-04	8.91E-08	6.33E-05	6.33E-05	1.90E-08	-7.66E-06	-3.83E-06	-7.66E-06	-4.48E-09
14	-1.29E-04	-1.29E-04	-4.47E-07	7.74E-05	7.74E-05	-1.01E-08	-9.37E-06	-4.68E-06	-9.36E-06	-7.69E-09
15	-1.53E-04	-1.53E-04	1.76E-08	9.15E-05	9.10E-05	4.61E-07	-1.11E-05	-5.54E-06	-1.11E-05	9.09E-09
16	-1.77E-04	-1.77E-04	4.82E-07	1.06E-04	1.06E-04	-4.68E-07	-1.28E-05	-6.39E-06	-1.28E-05	5.87E-09

L (left)

R (right)

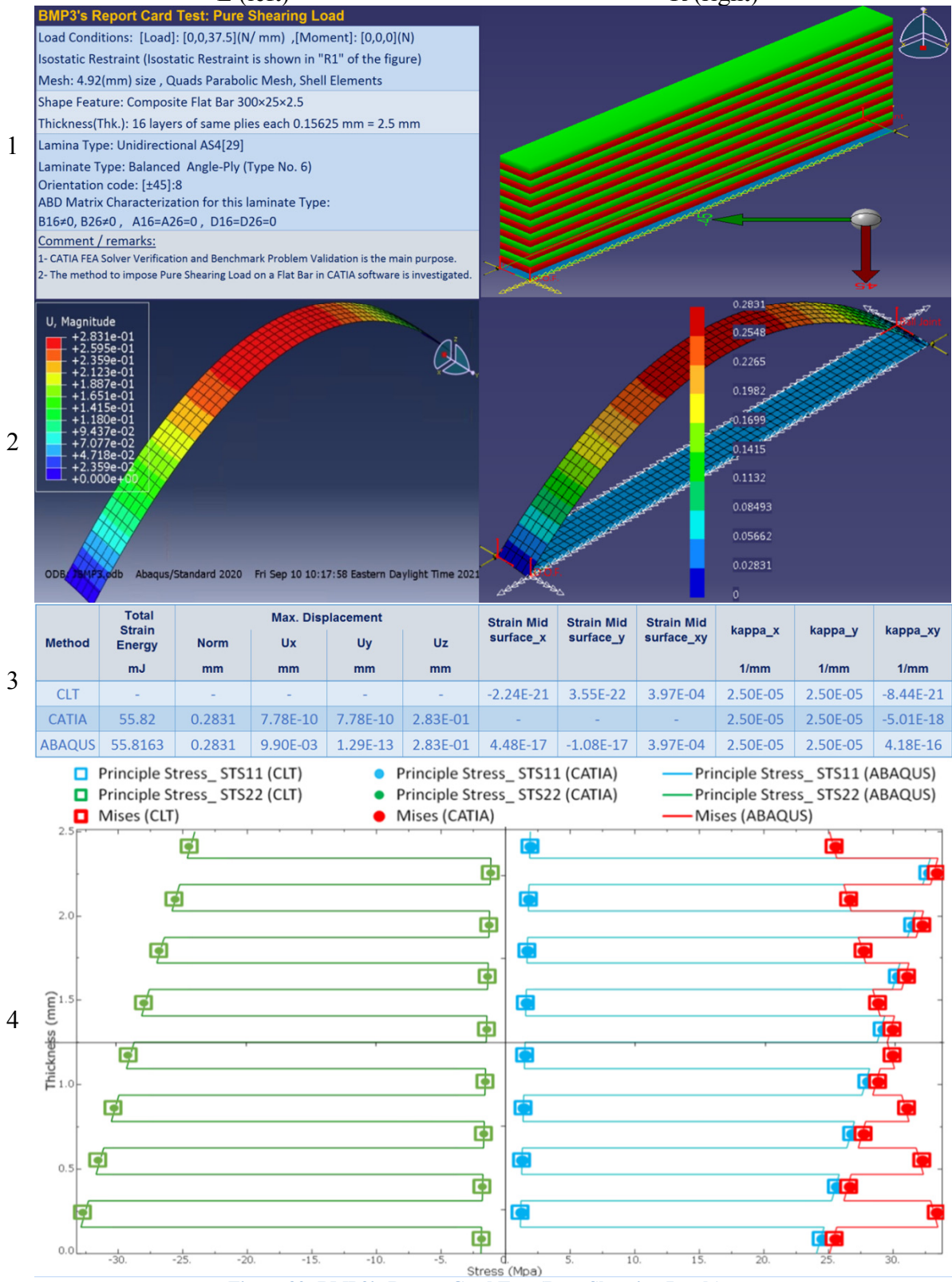


Figure 39: BMP3's Report Card Test (Pure Shearing Loads)

6.5 BMP4 (Twisting loading conditions)

The three primary purposes sought in BMP4 are as follows:

1. The method to impose pure twisting loads in CATIA software is investigated [39].
2. The CATIA FEA Solver is assessed by comparing the results to those of ABAQUS and ANSYS. Although the CATIA software and the other two respond almost identically to the same modelling method of the twisting loads, the magnitudes of Total Strain Energy from the ABAQUS are almost double that of CATIA and ANSYS.
3. Some errors in the results were reported when the FEA Solvers and the CLT were compared. Therefore, a more challenging condition is prevailing for in BMP4, even in such a simple geometry.

6.5.1 Problem statement

Figure 40 is assembled to illustrate the geometry, laminate parameters, and the loading conditions to explain the BMP4 problem case. A thin rectangular plate with $300 \times 200 \times 2.5$ (in millimetres) was used as the geometry (BLS).

Figure 40 shows the laminate parameters consisting of the rosette, the lamina, draping direction and mid-surface position. The axes of the global coordinate system (shown in red) and the rosette are in the same direction. The rosette shows -45° in light green, -30° in light blue, 0° in gray, 45° in red, and 90° in navy blue, indicating the plies' directions. Moreover, the 2D scaleless stacking sequence is illustrated using similar colours in the figure. In total, 16 layers of the unidirectional AS4 plies were employed to stack up a general laminated stacking sequence (Type8: Appendices Table A) with the orientation code as $[90/45/-30/(-45):2/0/45/(90):2/-45/0/(45):2/0/-45/90]$ on of the BLS. The join and the stacking sequence directions are opposite, respectively shown in red and dark green.

The loading conditions demonstrated in Figure 40 are as follows: two pairs of opposing twisting loads in yellow equal to 18.8 (N)—[Load]= $[0, 0, 0]$ (N/mm), [Moment]= $[0, 0, 18.8]$ (N)—are applied as shown on all four edges of the Reference Surface. The symmetrical option was selected; therefore, the Reference Surface and the mid-plane surface coincide. The BLS is meshed with Quads Parabolic Shell Elements with 5.26 mm size. Three vertices were selected as “support” to restrain the base laminate and are displayed in red.

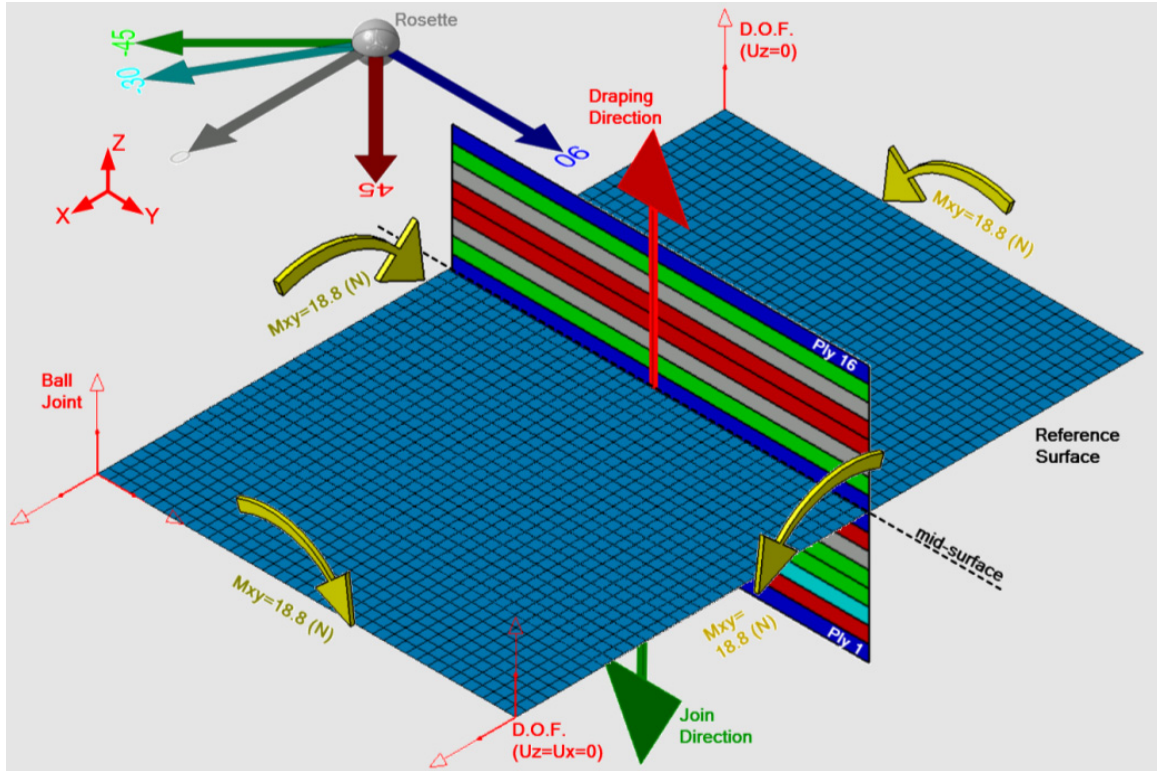


Figure 40: Simple illustration of the BMP4 problem case

6.5.2 Results and discussion

The general laminated stacking sequence was selected for this problem (Type8: Appendices Table A); therefore, the characteristics of the $[ABD]$ matrices for the laminate are as follows. The shear-extension coupling, and bend-twist coupling exist since " A_{16}, A_{26} " and " D_{16}, D_{26} " are not zero. Moreover, the entries in the $[B]$ matrix are not zero. Therefore, all types of strains and curvatures in the part will result, as demonstrated with state4 (S4), Type8 in Appendices Table B.

Figure 41 shows the RCT for the BMP4, which is organized slightly differently from the one discussed in 6.1.2. The shape deformation and the magnitudes of the "deformation," the Total Strain Energy, and the von Mises stress in different layers were extracted from the ANSYS software and are included in this RCT.

The problem case is summarized on the left side of row 1 (L1). Furthermore, on the right side of row 1 (R1), the problem status is shown as captured from the CATIA software.

In R1, the twisting loads are in yellow, placed in all four edges as "support," and a new combination of user-defined restraints located in three vertices are shown in red. Moreover, the rosette illustrates the colour-codes of the mentioned directions of the layers on the base surface.

In Figure 41, row 2 shows the deformation shapes of ABAQUS, ANSYS, and CATIA software captured respectively from left to right with almost identical appearances. The deformed shapes are screenshots of the Norm displacement in the isometric view with the same amplification magnitudes that shows identical shapes for all three.

Row 3 presents the deformation magnitudes in the Norm and the individual components in millimetres and the total strain energy magnitudes in millijoules in the table. The table demonstrates that the outcomes are not in good agreement as before.

It is unclear why the Total Strain Energy resulting from ABAQUS software is drastically higher than those from the CATIA and ANSYS software. Unable to resolve this issue, in BMP7 to BMP9, the ANSYS software will be used to compare the deformed shape, displacement values, and total strain energy.

In row 4, the Mises stresses, maximum and minimum principal stresses in the middle of each ply extracted from ABAQUS, CATIA and CLT method and the Mises stresses from ANSYS software are presented as “red triangle” symbol. Based on the comparison and similarities of the results from all three software, the displacements are in reasonable agreement, and a similar range of errors for the stress magnitudes.

The maximum differences of 15% occur in layer 14, which has a 45° direction. It can be seen in the graph for other layers, the differences are negligible. Compared to the CLT method, the stress magnitudes resulting from the CATIA software are slightly higher when compared to ANSYS or ABAQUS with the CLT for the proposed problem case. In addition, other software, especially CATIA, predicts the stresses larger than the CLT values, which requires special attention during the design stage. In this benchmark, the directions of the loading conditions, including the twisting loads, are based on [39].

L (left)

R (right)

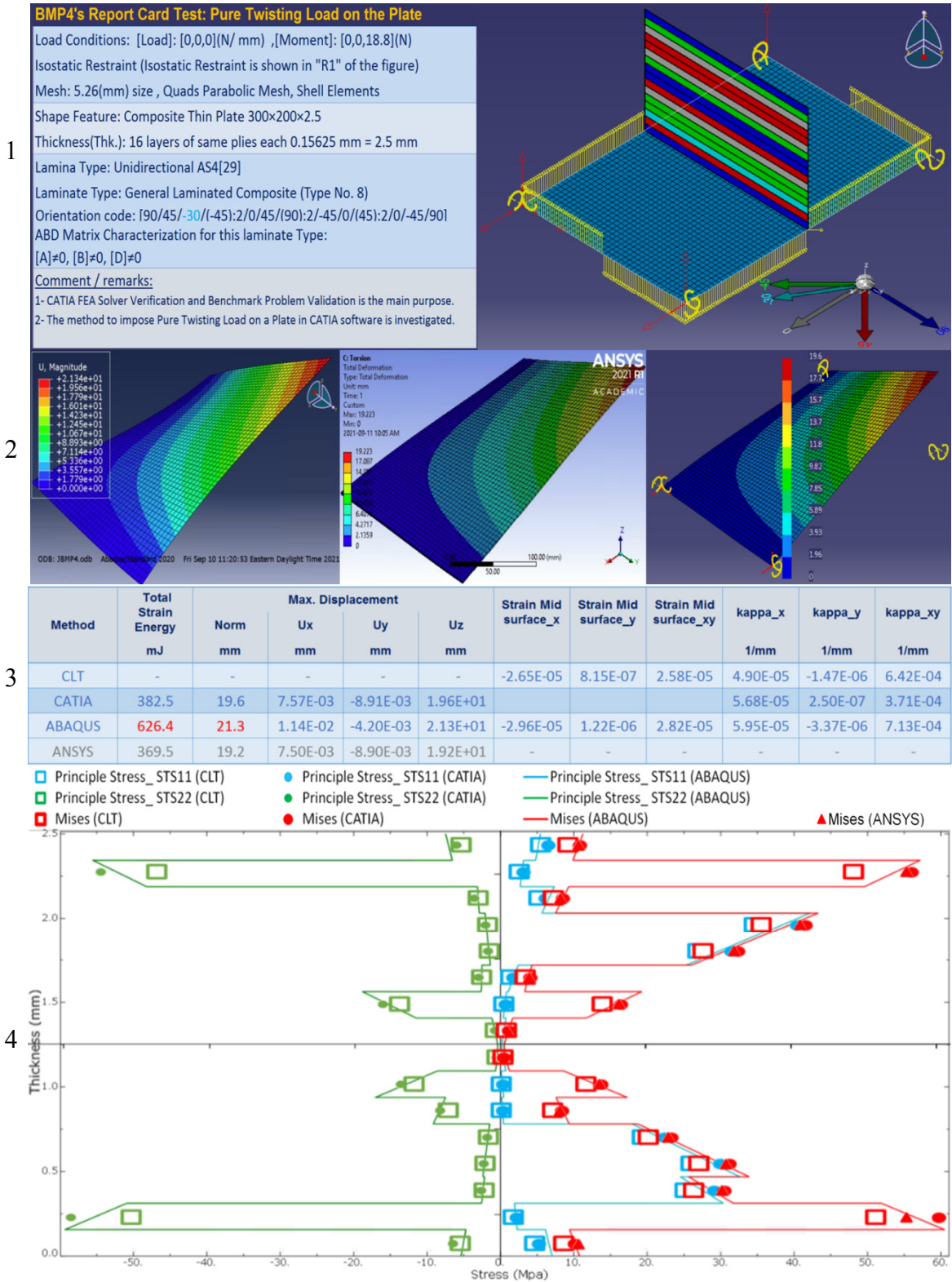


Figure 41: BMP4's Report Card Test (Pure Twisting Load on a Plate)

6.6 BMP5 (Temperature effect in unidirectional composites)

The three main goals of proposing BMP5 are as follows:

1. The method to impose a temperature effect using unidirectional lamina in CATIA software is investigated.
2. CATIA FEA Solver is employed to analyze the temperature effect condition applied to a composite part.
3. Two limitations are noticed and explored. First, the coefficient of thermal expansion is constant and defined only for the reference temperature. Second, the longitudinal thermal expansion coefficient must either be positive or, if it is negative, should be substantially small compared to the transverse thermal expansion coefficient.

6.6.1 Problem statement

Figure 42 is organized to illustrate the BMP5 problem consisting of three features: geometry, laminate parameters, and the loading conditions. A thin rectangular plate with $300 \times 200 \times 2.5$ (in millimetres) was employed as the geometry (BLS).

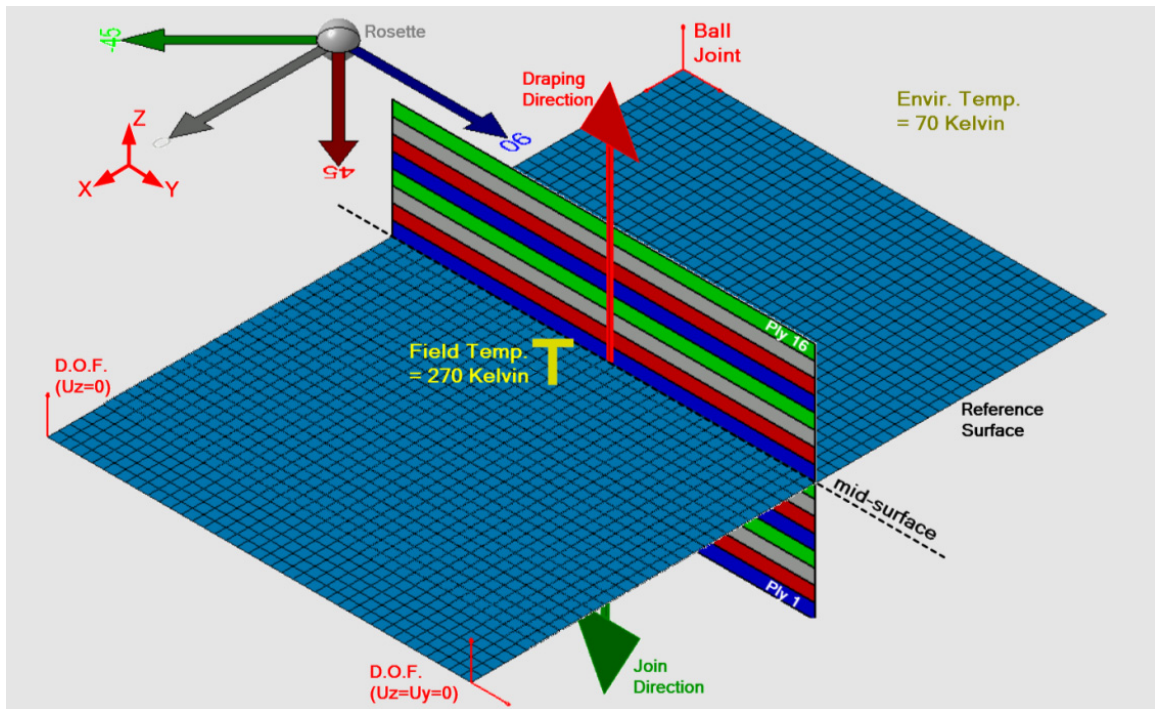


Figure 42: Simple illustration of the BMP5, MP6 problem case

The laminate parameters that are shown in Figure 42 consist of the rosette, the lamina, draping direction and mid-surface position. The axes of the global coordinate system (shown in red) and the rosette are in the same direction. The rosette shows -45° in light green, 0° in gray, 45° in red, and 90° in navy blue, indicating the plies' directions. Moreover, the 2D scaleless stacking sequence is illustrated using similar colours in the

figure. In total, 16 layers of the unidirectional lamina (AS4) from Table 10 were employed to stack up an unsymmetrical quasi-isotropic laminate (Type7: Appendices Table A) with the orientation code as [90/45/0/-45]:4 on the BLS. The join and the stacking sequence directions are opposite, respectively shown in red and dark green.

The yellow “T” symbol shown in the Reference Surface in Figure 42 represents the temperature effect decreased from 270 Kelvin (field temperature) to 70 Kelvin (environment temperature).

The thermal loads are mentioned here for computing in the CLT method, which is different based on the employed lamina and laminate types. The corresponding loads when the composite material is AS4 employed in the proposed laminate in BMP5 is [Load]= [-49.4, -49.4, 0] (N/mm), [Moment]= [2.2, -2.2, -2.2] (N) as recorded Table 12. The symmetrical option was selected; therefore, the Reference Surface and the mid-plane surface are coincident. The BLS is meshed with Quads Parabolic Shell Elements with 5.26 mm size. Three vertices were selected as “support” to restrain the base laminate, and shown in red.

6.6.2 Results and discussion

The unsymmetrical quasi-isotropic laminate is selected for this problem (Type7: Appendices Table A); therefore, the characteristics of the [ABD] matrices for the laminate are as follows. Since " $A_{16} = A_{26} = 0$ ", there is no shear-extension coupling. In addition, due to tetragonal characteristics ($A_{11} = A_{22}$), the [A] matrix results remain the same when the loads and the relative restraints are changed by 90°. The bend-extension coupling due to $[B] \neq 0$ and bend-twist coupling because of $D_{16} \neq 0$ and $D_{26} \neq 0$ are applicable (Appendices Table B). In this case, the bend-extension and bend-twist coupling intervene and cause shear, bending and twist in the part. Appendices Table B presents a similar example in the state5 (S5) Type7.

Figure 43 shows the RCT for the BMP5, and the organization of the information in an RCT was discussed in 6.1.2. The problem status is summarized in the problem case on the left side of row 1 (L1), explained in 6.6.1. In addition, on the right side of row 1 (R1), the problem states are shown as captured from the CATIA software.

In R1, the red “T” in the Reference Surface represents the temperature effect. Also, a new combination of user-defined restraints located in three vertices is shown in white. Moreover, the rosette and laminate stacking sequence with the colour consistent in the same ply directions are displayed.

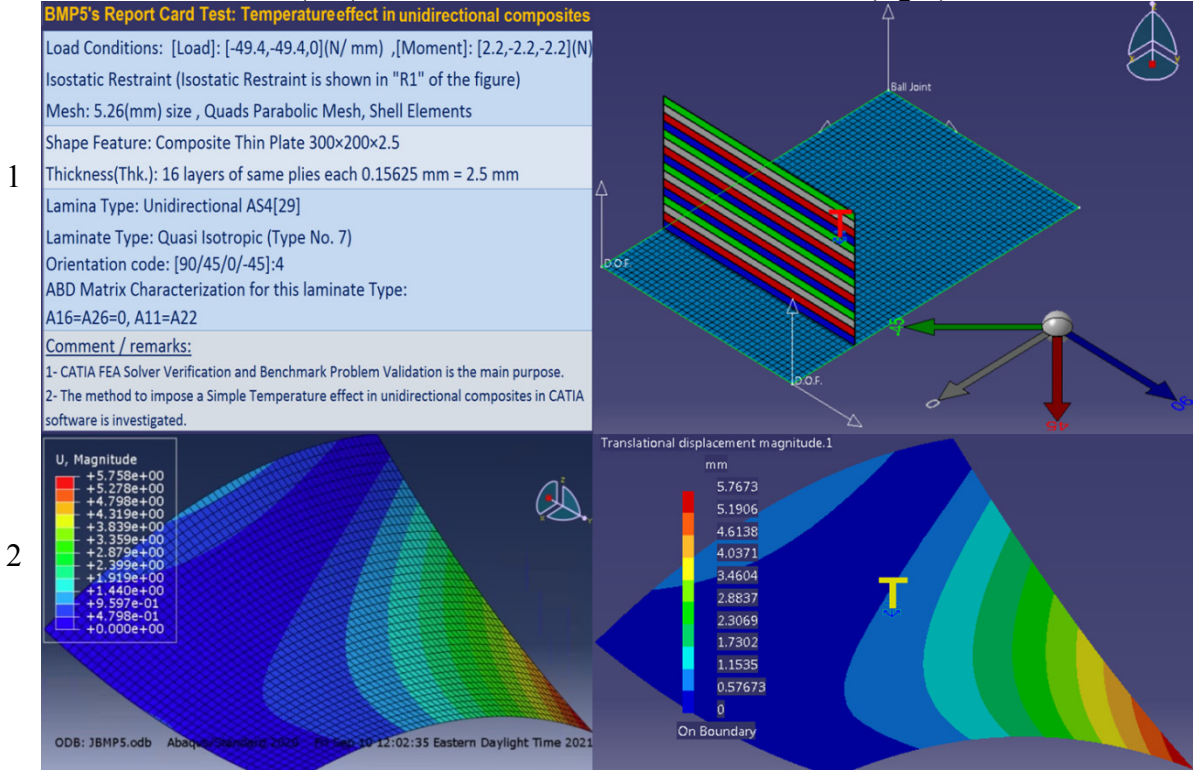
In row 2, the deformed shapes for ABAQUS software on the left and CATIA software on the right are captured, showing the Norm displacement in the isometric view with the same deformation amplification magnitude.

Row 3 presents the deformation magnitudes in the Norm and the individual components in millimetres and the total strain energy magnitudes in millijoules in the table. The differences are approximately 2% when comparing these magnitudes from the two GUIs (ABAQUS and CATIA software) and the CLT method. Row 4 presents the Mises stresses, maximum and minimum principal stresses in the middle of each ply extracted from three methods, and again, the discrepancies are of the order of 2%. To sum up, rows 2 to 4 in Figure 43 confirm that the CATIA software, CLT, and other software outcomes agree with each other, and the differences are negligible for the selected problem cases.

Two issues occur while solving the temperature effect problem employing the CATIA software. First, it is not possible to apply the negative sign for the thermal expansion while entering the mechanical properties of the lamina in the Material Library workbench. For instance, the Longitudinal Thermal Expansion Coefficient for AS4 is -0.9×10^{-6} (1/K) (see Table 10). Inevitably, the negative number entered in CATIA software was zero; nevertheless, the final results from different FEA software agreed. The reason is that the thermal expansion in the transverse direction is 30 times larger than the longitudinal coefficient. The second point to mention is that temperature-dependent coefficients cannot be modelled in CATIA.

L (left)

R (right)



Method	Total Strain Energy mJ	Max. Displacement				Strain Mid surface_x	Strain Mid surface_y	Strain Mid surface_xy	kappa_x 1/mm	kappa_y 1/mm	kappa_xy 1/mm
		Norm mm	Ux mm	Uy mm	Uz mm						
CLT	-	-	-	-	-	-2.48E-04	-2.59E-04	1.04E-05	-9.61E-05	9.61E-05	1.92E-04
CATIA	6213	5.7673	1.07E-01	-5.17E-02	-5.77E+00				9.61E-05	-9.61E-05	-9.61E-05
ABAQUS	6222.45	5.758	1.07E-01	-5.18E-02	-5.76E+00	-2.48E-04	-2.59E-04	1.04E-05	9.60E-05	-9.60E-05	-1.92E-04

- Principle Stress_STS11 (CLT) ● Principle Stress_STS11 (CATIA) — Principle Stress_STS11 (ABAQUS)
- Principle Stress_STS22 (CLT) ● Principle Stress_STS22 (CATIA) — Principle Stress_STS22 (ABAQUS)
- Mises (CLT) ● Mises (CATIA) — Mises (ABAQUS)

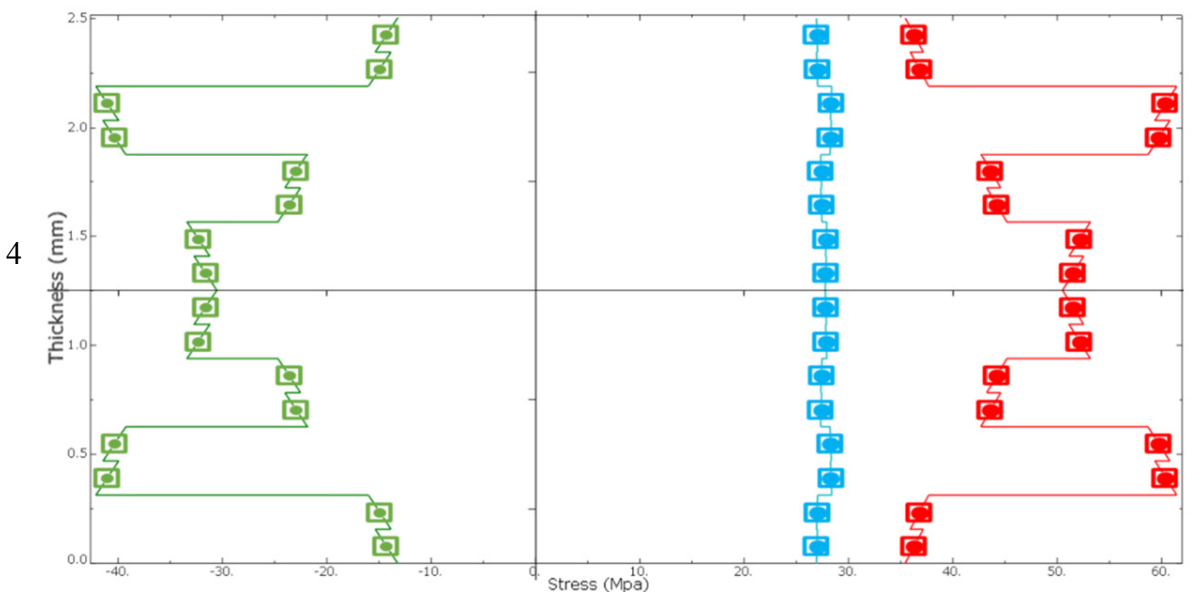


Figure 43: BMP5's Report Card Test (Temperature Effect using unidirectional lamina)

6.7 BMP6 (Temperature effect in woven fabric composites)

The benchmark problem BMP6 is very similar to BMP5, except for the lamina type. The lamina type in BMP6 is a woven fabric as opposed to a unidirectional fibre. The four primary goals sought in BMP6 are as follows:

1. CATIA FEA Solver is used in analyzing the temperature effect condition.
2. The problem cases for BMP5 and BMP6 are similar except for different employed materials. It is noticed that the results are remarkably different.
3. As in BMP5, it can be concluded from BMP6 that the CATIA software can handle a limited number of temperature cases.
4. The approach to handling a woven fabric in the CATIA software is introduced.

The critical point of employing woven fabric laminates is that they provide balanced mechanical properties in the 0° and 90° layers when compared to the unidirectional ones [54].

6.7.1 Problem statement

As mentioned before, due to similarities between BMP5 and BMP6, the BMP6 problem status is as stated in 6.6.1 except with respect to the composite material. See Table 10 for the mechanical properties of APG370, which is the woven fabric employed here. The loading conditions and the stacking sequence for computing in the CLT method is; [Load]= [-80.9, -80.9, 0] (N/mm), [Moment]= [0.2, -0.2, -0.2] (N).

6.7.2 Results and discussion

The unsymmetrical quasi-isotropic laminate is selected for BMP6, whose characteristics are discussed in 6.6.2. Figure 44 illustrates the RCT for the BMP6. The problem status is summarized in the problem case on the left side of row 1 (L1). In addition, on the right side of row 1 (R1), the problem states are shown as captured from the CATIA software.

In R1, the red “T” symbol in the Reference Surface represents the temperature effect. Also, a new combination of user-defined restraints located in three vertices is shown in white. Moreover, the rosette and laminate stacking sequence with the colour consistent in the same ply directions are illustrated.

In row 2, the deformed shapes for ABAQUS software on the left and CATIA software on the right are displayed, showing the Norm displacement in the isometric view with the same deformation amplification magnitude.

Row 3 presents the deformation magnitudes in the Norm and the individual components in millimetres and the total strain energy magnitudes in millijoules in the table. The differences are almost 2%. Row 4 presents the Mises stresses, maximum and

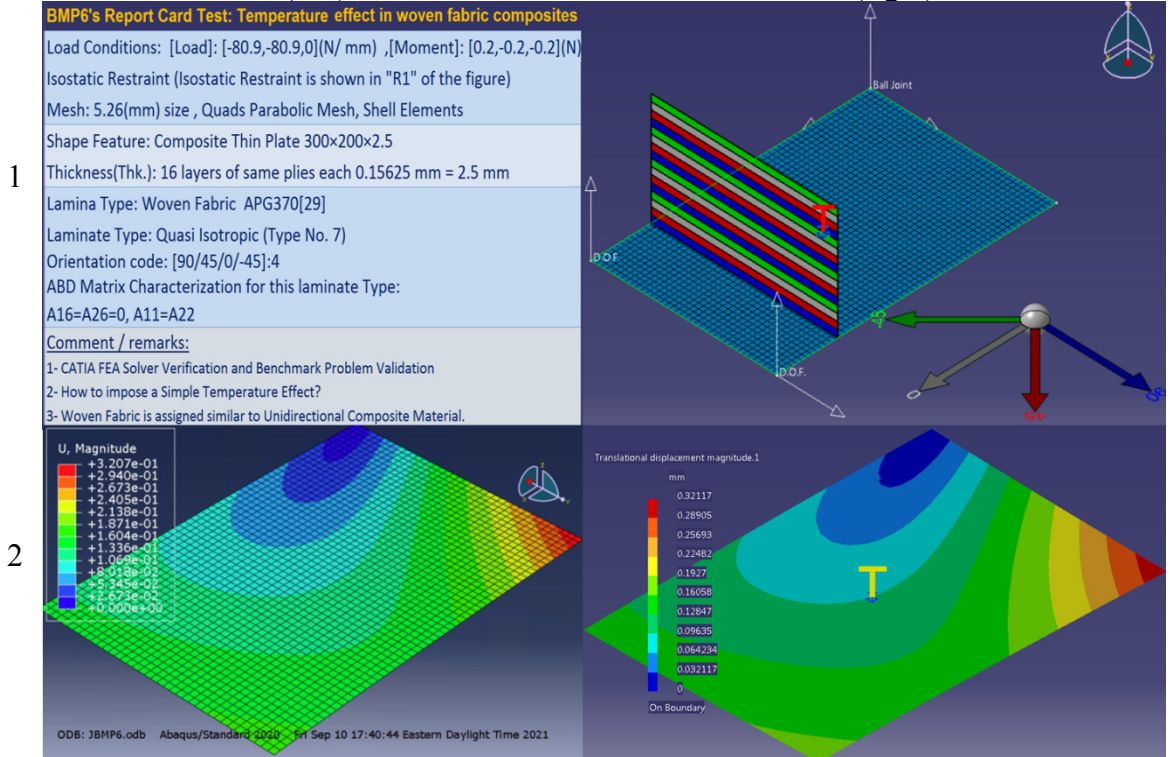
minimum principal stresses in the middle of each ply extracted from three methods, and again, the discrepancies are in the 2% range. To sum up, rows 2 to 4 in Figure 44 confirm that the CATIA software, CLT, and other software outcomes agree with each other, and the differences are negligible for the selected problem case.

As stated before, BMP5 and BMP6 share the same characteristics with one exception: namely, the lamina type. This seemingly minor difference, however, leads to significantly different behaviours. For instance, the maximum Mises stresses are reported about 60 MPa in BMP5 in comparison to 3 MPa in BMP6. Both configurations are selected from laminas made of similar Carbon fibres with identical density. See Table 10 to compare their mechanical properties.

There are two limitations to employing CATIA software to analyze the temperature effect problem. First, it is not possible to enter a negative coefficient of thermal expansion in the Material Library workbench. The Longitudinal Thermal Expansion Coefficient given for APG370 is $-3.4e-6$ (1/K), presented in see Table 10. Inevitably, the corresponding value in CATIA software was inputted as zero; nevertheless, the final results were not significantly affected. The justification is that the thermal expansion in the transverse direction is ten times larger than the longitudinal coefficient. The second issue to mention is that temperature-dependent coefficients cannot be modelled in CATIA.

L (left)

R (right)



3

Method	Total Strain Energy mJ	Max. Displacement			Strain Mid surface_x	Strain Mid surface_y	Strain Mid surface_xy	kappa_x 1/mm	kappa_y 1/mm	kappa_xy 1/mm
		Norm mm	Ux mm	Uy mm						
CLT	-	-	-	-	-3.99E-04	-4.00E-04	5.53E-07	-5.11E-06	5.11E-06	1.02E-05
CATIA	4.133	0.32117	-1.73E-01	1.60E-01	3.64E-01	-	-	5.11E-06	-5.11E-06	-5.11E-06
ABAQUS	4.13919	0.3207	-1.73E-01	1.60E-01	-3.63E-01	-3.99E-04	-4.00E-04	5.53E-07	5.10E-06	-5.10E-06

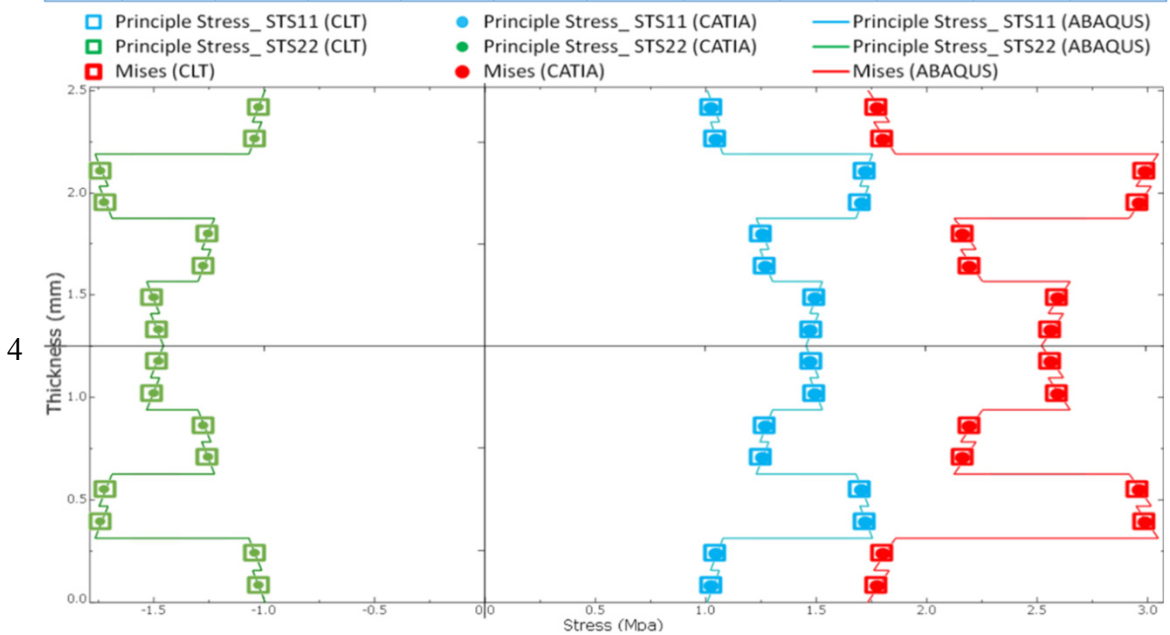


Figure 44: BMP6's Report Card Test (Temperature Effect using Woven Fabric)

6.8 BMP7 (Superposition load in unidirectional composites)

The three main goals of discussing BMP7 are as follows:

1. The CATIA FEA Solver is evaluated for the superposition loading conditions, while the unidirectional lamina is employed.
2. The results' differences for BMP7 are compared when 2D and 3D properties in the Material Library workbench were assigned individually.

It is important to note that the CATIA (2D, 3D) is mentioned in BMP7 to confirm that assigning 2D or 3D material properties do not influence final results. Here, the 2D and 3D material properties were separately entered into the Material Library workbench. Once the FEA analysis was conducted, and the results were found to be identical.

6.8.1 Problem statement

Figure 45 is organized to illustrate the BMP7 problem case consisting of three features: geometry, laminate parameters, and the loading conditions. A thin rectangular plate with $300 \times 200 \times 2.5$ (in millimetres) was employed as the geometry (BLS).

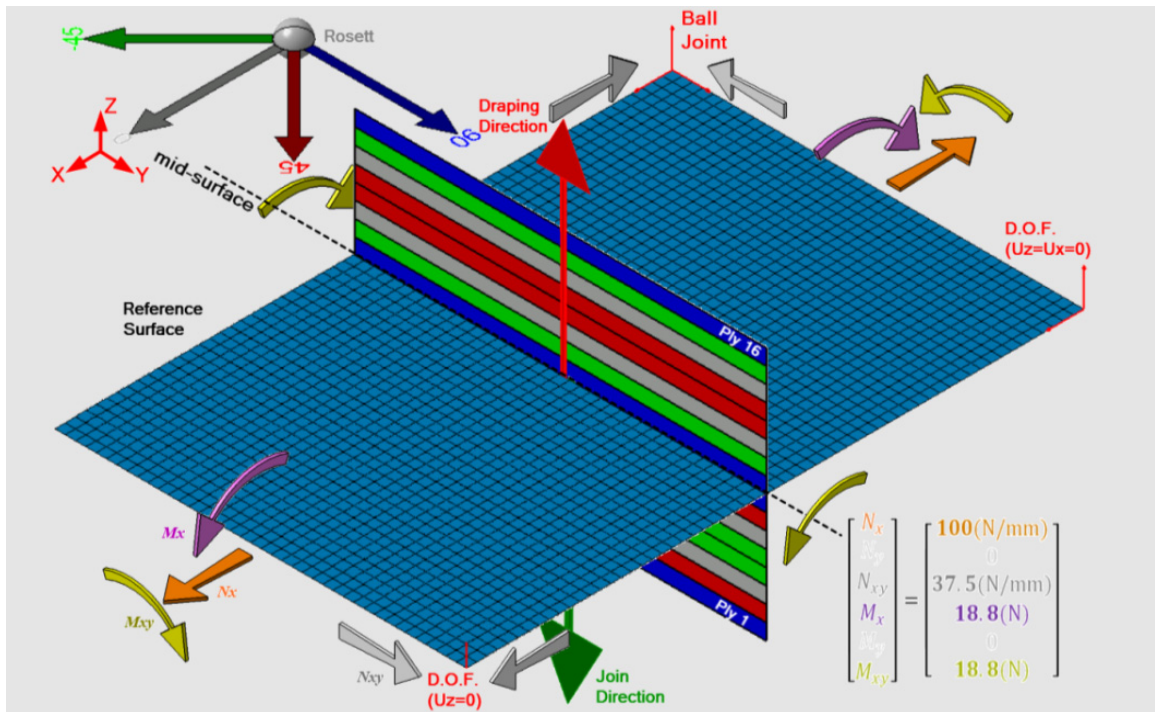


Figure 45: Simple illustration of the BMP7, MP8 problem case

The composite parameters are shown in Figure 45 consist of the rosette, the lamina, draping direction, and mid-surface position. The axes of the global coordinate system (shown in red) and the rosette are in the same direction. The rosette shows -45° in light green, 0° in gray, 45° in red, and 90° in navy blue, indicating the plies' directions. Moreover, the 2D scaleless stacking sequence is illustrated using similar colours in the

figure. In total, 16 layers of the unidirectional lamina (AS4) were employed to stack up Balanced Modified Quasi Isotropic laminate with the orientation code as [(90/45/0/-45):s/(90/-45/0/45):s]. (Type 1: Appendices Table A) on the BLS. The join and the stacking sequence directions are opposite, respectively shown in red and dark green.

The loading conditions presented in Figure 45 are listed as follows: The applied loads are tensile loads in orange, shearing loads in white, bending loads in green, and twisting loads in yellow as shown on the edges of the Reference Surface. The load and moment matrices are; [Load]=[100, 0, 37.5] (N/mm), [Moment]=[18.8, 0, 18.8] (N). Symmetrical option was selected; therefore, the Reference Surface and the mid-plane surface are coincident. The BLS is meshed with Quads Parabolic Shell Elements with 5.26 mm size. Three vertices are selected as “support” to restrain the base laminate.

6.8.2 Results and discussion

The Balanced Modified Quasi Isotropic laminate is selected for this problem (Type 1: Appendices Table A); therefore, the characteristics of the [ABD] matrices for the laminate are as follows. Since " $A_{16} = A_{26} = 0, D_{16} = D_{26} = 0, [B] = 0$ ", there is no shear-extension coupling, bend-twist coupling, and bend-extension coupling. Therefore, all types of deformations (stretches, bending, and twisting) will be directly caused by corresponding loads (state5 (S5) in Appendices Table B).

Figure 46 shows the RCT for the BMP7. The organization of the information in an RCT was discussed in 6.1.2 except that ANSYS is employed instead ABAQUS software. The problem status is summarized in the problem case on the left side of row 1 (L1). In addition, on the right side of row 1 (R1), the problem states are shown as captured from the CATIA software.

In R1, the tensile loads are shown in orange, shearing loads are shown in white, bending loads are shown in green, and the twisting loads are shown in yellow, and a new combination of user-defined restraints located in three vertices are shown in red. Moreover, the rosette illustrates the colour-codes of the mentioned directions of the layers illustrated on the base surface.

In row 2, the deformed shapes for ANSYS software on the left and CATIA software on the right are captured, showing the Norm displacement in the isometric view with the same deformation amplification magnitude.

Row 3 presents the deformation magnitudes in the Norm and the individual components in millimetres and the total strain energy magnitudes in millijoules in the table. The table shows that the outcomes are quite similar except for Kappa_xy shown in red. The reason is due to employing laminate Type1; the response to each loading condition is comparable with the CLT methods, which confirms the linear response of CATIA FEA Solver in a complex loading condition. Accordingly, the tensile loads'

responses are present in “Strain Mid surface_x” and “Strain Mid surface_y”. The bending load’s responses are present in Kappa_x and Kappa_y, and the shearing load’s response is presented in “Strain Mid surface_xy”. The response to the twisting loads is present in Kappa_xy (shown in red), which is the only one showing the discrepancies, however, this error does not affect the other strains and curvatures.

The method to compute the strains with the “x”, “y”, and “xy” components are presented in equations (25) and (26). The strains (STN) in the mid-plane surface (Mid_S) for the CATIA software are calculated from the Tensor Components (C) strains in layers 8 and 9. These two layers are above and below the mid-plane surface.

Table 14 shows the magnitudes and the average value of two independent computations using layers 8 and 9 for this purpose, shown in Figure 46 in green. Other layers can be employed; only the distances from the mid-plane surface would be different.

$$\text{Ply 8:} \quad STN(C) - \left(-\frac{\text{Ply thickness}}{2} \times \text{related curvature}\right) = STN(\text{Mid}_S) \quad 25$$

$$\text{Ply 9:} \quad STN(C) - \left(+\frac{\text{Ply thickness}}{2} \times \text{related curvature}\right) = STN(\text{Mid}_S) \quad 26$$

The “related curvature” is the curvature in the same direction (X or Y).

Table 14: BMP7 mid-plane surface strain computation

	Tensor Comonents			Midplane Surface		
BMP7	STN_x	STN_y	STN_xy	STN_x	STN_y	STN_xy
Ply 8	6.66E-04	-1.94E-04	3.02E-04	6.70E-04	-1.94E-04	3.31E-04
Ply 9	7.09E-04	-2.04E-04	3.63E-04	7.05E-04	-2.04E-04	3.34E-04
	STN Average			6.88E-04	-1.99E-04	3.33E-04

The graph in row 4 presents the maximum and minimum principal stresses of CLT and CATIA (2D, 3D) and the von Mises stresses of the three methods (ANSYS is included). As in BMP4, the FEA solvers agree with each other; however, they do not agree with the CLT method when examined separately. In BMP7, the error that occurred in the ply with the maximum stress is reduced to 4%, while it was 15% in BMP4. Two reasons can be influential:

1. The contribution of other types of loads in which their results are in compliance with different FEA tools (considered in BMP1 to BMP3) causes a decrease in the error percentage that results from imposing the twisting loads.
2. The employed laminate in BMP4 was a general laminate composite, and the [ABD] Matrix characteristics for that laminate type caused the intervention of the twisting loads in all types of strain and curvature ($[B] \neq 0$, $A_{16} \neq 0$, $A_{26} \neq 0$, $D_{16} \neq 0$, $D_{26} \neq 0$), as discussed in Appendix A. In other words, the applied load in BMP4 caused extra resistance such as tensile, shearing, and bending in the model due to

unintended strains and curvatures, which increased the stresses. Appendices Table B shows the extra strains and curvatures resulting from using Type8 in comparison to Type1 in state5 (S5) loading conditions.

L (left)

R (right)

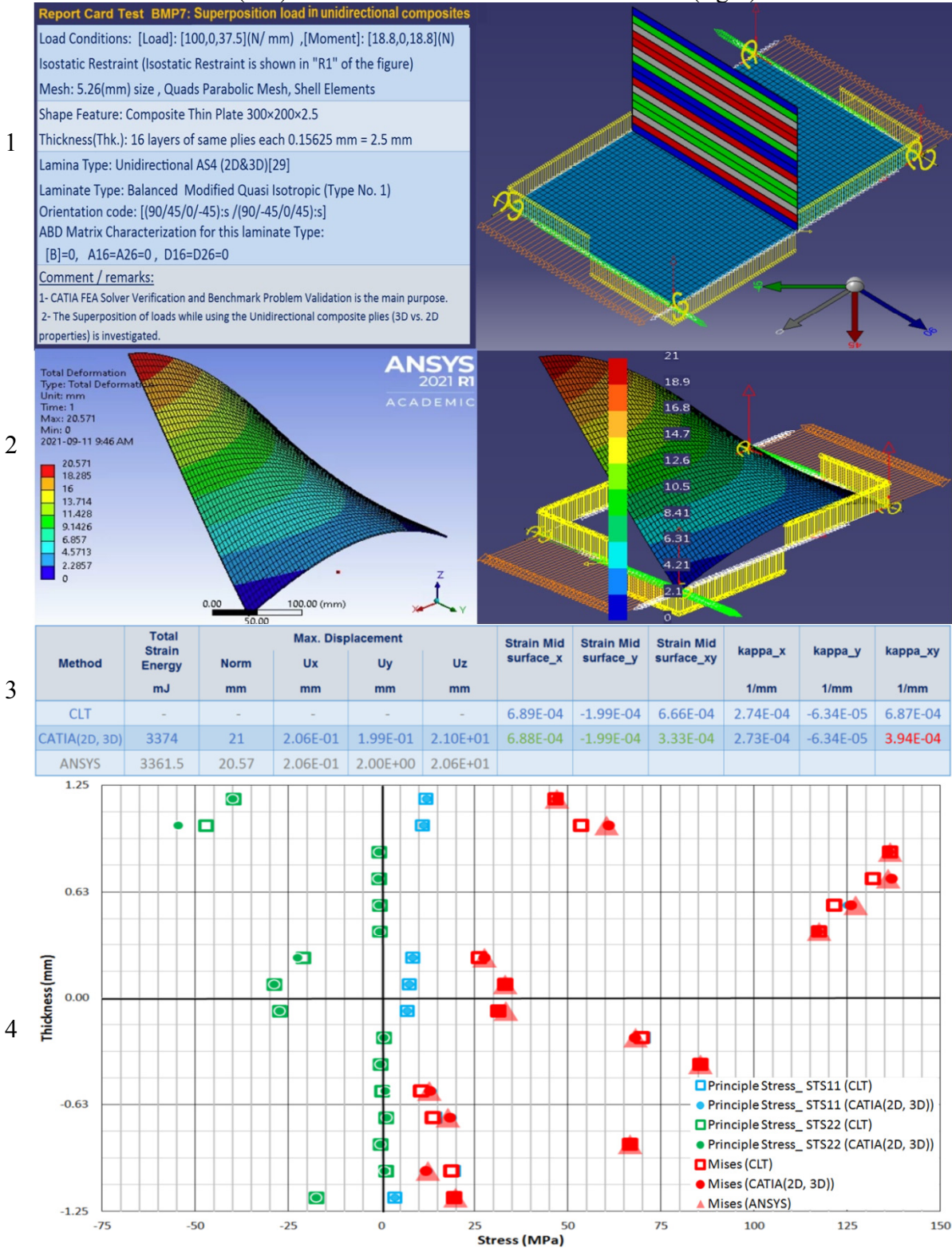


Figure 46: BMP7's Report Card Test (Unidirectional plies (3D vs. 2D properties))

6.9 BMP8 (Superposition load in woven fabric composites)

The benchmark problem BMP8 is exactly the same as BMP7, except for the lamina type. The lamina type in BMP8 is a woven fabric. The three main goals of proposing BMP8 are as follows:

1. The CATIA FEA Solver is considered under superposition loading conditions while the woven fabric is employed.
2. The results' differences for BMP8 are compared when separately 2D and 3D properties in the Material Library workbench were assigned.

It is important to note that the CATIA (2D, 3D) is mentioned in BMP7 to confirm that assigning 2D or 3D material properties do not influence final results. Here, the 2D and 3D material properties were separately entered into the Material Library workbench. Once the FEA analysis was conducted, and the results were found to be identical.

6.9.1 Problem statement

The BMP8 is similar to BMP7 except for material properties. It is assumed to be made of APG370, which is the woven fabric laminate. To save space, the information of BMP7 is not repeated here but one can consult the previous benchmark.

6.9.2 Results and discussion

As in the previous benchmark, the Balanced Modified Quasi Isotropic laminate is selected for BMP8, whose characteristics are discussed in 6.8.2.

Figure 47 illustrates the RCT for the BMP8. The problem status is summarized in the problem case on the left side of row 1 (L1). In addition, on the right side of row 1 (R1), the problem status is shown as captured from the CATIA software, which is identical to the BMP7.

In row 2, the deformed shapes for ANSYS software on the left and CATIA software on the right are displayed, showing the Norm displacement in the isometric view with the same deformation amplification magnitude.

Row 3 presents the magnitude of the deformations in the Norm and the individual components in millimetres, and the total strain energy magnitudes in millijoules in the embedded table. Comparing the BMP7 and BMP8, shows parallel behaviour, unlike the significant discrepancies between BMP5 and BMP6. As in BMP7, the table shows that the outcomes are similar except for Kappa_xy shown in red.

The tensile loads' responses are manifested by the "Strain Mid surface_x" and "Strain Mid surface_y", the bending load's responses are reflected in "Kappa_x" and "Kappa_y", and the shearing load's response is presented in "Strain Mid surface_xy". The response to

the twisting loads is present in “Kappa_xy” (shown in red), which is the only one showing the anomalies, as in BMP4.

The method to compute the strains in the “x”, “y”, and “xy” components are presented in equations (25) and (26) in 6.8.2, which will not be repeated here. Table 15 shows the magnitudes and the average value of two independent computations using layers 8 and 9 for this purpose, shown in Figure 46 in green.

Table 15: BMP8 mid-plane surface strain computation

	Tensor Components			Midplane Surface		
BMP8	STN_x	STN_y	STN_xy	STN_x	STN_y	STN_xy
Ply 8	7.00E-04	-2.19E-04	3.22E-04	7.04E-04	-2.19E-04	3.51E-04
Ply 9	7.39E-04	-2.30E-04	3.86E-04	7.35E-04	-2.30E-04	3.57E-04
	STN Average			7.20E-04	-2.25E-04	3.54E-04

The graph in row 4 presents the reported von Mises stresses of CLT and CATIA (2D, 3D) and ANSYS software, also, the maximum and minimum principal stresses of the tools except for ANSYS software. Similar to BMP4, the FEA solvers agree with each other; however, they do not agree with the CLT method.

In BMP8, the error that occurred in the ply with the maximum stress is reduced to 7%, while it was 15% in BMP4. In summary, are: First, applying loads when the results comply with different FEA tools (confirmed in BMP1 to BMP3) causes decreases in the error percentage.

The employed laminate in BMP4 was a general laminate composite, and the [ABD] Matrix characteristics for that laminate type cause the intervention of applied loads in all types of strain and curvature ($[B] \neq 0$, $A_{16} \neq 0$, $A_{26} \neq 0$, $D_{16} \neq 0$, $D_{26} \neq 0$), as discussed in Appendix A.

L (left)

R (right)

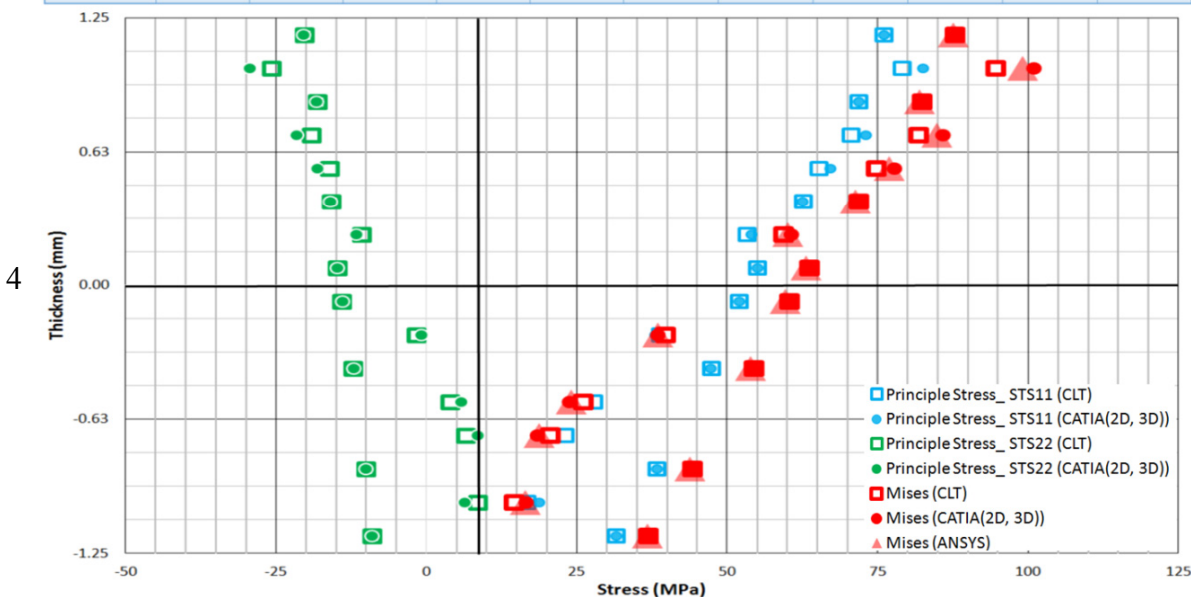
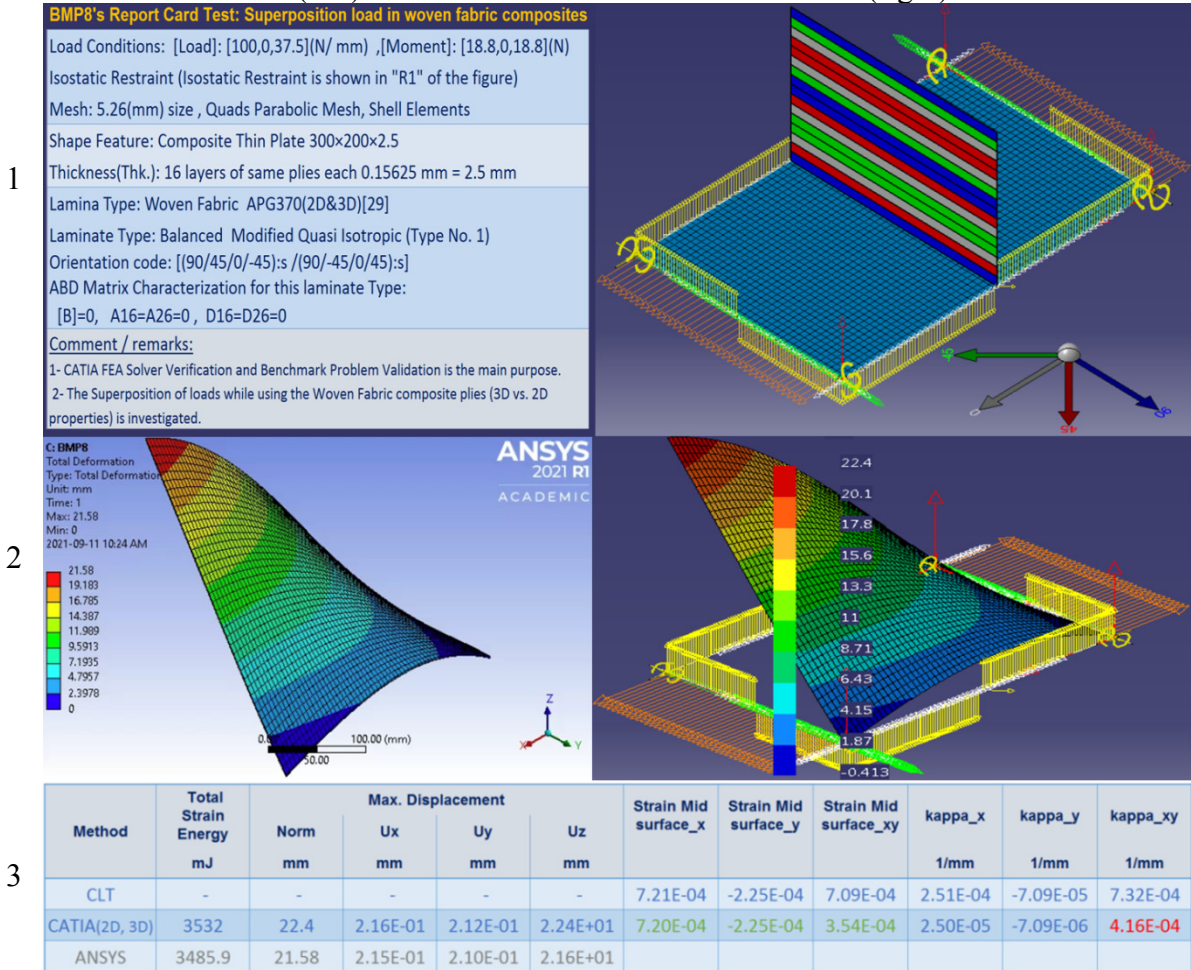


Figure 47: BMP8's Report Card Test (Woven Fabric (3D vs. 2D properties))

6.10 BMP9 (Draping in the "+Z" vs. "-Z" directions)

It is noticed that CATIA software can model the same stacking sequence in two directions ($\pm Z$). In the previous problems, the draping in the "+Z" direction (the laminate stacked up on top of the base surface) with different types of loading conditions and laminate types has already been validated. Accordingly, the Join's direction was in the "-Z" and the stacking sequence was in the "+Z" direction.

The main goal in BMP9 is to explore the response of the CATIA FEA Solver when the draping is in the "-Z" direction (the laminate stacked under the base surface). Inevitably, the problem condition is modelled for both draping directions, and the results are presented and compared. In addition, the results of CLT and ANSYS software are included.

When the draping is in the "-Z" direction (the laminate laid up under the base surface), the results are acceptable only after imposing the following two conditions. First, the rosette direction should follow the new direction of the stacking sequence in order to match the plies' orientations with the original problem. It is possible to reverse the sign of each direction one by one due to changing the draping directions. However, it is safer and easier to change only the rosette direction, aligned with the draping direction, and as a result, the plies direction will be matched automatically.

Second, the sign of bending loads and shearing loads applied to the new problem should be reversed. It is important to mention that the axial loads and the twisting loads remain unchanged.

The two primary purposes explored in BMP9 are as follows:

1. The method to impose superposition loading condition when the draping is in the "+Z" vs. "-Z" directions in CATIA software is investigated. The supports for the loads and restraints are presented in Table 12 for each of them separately.
2. Identical results from CATIA FEA Solver are expected while the draping is in the "+Z" and "-Z" directions.

6.10.1 Problem statement (Draping in the "+Z" and "-Z" directions)

Figure 48 and Figure 49 are organized to explain the BMP9 problem case, respectively, when the draping (stacking sequence) is in the "+Z" direction and when the draping is in the "-Z" direction. The geometry is defined as a thin rectangular plate with $300 \times 200 \times 2.5$ (in millimetres). The laminate parameters and the loading conditions are as follows:

The laminate parameters are shown in Figure 48, and Figure 49 consists of the rosette, the lamina, draping direction and mid-surface position. Similar parameters are in

this manner: The rosette shows -45° in light green, -30° in light blue, 0° in gray, 45° in red, and 90° in navy blue, indicating the plies' directions. Moreover, the 2D scaleless stacking sequence is illustrated using similar colours in the figure. The general laminate composite used in BMP4 is again employed to compare the stacking sequences while all the couplings in the $[ABD]$ matrices influence the strains and the curvatures. Therefore, 16 layers of unidirectional AS4 plies (see Table 10) are employed to stack up a general laminated stacking sequence (Type8: Appendices Table A) with the orientation code as $[90/45/-30/(-45):2/0/45/(90):2/-45/0/(45):2/0/-45/90]$ on the BLS.

The particular parameters applied to each draping direction are as follows: In Figure 48, the axes of the global coordinate system (CS) shown in red and the rosette CS shown in orange are in the same direction; on the contrary, in Figure 49, they are in the opposite directions. The rosette CS in the “-Z” direction is based on a new Axis System (x, y, z) rotated around the “X” axis; therefore, the “x” direction is unchanged, the “y” axis is in the opposite direction (in “-Y” direction), and the new “z” axis (in orange) is in the “-Z” direction of the global coordinate system (X, Y, Z). As a result, for example, the new orientations are rotated around the “X” axis. See the same directions in two rosettes for better comparison.

This causes a change in the directions of stacking sequence, join, shown in dark green and red. The join and the stacking sequence directions are still opposite to each other. Also, it is important to pay special attention to ply numbers 1 and 16, shown in the figures and the position of the layer with -30° located in the third layer of the layup.

Moreover, the corresponding loading conditions—For both stacking sequences, the $[N]$ and $[M]$ matrices meant to be unchanged—applied to each stacking sequence are shown in Figure 48 and Figure 49.

The common features are as follows:

First, the BLS is meshed with Quads Parabolic Shell Elements with 5.26 mm size. Three vertices are selected as “support” to restrain the base laminate, are shown in red. The symmetrical option was selected; therefore, the reference surface and the mid-plane surface are coincident.

Second, the applied loads are tensile loads in orange, shearing loads in white, bending loads in green, and twisting loads in yellow, as shown on the edges of the Reference Surface. The load and moment matrices are $[Load] = [100, 0, 37.5]$ (N/mm), $[Moment] = [12.4, 6.2, 18.8]$ (N) computed by the CLT method.

Specifically for each draping direction, the applied loading conditions in CATIA software consist of the positions and the directions are altered as shown in figures. The corresponding magnitudes to enter into CATIA software are presented in Table 12. Also,

as mentioned before, it is important to pay special attention that the sign of shearing loads and bending loads are reversed by applying new stacking sequence directions.

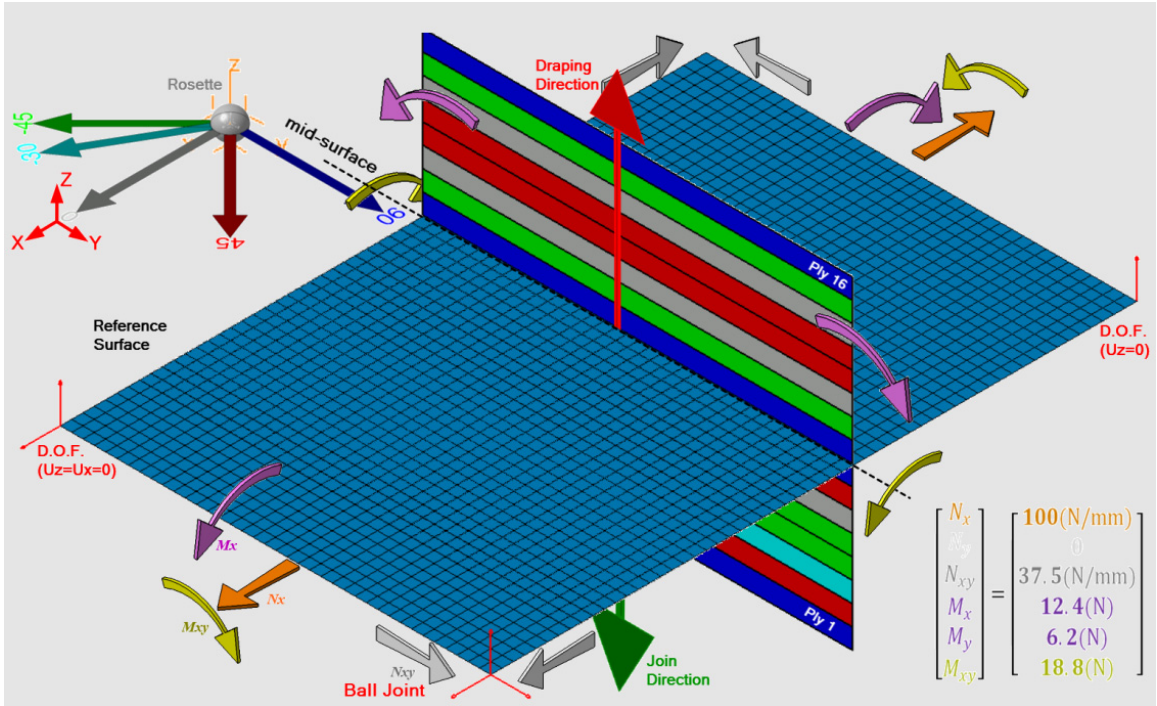


Figure 48: Simple illustration of the BMP9 (Draping in the "+Z" directions)

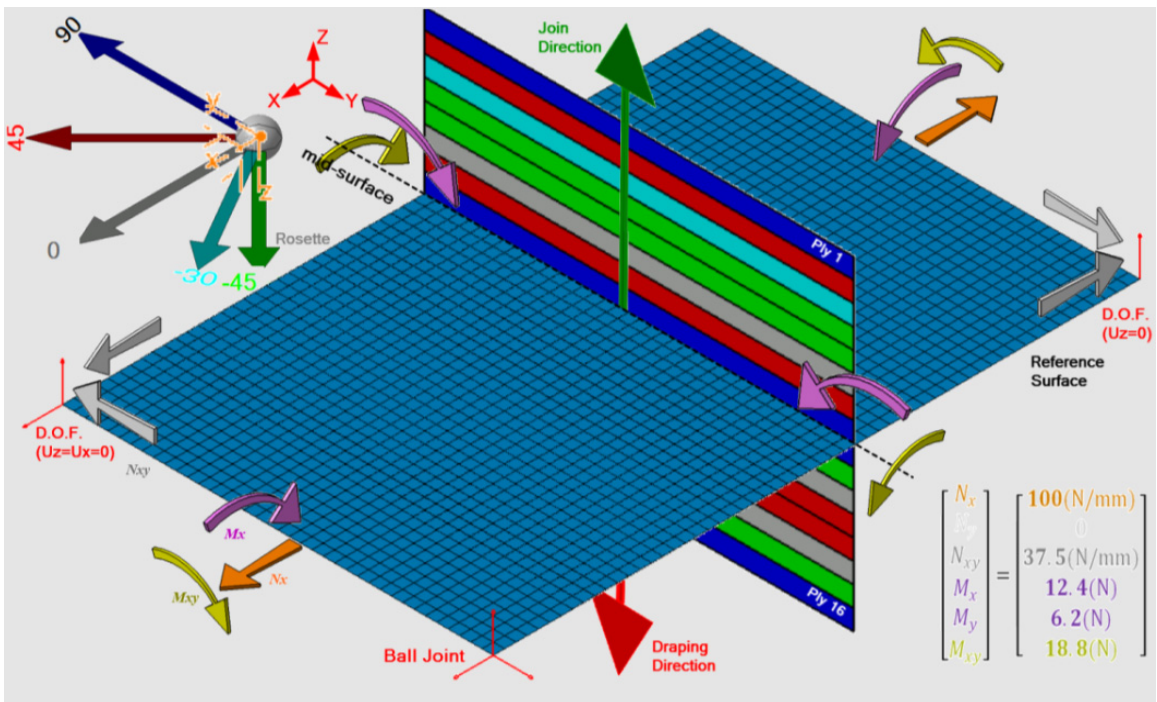


Figure 49: Simple illustration of the BMP9 (Draping in the "-Z" directions)

6.10.2 Results and discussion

The general laminated stacking sequence was selected for this problem (Type8: Appendices Table A); therefore, the characteristics of the [ABD] matrices for the laminate are as follows. The “ $A_{16}, A_{26}, D_{16}, D_{26}$ ” and “[B]” are not zero; hence, all the couplings—respectively shear-extension, bend-twist, and bend-extension couplings—intervene the results. For instance, each of the strains and curvature values in the mid-plane surface are resulted from all the imposing loads. Similar condition is presented for Type8 laminate in state5, shown in Appendices Table B.

Figure 50 shows the RCT for BMP9, which is organized slightly different from the one discussed in 6.1.2. Here, since the results concluded from two draping directions are the same, both are studied in one RCT. The problem status is summarized on the left side of row 1 (L1). In addition, on the right side of row 1 (R1), the problem case is shown as captured from the CATIA software.

in R1, from left to right the base surface is displayed while the rosette and draping in the “+Z” direction are shown first. Then, at the right end, the rosette and the draping in the “-Z” direction are given. It is important to notice how the directions of the same orientation’s magnitudes in two rosettes’ colour-coding are different.

The tensile loads are shown in orange, shearing loads are shown in white, bending loads are shown in green, and the twisting loads are shown in yellow, and a new combination of user-defined restraints located in three vertices are shown in red. Moreover, the rosette illustrates the colour-codes of the mentioned directions of the layers illustrated on the base surface.

Row 2 consists of three deformed shapes using with the same amplification factor while generating the Norm displacement magnitude. First, from the left, the deformed shape extracted from ANSYS software is presented. The deformed shape of draping in the “+Z” and “-Z” directions extracted from the CATIA are shown from left to right. The tensile loads are illustrated in orange, twisting in yellow, bending in green, and shearing loads are in white. As mentioned earlier, the tensile and twisting loads remain unchanged; however, the direction of the moment (in two directions) and shearing loads are reversed.

In rows 3 and 4, the CATIA FEA Solver generated results are presented in both rosette directions shown as CATIA $R\pm Z$ since the results for both directions are exactly the same. The only difference is in the displacement in the “Y” direction (shown in yellow); however, it is resulted from changing the “y” direction, and displacement is a vector from an observer’s point of view. Table 16 shows the magnitudes and the average value of two independent computations using layers 8 and 9 for this purpose. From equations (25) and (26), the strains (STN) in the mid-plane surface (Mid_S) for the CATIA software are calculated and placed in the figure, row 3 in green.

Table 16: BMP9 mid-plane surface strain computation

BMP9-R-Z	Tensor Components			Midplane Surface		
	STN_x	STN_y	STN_xy	STN_x	STN_y	STN_xy
Ply 8	7.44E-04	-2.34E-04	3.38E-04	7.48E-04	-2.33E-04	3.67E-04
Ply 9	7.52E-04	-2.23E-04	3.91E-04	7.48E-04	-2.23E-04	3.62E-04
	STN Average			7.48E-04	-2.28E-04	3.65E-04

The error in the ply with the maximum stress is 5%, while in that layer, the resulting stresses from the CATA and ANSYS software are almost identical. Stresses in other layers are presented in the graph in row 4.

L (left)

R (right)

BMP9's Report Card Test: Draping in the "+Z" vs. "-Z" directions

Load Conditions: [Load]: [100,0,37.5](N/mm) , [Moment]: [12.4,6.2,18.8](N)

Isostatic Restraint (Isostatic Restraint is shown in "R1" of the figure)

Mesh: 5.26(mm) size , Quads Parabolic Mesh, Shell Elements

Shape Feature: Composite Thin Plate 300x200x2.5

1 Thickness(Thk.): 16 layers of same plies each 0.15625 mm = 2.5 mm

Lamina Type: Unidirectional AS4[29]

Laminate Type: General Laminated Composite (Type No. 8)

Orientation code: [90/45/-30/(-45):2/0/45/(90):2/-45/0/(45):2/0/-45/90]

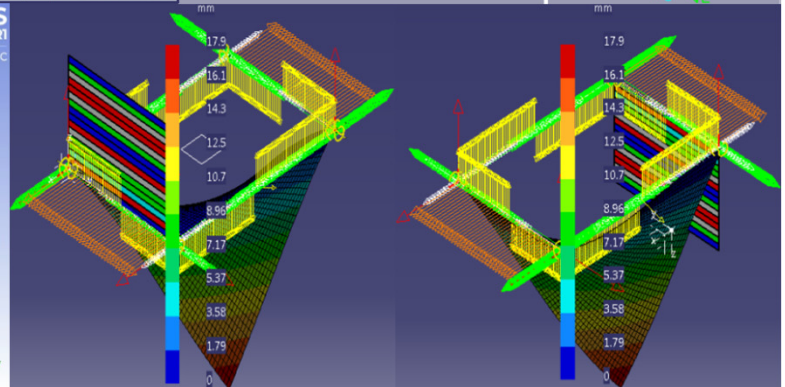
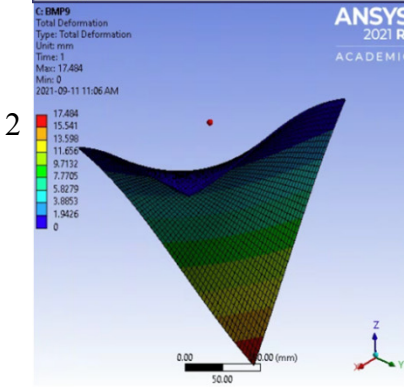
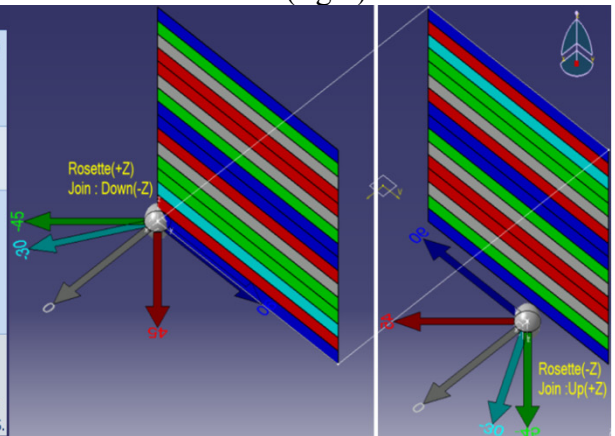
ABD Matrix Characterization for this laminate Type:

[A]≠0, [B]≠0, [D]≠0

Comment / remarks:

1- CATIA FEA Solver Verification and Benchmark Problem Validation is the main purpose.

2- Rosette in the "+Z" direction and the "-Z" direction is investigated. Therefore, the Join, the Draping directions and the loads' CS respectively are defined as "+Z," "-Z," and the rosette CS.



3

Method	Total Strain Energy mJ	Norm mm	Max. Displacement			Strain Mid surface_x	Strain Mid surface_y	Strain Mid surface_xy	kappa_x 1/mm	kappa_y 1/mm	kappa_xy 1/mm
			Ux mm	Uy mm	Uz mm						
CLT	-	-	-	-	-	7.54E-04	-2.28E-04	7.24E-04	4.28E-05	6.97E-05	5.84E-04
CatiaR±Z	3450	17.9	-2.27E-01	-8.217	-1.79E+01	7.48E-04	-2.28E-04	3.65E-04	5.04E-05	7.07E-05	3.43E-04
ANSYS	3444	17.484	-2.28E-01	-2.18E-01	-1.75E+01						

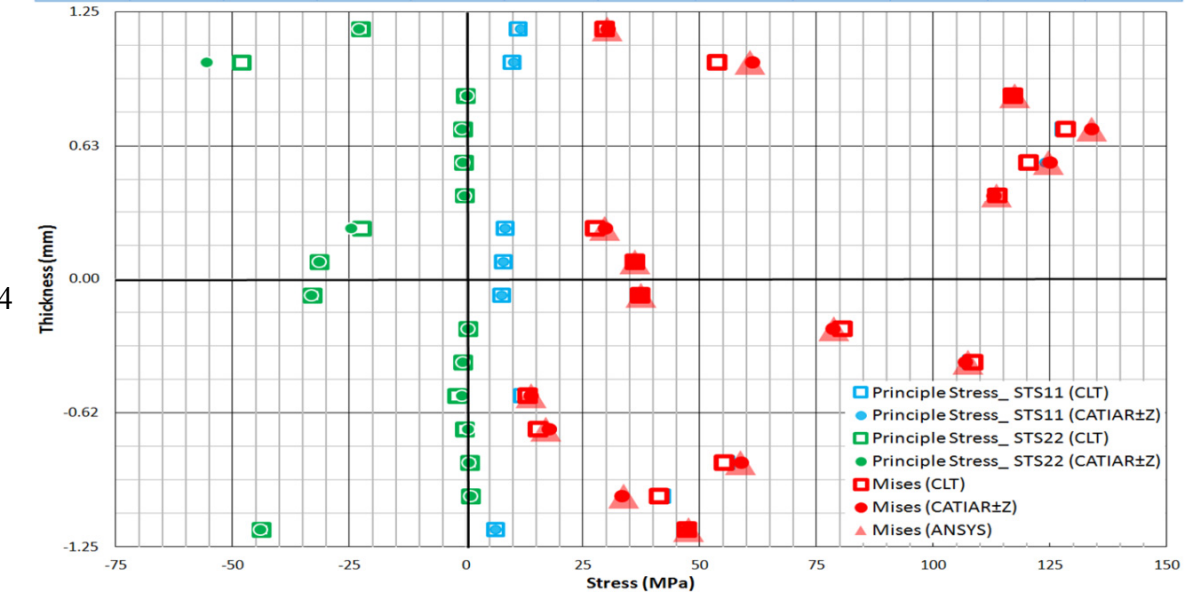


Figure 50: BMP9's Report Card Test (Draping in the "+Z" vs. "-Z" directions)

6.11 BMP10 (Torsion of a cylinder)

In the next two benchmark problems curved surfaces are considered. Cylindrical and spherical geometries are respectively modelled in BMP10 and BMP11. The following outcomes are sought from conducting the BMP10 FEA analysis;

1. The method to impose torsion on cylindrical shape geometry in CATIA software is investigated.
2. It is important to notice that in this case, only symmetrical laminates with small thicknesses in comparison to the radius can be compared with the CLT method. For the sake of exploration, an asymmetrical laminate was examined in BMP10, and the results show that the asymmetrical laminate is acceptable; however, this is not a general statement or conclusion for other asymmetrical laminates.

6.11.1 Problem statement

Figure 51 (a, b) is organized to illustrate the geometry, laminate parameters, and the loading conditions to explain the BMP10. The cylindrical shape geometry with length, diameters and thickness equal to 140, 100 and 6 millimetres respectively is considered (dimensions extracted from ASTM D5448 [52]).

The axes of the global coordinate system (shown in red) and the rosette are assigned in a way that the orientation with 90° is aligned with the perimeter of the cross-section parallel to the “YZ” plane. Figure 51 (a) shows the 2D scaleless stacking sequence is illustrated using -45° and 45° in light green and red, indicating the plies’ directions. Fifteen layers of unidirectional AS4 plies (Table 10) are employed to stack up the laminate with the orientation code as $[-45/+45/-45]_s:3$ (Type3: Appendices Table A) on the BLS in Figure 51 (a). The join and the stacking sequence directions are opposite, respectively shown in red and dark green.

The loading conditions presented in Figure 51 (b) are as follows: The torsion shown in yellow equal to $1e+006$ N.mm is applied on one side of the cylinder. The corresponding load used in CLT method is $N_{xy} = 63.67$ (N/mm)—[Load]=[0,0,63.67](N/mm), [Moment]=[0,0,0](N)—computed from equation (14) in 3.2.1.1.

The symmetrical option was selected; therefore, the Reference Surface (The meshed BLS) and the mid-plane surface (the middle of the laminate’s thickness) are located exactly in the middle of layer number eight shown in Figure 51 (b). The BLS is meshed with Quads Parabolic Shell Elements with 3.491 mm size. The other side of the cylindrical tube is clamped, which is displayed in blue.

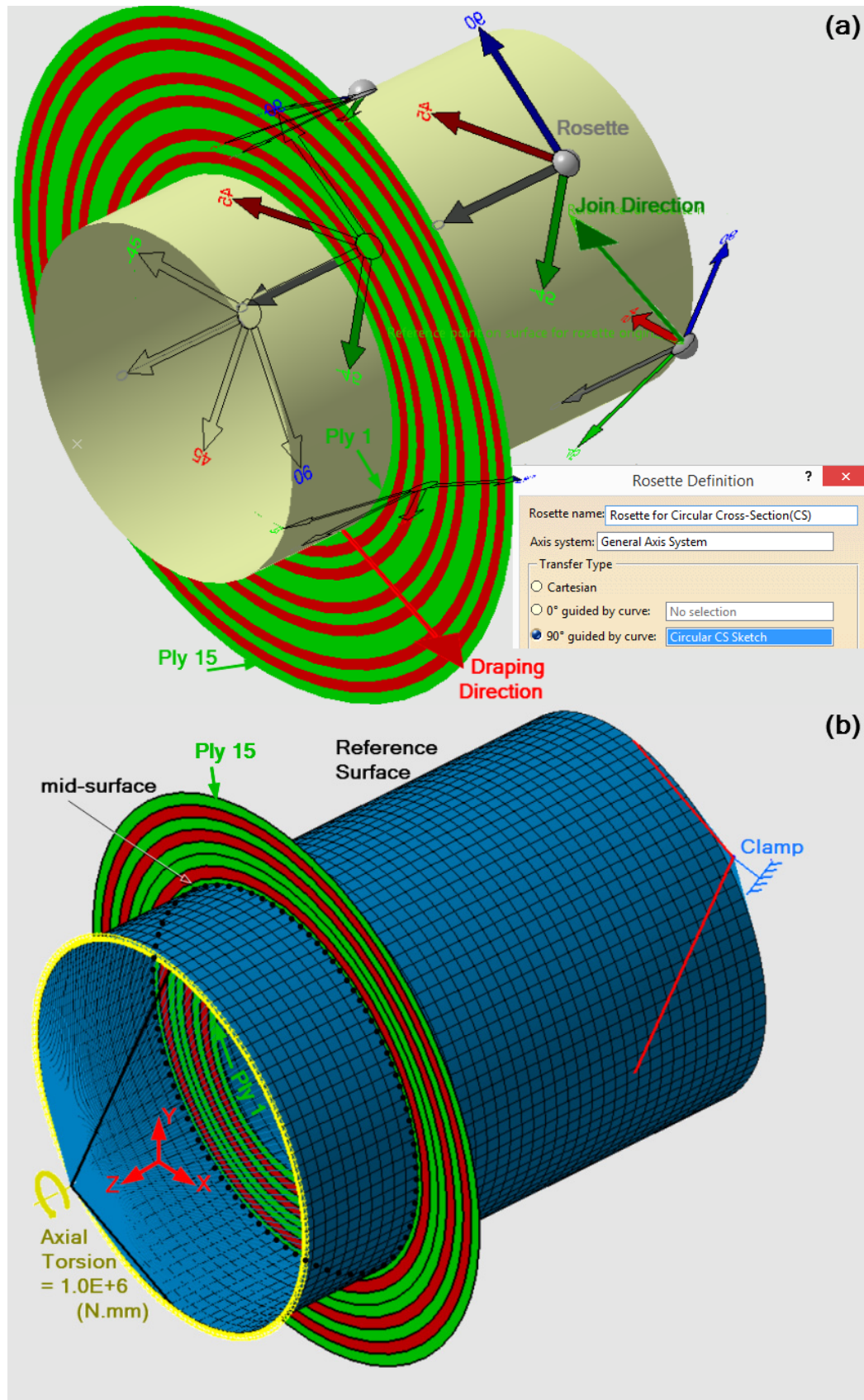


Figure 51: Simple illustration of the BMP10 problem case; (a) BLS, (b) Reference Surface

6.11.2 Results and discussion

The symmetric laminate is selected for this problem (Type3: Appendices Table A); therefore, the characteristics of the [ABD] matrices for the laminate are as follows. Due to "[B] = 0", there is no bend-extension coupling. Furthermore, since " $A_{16} \neq 0$, $A_{26} \neq 0$ " and " $D_{16} \neq 0$, $D_{26} \neq 0$ ", there are shear-extension coupling and bend-twist coupling. In view of these facts, the current loading conditions (N_{xy}) cause some stretching in the "X" axis and contraction in the "Y" and "Z" axis due to shear-extension coupling. (See Appendices Table B).

Figure 52 shows the RCT for the BMP10. The problem case is summarized on the left side of row 1 (L1). In addition, on the right side of row 1 (R1), the problem status is shown as captured from the CATIA software.

In R1, the torsion load is in yellow, placed on one side of the cylinder as "support," and clamped on the other side shown in blue. Moreover, the rosette and laminate stacking sequence with the colour consistent in the same ply directions are illustrated.

In Figure 52, row 2, the deformed shapes for ABAQUS software on the left and CATIA software on the right are captured, showing the Norm displacement in the isometric view with the same deformation amplification magnitude. Also, the torsion and clamp supports are illustrated as points connected to the edges through Rigid Virtual Parts shown in the black colour.

In row 3, the magnitudes of the deformations—in the Norm and the individual components—in millimetres, the total strain energy magnitudes in millijoules, and the strains and curvatures in the mid surface. All the methods comply with each other, except for curvature magnitudes. The curvatures resulting from the ABAQUS and CATIA are totally different from the CLT method; however, ABAQUS and CATIA do share some similarities.

In row 4, the von Mises, maximum principal, and minimum principal stresses for the CLT method and two FEA solvers are presented for comparison. It shows that the magnitudes in the mid-surface are almost the same. The differences between the CLT method and the two FEA solvers' results are linearly increasing from the mid-surface toward the outside plies. This occurs due to the relation between the distance from the mid-surface and the radius that each ply surface is located. To sum up, the discrepancies between the CLT and the FEA solvers diminish when the ply thicknesses are substantially smaller than the tube diameter. This is based on the assumption that the laminate is symmetric.

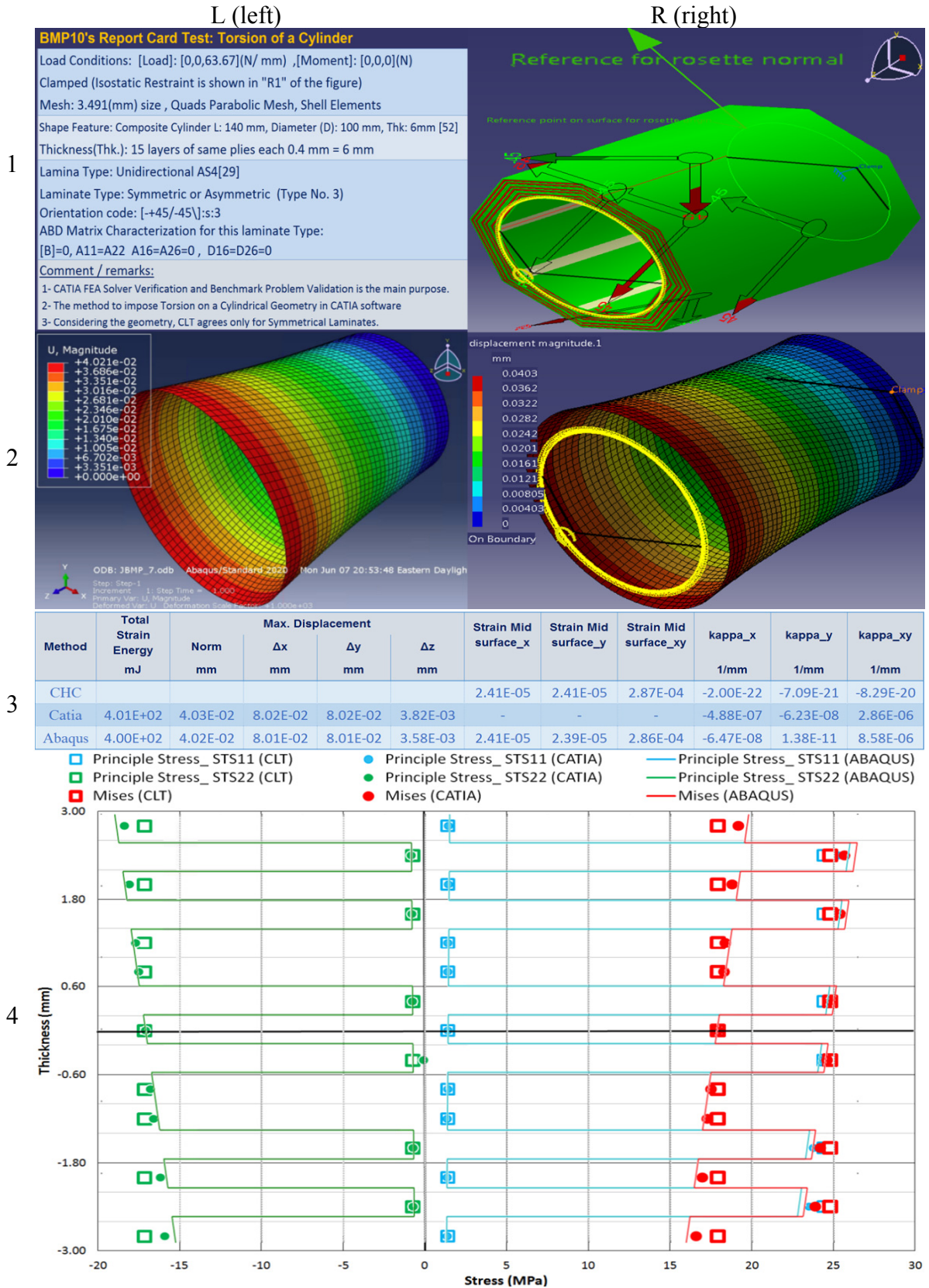


Figure 52: BMP10's Report Card Test (Torsion on a Cylinder)

6.12 BMP11 (Externally applied pressure on a sphere)

In BMP11, a rather challenging geometry to model and analyze, namely a sphere, is proposed. In this context, there are two primary issues: applying the boundary conditions and designing the composite parameters. The first occurs since there are no edges or vertices, and the second is the laminas' direction and rosette in the sphere surroundings. CATIA FEA Solver's results are compared with the CLT and the ABAQUS. This study investigates the method to apply the rosette and the restraint while imposing pressure load on the outside surface of a sphere in CATIA. It is important to notice that, for this type of cross-section, only symmetrical laminates with small thicknesses (with respect to the radius) can be compared with the CLT method.

6.12.1 Problem statement

Figure 53 (a, b) is organized to illustrate the geometry, laminate parameters, and the loading conditions to explain the BMP11 problem case. Here, only half of the sphere is shown to illustrate the components located inside of the sphere. The geometry, stacking sequence, and the type of loads and restraints have changed in comparison to previous BMPs. The spherical geometry with the diameter and thickness equal to 300 and 6 millimetres is modelled as the Base Laminate Surface in BMP11.

The axes of the global coordinate system (shown in red) and the rosette are assigned in a way that the orientation with 90° is aligned with the circular cross-section in the YZ plane. In some points in Figure 53 (a), the rosette with 0° in gray, 2.5° in purple, and 90° in navy blue. The polar winding method with fibre angles from 0° to 5° is frequently used for the domed ends caps, spherical components, and road tankers applications [55]. That is why; the ply direction equal to 2.5° was selected for this BMP. Therefore, the 2D scaleless stacking sequence is illustrated, indicating the plies with 2.5° directions. In total, 15 layers of unidirectional AS4 plies (Table 10) are employed to stack up the laminate with the orientation code as [2.5]:15 (Type4 in Appendices Table A) on the BLS in Figure 53 (a). The join and the stacking sequence directions are opposite, shown in red and dark green.

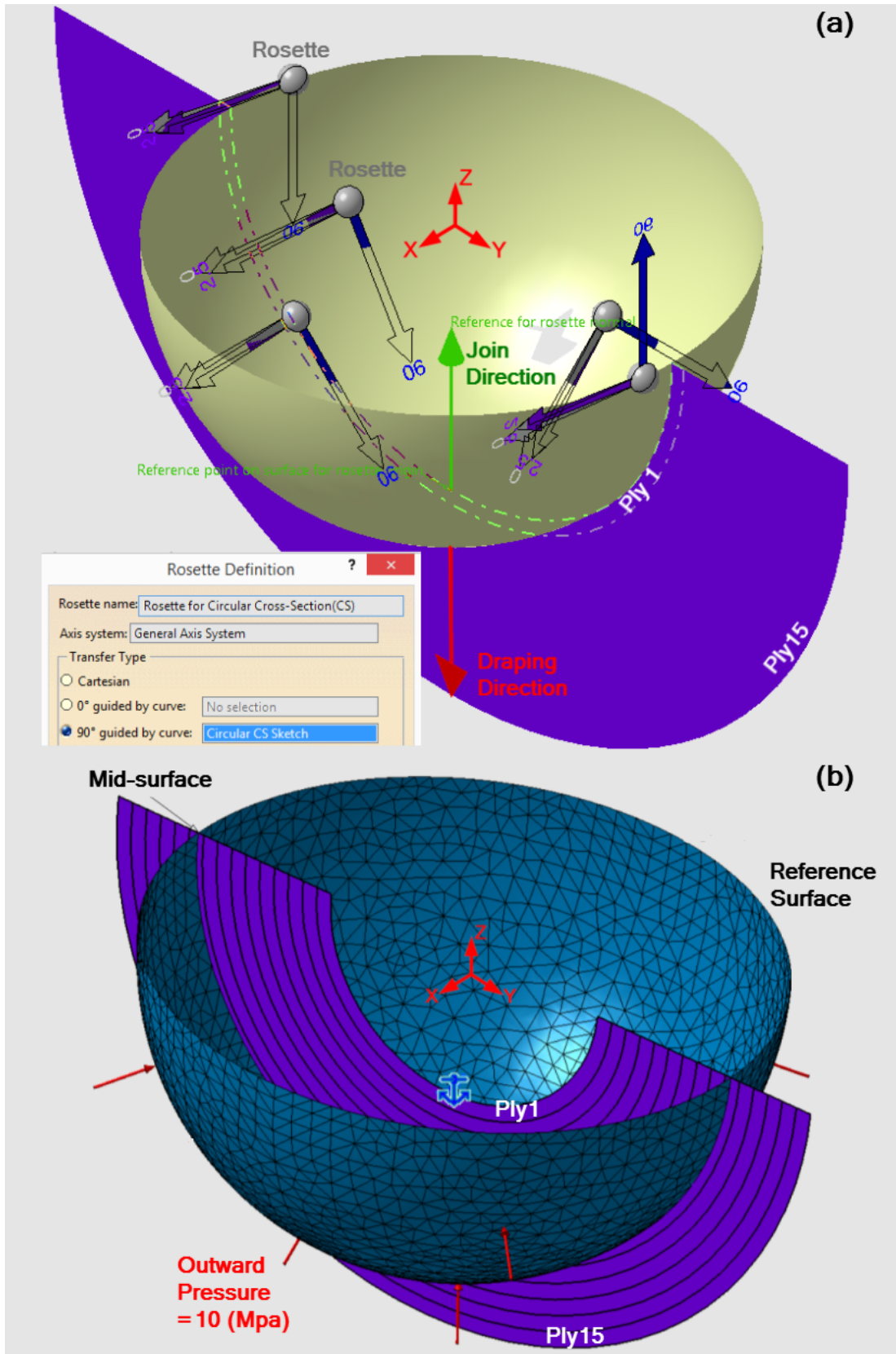


Figure 53: Simple illustration of the BMP11—half of the sphere is shown—problem case; (a) BLS, (b) Reference Surface.

The loading conditions presented in Figure 53 (b) are as follows: The pressure load shown by the red vectors equal to 10 MPa is applied on the outside of the sphere. The corresponding load used in CLT method is $N_x = N_y = -750$ (N/mm)—[Load] = $[-750, -750]$ (N/mm), [Moment] = $[0,0,0]$ (N)—computed from equation (15) discussed in 3.2.1.2. The symmetrical option was selected; therefore, the Reference Surface is located exactly in the middle of layer number eight shown in Figure 53 (b). The BLS is meshed with 10 mm size, Octree Triangle shell elements mesh. The isostatic restraint (blue anchor) in the middle of the figure is imposed to prevent rigid body motion.

6.12.2 Results and discussion

The Symmetric laminate is selected for this problem (Type4: Appendices Table A); therefore, the characteristics of the [ABD] matrices for the laminate are as follows. Due to "[B] = 0", there is no bend-extension coupling, in addition, since " $A_{16} \neq 0, A_{26} \neq 0$ " and " $D_{16} \neq 0, D_{26} \neq 0$ ", there are shear-extension coupling and bend-twist coupling. In this way, the current loading conditions— $N_x = N_y = -750$ (N/mm)—cause some contraction in the “X,” “Y,” and “Z” axis (See Appendices Table B).

Figure 54 shows the RCT for the BMP11, which is organized slightly differently from the one discussed in 6.1.2. The problem case is summarized on the left side of row 1 (L1). Furthermore, on the right side of row 1 (R1), the problem status is shown as captured from the CATIA software.

In R1, from left to right, the pressure load is shown in yellow vectors, applied on the outside of the sphere. In the same frame, the “composite angle symbol” is generated, showing the plies angles in the pre-processing step, which are similar to a screenshot captured from a YouTube video [56] added to the R1 showing the polar winding method in practice. On the right end, the rosette is presented. The rosette showing the 2.5° direction in beige captured from the “composite design” workbench in different points on the outside surface of the sphere are shown (the arrows with no colour are located on the other side of the sphere).

Since there are no vertices or edges, using the “user define restraints” in an exact location in both FEA software is not straightforward. Therefore, for the CATIA software, this is accomplished by using the isostatic restraint (blue anchor in R1), and for the ABAQUS software, inevitably, the “dynamic implicit analysis” is conducted using the Inertia Relief functionality. This approach dramatically increases the run time and the storage capacity requirement in the ABAQUS software.

In row 2 (R2), the deformed shapes extracted from the ABAQUS and CATIA software are illustrated from left to right with the same amplification magnitudes. The distance between two points on each side of the sphere on the “X” axis for both

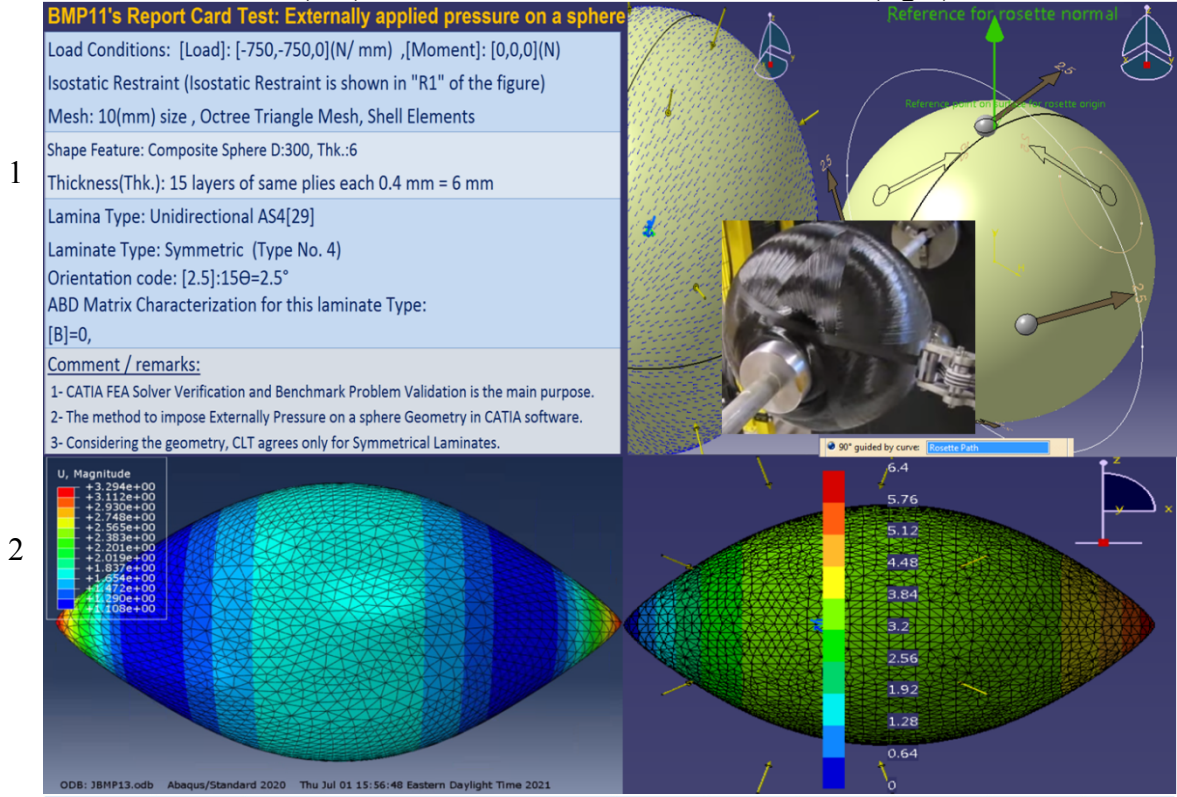
commercial FEA solvers shown in R2 is almost equal to 6.4 millimeters (see Figure 54, R2). However, the displacements values shown in row 3 (R3) reported from the two solvers are not comparable, and they are based on the vertices generated for the boundary condition automatically by the solvers. The “±” sign is shown in the table’s displacements’ magnitudes, representing the displacements in the opposite directions of the two sides of the sphere. It is important to note that, since the restraints are different in two FEA solvers, the “ U_x ” is different.

Using the Isostatic and Inertia Relief for the CATIA and ABAQUS software has more drawbacks. There are no similar elements to compare the strains and curvatures values in the two solvers. That is why no values added to the table in R3 presenting the strains for three tools are comparable. In addition, the curvature values resulting from the two FEA solvers are not zero, similar to the curvature values for the CLT methods due to modelled geometry.

In row 4 (R4), the von Mises, maximum principal, and minimum principal stresses for the CLT method and two FEA solvers are presented for comparison. As in BMP10, the differences between the CLT method and the two FEA solvers’ results are linearly increasing from the mid-surface toward the outside plies. The first reason is the relation between the distance from the mid-surface and the radius where each ply surface is located are changing linearly. The second one is caused by the natural spherical shape results in curvature values for the two software cause discrepancies between FEA software (CATIA and ABAQUS) and the CLT method. This implies that FEA solver such as CATIA is comparable with the CLT method only for thin symmetric laminate where the radius is much larger than the thickness.

L (left)

R (right)



Method	Total Strain Energy mJ	Max. Displacement			Strain Mid surface_x	Strain Mid surface_y	Strain Mid surface_xy	kappa_x 1/mm	kappa_y 1/mm	kappa_xy 1/mm
		Norm mm	Ux mm	Uy mm						
CLT	-	-	-	-	-6.42E-04	-1.19E-02	9.84E-04	1.83E-19	2.08E-18	-2.46E-19
CATIA	1288	6.4	6.40E+00	±1.793	-	-	-	-	-	-
ABAQUS	-	3.294	±3.294	±1.793	-	-	-	-	-	-

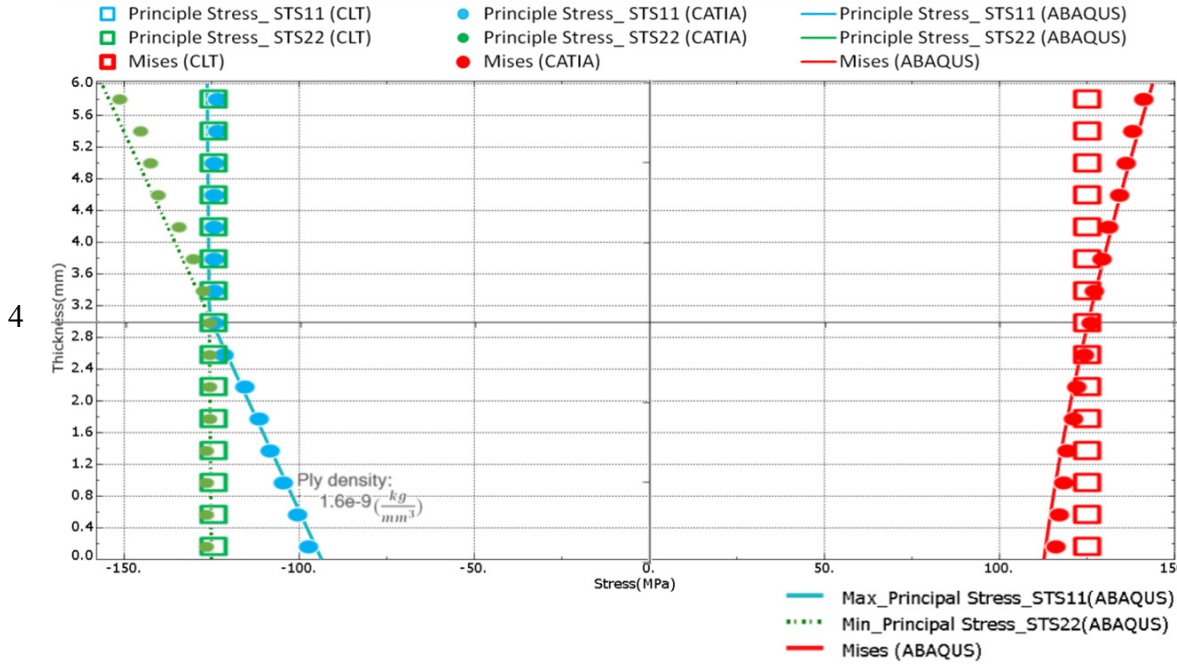


Figure 54: BMP11's Report Card Test (Pressure on the outside surface of a Sphere)

CHAPTER SEVEN: INTERMEDIATE BENCHMARKS (BMP12 to BMP14)

7.1 Introduction:

Chapter Seven investigates the CATIA software's ability to conduct an FEA analysis of three benchmark problems (BMP12 to BMP14), which are more complicated than the ones presented in Chapter Six. These benchmark problems are difficult (BMP12) or impossible (BMP13 and BMP14) to be solved using the CLT method. Therefore, they should be validated against published references.

BMP12 is the only benchmark where the Reference Surface (the meshed BLS) and the Mid-Surface (located in the middle of the laminate) are not coincident. This is because there is an issue when modelling the drop-off condition (adjacent laminates with different thicknesses) while moving from one BLS to the next. Three BLSs are modelled with their different stacking sequences. In BMP12, four different methods are employed and validated to design the stacking sequences. The methods to model them can be found in CAD/CAM references; however, this study only addresses their FEA results.

In BMP13, several FEA scenarios are considered. These FEA scenarios are the Static, the Frequency, and the Transient Dynamic Response. Obtaining the natural frequencies is the first step of performing any dynamic analysis in CATIA. The natural frequency results computed by CATIA are compared against an analytical expression available in composites literature.

BMP14 is the first benchmark dealing with the buckling loads in which different geometry and stacking sequences are proposed. The thermal buckling of a sandwich panel has resulted directly from the values of the lowest multiplier and the applied temperature difference. The verification is achieved by comparing to the published literature. The reference employs equations from higher-order shear deformation theories while each node had nine degrees of freedom (DOF). CATIA generally uses nodes with five DOF and nodes with six DOF at the edges only. However, the results agree with the proposed reference.

7.2 BMP12 (Drop-off condition)

The CATIA FEA solver is employed to analyze an example of a drop-off condition. When modelling the drop-off condition in the CATIA software, the transition zone influences as discussed in 3.2.1.5, are ignored; however, the results agree with compared available reference publications. In this example, the option to import the properties as Symmetrical is unchecked; therefore, the loading condition under this situation is investigated. Four different methods to model the composite parameters are employed, and their final results are compared with the reference.

7.2.1 Problem statement

Figure 55 is organized to illustrate the BMP12 problem, which consists of three features: geometry, laminate parameters, and the loading conditions. The geometry is a thin flat strip consisting of three Base Laminate Surfaces: Section A, Section AB, and Section B. The thicknesses (Thk.) of the composite laminates vary based on the number of unidirectional layers stacked, in different sections. The total area is 120×50 (in millimetres).

The composite parameters consist of the rosette, the lamina, draping direction and the Reference Surface position, as shown in Figure 55. The axes of the global coordinate system (shown in red) and the rosette are in the same direction. The rosette shows -45° in light green, 0° in gray, 45° in red, and 90° in navy blue, indicating the plies' directions. The join and the stacking sequence directions are opposite, respectively shown in red and dark green. Moreover, the scaleless stacking sequence is illustrated using similar colours in Figure 55. A table is embedded in the figure that reports on three critical parameters: the area, stacking sequence, and the number of the CFRP unidirectional lamina lined upon each section. The thickness of each lamina is 1.2 millimetres, and the mechanical properties are presented in Table 17.

The loading conditions shown in Figure 55 are as follows. The tensile load in orange is equal to 10 (N/mm), is aligned with the “X” direction, and is applied on edge from Section B. The other edge from Section A is clamped, shown in blue, and the entire side edge of the geometry is constrained. This is shown in red using the user-defined restraint as follows: $U_y = 0$, and $R_x = R_z = 0$. The Reference Surface is the meshed BLS located in the mid-surface of layer number 1 (45° direction in red) and consists of PLY1, PLY6, and PLY10. The laminate properties are imported, while the symmetrical option is not selected (discussed in 5.3.1). The three Base Laminate Surfaces are meshed with Quads Parabolic Shell Elements (5 mm size). The method to mesh geometries consisting of multiple BLSs is discussed in 5.2.1.

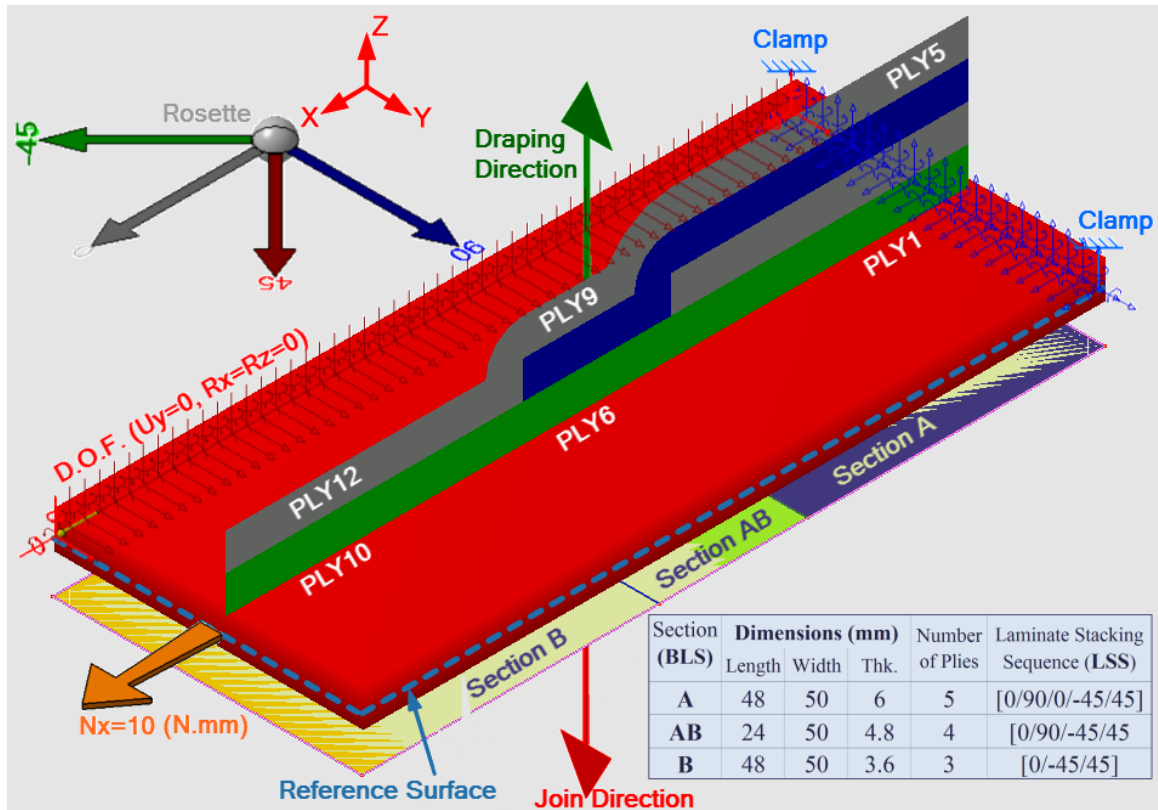


Figure 55: Simple illustration of the BMP12

Table 17: CFRP lamina properties (extracted from [57])

Property (Unit)	Unidirectional Lamina	
	CFRP (AS4D[50])	
Young's modulus E_1 (MPa)	137895	
Young's modulus E_2 and E_3 (MPa)	8273	
Poisson's Ratio ν_{23}	0.5	
Poisson's Ratio ν_{12} and ν_{13}	0.25	
Shear Modulus G_{23} (MPa)	2758	
Shear Modulus G_{12} and G_{13} (MPa)	5516	

7.2.2 Different methods to stack up the laminate

Figure 56 shows the four methods—(a), (b), (c), and (d)—to model the composite parameters in CATIA software examined in BMP12. The Join's direction for all the methods is in the “-Z” direction of the CS shown in (b) and (d). Therefore, as discussed in 5.1.2, the stacking sequence is on the opposite side. The scaleless stacking sequence generated while using different methods is shown in Figure 56: The rosette shows -45° in light green, 0° in gray, 45° in red, and 90° in navy blue, indicating the plies' directions shown in Figure 56 (a).

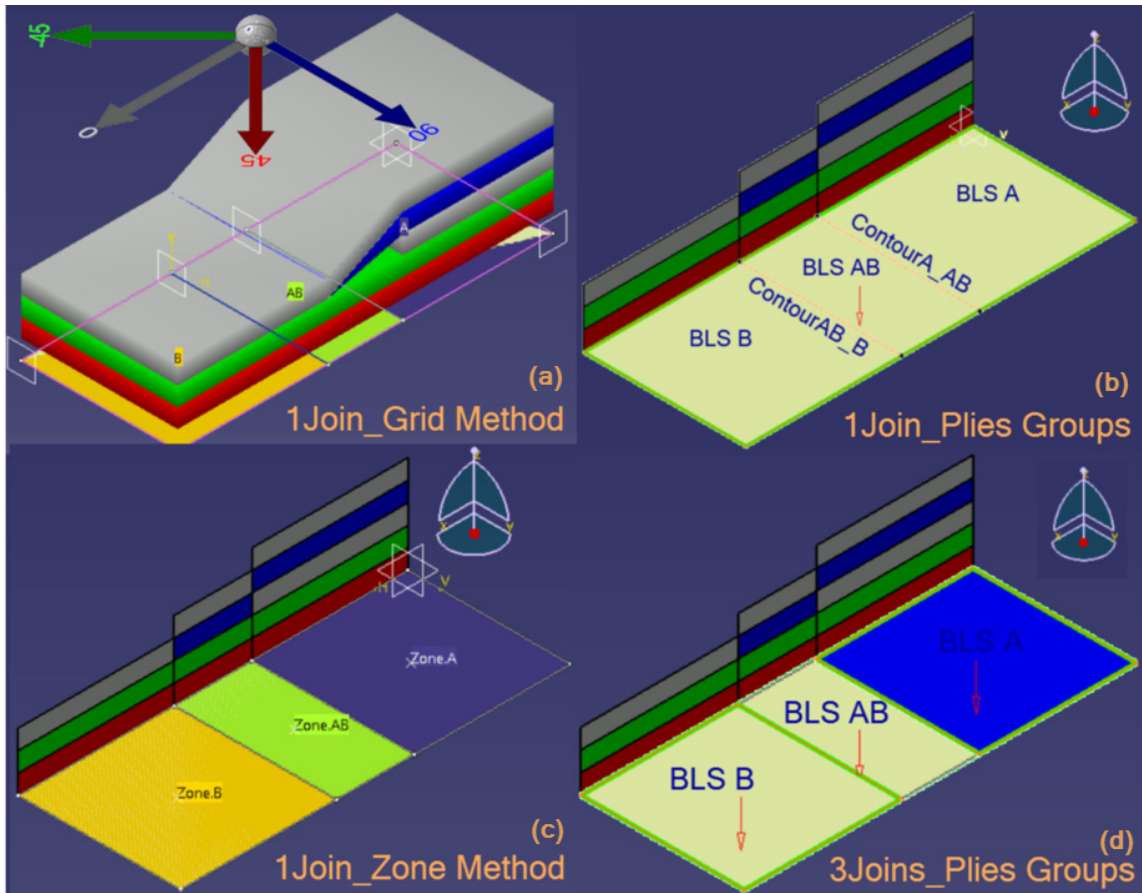


Figure 56: Some methods to stack up the laminate in CATIA software; (a) the Grid method, (b) the manual ply creation when all the BLSs are joined, (c) the Zone method, and (d) the manual ply creation when the BLSs are joined separately.

The stage to model the composite parameters takes place between modelling and meshing the geometry. As discussed in 4.4.2, the simplest way is Manual Ply Creation and using the Stacking (Engineering) directly to design the Plies Groups, Sequences, and Plies. This method is summarized to some extent in Chapter Four. In this problem, to design according to Figure 56 (d), the technique is similar to the video tutorial in [10]. The main step is to join the three sections into a single unified surface. For Figure 56 (b), they can form one single join covering all the BLSs. In comparison, both are applicable; however, the number of times we need to mesh the Joins is decreased in the second method.

Another option is the Grid method shown in Figure 56 (a) which is preferred when a large number of BLSs are supposed to be laminated. In that case, a Composite Grid Design workbench will be used to design the composite parameters. The basic concept is that the BLSs should be limited with perpendicular planes listed in the Grid Panel. Then the stacking sequence for each BLS is stacked up in the Grid interactive window, after which they can finally be modified or controlled in the Grid Virtual Stacking function. After these steps, the Stacking (Engineering) can be generated automatically, including Group plies, Sequences and Layers. The drawback of this method is that the results are

only available layer by layer. For instance, the results of layer number 1 (45° direction in red)—which consists of PLY1, PLY6, and PLY10—are only available without separation for each ply.

The fourth and final option is the Zone method (see Figure 56 (c)). The Zone method is directly designed in the Composite Design workbench and can automatically produce the Stacking (Engineering), as in the Grid Design method. However, the Zone method changes the orders of the plies, and the orders should be controlled and modified before conducting the FEA analysis. Therefore, the zone method’s final stage is similar to the Manual Ply Creation method. Some references explain how to model composite laminate using the Grid method such as [50] and [15], and zone method such as [50], [10], and [15]. The present study focuses on the final results reported from these methods. After the laminate is modelled using any aforementioned methods, the properties are imported to the Generative Structural Analysis workbench through the Ply method.

7.2.3 ABAQUS simulation for compiling the needed data

The employed reference uses the ABAQUS software to model the composite laminate, the instructions of which are available via video tutorial [58] and the “print form” [57]. Since the results reported in the book and the synchronized video are not presented in detail, the author of this thesis, first simulates the problem case in the ABAQUS software to extract additional information. This duplicated work is referred to as “RAS” standing for **R**epeated **A**baqus **S**imulation. These simulation results will be used in the thesis to validate the CATIA FEA solver.

The total deformation in the original reference equals to 0.6075 mm, and in the RAS is 0.609 mm. Moreover, Table 18 presents the maximum stress values at the top of each layer generated by RAS. The needed results for comparison purposes are Total Strain Energy, Deformation, Curvature, and different types of stresses—the von Mises, the maximum principal stresses, and minimum principal stresses—in specific elements.

Table 18: Validate the new repeated ABAQUS simulation

Maximum values of stress at the top surface (MPa)			
Layer	Thickness (mm)	Table 3.4 reported from [57]	Repeated ABAQUS Simulation (RAS)
1	1.2	10.1	10.1
2	2.4	17.88	17.91
3	3.6	17.63	17.63
4	4.8	4.303	4.363
5	6	9.632	9.633

7.2.4 Results and discussion

The RCT for BMP12 consists of six rows and two columns (see Figure 57). The rows are numbered “1” to “6,” and the columns are “L” and “R,” representing the left and the right side of the figure. The exact condition of the problem, given in the first row, consists of L1 and R1. The condition is summarized in the left of row 1 (L1). On the right (R1), a screenshot from the reference [58] explaining the problem case is presented. It shows the number of layers, the three sections (A, AB, and B), and the drop-off areas. The drop-off areas are shown as a white rectangle between the sections. The CATIA software graphical presentation of the laminate parameters are shown in Figure 56.

In Figure 57, row 2 (R2) shows the deformation shapes of ABAQUS and CATIA software captured respectively from left to right with almost identical appearances. The deformed shapes are screenshots of the Norm displacement in the isometric view with the same amplification magnitudes that shows identical shapes for all three methods.

In R2, three sample elements in orange are specified on the three Reference Surfaces (the meshed BLS A, BLS AB, and BLS B): The “Ele. 6×6,” “Ele. 13×6,” and “Ele. 20×6”. These are the element numbers 6, 13, and 20 in the “X” direction and 6 in the “Y” direction from the Reference Surface counting from the “YZ” plane. In addition, the tensile load and the boundary conditions consisting of the clamp edge and the user-defined restraint are respectively shown in blue and red.

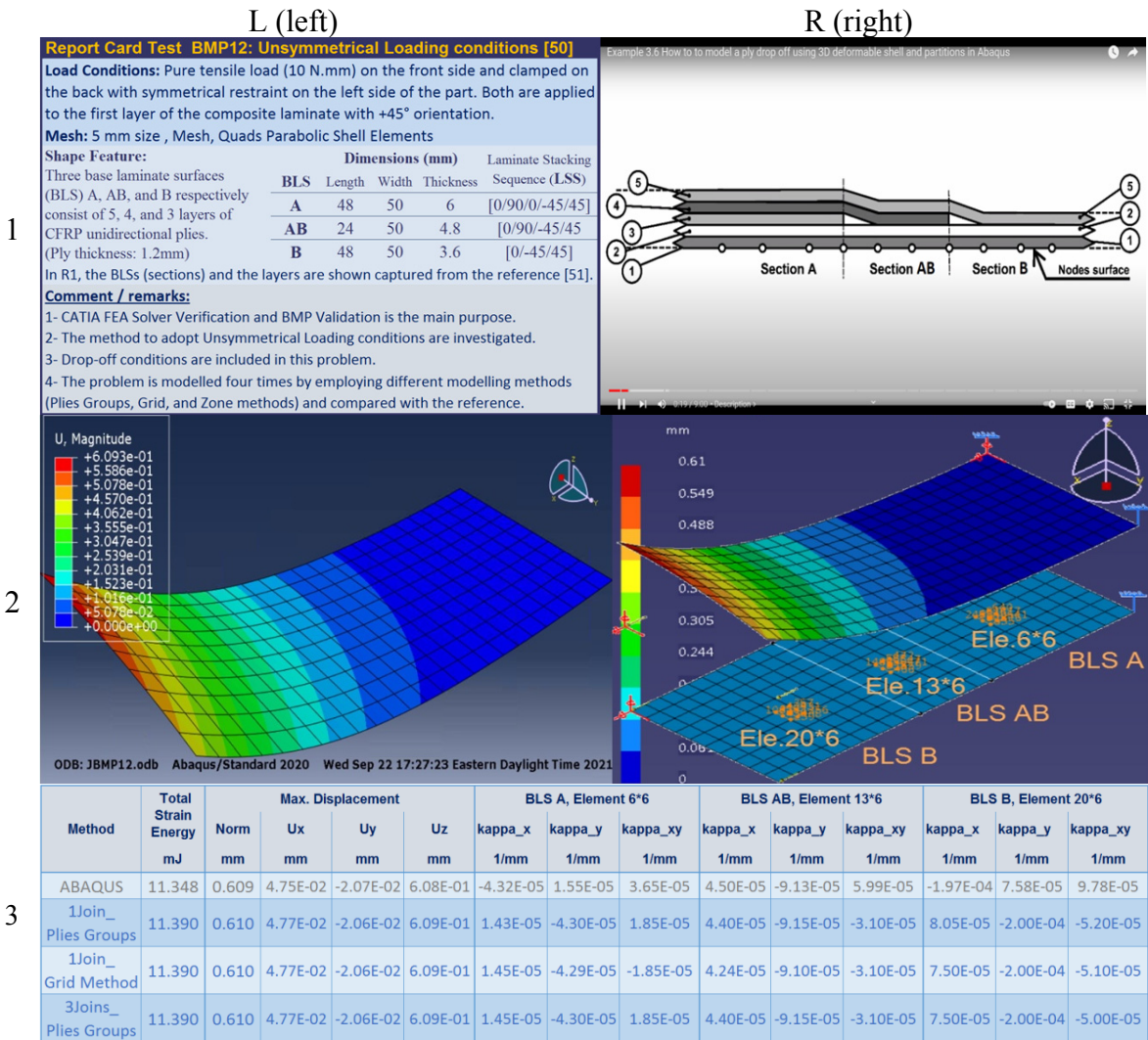
In row 3, an embedded table within Figure 57 presents three columns comparing the results from the reference with the Manual Ply Creation methods (two options) and the Grid method as follows.

1. The magnitudes of the total strain energy magnitudes in millijoules.
2. The magnitudes of the deformations in the Norm and three main coordinate directions in millimetres.
3. The curvature magnitude extracted from each of the sample elements shown in orange the CATIA meshed model in R2.

In rows 4, 5, and 6, three graphs are organized comparing von Mises and the principal stresses (plane stress) at the middle of the plies through the thickness of the laminate from the selected elements (the “Ele. 6×6,” “Ele. 13×6,” and “Ele. 20×6”). The selected elements are located at the same location, far from the edges and the applied loads and restraints, with respect to the reference (RAS) and all the methods.

In all the graphs, “solid line,” “square,” “circle,” and “hollow circle” respectively represent ABAQUS, Manual Ply Creation with one Join (1Join_Ply Groups), the Grid method, and Manual Ply Creation with three Join (3Join_Ply Groups) results. The lines and symbols are selected in red, blue, and green to show the von Mises, the maximum principal stresses, and minimum principal stresses, respectively. When comparing the

Mises stresses, the differences are less than 2%, and both the maximum and minimum principal stresses in the middle of each ply extracted from three methods precisely in the same location in rows 4, 5, and 6. To sum up, rows 2 to 6 show that the results reported from the CATIA software—which resulted from all three methods to design laminate—and the reference are all in compliance with each other, and the errors are negligible.



... Continued from the previous page (BMP12):

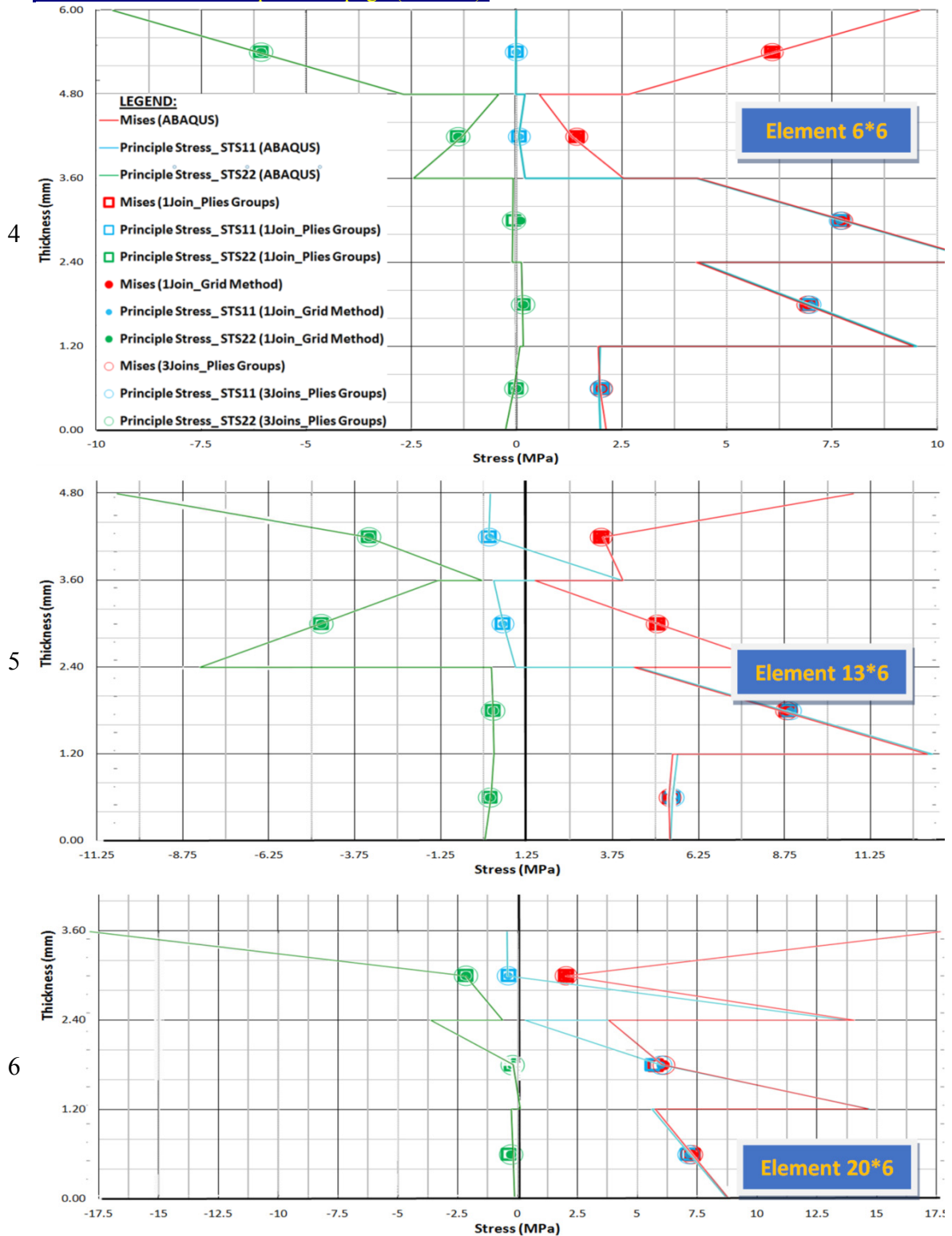


Figure 57: BMP12's Report Card Test (Unsymmetrical Loading conditions)

7.2.5 The symmetry plane presumed by the original reference

It is noticed that the original reference [51] presumes that the problem with the “X” axis is symmetric. Therefore, the red constraint shown in Figure 55 (also shown in Figure 58) is applied, and the problem is solved with the new width equal to 50 millimetres. Inevitably, the problem status for BMP12 was suggested based on the reference and found the same results due to new constraints. However, the laminate does not have any plane of symmetry about the “X” axis. Figure 58 shows the deformed shapes of the two mentioned cases: on the left, the problem status when the plane of symmetry is considered, while on the right, the deformed shape when the total width of the geometry (no plane of symmetry) is modelled and analyzed. It can be seen that the deformed shape is not symmetrical.

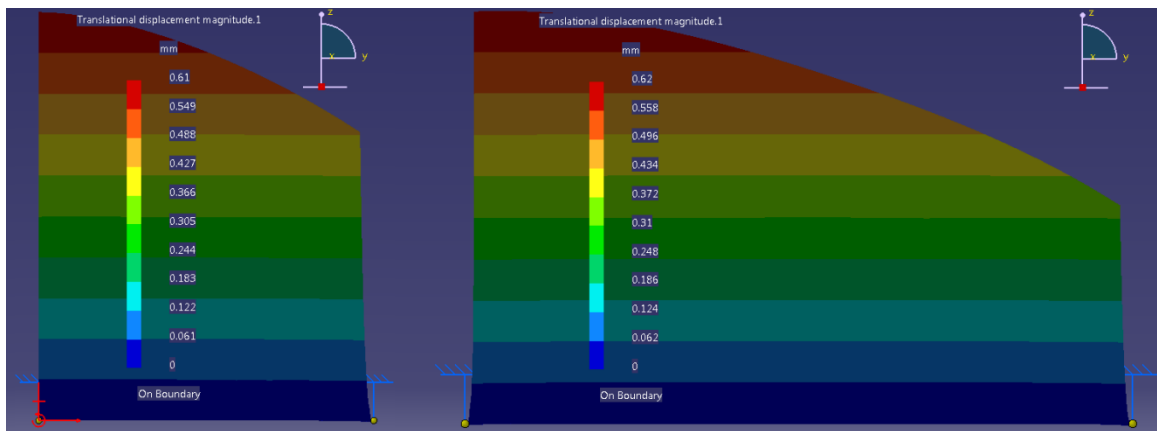


Figure 58: The deformed shapes when considering or not considering the symmetric condition, respectively

7.3 BMP13 (The dynamic response of a composite plate)

In BMP13, the CATIA FEA software's ability to solve three different composite plates under dynamic loading conditions is considered. More specifically, the transient responses for two different stacking sequences and geometries are validated when compared with Example 1 from the reference [59]. While the CATIA software uses the first-order shear deformation theory, the reference uses a new mathematical model for the composite rectangular plate.

In this context, it is important to understand the method employed in BMP13. Since the problem case was defined parametrically, the primary arranged reference problem case—Case I—was suggested, and the CATIA results are compared with the reference. Then, to explore the effect of different parameters, Case II and Case III were introduced. Only one parameter was altered from Case I. There, the laminate in Case II and the aspect ratio—length per width—in Case III were changed. The correlation between the graphs reported from CATIA FEA Solver and the reference were then compared. Lastly, the natural frequency for Case I was validated using classical hand calculation.

7.3.1 Basics of modal superposition

Since the CATIA software relies in the modal superposition approach to solve the transient dynamic problems, a brief discussion of the method is presented in this section. Figure 59 illustrates the components in the single degree of freedom Modal Superposition system presented in equation (27), and the undamped natural frequency of the system is presented in equation (28) [60], [61].

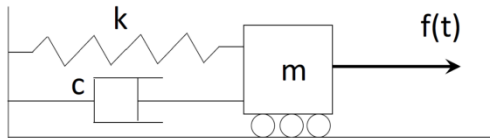


Figure 59: Single degree of freedom, Mass-Spring-Damper System

$$f(t) = m\ddot{x} + c\dot{x} + kx \quad 27$$

$$\omega_n = \sqrt{k/m} \quad 28$$

m: mass, k: stiffness, c: damping

Considering zero displacements and velocity (zero initial conditions), the solution to the equation (29) can be reconstructed to arrive at $x(t)$, employing the convolution integral (Duhamel integral), which results in inhomogeneous linear evolution equations like the vibrating plate, wave, or heat equation [62]. The damped impulsive response, $h(t)$, is given from equation (30).

$$x(t) = \int_0^t f(\tau) h(t - \tau) d\tau \quad 29$$

$$h(t) = \frac{1}{m\omega_d} e^{-\xi\omega_n t} \sin\omega_d t \quad 30$$

ω_d : damped natural frequency, ξ : damping ratio

An infinite number of modes are expected when a continuum system is suggested, such as distributed mass. Therefore, equation (31) [63] is suggested to develop a multi-degree freedom system of Mass-Spring-Damper in equation (27). The only difference between the two equations is that mass, damping, and stiffness are matrices, whereas the components put in the curly bracket ($\{ \}$) are vectors.

$$\{F\} = [M]\{\ddot{x}\} + [C]\{\dot{x}\} + [K]\{x\} \quad 31$$

In practice, there was no need to include an infinite number of modes since the smaller frequencies dominate the transient (dynamic) response. Thus, in the finite element method, a finite number of modes are reported.

7.3.1 Case I

7.3.1.1 Problem statement (Case I)

Figure 60 is organized to illustrate Case I, which consists of three features: geometry, laminate parameters, and the loading conditions. The geometry is a square plate with $a = b = 250 \text{ mm}$ and the thickness of the laminate is 10 millimetres.

The composite parameters consist of the rosette, the lamina, draping direction, and the Reference Surface position. The axes of the global coordinate system (shown in red) and the rosette are in the same direction. The rosette shows 0° in gray and 90° in navy blue, indicating the plies' directions. The join and the stacking sequence directions are opposite, respectively shown in red and dark green. In total, 10 layers of the unidirectional CFRP laminas were employed to stack up a general laminated stacking sequence with the orientation code as [0:4/90:4] on the BLS. The thickness of each lamina is 1.25 millimetres, and the mechanical properties of the lamina are presented in Table 19.

The loading conditions shown in Figure 60 are as follows. The uniform pressure load equal to 0.6 MPa, which is normal to the surface in red vectors (aligned with the "Z" direction), is suddenly applied on the plate. The boundary conditions imposed on the edges are simply supports and presented in equations (32) and (33). As discussed in 5.3.1, the symmetrical option was selected; therefore, the Reference Surface and the mid-plane

surface are coincident. The BLS is meshed with Quads Parabolic Shell Elements with 12.5 mm size. The simple support condition are mathematically described by

$$x = \text{constnt} , \quad U_y = U_z = 0 \quad 32$$

$$y = \text{constnt} , \quad U_x = U_z = 0 \quad 33$$

Since the displacements change with time, the equation of motions needs to be integrated in time using a technique such as the Newmark integration scheme [59]. However, using the Linear Dynamic Analysis, CATIA FEA Solver computes the results in the progressive steps to solve problems under dynamic loading conditions instead of direct integration in time [1]. The number of steps is equal to 1000 times during the 0.001 seconds, whereas the minimum sampling is equal to zero seconds. The modal damping, equal to 0%, is assigned to the problem case; therefore, the displacement's responses graph during the time calculations does not decay.

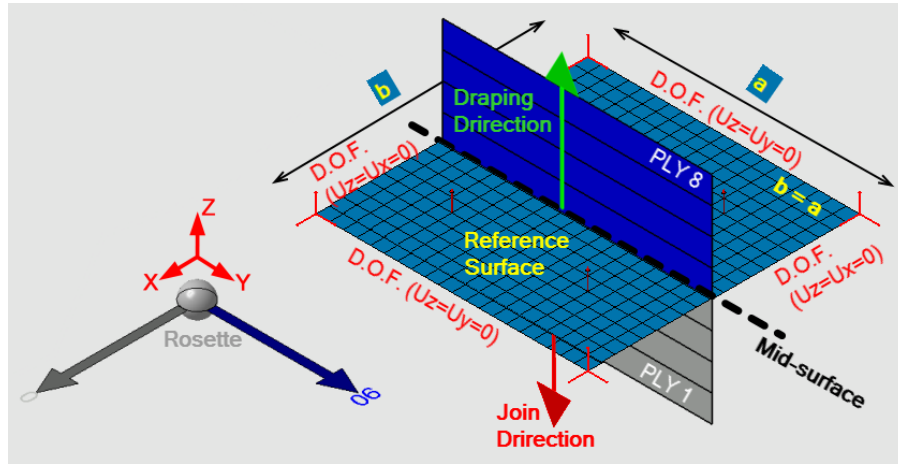


Figure 60: Simple illustration of the BMP13 (Case I)

Table 19: CFRP lamina properties (extracted from [59])

Property (Unit)	Unidirectional Lamina
	CFRP (AS4D[50])
Density (g.cm ⁻³)	0.8
Young's modulus E_1 (MPa)	$E_1 = 25 \times E_2 = 525000$
Young's modulus E_2 and E_3 (MPa)	21000
Poisson's Ratio ν_{12} and ν_{13}	0.25
Shear Modulus G_{23} (MPa)	$G_{23} = 0.2 \times E_2 = 4200$
Shear Modulus G_{12} and G_{13} (MPa)	$G_{12} = G_{13} = 0.5 \times E_2 = 10500$

7.3.1.2 Results and discussion (Case I)

The pressure equals to 0.6 (MPa) and simply supported edges lead to the maximum center node deflection of 3.5 mm, which is almost the result from predicted in [59]. Figure 61 illustrates that the points (10 points) extracted from the indicated reference, which are matched into the displacements' responses graph captured from the CATIA

FEA Solver. The graph illustrates the center node's deformation history in the first 0.001 seconds of the analysis.

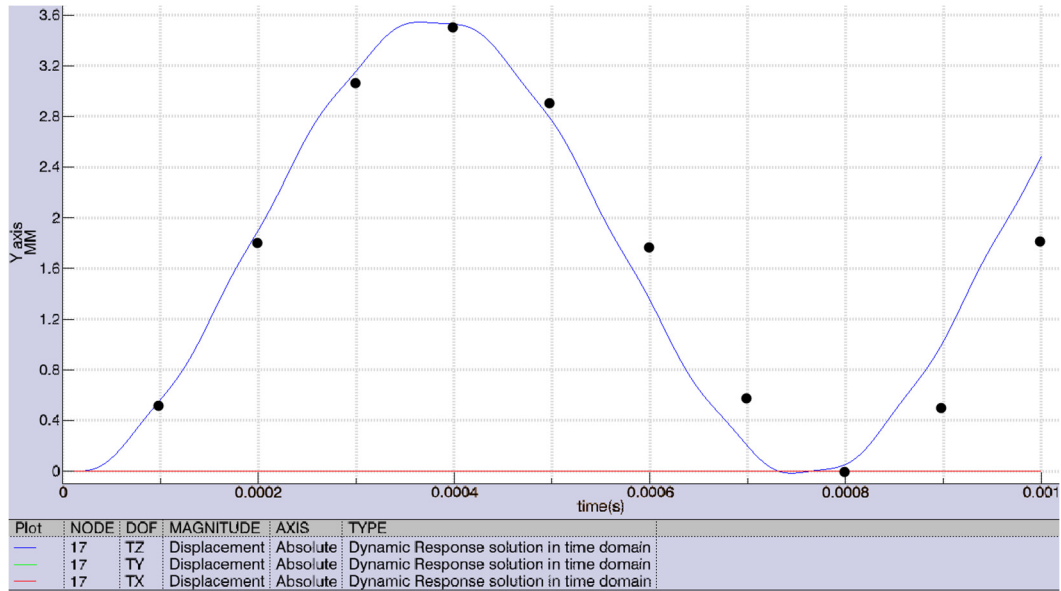


Figure 61: transient responses of the center node deflection (Case I)

7.3.2 Case II

7.3.2.1 Problem statement (Case II)

The Case II problem status is identical to Case I except for the stacking sequence of the laminate. For example, it has the same lamina type and thickness. However, the stacking sequence, which is located on top of the BLS, is $[0/90]_4$, as shown in Figure 62.

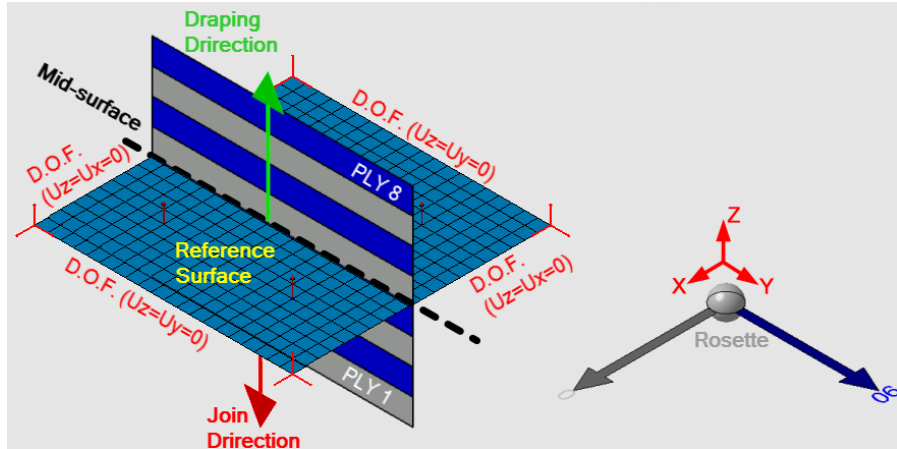


Figure 62: Simple illustration of the BMP13 (Case II)

7.3.2.2 Results and discussion (Case II)

For Case II, the maximum center node deflection was equal to 1.67 mm, once again acceptably close to 1.62 mm prediction from the reference. Figure 66 shows the center node's deformation during the first 0.001 seconds as generated by CATIA and 10 arbitrarily selected discrete points from [59].

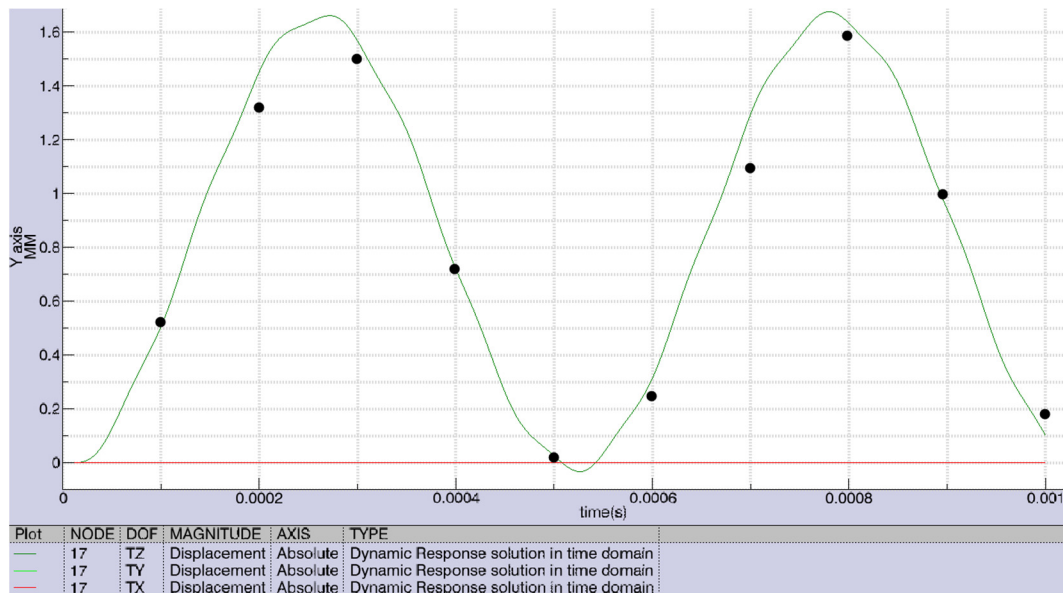


Figure 63: transient responses of the center node deflection (Case II)

7.3.3 Case III

7.3.3.1 Problem statement (Case III)

Finally, the Case III problem case is explored, which is similar to Case I except for the aspect ratio. Figure 67 illustrates the condition for Case III. Here, the plate dimensions are $b' = 2a = 500 \text{ mm}$.

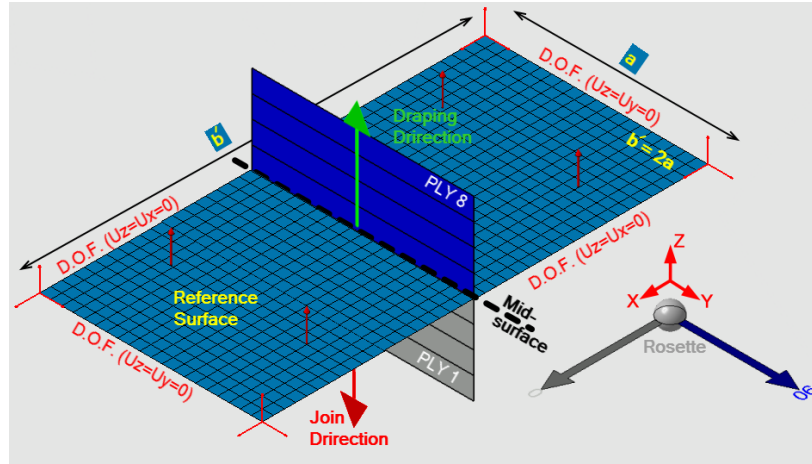


Figure 64: Simple illustration of the BMP13 (Case III)

7.3.3.2 Results and discussion (Case III)

For Case III, Figure 65 displays the center node's deformation history in the first 0.001 seconds of the analysis. The comparison with the ten selected points in reference [59] is quite satisfactory.

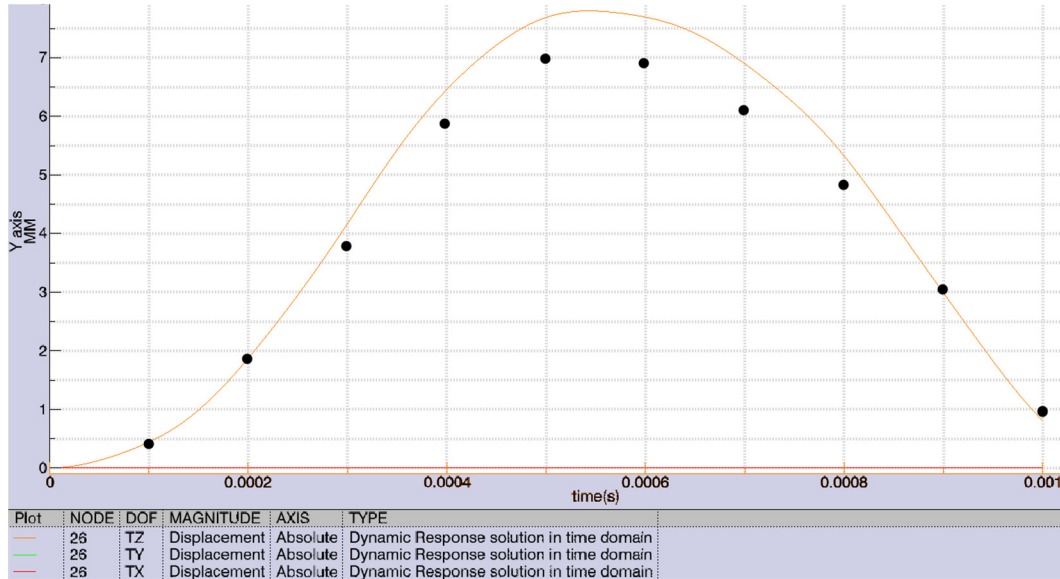


Figure 65: transient responses of the center node deflection (Case III)

7.3.4 Natural frequency validation

The natural frequencies of composite structures are dictated by the mass and elasticity properties or effective mechanical properties, as shown in equation (34). Therefore, problem cases have different natural frequencies based on geometry, composite parameters, and boundary conditions. If the load excitation frequencies match the natural frequencies, vibration results in resonance [64]. For the stacking sequence of Case I, the natural frequencies of a special orthotropic laminated rectangular plate, where the boundary condition is simply supported, are calculated from the equation (34).

$$\omega = \sqrt{\frac{\pi^4}{\rho} \left(D_{11} \left(\frac{m}{a} \right)^4 + 2(D_{12} + 2 \times D_{66}) \left(\frac{m}{a} \right)^2 \left(\frac{n}{b} \right)^2 + D_{22} \left(\frac{n}{b} \right)^4 \right)} \quad 34$$

Different values of “m” and “n” in the above equation correspond to different mode shapes, as are the various natural frequencies modes, ω , [32], [64]. The components employed from [D] matrix— D_{11} , D_{12} , D_{22} , and D_{66} —are computed from equation (10). In Table 20, the first ten modes resulting from the equation (34) and CATIA software are listed. It is important to note that the mesh size is one of the vital factors influencing the FEA software mode magnitudes reported in Table 20. Practically speaking, the first few mode numbers are the most important ones in this problem. For the current condition, the mentioned parameters are equal as follows: $a = b = 0.250$ (m), $\rho = 800 \text{ kg/m}^3$, $D_{11} = 2.28E + 04$ (N.m), $D_{12} = 4.39E + 02$ (N.m), $D_{66} = 8.75E + 02$ (N.m), and $D_{22} = 2.28E + 04$ (N.m).

Table 20: The various natural frequencies modes, ω ,

Mode	m	n	Equation (34) in Hertz	CATIA (Hertz)	Error
1	1	1	1248	1234	1%
2	2	1	3554	3327	6%
3	1	2	3554	3327	6%
4	2	2	4993	4737	5%
5	3	1	7715	6781	12%
6	1	3	7715	6781	12%
7	2	3	8595	7246	16%
8	3	2	8595	7246	16%
9	3	3	11235	7735	31%
10	4	1	13597	7735	43%

7.4 BMP14 (Thermal buckling of a sandwich panel)

With regard to BMP14, the present study investigated CATIA FEA software's ability to predict the buckling modes of a sandwich panel caused by stresses under thermal loading conditions. Twelve combinations of four parameters were arranged to validate in BMP14: (1) the length of the sample, which is a square plate; (2) the total thickness of the sandwich panels; (3) the total thickness of one of the face sheets; and (4) the ply's direction. The results are validated by comparing them with Example 3 from the reference [65]. It employs the higher-order shear deformation theories (HSDT) to develop the finite element models for the thermal buckling analysis of composite plates and sandwich panels. Sections 6.6 and 6.7 discuss two limitations regarding the deployment of FEA analyses using CATIA FEA Solver. The longitudinal thermal expansion coefficient “ α_1 ” is positive; therefore, the limitation is that temperature-dependent coefficients cannot be modelled in CATIA. However, the results agree with compared available reference publications.

7.4.1 Thermal buckling analysis

The CATIA FEA solver uses FSDT for its formulation. The main goal for both FSDT and HSDT is to analyze the shear stress and strain, which are considered when the thickness of the part is large. The CLT approach is not appropriate for thick sandwich panels and leads to erroneous predictions.

The sandwich panel exhibits anisotropic behaviour [26] containing face sheets—thin skin-layer bonded to each side—with a core layer in between. The core is the inner layer and is comprised of low-density materials that are often substantially thicker than the surface layers. In other words, the core is generally employed to separate the face sheets from each other and stabilize them by increasing the bending rigidity. The cores can be from light materials, such as foam, or formed from a wide range of cell configurations, such as hexagons or other shapes.

Altering the temperature on a restrained part can cause thermal buckling, which results from increasing the stresses due to constrained boundaries. Section 3.2.1.4 discusses the linear buckling analysis, which consists of critical load, the multiplier, and the various buckling modes. The temperature and the compressive force have a linear relation, as shown in equation (35). If the parameters of the Young's modulus, the area of cross-section, and the thermal expansion coefficient remain constant, the equation (36), reported from [65], is similar to equation (18) in Chapter Three.

$$\Delta F = E \times A \times \alpha \times \Delta T \quad 35$$

$$\Delta T_{cr} = \lambda \times \Delta T_{applied} \quad 36$$

$\Delta T_{APPLIED}$: The specified rise or drop of temperature

λ : The least eigenvalue (the associated mode shape)

ΔT_{cr} : The critical temperature rise from the T_0 (temperature of the environment)

7.4.2 Problem statement

Figure 66 is organized to illustrate the BMP14 in which the CATIA FEA Solver is employed to report the results for twelve different case numbers. Each consists of different geometry and laminate parameters. For all case numbers, the restraints are identical, as shown in equations (37) and (38), and the same environment and field temperature are applied, which are equal to 273.15 (K) and 274.15 (K), $\Delta T_{applied} = 1(K)$.

$$x = \text{const}, \quad U_y = U_z = 0, \quad R_x = R_y = 0 \quad 37$$

$$y = \text{const}, \quad U_x = U_z = 0, \quad R_x = R_y = 0 \quad 38$$

The symmetrical option was selected; therefore, the Reference Surface and the mid-plane surface are precisely in the middle of the core (Ply 11). The BLS is meshed with Quads Parabolic Shell Elements with 12.5 mm size.

The geometry is parametric and different values of the mentioned parameters for case numbers 1-12 were selected, presented in Table 21. The geometry of the sandwich panel is a square plate “a” × “a” and its total thickness is “h”. The sandwich panel stacking sequence is symmetric about the core bounded with two balanced laminates as the face sheets are located on the top and the bottom. To be more precise, “ h_c ,” and “ h_f ” are the thickness of the core and the thickness of each face sheet. The thickness of each ply is equal to 0.0625 millimetres for case numbers 1, 2, 3, 7, 8, and 9; thus, it is equal to 0.125 millimetres for case numbers 4, 5, 6, 10, 11, and 12.

The mechanical properties of both plies and the core are presented in Table 22. It is important to note that only the central core's mechanical properties are sufficient for the FEA analyses purposes. There is no need to model the exact structure of the core. Each face sheet is a balanced, antisymmetric angle-ply laminate $[(\theta/-\theta):5]$ that employs identical unidirectional CFRP laminas. The general form of the complete laminate stacking sequence is $[(\theta/-\theta):5/\text{Core}]_s$ and consists of 21 layers on top of the BLS, as shown in Figure 66. Ply numbers 1-10 and 12-21 are those face sheets, while the central core is Ply 11. In addition, the figure illustrates the composite parameters consisting of the rosette, the lamina, draping direction, and the Reference Surface position. The axes of the global coordinate system, shown in red, and the rosette are in the same direction. Moreover, the rosette shows the ply's direction in Figure 66 in different colours. The ply's direction for each case number is presented in Table 21. The join and the stacking sequence directions are opposite, respectively shown in red and dark green.

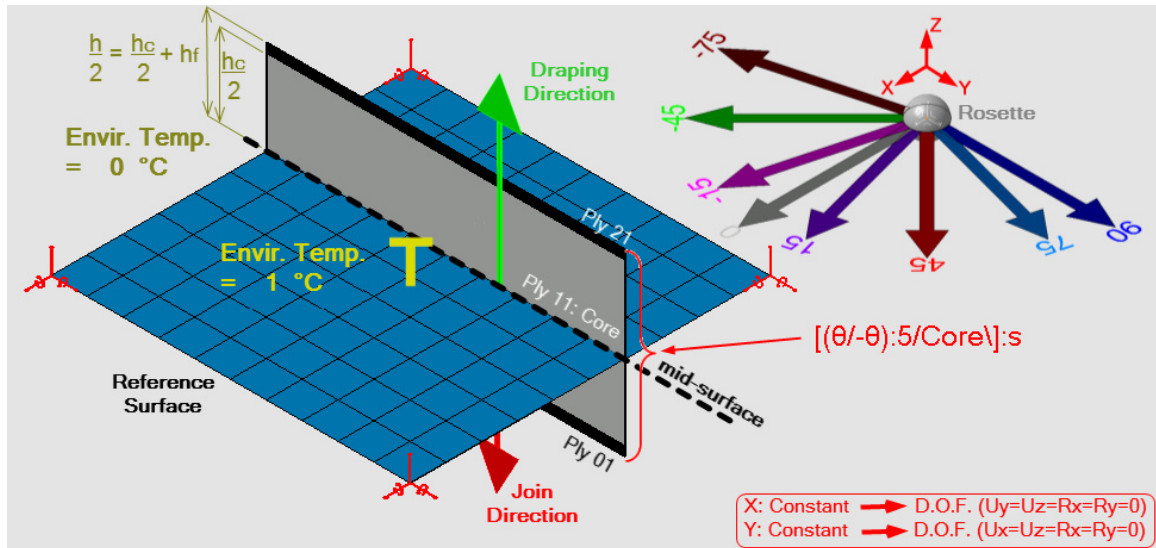


Figure 66: Simple illustration of the BMP14

Table 21: Parameters involved in problem cases for BMP14

Case #	a (mm)	h (mm)	a/h	h_f (mm)	$h_c = h - 2 \times h_f$ (mm)	h_f/h	Angle (θ°)	Laminate Stacking Sequence (LSS)
1	250	12.5	20	0.625	11.25	0.05	45	[(45/-45):5/Core\]:s
2	250	12.5	20	0.625	11.25	0.05	0	[(0):10/Core\]:s
3	250	12.5	20	0.625	11.25	0.05	15	[(15/-15):5/Core\]:s
4	250	12.5	20	1.25	10	0.1	45	[(45/-45):5/Core\]:s
5	250	12.5	20	1.25	10	0.1	0	[(0):10/Core\]:s
6	250	12.5	20	1.25	10	0.1	15	[(15/-15):5/Core\]:s
7	125	12.5	10	0.625	11.25	0.05	45	[(45/-45):5/Core\]:s
8	125	12.5	10	0.625	11.25	0.05	0	[(0):10/Core\]:s
9	125	12.5	10	0.625	11.25	0.05	75	[(75/-75):5/Core\]:s
10	125	12.5	10	1.25	10	0.1	45	[(45/-45):5/Core\]:s
11	125	12.5	10	1.25	10	0.1	0	[(0):10/Core\]:s
12	125	12.5	10	1.25	10	0.1	75	[(75/-75):5/Core\]:s

Table 22: Lamina and core properties (extracted from [65])

Property (Unit)	Unidirectional	Core
Young's modulus E_1 (MPa)	$E_1 = 19 \times E_2 = 133000$	
Young's modulus E_2 and E_3 (MPa)	7000	2800
Poisson's Ratio ν_{23}	0.49	
Poisson's Ratio ν_{12} and ν_{13}	0.32	
Shear Modulus G_{23} (MPa)	$G_{23} = 0.338 \times E_2 = 2366$	462
Shear Modulus G_{12} and G_{13} (MPa)	$G_{12} = G_{13} = 0.52 \times E_2 = 3640$	553
Thermal Expansion Coefficient		
normalization factor for the coefficient of the thermal expansion $\alpha_0 \cdot 10^{-6}/\text{K}$	27	27
Longitudinal Thermal Expansion Coefficient $\alpha_1 \cdot 10^{-6}/\text{K}$	$= \alpha_0 \times 0.001 = 0.027$	-
Transverse and Out-of-plane Thermal Expansion Coefficient $\alpha_2, \alpha_3 \cdot 10^{-6}/\text{K}$	$= \alpha_0 = 27$	$\alpha_0 \times 1.36 = 36.7$

7.4.3 Results and discussion

The reference uses three parameters to report the results. These parameters consist of two different ratios: first, the length of the square plate “a” and second, the face sheet thickness “ h_f ” both divided by the sandwich panel thickness “h,” respectively a/h and “ h_f/h ”. Moreover, the third parameter is the ply’s directions “ θ ”. These parameters are first calculated or presented in Table 21 and then repeated in Table 23 as the inputs of each case number.

Case numbers 1 to 12 were loaded into the CATIA software, and the lowest multipliers were reported in Table 23. The critical temperature difference— ΔT_{cr} (K)—for all case numbers are reported in Table 23. They are obtained by multiplying the lowest multiplier into the applied temperature difference which is $\Delta T_{applied} = 1$ (K), using equation (36). Then the values for each Thermal stability parameter “ λ_T ” is presented by scaling it to 100. They are resulted from equation (39) extracted from [65] in which the normalization factor for the coefficient of the thermal expansion “ α_0 ” is equal to 27×10^{-6} (1/ K).

$$\lambda_T = \alpha_0 \times \Delta T_{cr} \quad 39$$

Figure 67 shows the results from Table 23 for each case number in light green displayed on the graphs extracted from the reference [65]. The graph illustrates the effects of thickness ratio “ h_f/h ” and fibre orientation angle “ θ ” on the Thermal stability parameter “ λ_T ” of square sandwich panels. The graph on the right corresponds to the ratio of “ a/h ” being equal to 10, while the one in the left is equal to 20. Comparing the twelve case numbers display an excellent agreement.

Table 23: Critical Temperature (T_{cr}) values reported from CATIA FEA Solver corresponding each Case # and the computed Thermal stability parameter ($\lambda_T \times 100$)

Case #	a/h	h_f/h	Angle (θ°)	Multiplier (CATIA Results)	ΔT (K)	ΔT_{cr} (K)	$(\lambda_T = \alpha_0 \times \Delta T_{cr}) \times 100$
1	20	0.05	45	15294	1	15294	41.3
2	20	0.05	0	10365	1	10365	28.0
3	20	0.05	15	6805	1	6805	18.4
4	20	0.1	45	11339	1	11339	30.6
5	20	0.1	0	7629	1	7629	20.6
6	20	0.1	15	4888	1	4888	13.2
7	10	0.05	45	34085	1	34085	92.0
8	10	0.05	0	23405	1	23405	63.2
9	10	0.05	75	15392	1	15392	41.6
10	10	0.1	45	21074	1	21074	56.9
11	10	0.1	0	15320	1	15320	41.4
12	10	0.1	75	10021	1	10021	27.1

P.S.: $\alpha_0 = 27 \times 10^{-6} / ^\circ\text{K}$

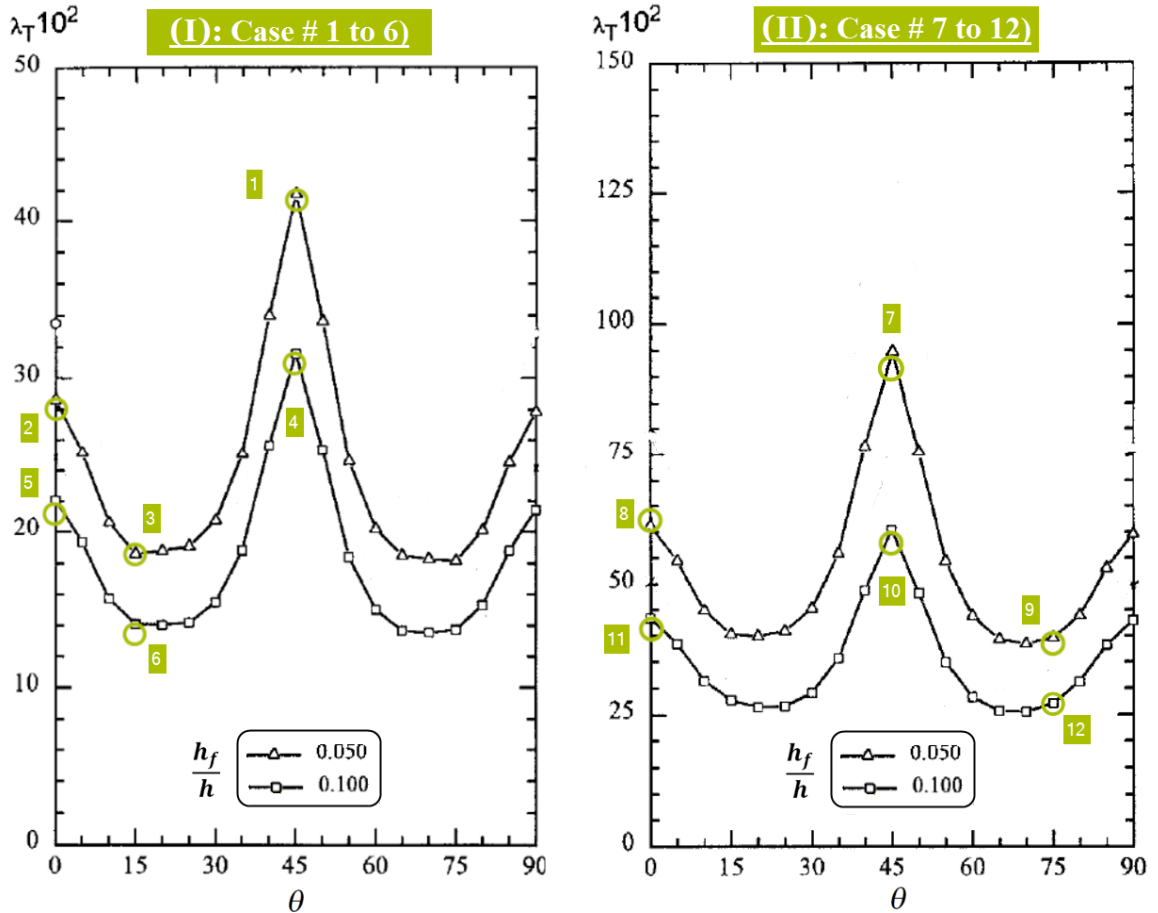


Figure 67: Effects of thickness ratio (h_f/h) and fibre orientation angle (θ) on the Thermal stability parameter (λ_T) of square sandwich panels; Left: $a/h=20$, right: $a/h=10$

CHAPTER EIGHT: PRACTICAL ANALYTICAL MODELS

8.1 Introduction:

The benchmark problems suggested in Chapter Eight are rather more practical engineering problems than Chapter Six and Chapter Seven. In other words, in Chapter Eight, three complex geometries are proposed to challenge the CATIA FEA Solver's ability to model and conduct FEA analysis. BMP15 is the only benchmark problem validated using published references. No proper references are publicly available for the complex geometries proposed in BMP16 and BMP17.

In BMP15, the stiffened panel is designed in which two perpendicular plates are assembled with various rosettes, and an intersection between two plates is meshed while the nodes on two panels are identical. The stiffened panels are mostly used to increase the bending rigidity and the critical buckling load of the panel. Here, CATIA's ability to predict the stiffener's optimal height in which the critical buckling load will reach the maximum amount is investigated. In this study two different locations for the stiffener are considered.

In BMP16 and BMP17, the geometrical data and material properties were taken from two publicly available sources and seem to be reasonable for the purpose in mind. BMP16 is a two-step numerical computation problem on an aircraft propeller. The first model failed, but after adding some extra laminates in different locations, the final model passed the Tsai-Hill criteria. The first topic to discuss in both BMPs is modeling of the geometry and laminating an actual aircraft propeller or wing. The second and the more critical issue is how to create proper meshes that encompass the entire geometry and composite parameters. The assembled compartments in different angles and sizes with various laminates and rosettes are modelled. Afterwards, the FEA analysis method for such cases is investigated, and some tools and toolbars provided in CATIA software are discussed for the first time in thesis which needed to the part complexity.

8.2 BMP15 (Buckling of a stiffened panel)

BMP15 focuses on analyzing the buckling modes of a stiffened plate with different widths and stiffener heights under uniaxial compressive load. Each plate at a certain stiffener height has a critical buckling load. Here, the CATIA FEA Solver's ability to predict the lowest buckling mode is assessed and compared with the references [66], [67]. Mittelstedt [67] used the classical Ritz method, while Zhao et al. [66] employed the FSDT in MSC NASTRAN. Two different positions of the stiffener based on the plate's width are employed on each of the stiffeners' heights used. These factors create the different buckled shapes and values of the first mode, which are then compared with the available references. To model the stiffener and the plate, two perpendicular BLSs, are employed.

8.2.1 Problem statement

Figure 68 is arranged to illustrate the BMP15 setup in which the CATIA FEA Solver is employed to report the results for fifteen different case numbers. Assuming that the width of the plate is “b”, the stiffener is assumed to be two locations “b/2” and “b/4”. For each of these two stiffener locations and different height values “h” are employed. The plate width is 100 millimetres. Both the plate and the stiffener have the length of 300 millimetres and thickness of 1 millimetre. The center of the mass of the stiffener is assumed to be located at the middle plane of the composite plate.

The 2D scaleless stacking sequences are Symmetric Cross-Ply (or Specially orthotropic), [(0/90):2]:s and consist of eight layers stacked in the Draping Directions on each BLS, as shown in Figure 68. The join and the stacking sequence directions are opposite, respectively shown in red and dark green. The thickness of each unidirectional CFRP lamina equals 0.125 millimetres, and the mechanical properties of both plies and the core are presented in Table 24. The figure also illustrates the composite parameters: the rosette, the lamina, draping direction, and the Reference Surface position. The axes of the global coordinate system (shown in red) and the rosette's directions designed for the plate (shown in orange) are in the same direction. The rosette's directions designed for the stiffener, “rosette-stiffener,” are shown in Figure 68: The rosettes show 0° in grey and 90° in navy blue. The layer with 0° direction for the “rosette-stiffener” is aligned with the “X” direction of the GCS (Global Coordinate System). The References for rosette's normal (shown in yellow) are aligned with the Draping Direction, as discussed in 6.10.

Identical mesh type and size, Quads Parabolic Shell Elements with 5 mm size, for both BLSs are used, and the tolerance for the Automatic Mesh Captures 0.1 millimetres is imposed. The symmetrical option was selected for both BLSs; therefore, the Reference Surfaces (the meshed BLSs) are in the middle of the laminate's thickness, the Mid-Surfaces (shown in orange).

A unidirectional compressive load in the “X” direction equal to 1 (N/mm) is applied to the plate on both ends. Rigid body motion is prevented using three restraint conditions:

1. All edges are restraint in the “Z” direction
2. The vertices “3” and “4” limit the movement in the “X” direction
3. The vertex “4” restrains the movement in the “Y” direction

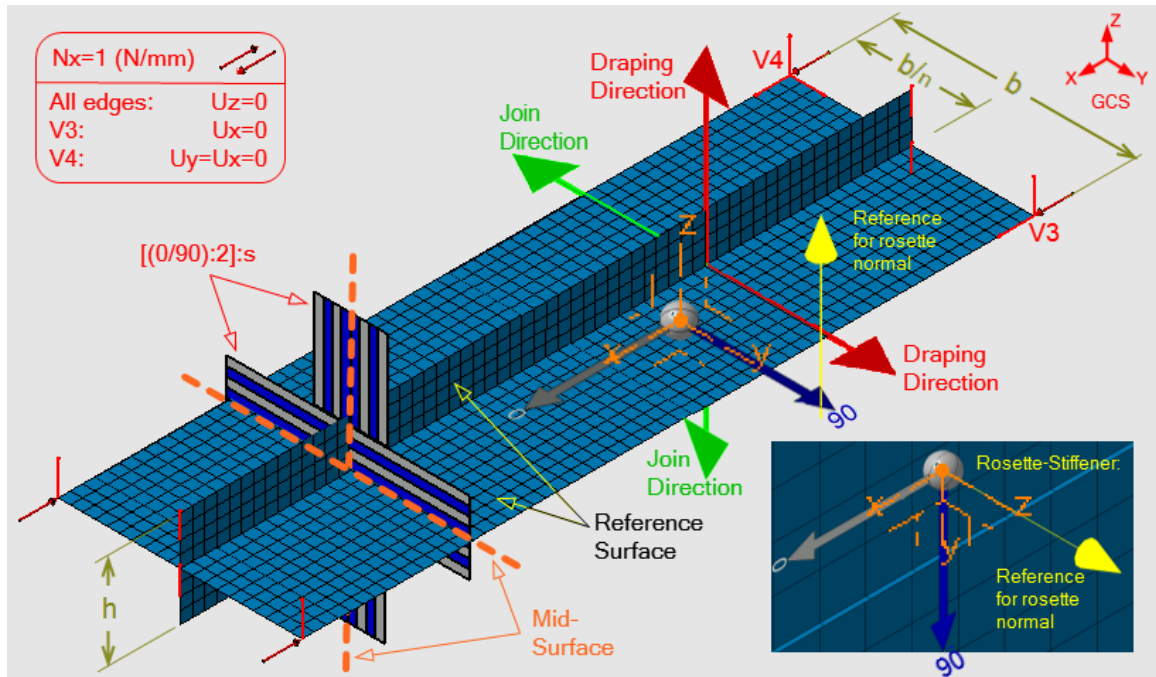


Figure 68: Simple illustration of the BMP15

Table 24: Lamina and Core properties (extracted from [67])

Property (Unit)	Unidirectional
Young's modulus E_1 (MPa)	138000
Young's modulus E_2 and E_3 (MPa)	8960
Poisson's Ratio ν_{12} and ν_{13}	0.3
Shear Modulus G_{23} (MPa)	3600
Shear Modulus G_{12} and G_{13} (MPa)	7100

8.2.2 Results and discussion

The Symmetric Cross-Ply (or Specially orthotropic) laminate is employed (Type 1: Appendices Table A); thus, the characteristics of the $[ABD]$ matrices for the laminate are as follows: " $A_{16} = A_{26} = 0, D_{16} = D_{26} = 0, [B] = 0$ ".

Therefore, there is no shear-extension, bend-twist, or bend-extension coupling. In view of these, all types of deformations (stretches, bending, and twisting) are present. See state5 (S5) in Appendices Table B.

Figure 69 shows half-wave mode shapes of case number 1-9; when “n” is 2, the stiffener is located at the middle of the plate’s width. All the half-wave mode shapes are captured while the isometric view with the amplification magnitudes of 10 was assigned.

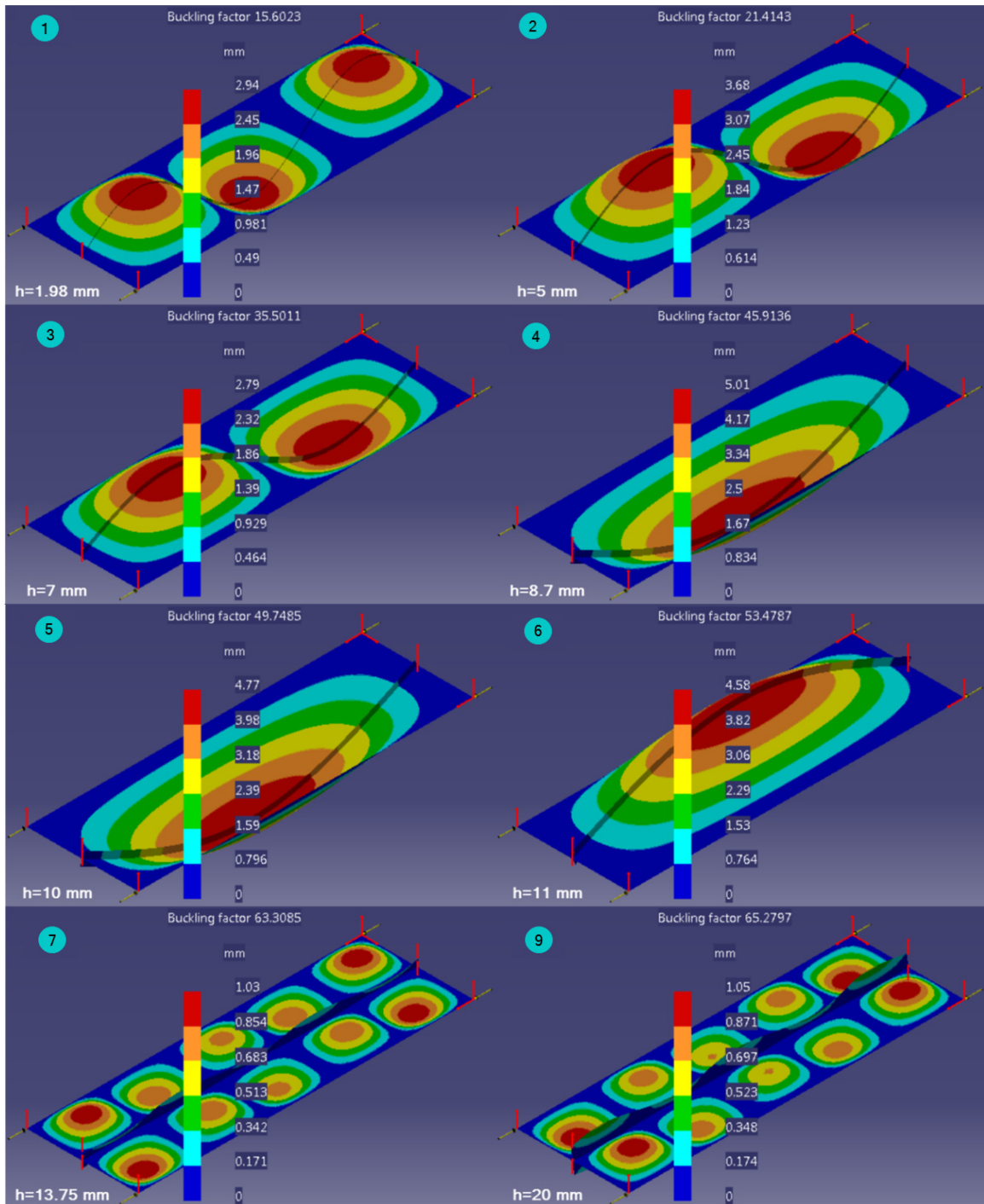


Figure 69: First mode shape and values for various “h,” when the stiffener is located at half of the plate’s width

Figure 70 reports the variation of the buckling load with stiffener height and the half-wave mode shapes results from [66] with blue line when the stiffener is located at the center of the plate's width. Moreover, the results from [67] are added and shown as red squares for some stiffener height. Mittelstedt [67] assumed that the equivalent torsion stiffener GJ is zero. This was explored by setting the value of Shear Modulus of the stiffener to zero in the CATIA software, and the final results were almost the identical to [67].

The case number 1-9 values extracted from CATIA FEA Solver reported in Figure 69 are shown in Figure 70 by light blue dots marked from 1-9. In addition, the half-wave mode shapes illustrated in Figure 69 match the illustrations given in Figure 70.

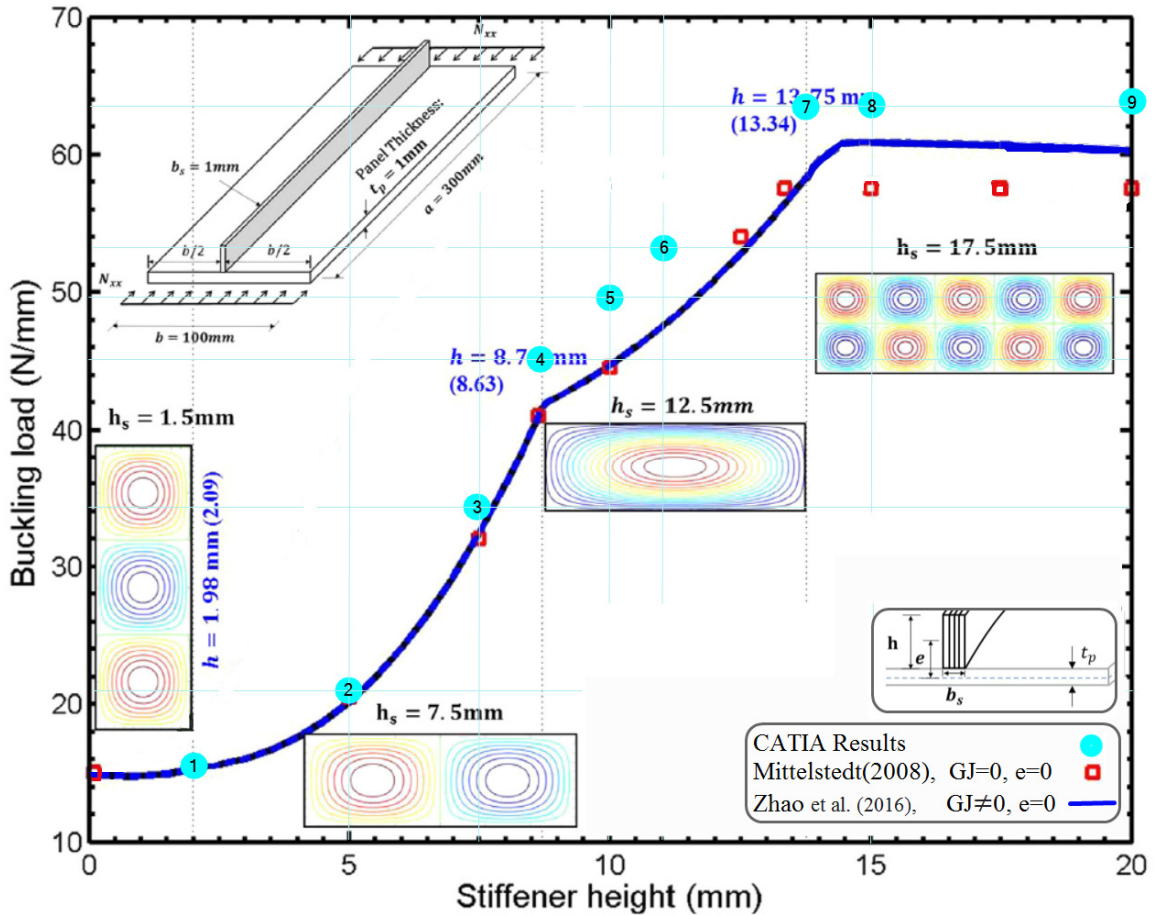


Figure 70: Varied buckling loads with stiffener height. The stiffener is located in the middle of the plate's width.

Figure 71 illustrates half-wave mode shapes of case number 10-15: When "n" is equal to 4, the stiffener is located at the quarter of the plate's width. All the half-wave mode shapes are captured as displayed.

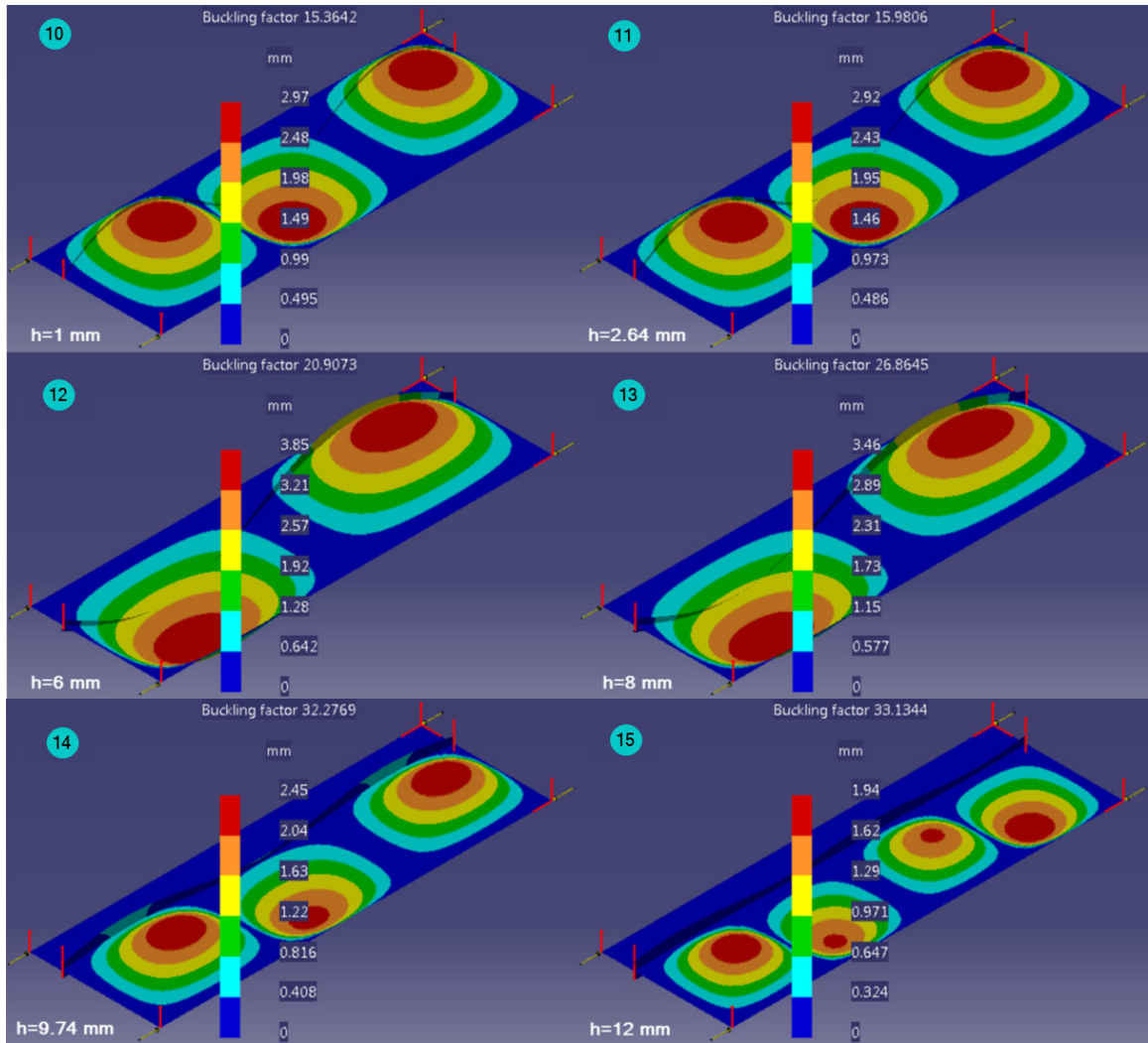


Figure 71: First mode shape and values for various “h,” when the stiffener is located at one-quarter of the plate’s width

Figure 72 extracted from [67] shows the changing buckling loads with stiffener height, and the half-wave mode shape results with a continuous black line when the stiffener is located at a quarter of the plate’s width.

The case number 10-15 values reported from CATIA FEA Solver presented in Figure 71 are shown in Figure 72 with light blue dots marked from 10-15. In addition, the half-wave mode shapes illustrated in Figure 71 are matched with the illustrations given in Figure 72.

Table 25 presents fifteen different problem states applied into CATIA software varied by the height and location of the stiffener. Moreover, the first buckling factor’s magnitudes for the case numbers reported from the CATIA FEA Solver and references are presented. The different percentages between these two are provided in the last column, and the errors vary between zero to 11%.

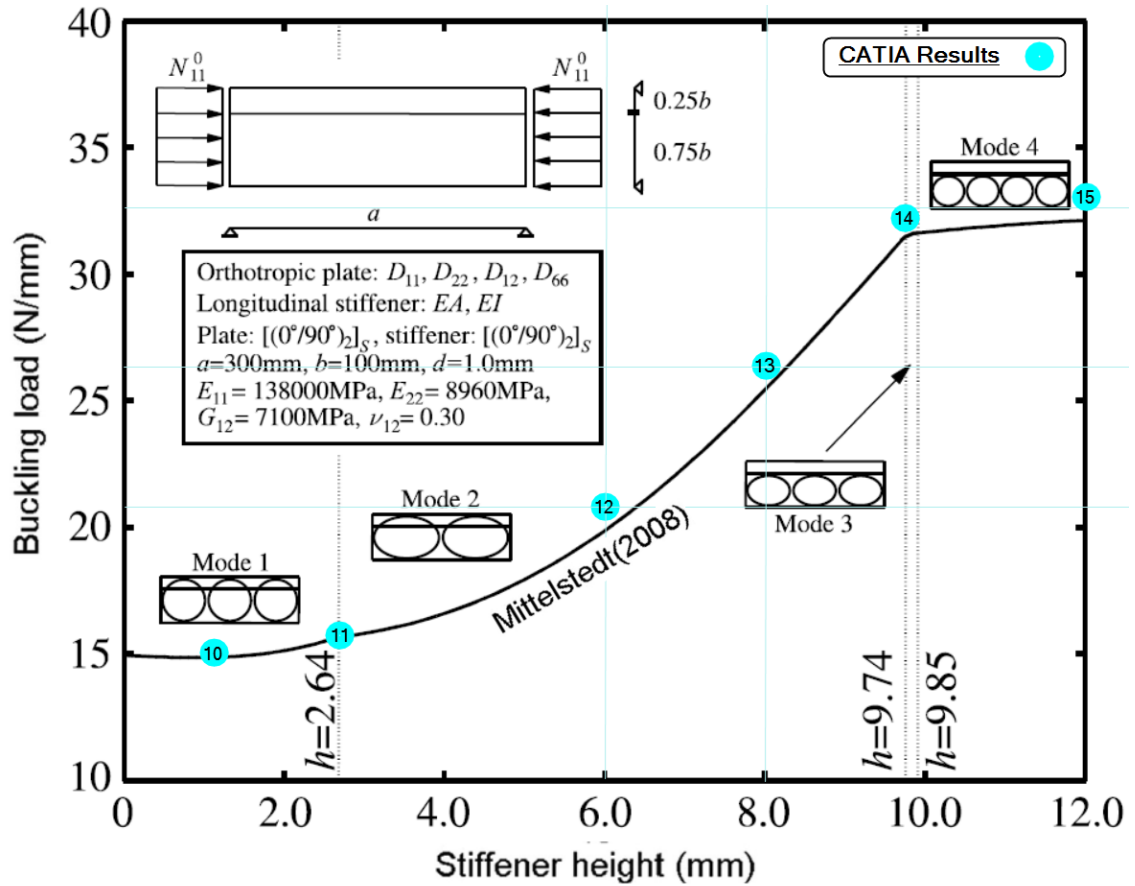


Figure 72: Varied buckling loads with stiffener height. The stiffener is located at a quarter of the plate's width.

Table 25: Different stiffener height and location used in BMP15

Case number	Stiffener height: "h" (mm)	Stiffener position in proportion of plate's width	Buckling Factor		
			CATIA	References	Error %
1	1.98	n =2, at the middle	15.6	15.5	1%
2	5	n =2, at the middle	21.4	20.5	4%
3	7	n =2, at the middle	35.5	32.5	9%
4	8.7	n =2, at the middle	45.9	42	9%
5	10	n =2, at the middle	49.7	45	11%
6	11	n =2, at the middle	53.5	48	11%
7	13.75	n =2, at the middle	63.3	58.5	8%
8	15	n =2, at the middle	63.6	60.5	5%
9	20	n =2, at the middle	65.3	60.5	8%
10	1	n =4, at a quarter	15.4	15	3%
11	2.64	n =4, at a quarter	16	16	0%
12	6	n =4, at a quarter	20.9	20	4%
13	8	n =4, at a quarter	26.9	25.5	5%
14	9.74	n =4, at a quarter	32.3	31.5	3%
15	12	n =4, at a quarter	33.1	32	3%

8.3 BMP16 (An idealized propeller blade)

In BMP16, the Tsai-Hill failure criterion is employed to predict the failure of the elements on a propeller blade. The Tsai-Hill failure criterion and the inverse reserve factor (IRF) are briefly explained in 3.4. A base design of the propeller was extracted from [49] and shown in Figure 73. Its laminate stacking sequence was defined as $[\pm 45/90/0]_s$ and loaded by 0.05 MPa pressure and rotational speed corresponding to 2000 rpm. The ANSYS software was used in [49], while [10] used almost the same problem case to model the propeller employing the CATIA software. However, the results were not finalized in either study. The techniques (as opposed accuracy) to use ANSYS and CATIA software were the primary concern of these references. In this study, the approach in [10] is mostly followed.

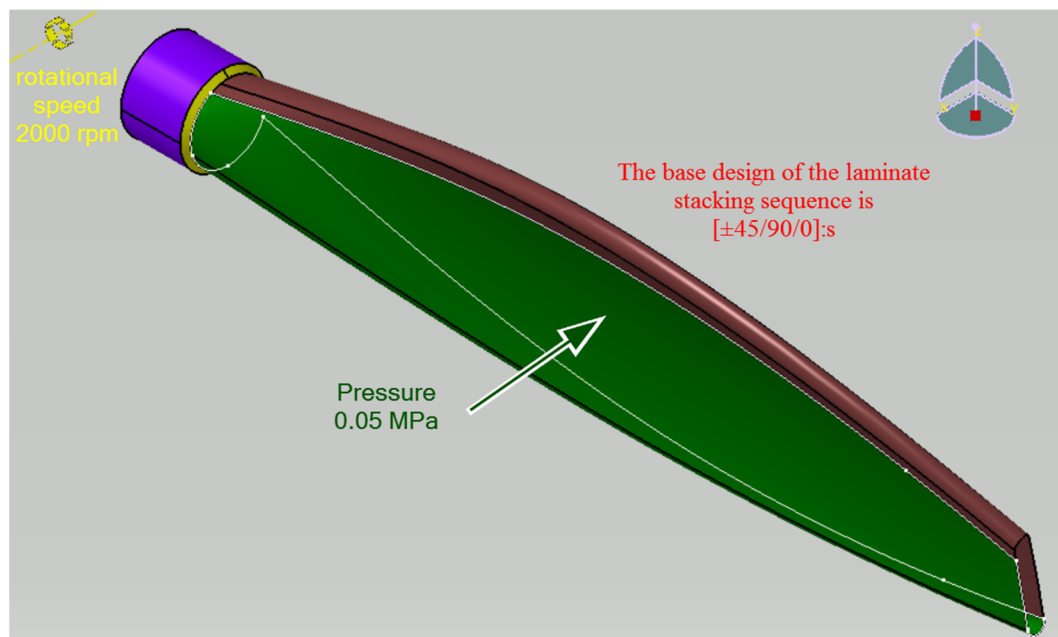


Figure 73: The base design of the propeller extracted from [49]

The first step is to model the basic problem case to locate the failed elements. Considering the design problem limitations and assumptions, a new model is proposed. The IRF (Inverse Reserve Factor) for all the elements in the new model is <1 , based on four considerations. First, the geometry and the employed ply remain unchanged. Second, the basic stacking sequence remains to be the original laminate, and the modification will be examined after that. Third, the laminates are stacked inside the propeller mold; therefore, the laminates inside the mold should not fill all the way between two surfaces. Lastly, the total weight of the propeller should be reduced.

Figure 70 shows the failed elements from lamina No.1 ($IRF > 1$) using the Tsai-Hill failure criterion. The acceptable elements are excluded, implying that only those demonstrated in the figure must be strengthened to fulfill the minimum weight requirement.

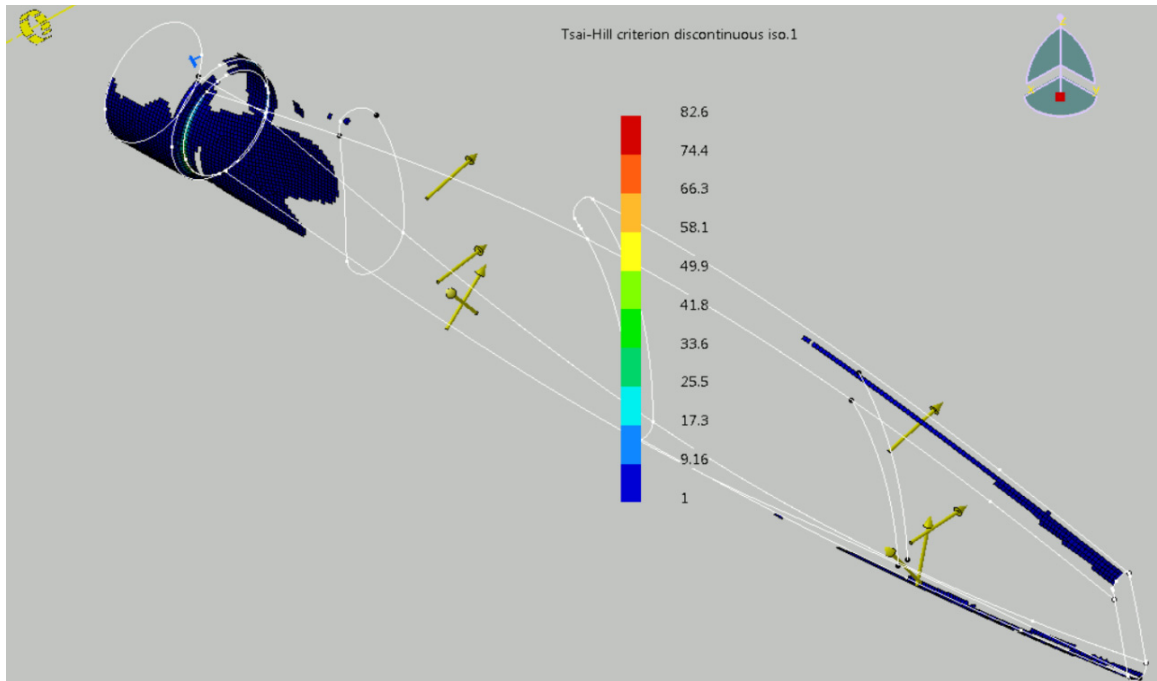


Figure 74: The reference problem case, failed elements (IRF>1)

8.3.1 Modelling the geometry and the composite parameters

The basic problem case extracted from [49] was an Initial Graphics Exchange Specifications (.iges file). Figure 75 shows four main Base Laminate Surfaces: the “Base” in purple, the “Ring” in yellow, the “Back” in brown, and the Front in green. The geometry is approximately 84mm, 807mm, 209mm respectively in the “X,” “Y,” and “Z” directions.

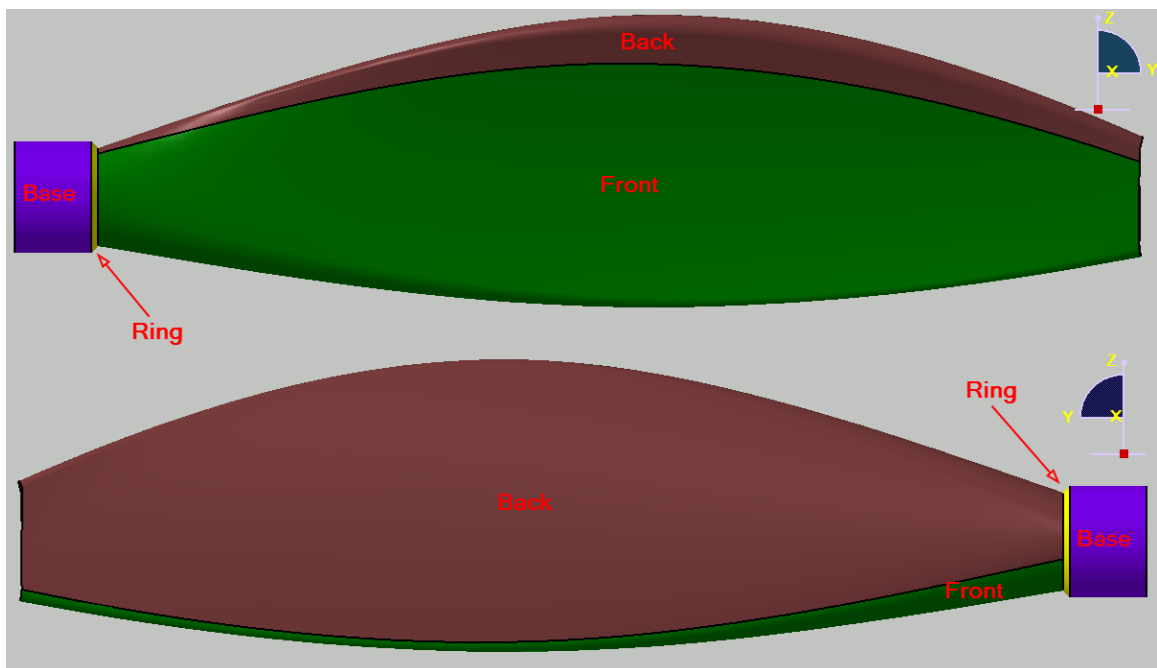


Figure 75: main Base Laminate Surfaces

Figure 76 shows the assembly view and the separate view of five Sub-BLSs located at the weak areas illustrated in Figure 70 (RVF>1). The “Back_Close to Base” and “Back_Top U” are located inside the Back BLS. Also, the pieces labelled “Front_Close to Base,” the “Front_Closer to the Base,” and “Front_Bottom U” are located inside the “Front BLS,” and the “Base” and the “Ring” are employed for extra layers of the lamina in BMP16. It is important to note that all the BLSs are making one “Join” and only the boundaries of all the Sub-BLSs and that the main BLSs are employed in further modelling. In this context, a “Boundary” is an area around the surface or a general term for the contours discussed in 5.2.1.

The stacking sequences are stacked in the Draping Directions inside the mold on top of all boundaries. The “Join” and the stacking sequence directions are opposite in which all the “Joins” are directed outward.

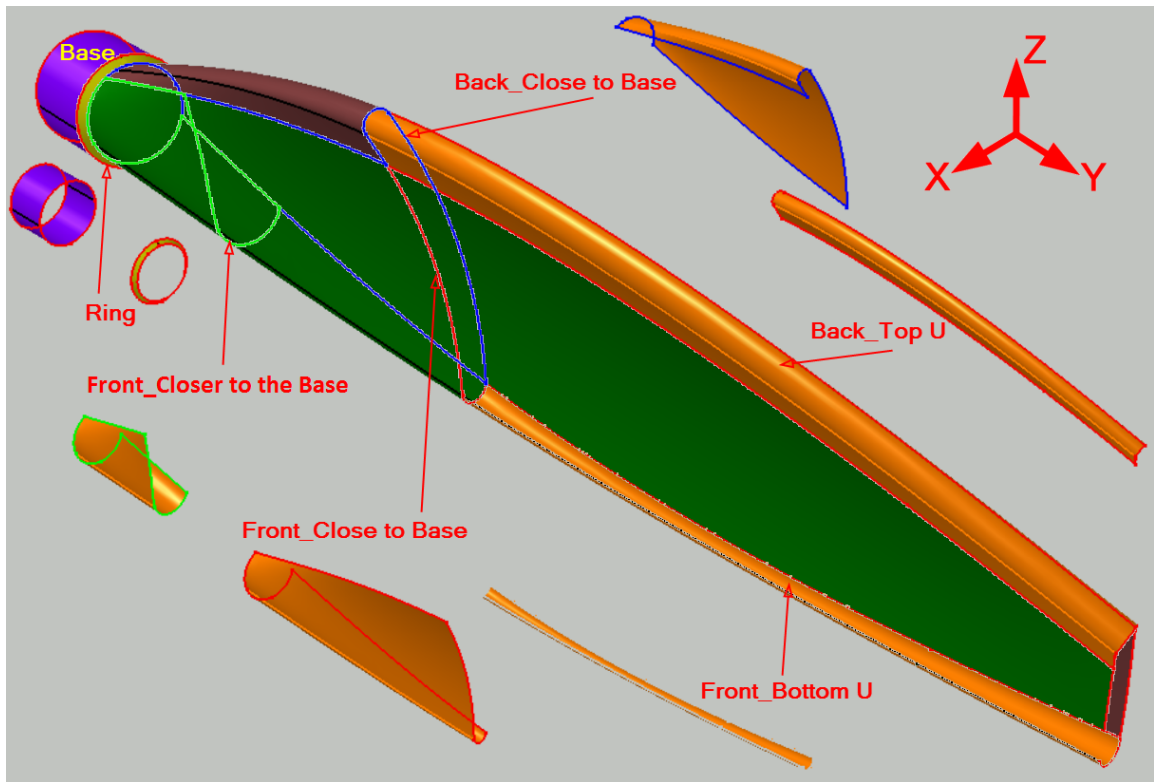


Figure 76: the Sub_BLSs inside the main BLSs

Table 26 reports the number of the layers and their laminate stacking sequence, including the original and the added ones in BMP16 for each “Boundary”. For all the boundaries, lamina numbers 1-8 remain similar to the base design, $[\pm 45/90/0]:s$. In three boundaries (“Base,” the “Ring” and the “Front_Closer to the Base”), the layers are stacked from 9-20 presented by $[(\pm 45/0):s]:2$. In the other three boundaries (the “Front_Close” to “Base,” “Back_Close to Base,” and “Back_Top U”), the layers are stacked from 9-14 presented by $[\pm 45/0]:s$, and the Boundary around the “Front_Bottom U” six layers of plies with zero degrees is stacked up from 9-14.

In other words, from the layers forming each lamina, the first ply in the “Front,” “Back,” “Ring,” and “Base” boundaries with 45°, located at Lamina 1 next to the mold. Similarly, all other Laminas (from 2-20) are formed by the next Ply in row for each lamina. In that case, Lamina 1-8 consists of four main BLSs (“Back,” “Ring,” “Front,” and “Back”); Lamina 9-14 consists of six Sub_BLSs (from “Base” toward the end of propeller: the “Base”,, “Ring,” “Front_Close to Base,” “Back_Close to Base,” “Front_Bottom U” and “Back_Top U”) and Lamina 15-20 consists of three Sub_BLSs the “Base,” “Ring,” and “Front_Closer to the Base”).

The thickness of each unidirectional CFRP lamina is equal to 0.25mm. The mechanical properties of the unidirectional lamina (AS4) are presented in Table 10.

Table 26: Boundary conditions and their LSS

Row	Boundary	Laminate Stacking Sequence (LSS)		Stacked up from Lamina No.	Laminate Thk. (mm)
		Base design	Added in BMP16		
1	Base BLS	[±45/90/0]:s	[(±45/0):s]:2	1 to 20	5
2	Ring BLS	[±45/90/0]:s	[(±45/0):s]:2	1 to 20	5
3	Front BLS	[±45/90/0]:s	-	1 to 8	2
4	Back BLS	[±45/90/0]:s	-	1 to 8	2
5	Front_Close to Base	[±45/90/0]:s	[±45/0]:s	1 to 14	3.5
6	Back_Close to Base	[±45/90/0]:s	[±45/0]:s	1 to 14	3.5
7	Front_Closer to the Base	[±45/90/0]:s	[(±45/0):s]:2	1 to 20	5
8	Front_Bottom U	[±45/90/0]:s	[0]:6	1 to 14	3.5
9	Back_Top U	[±45/90/0]:s	[(±45/0):s]:2	1 to 14	3.5

The 2D scaleless stacking sequences in the isometric view and the right view are presented at the top and bottom of Figure 77. The right view is selected from the plane that the sides are the minimum distance from each other. As shown, there is no overlap between the layers in the “Front_Bottom U” and” Boundary” of the other areas.

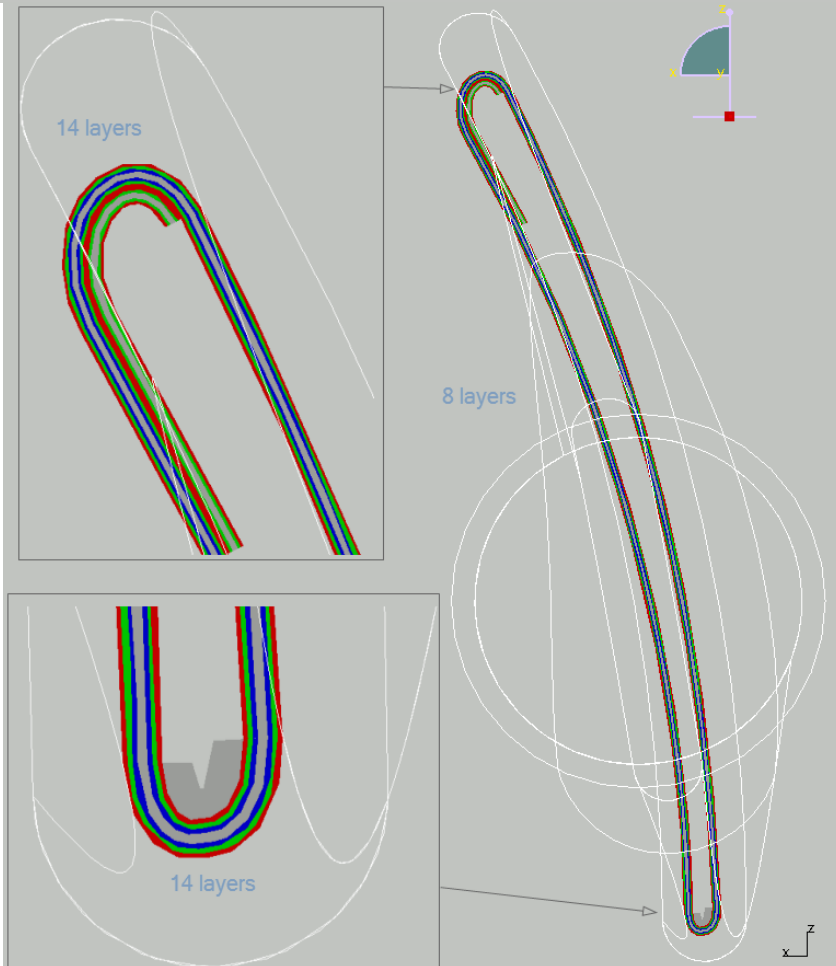
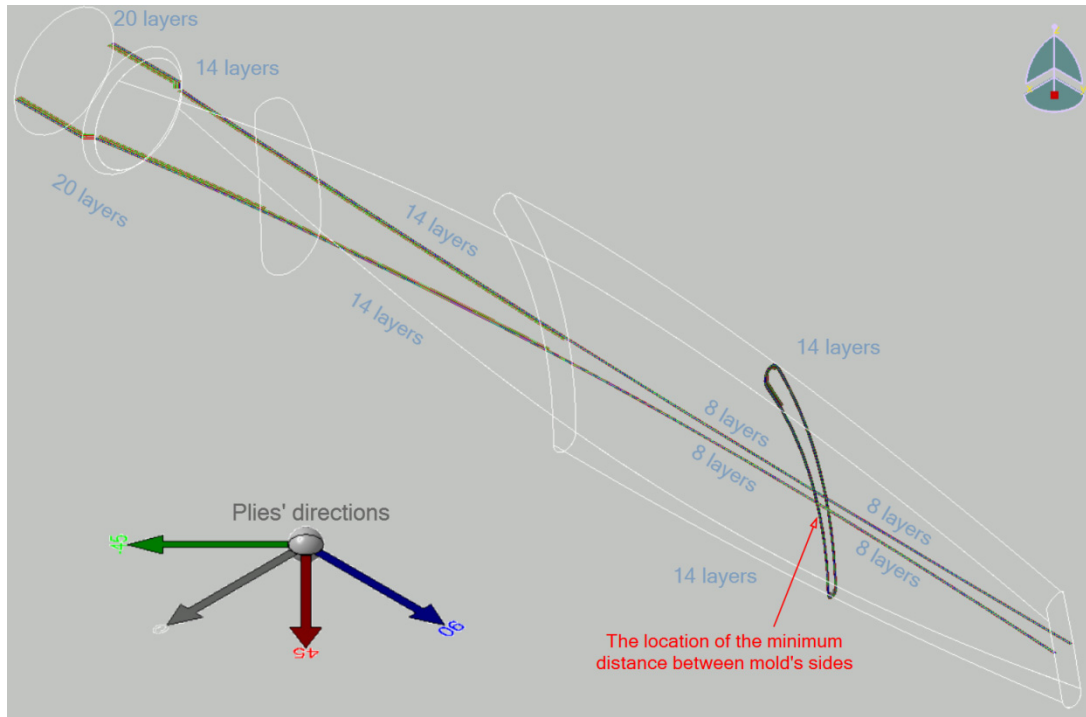


Figure 77: Isometric view (top) and the right view (bottom) of the 2D stacking sequences

The top view of the 2D scaleless stacking sequences is presented in Figure 78, which is presented on the XY plane. In addition, the four boundaries and the minimum distance area are shown in detail. The plies' directions are -45° in light green, 0° in gray, 45° in red, and 90° in navy blue.

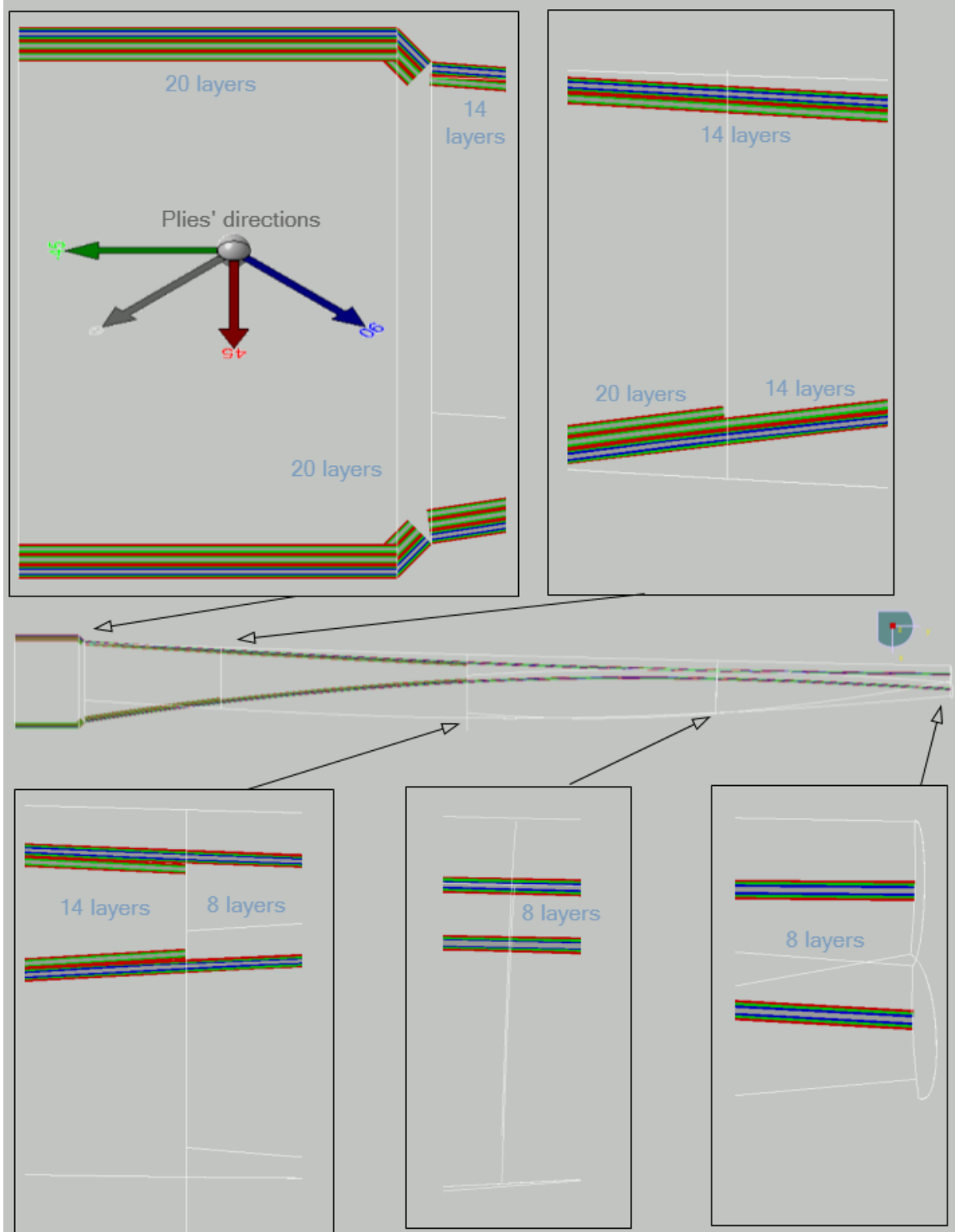


Figure 78: Top view of the 2D stacking sequences on the XY plane

Two Ply Groups for two rosettes were assigned for BMP16. The rosette for the “Base” and the “Ring” is shown in Figure 79 (a), and the rosette for the “Front” and the “Back” is illustrated in Figure 79 (b). For both rosettes, the plies with 90° are aligned with the perimeter of the cross-section parallel to the “YZ” plane. In the figure, more points are selected to show the plies’ directions in different points. The composite angle symbols for layers with 90° are displayed in Figure 79 (c) to show the results.

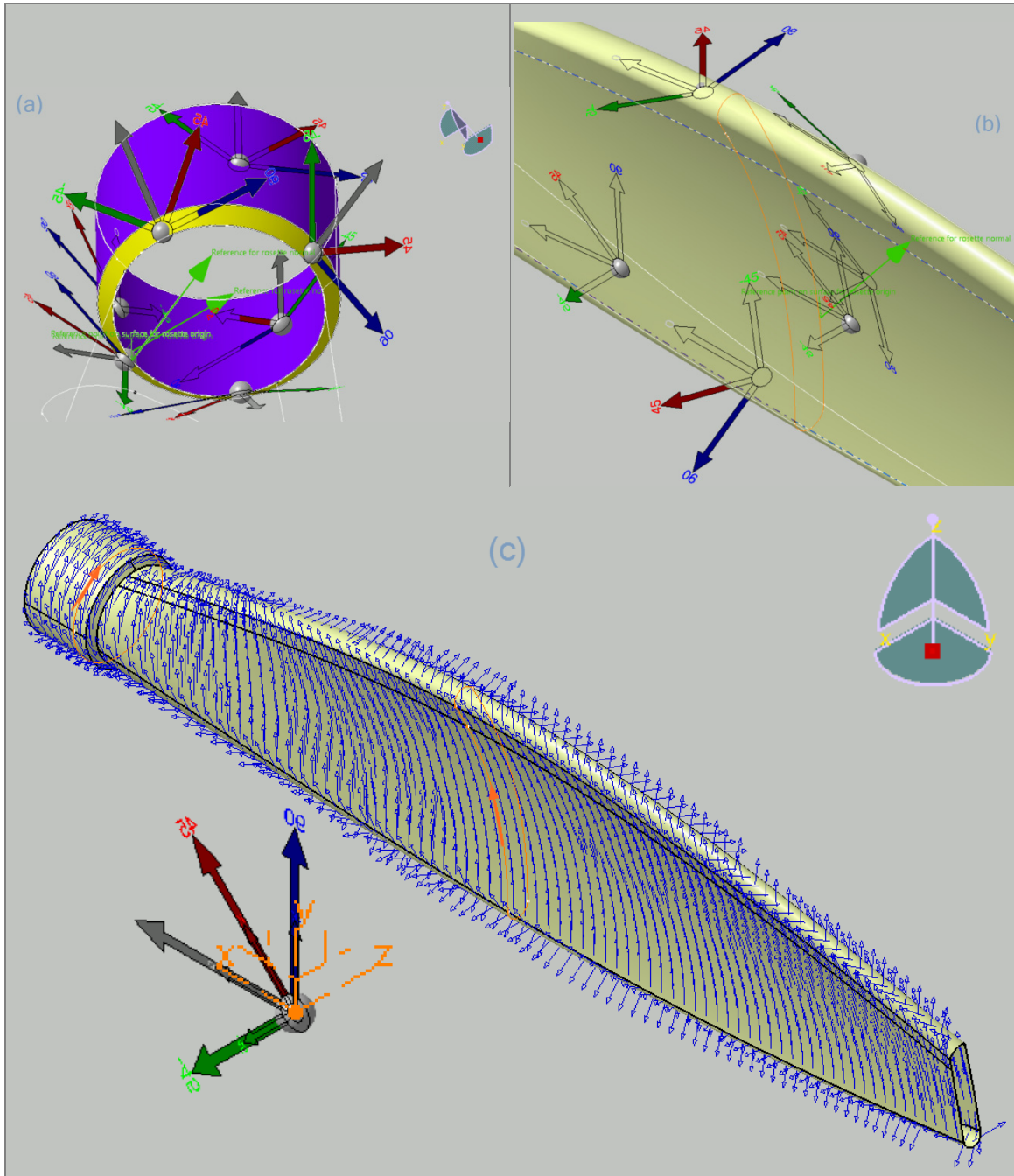


Figure 79: (a) Rosettes for the Base and Ring, (b) rosette for the Front and Back, (c) the composite angle symbol for plies with 90°

For more accurate results, one may decide to define extra rosettes in the “Front” and “Back” BLS. In that case, for each area, one Ply Group should be assigned.

8.3.2 *Imposing loads and restraints*

The current composite design consists of one complete “Join” for all the BLSs, two “Ply Groups” for two rosettes, five main boundaries for the main BLSs and another five boundaries for the Sub_BLSs. As discussed in 5.3.1, the symmetrical option was selected; therefore, the “Reference Surface” and the laminate mid-plane surface are coincident.

Figure 80 shows the mesh and loading conditions applied to BMP16. The Advanced Surface Mesh is used to mesh the “Join” mostly by parabolic triangle meshes (TR6). The global meshing parameters are element mesh sizes equal to 10mm, and the tolerance for the Automatic Mesh Capture 0.1mm. The mesh size in the boundaries edges and the “Ring” is 2.5 millimetres, and the mesh sizes on the “U” shape on the propeller's top and bottom are 5 millimetres. Other mesh sizes in the area inside the boundaries are in yellow, shown in Figure 80.

In addition, the loading conditions are shown in Figure 80. First, the “Base” is clamped shown in pink. Second, A uniform pressure load equal to 0.05 (MPa) is applied to the “Front” illustrated with the orange arrows, and third, the “Rotation Force” is assigned to the propeller about the “X” axis equal to 2000 (rpm) is shown in yellow.

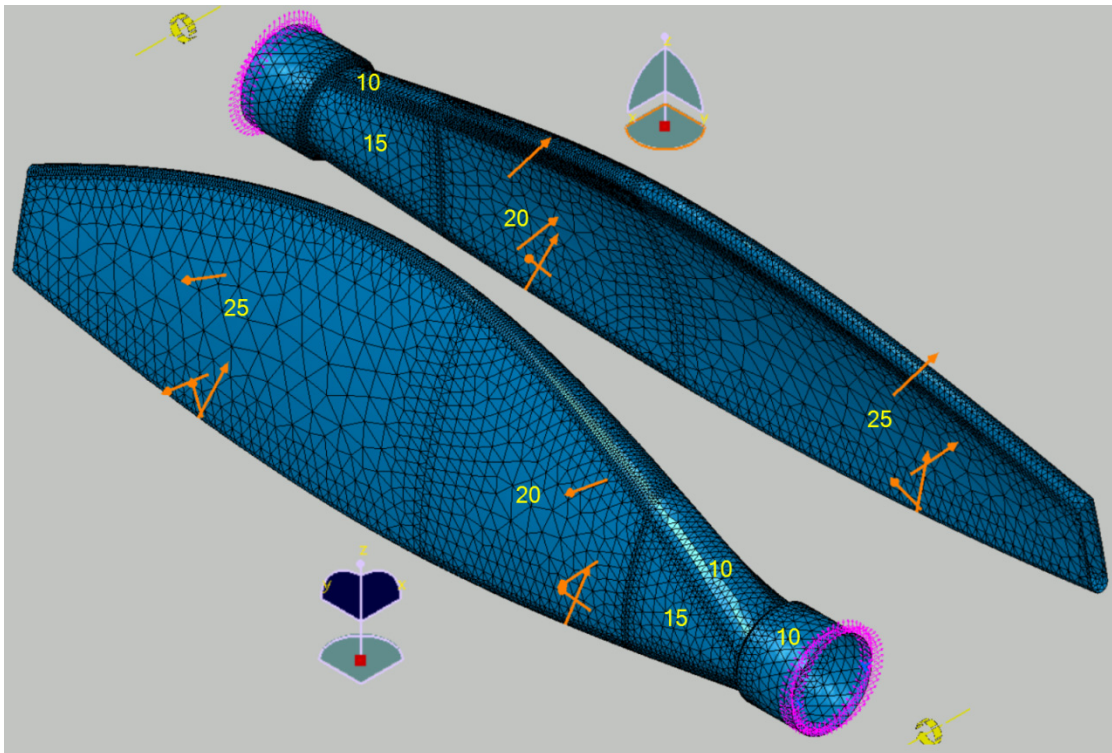


Figure 80: the element meshes and loading conditions in different Bboundaries

8.3.3 Results and discussion

When a global mesh size of 5mm was employed, the number of the elements increased by a factor of four. The method to assign different mesh sizes are as follows:

1. Use the ADD/Remove Constraints icon (discussed in 5.2.1) and select all the boundaries.
2. Use the imposed elements in the “edition tools” toolbar to add the boundaries’ edges and assign the desired mesh sizes.
3. Use the Remesh Domain tools to assign the mesh sizes for all the boundaries.
4. Use the Edit Mesh tools and the Global Optimization while selecting its features.
5. Control the mesh quality to ensure all the elements are of good quality.

If some elements are in displayed in red, they should be modified using the Edit Mesh tools manually. Note that the elements with yellow colour can be acceptable. The total number of elements is 13630; only three are quadrangle parabolic type (QD8), as shown in the quality reports in Figure 81.

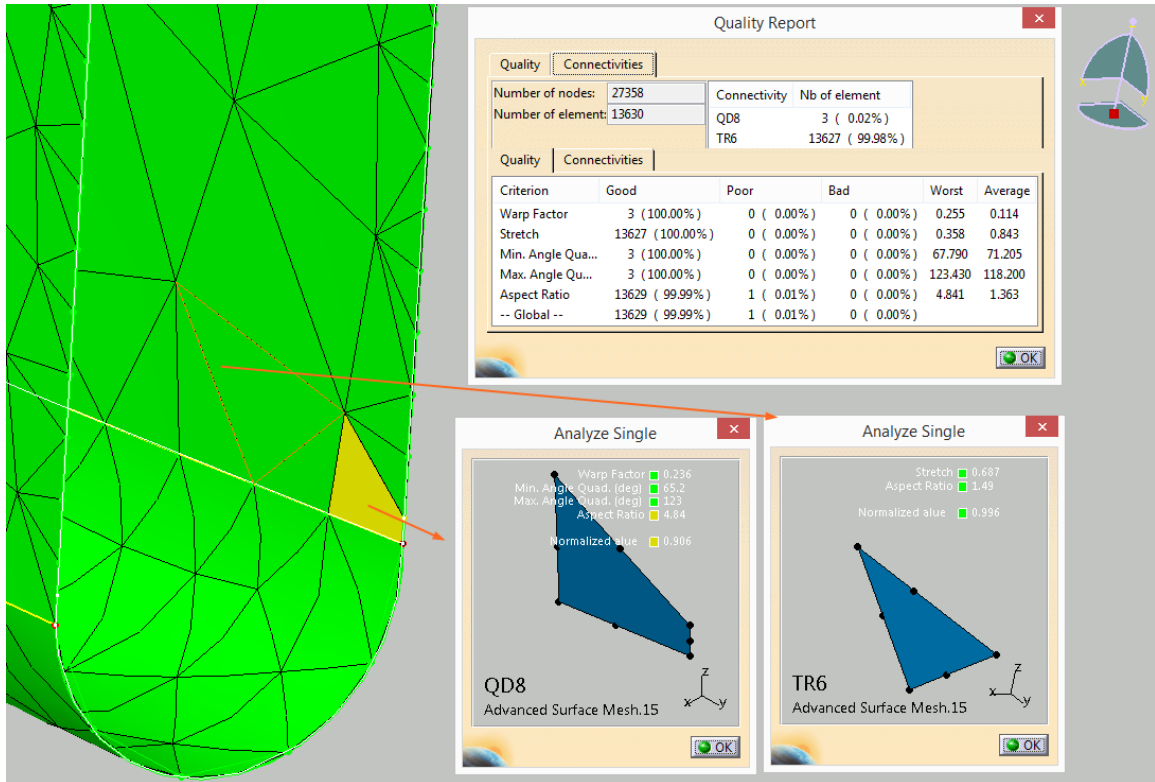


Figure 81: Mesh types used on BMP16: TR6 and QD8

Table 27 reports the maximum IRF factor presented by the CATIA FEA Solver. As shown, All IRF values are less than unity, implying that none of the elements will fail for the suggested problem case. Only to exemplify the Tsai-Hill criterion discontinuous

colour map report extracted from the CATIA software, the Plies forming the Lamina 1 and Lamina 20 in which all the plies are 45° are shown in Figure 82. In addition, the same information for Lamina 10 and Lamina 17 with -45° and 0° are shown in Figure 83. Note that the boundaries around each lamina match the assigned colour for corresponding directions (45° in red, -45° in light green, and 0° in gray).

Table 27: RSF values for lamina 1-20

Row	Lamina No.	IRF	Row	Lamina No.	IRF
1	Lamina 1	0.994	11	Lamina 11	0.208
2	Lamina 2	0.602	12	Lamina 12	0.236
3	Lamina 3	0.779	13	Lamina 13	0.266
4	Lamina 4	0.311	14	Lamina 14	0.299
5	Lamina 5	0.176	15	Lamina 15	0.337
6	Lamina 6	0.441	16	Lamina 16	0.373
7	Lamina 7	0.247	17	Lamina 17	0.123
8	Lamina 8	0.243	18	Lamina 18	0.132
9	Lamina 9	0.185	19	Lamina 19	0.548
10	Lamina 10	0.193	20	Lamina 20	0.628

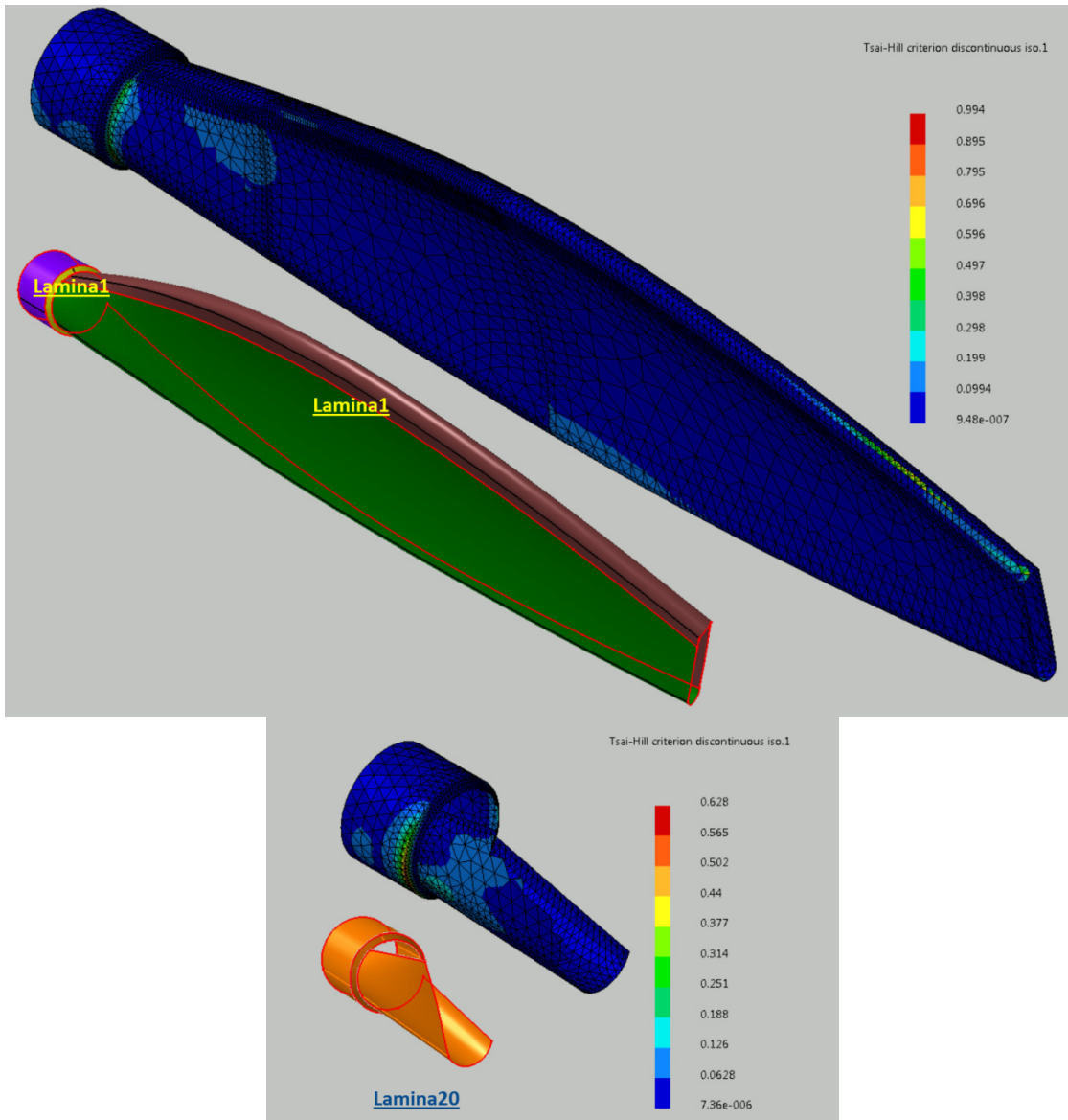


Figure 82: Tsai-Hill criterion discontinuous color map report for the elements in Lamina1 (top) and Lamina 20 (bottom)

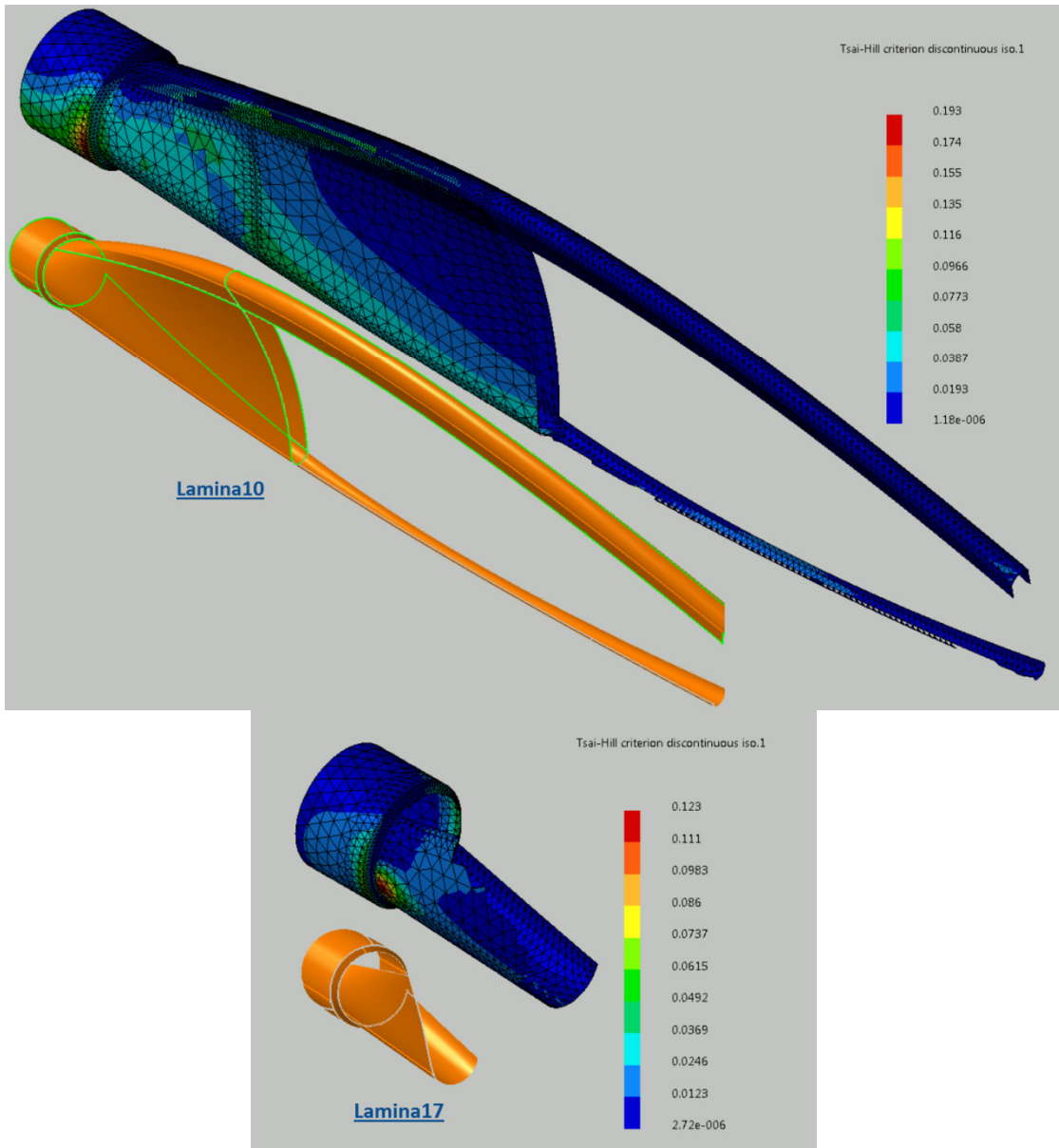


Figure 83: Tsai-Hill criterion discontinuous color map report for the elements in Lamina10 (top) and Lamina 17 (bottom)

8.4 BMP17 (Loading acting on an Aircraft Wing in Pull up Maneuver)

In BMP17, another applied engineering problem is analyzed. The maximum deflection of an aircraft wing is predicted using the geometry, composite parameters, and loading condition proposed in [68], [69], [70], [71]. As in BMP16, the aim of this benchmark problem is to describe the thought process behind using CATIA in modelling and analyzing a complicated, yet real engineering component. The study's main focus is to model roughly 1000 plies associated with an actual aircraft wing. In the process, some important yet nontrivial issues in the present problem are discussed and elaborated upon.

8.4.1 Modelling the geometry and the composite parameters

Figure 84 shows the general components of an aircraft wing consisting of the bars shown in navy blue and the spars shown in brown inside the external shell. The external shell consists of the airfoil shells shown in yellow, the “Stiffener Shell.Top” in orange and “Stiffener Shell.Bottom” in pink.

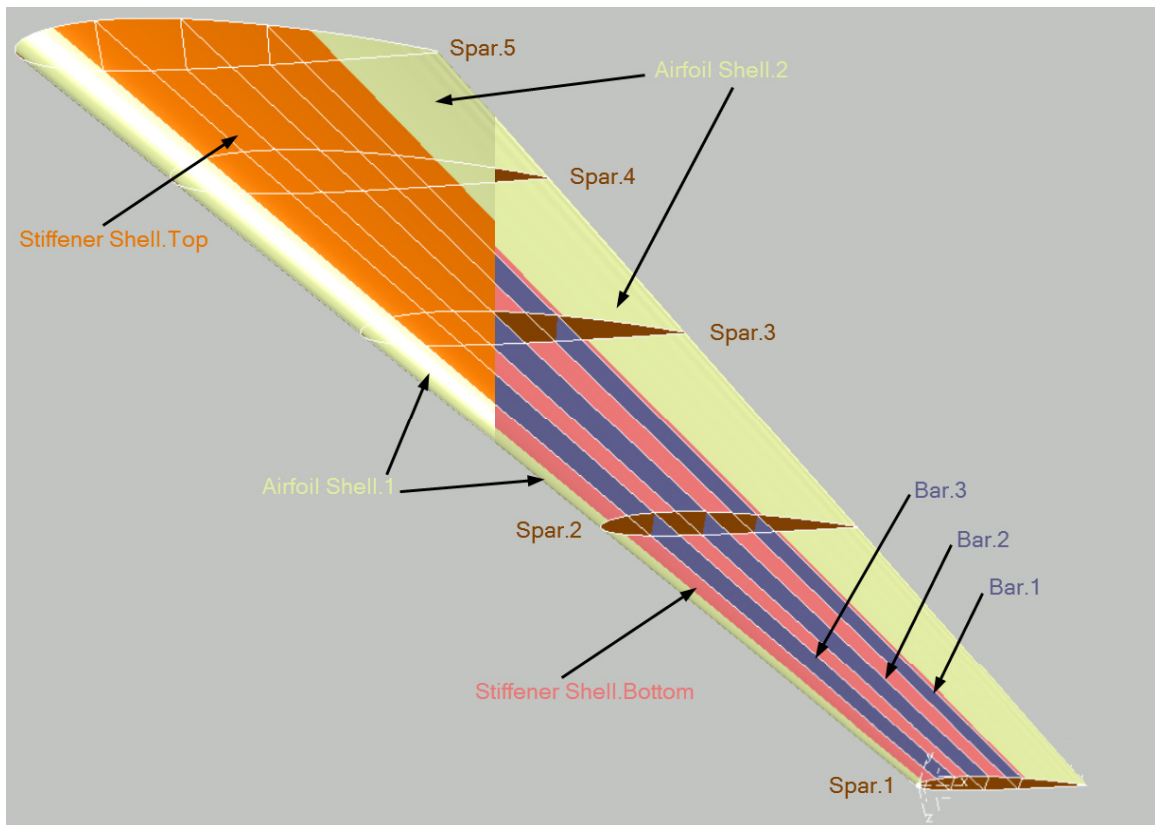


Figure 84: Airfoil Wing's compartments

Figure 85 illustrates the “Top Curve”, “Bottom Curve”, and the “Spar.1” constrained by lines parallel to the “x” and “y” axis. Sixty guide points are used to model the geometry of “Spar.1” as shown in Table 28. “Point.A” (see row31 in Table 28) is the origin of the LCS (Local Coordinate System” used to model the aircraft wing shown in

Figure 85. The points reported in row 1 and row 61 are identical, shown as “Point.B” in Table 28.

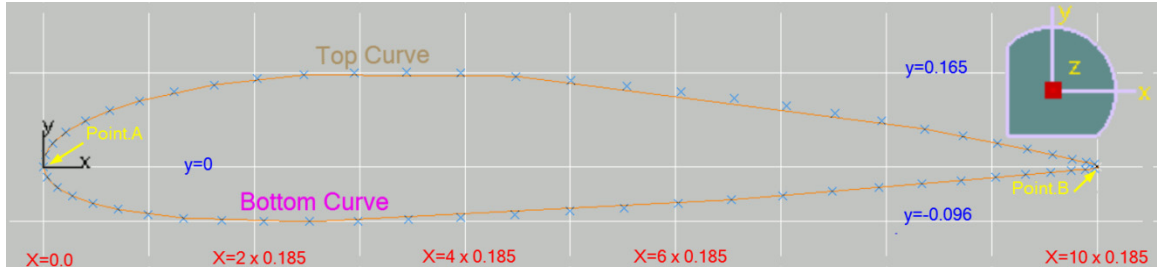


Figure 85: the guide points, Top Curve, Bottom Curve, and LCS for “Spar.1”

Table 28: The guide points used to model the “Spar.1”

Top Curve				Bottom Curve			
Row	X (m)	y (m)	z (m)	Row	x (m)	y (m)	z (m)
1	1.850	0.000	0.000	32	0.007	-0.019	0.000
2	1.845	0.004	0.000	33	0.024	-0.036	0.000
3	1.830	0.007	0.000	34	0.051	-0.051	0.000
4	1.805	0.013	0.000	35	0.086	-0.064	0.000
5	1.771	0.021	0.000	36	0.131	-0.075	0.000
6	1.727	0.030	0.000	37	0.184	-0.084	0.000
7	1.675	0.041	0.000	38	0.245	-0.090	0.000
8	1.614	0.053	0.000	39	0.313	-0.094	0.000
9	1.546	0.066	0.000	40	0.387	-0.096	0.000
10	1.471	0.079	0.000	41	0.467	-0.096	0.000
11	1.390	0.093	0.000	42	0.552	-0.095	0.000
12	1.304	0.106	0.000	43	0.641	-0.092	0.000
13	1.213	0.119	0.000	44	0.733	-0.089	0.000
14	1.120	0.130	0.000	45	0.828	-0.084	0.000
15	1.023	0.141	0.000	46	0.924	-0.078	0.000
16	0.926	0.150	0.000	47	1.020	-0.072	0.000
17	0.829	0.157	0.000	48	1.115	-0.065	0.000
18	0.733	0.163	0.000	49	1.208	-0.058	0.000
19	0.637	0.165	0.000	50	1.299	-0.051	0.000
20	0.545	0.164	0.000	51	1.385	-0.044	0.000
21	0.458	0.160	0.000	52	1.466	-0.037	0.000
22	0.375	0.153	0.000	53	1.542	-0.031	0.000
23	0.299	0.143	0.000	54	1.610	-0.025	0.000
24	0.230	0.130	0.000	55	1.672	-0.019	0.000
25	0.169	0.115	0.000	56	1.725	-0.014	0.000
26	0.117	0.098	0.000	57	1.769	-0.010	0.000
27	0.074	0.079	0.000	58	1.804	-0.007	0.000
28	0.040	0.060	0.000	59	1.829	-0.005	0.000
29	0.017	0.040	0.000	60	1.845	-0.003	0.000
30	0.003	0.020	0.000	61	1.850	0.000	0.000
31	0.000	0.000	0.000				

Table 29: the “Point.A” and “Point.B” for all the spars

Wing spars	Point	X	Y	Z	Scale Factor	Point	X	Y	Z
Spar.1	A1	0	0	0	1	B1	1.850	0	0.000
Spar.2	A2	-3.148	0	-3.688	1.753	B2	0.095	0	-3.688
Spar.3	A3	-6.295	0	-7.375	2.505	B3	-1.660	0	-7.375
Spar.4	A4	-9.443	0	-11.063	3.258	B4	-3.415	0	-11.063
Spar.5	A5	-12.590	0	-14.750	7.011	B5	-5.170	0	-14.750

The geometries of other wing spars (from “Spar.2” to “Spar.5”) are generated by translating “Point.A1” from “Spar.1.” Then, by applying the scale factor, other wing spars are generated. Table 29 presents different points (“Point.A1” to “Point.A5”) for all

the spars. Also, “Point.B1” to “Point.B5” are presented only for additional checking purposes.

Figure 86 illustrates the location of different components such as “Rib”, “Stiffener”, and “Airfoil Shell”. Moreover, in this figure, the “Point.A” and “Point.B” in the “Spar.1” are displayed. The ribs are along the white lines extended from “Point.A1” and “Point.B1” to “Point.A5” and “Point.B5.” The span between these two is separated into ten equal areas, each 0.185 m.

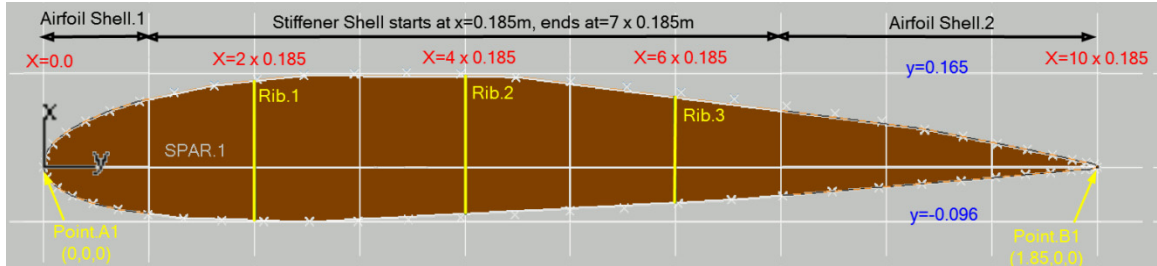


Figure 86: The location of different ribs, stiffeners and Airfoil shells in "Spar.1"

Twelve “Joins” were employed. Five for spars, three for bars and four for the shell. The shell consists of “Airfoil Shell.1,” “Airfoil Shell.2,” and two for the “Stiffener Shells,” one for each top and the bottom. Twelve boundaries for all the “Joins” are generated. Eight “Joins” for the spars and bars and one for all the shells. The number of Joins was reduced to nine “Joins” to simplify the meshing process.

The Joins and the stacking sequence directions are opposite. The Joins’ direction are outward from the aircraft wing, implying that the laminates are stacked up inside the wing. The laminates for some of these parts are identical; however, different rosettes resulted from perpendicular parts, and separated Boundaries resulted in the increase of the number of Joins.

The laminate for the bars, spars, and the “Stiffener Shells” is [(0/(45):2/90/):s]:100. Simultaneously, the laminate defined for “Airfoil Shell.1” and “Airfoil Shell.2” is [(0/+30/90/-30/0):s]:100. In total, eight Ply Groups for the eight Joins (“Spar.1” is excluded), three rosettes for the bars, spars, and the shells, 100 laminae resulting from 1000 plies in all the BLSs are modelled for the composite parameters. The thickness of each unidirectional CFRP lamina is equal to 0.21mm. The mechanical properties of the unidirectional lamina (AS4) are presented in Table 30.

Table 30: Lamina and Core properties (extracted from [69])

Property (Unit)	Woven Fabric
Young's modulus E_1 (MPa)	55000
Young's modulus E_2 and E_3 (MPa)	55000
Poisson's Ratio ν_{12} and ν_{13}	0.04
Shear Modulus G_{23} (MPa)	4300
Shear Modulus G_{12} and G_{13} (MPa)	1000

Figure 87 (a) shows the rosettes assigned to the bars, spars, and the top and bottom sides of the airfoil shells. To show the results, the composite angle symbols for layers with 90° are shown in Figure 87 (b). It is important to note that 90° directions on the top and bottom curves are opposite since the “Join” consists of both curves. If the Joins on the top and bottom are assigned to the Ply Group separately, the directions follow the “y” direction of LCS (Local Coordinate System). For better accuracy, one may define more rosettes between two spars. If that strategy is followed, for each area, one Ply Group should be created and assigned.

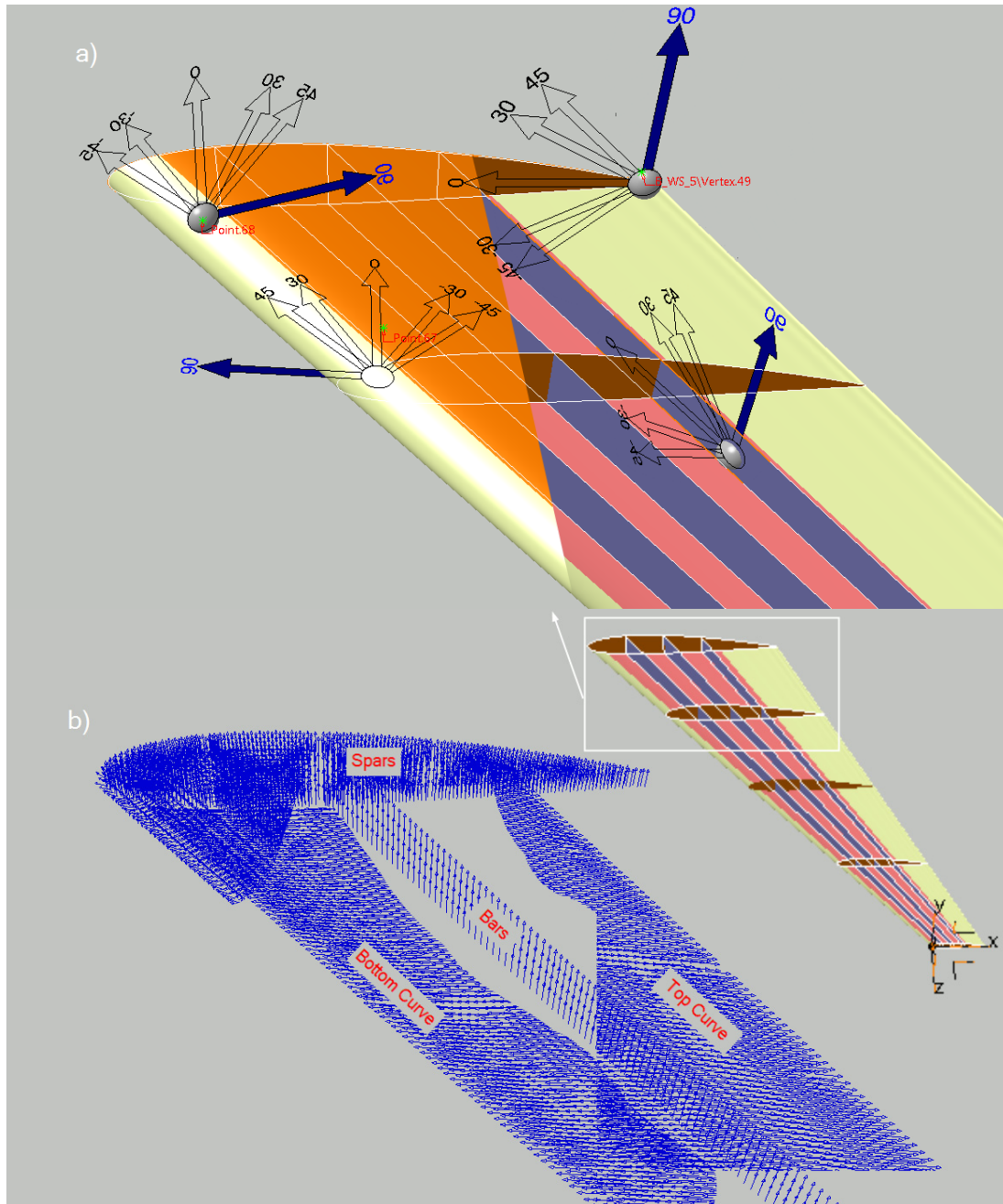


Figure 87: (a) Rosettes for the Bars, Spars, Top Curve and the Bottom Curve (b) the composite angle symbol for plies with 90°

8.4.2 Imposing loads and restraints

The composite design under consideration consists of eight complete Joins for all the BLSs (Base Laminate Surfaces). The symmetrical option was selected; therefore, the Reference Surface and the laminate mid-plane surface are coincident. Figure 88 illustrates the mesh and the loading conditions for BMP17. The “Spar.5” at the fuselage is clamped, shown by the blue icons, and a uniform pressure load equal to 33.6 (kPa) is applied to the shell on the bottom curve shown in red arrows (also shown in Figure 85).

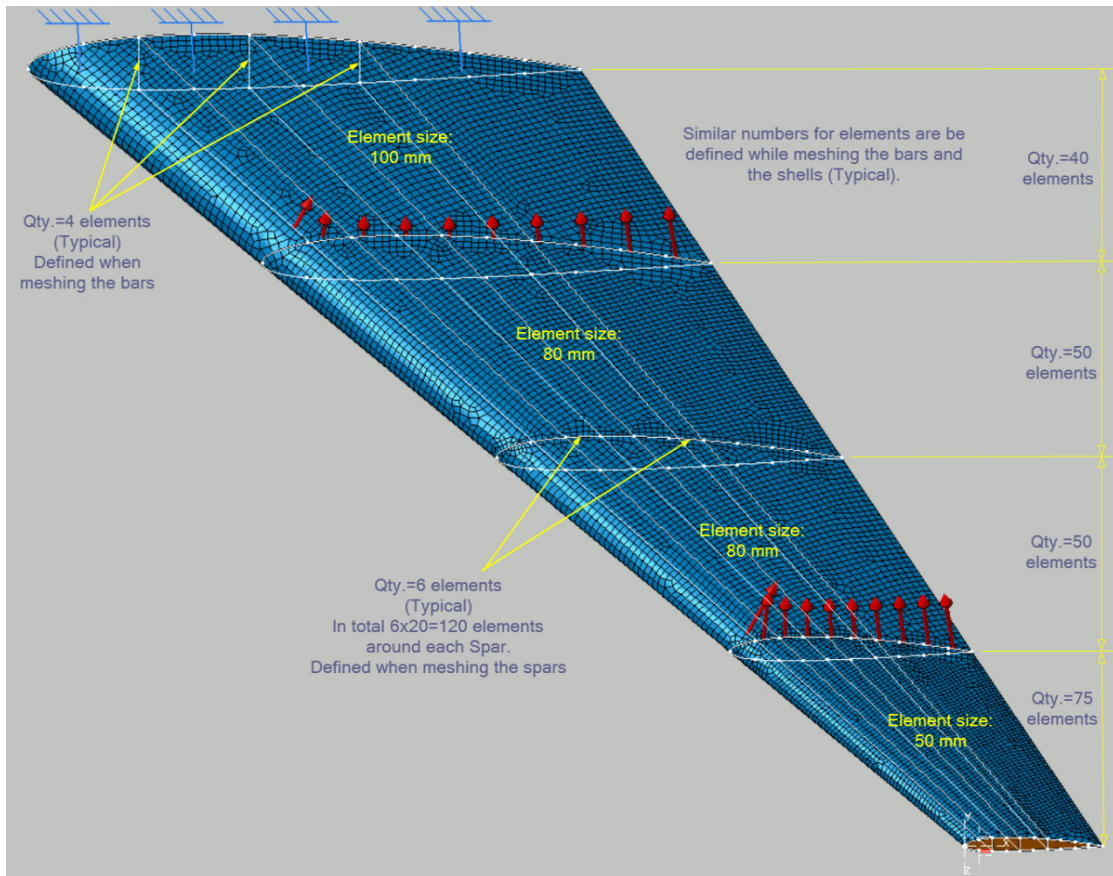


Figure 88: the element meshes and loading conditions in different Boundaries

The Advanced Surface Mesh is employed to mesh the Joins mostly by global quadrangle parabolic mesh of size 75 mm. The tolerance value for the Automatic Mesh Capture is set to 1mm. The mesh was created for each Join as presented below.

- 1- The three bars were meshed while the shared edges between spars and the bars were consisting of four elements, and the shared edges between the bars and the shells were assigned 75, 50, 50, and 40 elements from “Spar.1” to “Spar.5” (see Figure 88). The mesh sizes between spars were assigned a 75 mm using the Mapped quads method in the Remesh Domain tools. The Imposed Elements tool in the Edition Tools toolbar was used to add the Boundaries’ edges and assign the correct number of elements.

- 2- Four spars were meshed while the shared elements between spars and bars were already assigned. They should be defined as constrained using ADD/Remove Constraints (as discussed in 5.2.1). Six elements were assigned to each section of the curve around the shell, as shown in Figure 88. The mesh sizes for each spar were assigned 100 mm, 200 mm, 200 mm, and 300 mm from “Spar.2” to “Spar.5” using the Front trias method in the Remesh Domain tools.
- 3- The shell was meshed while the shared elements between the shell with the spars and bars were already assigned. They should be defined as constrained using ADD/Remove Constraints. Afterwards, those edges parallel to the spars and bars were assigned the same number of elements. The mesh sizes for each area between spars were 50 mm, 80 mm, 80 mm, and 100 mm from “Spar.1” to “Spar.5” using the Front quads method in the Remesh Domain tools as shown in yellow (see Figure 88).

8.4.3 Results and discussion

It is always challenging to create a good mesh for complex geometries. CATIA software meshing tools were discussed in 5.1, and some steps are introduced in 8.3.3. There are other tools and toolbars that one can use to create a satisfactory mesh. For all the components, Mesh Part Statistics tools should be used for a quick review of the quality of the mesh. The general rule is that the green colored elements are recommended, the yellow elements can be acceptable to some extent, and the red elements are deemed unacceptable. Sometimes the user may need to eliminate extra edges or clean small holes using Edit Simplification tools (see Figure 89, in which the orange lines on the left are eliminated and the results are shown below on the right) or Clean Holes in the Edition Tools toolbar. In addition, there are other tools that show the unmeshed domains, duplicate nodes, and duplicate elements.

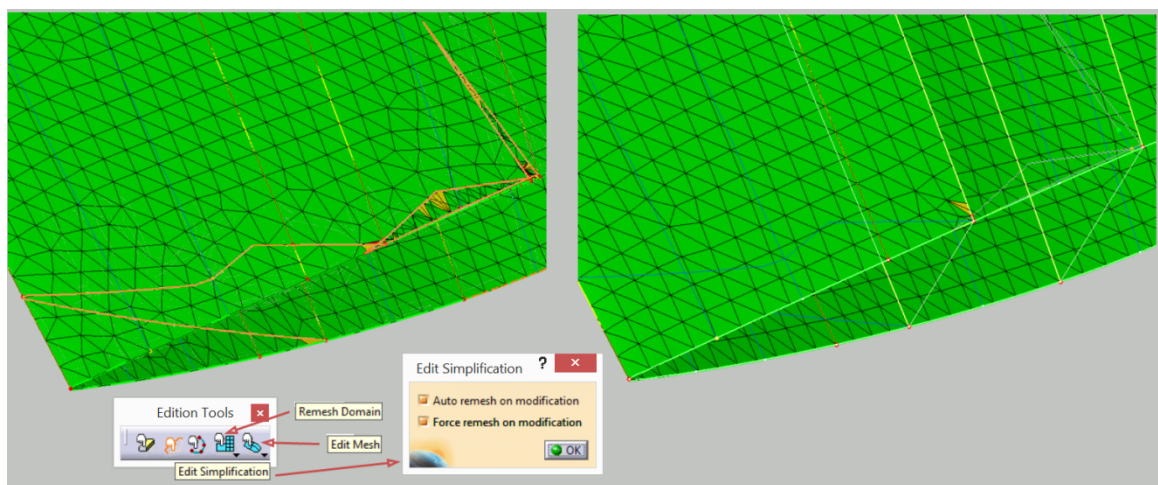


Figure 89: Edit Simplification tools used for eliminating the extra edges

The “Worst Element Browser” with the ability to Autofocus on individual elements is provided in the Quality Analysis tools in the Mesh Analysis Tools toolbar. Using this

feature, once features are selected, the Edit Mesh tools can be used to modify (add or erase some node connections) the unsatisfactory elements. In any case, the node connections can be changed by not selecting the “Propagate to neighbour domains” option. Figure 90 illustrates how to modify the red element captured from one of the spars. The Mesh Part Statistics tools were used to review the mesh quality at each stage. The Edit Mesh tool was employed to modify the red elements and transform them to the yellow ones by adding a new node connection in stage1, and then erasing an old node connection in stage2 resulting in a modified green desirable element.

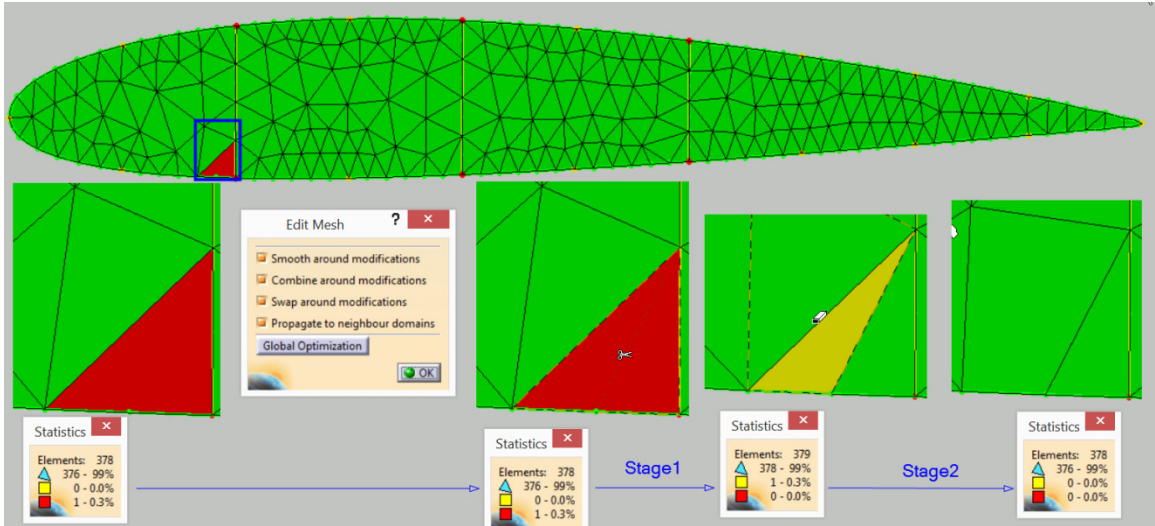


Figure 90: Using different tools to modify one sample of unsatisfactory elements, stages from bottom left to right

Figure 91 shows a sample of the final arrangement of the nodes at the edges and corners located in more than one component. The nodes 1063, 1071, 11833, 11821, 1275, and 1225 are simultaneously located on different components.

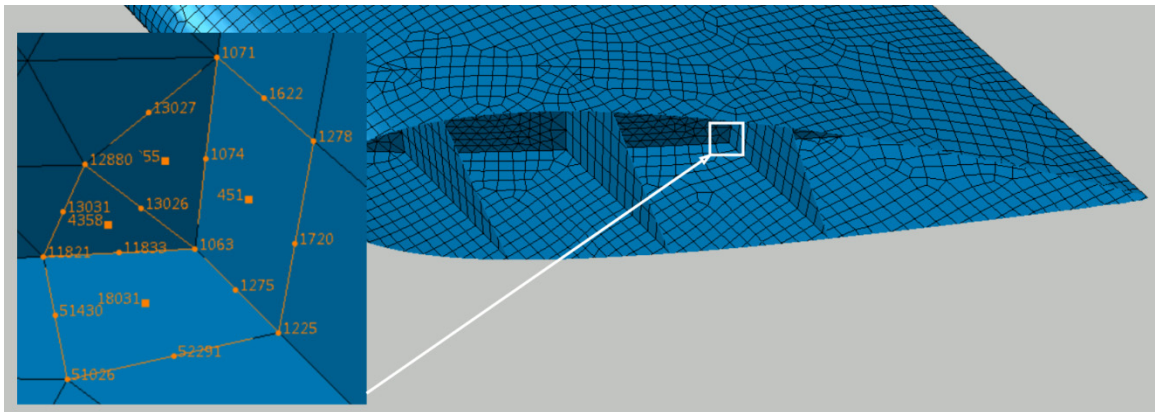


Figure 91: A sample of the nodes at the edges and corners located in different components

The Quality Report of the conducted mesh is shown in Figure 92. It is reported that the total number of elements is 25507, in which less than seven percent of them are triangular parabolic type (TR6) and the rest are quadrangle parabolic type (QD8).

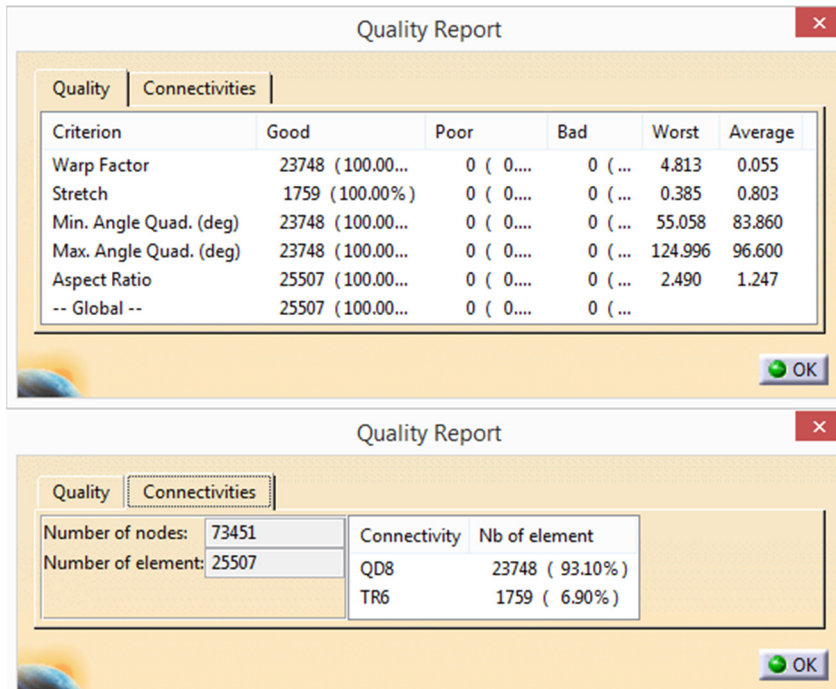


Figure 92: Quality Report for BMP17

Although the results (in terms of accuracy) are not compared with any references, they seem to be reasonable. Experimental and numerical data are mainly proprietary in nature and therefore missing from the public domain. The maximum deflection at the tip of the 14.75m long wing is 1.81m, and the compression strains elongation in each ply is less than the allowable value (0.5%). Also, the CATIA results are matched with the ABAQUS outcomes presented in the video tutorial [71], with less than 15% differences. Considering that the discretizations are not identical and the details are not presented in [71], the agreement is reasonable. Figure 93 shows the deflection of the aircraft wing.

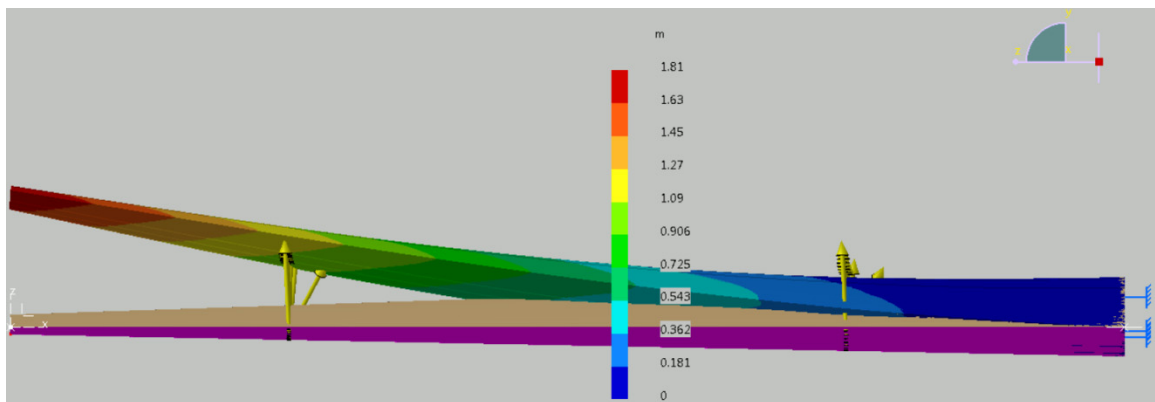


Figure 93: the deflection of the aircraft wing

CHAPTER NINE:

CONCLUSIONS and DISCUSSION

This study addresses and documents the techniques to model the composite parameters in CATIA software for FEA purposes. CATIA developers considered a very limited and basic attempt to assess the FEA features of the software for composites. The focus of the thesis is to rectify this serious shortcoming of CATIA through systematically exploring the neglected task of the developers. In reference to the validation of CATIA's Native FEA Solver, the Benchmark Problems (BMPs) suggested here are mostly new and not available in the public domain. Chapter one introduced four major topics discussed through the study:

1. The relationships and links between the nine chapters,
2. the workflow for the modelling, analyzing, validating, and the corresponding complementary information for composites finite element design.
3. the topics and comments for all the seventeen BMPs, and
4. some challenging issues that were confronted in this study.

Chapters Four and Five discussed the basic principles to generate the composite parameters and the steps towards employing CATIA FEA Solver. As previously mentioned, the study was simulation-based and involved progressively more complex problems. Simple theoretical BMPs were investigated in Chapter Six, the intermediate level BMPs in Chapter Seven, and the practical engineering BMPs in Chapter eight. A total of seventeen benchmark problems were selected to represent a variety of geometric types, laminate stacking sequences, loading conditions, and restraints.

The benchmark problems considered in Chapter Six were compared with the Classical Lamination Theory (CLT). In addition, two well-known FEA solvers (ABAQUS and ANSYS) were employed for the BMPs where the Lamination Theory was not applicable. For each of them, an RCT was generated. ANSYS results are also employed in BMP1, 2, 3, 5, 6; however, they were not presented in the RCT as their results are identical to ABAQUS software.

The comprehensive results comparing the CATIA FEA Solver with the CLT method or ABAQUS and ANSYS software are presented in Table 31. The BMPs with the same comparison results are listed in the same group columns. Beneath each group, two columns (one for the CLT method and one for the other software) are displayed. Table 31 uses symbols to show the extent of correlation between the CATIA predictions with the CLT and the other two software. The legend at the bottom of the table is presented to define the symbols used in the table.

In BMPs 1,2,3,5, and 6, the results extracted from the CLT method or ABAQUS and ANSYS software are in compliance with the CATIA FEA solver. The discrepancies of stress value are almost zero percent. The “Totally in compliance” sign (☑) is used in front of each parameter at least once, showing that the CATIA FEA Solver presenting the acceptable results. It is important to note that all the Observed Results listed in the rows are different, yet the concepts are identical.

It is not easy to use the CLT method to compare the deformed shape, the displacement values, and the “Total Strain Energy” of the proposed BMPs. That is why in front of mentioned parameters, the faded “No comparison has been conducted” sign (⊗) is shown in the table. ABAQUS and ANSYS, however, are employed to validate these types of results and are indicted in the table.

In BMPs 7, 8, 9, and 10, the “In compliance mostly” sign (✓)—differences between 2% to 8%—is added in front of stress components reminding the reader that the modelling of the twisting load and the circular cross-section causes some issues; however, all the FEA solvers were in compliance with each other. Similarly, in BMP4 and BMP11, discussed in 6.5 and 6.12, it was shown that the modelling considerations are the cause of being partially in compliance and the “Partially in compliance” sign (⊙) in front of stress components are presented in red.

Table 31: Benchmark problems validation BMP1 to BMP11

Benchmark Problem:	BMP1, 2, 3, 5, 6		BMP4		BMP7, 8		BMP9		BMP10		BMP11	
Verification Methods (CATIA vs. ...)	Classical Laminate Theory (CLT)	ABAQU S & ANSYS	CLT	ABAQU S & ANSYS	CLT	ANSYS	CLT	ANSYS	CLT	ABAQU S	CLT	ABAQU S
Observed Results												
Deformed Shape	⊗	☑	⊗	☑	⊗	☑	⊗	☑	⊗	☑	⊗	☑
von Mises Stresses	☑	☑	⊙	☑	✓	☑	✓	☑	✓	☑	⊙	☑
Tensor component (Stress and Strain)	☑	⊗	⊙	⊗	✓	⊗	✓	⊗	✓	⊗	⊙	⊗
Principle Values (Stress and Strain)	☑	☑	⊙	☑	✓	⊗	✓	⊗	✓	☑	⊙	☑
Deformation (Norm, principle directions)	⊗	☑	⊗	☑	⊗	☑	⊗	☑	⊗	☑	⊗	⊗
Strain Energy	⊗	☑	⊗	☑	⊗	☑	⊗	☑	⊗	☑	⊗	⊗

Legend:
 "No comparison" has been conducted ⊗
 The errors of stresses value in all the Layers are less than 2% or the comparison was acceptable ☑ (Totally in compliance).
 The errors in the ply with a maximum value of stresses are between 2% to 8% it is illustrated with ✓ (In compliance mostly).
 The errors in the ply with a maximum value of stresses are between 9% to 17% it is illustrated with ⊙ (Partially In compliance).

In Chapters Seven and Eight, the comparison data for BMPs 12, 13, 14, and 15 were extracted from published references. Even for the isotropic materials, the thermal-buckling analysis employing CATIA software was not discussed in the literature [1], while it is validated for the composite materials in BMP14. The benchmarks BMP16 and BMP17 in Chapter Eight were presented only to raise some advanced guidelines for modelling, meshing, and analyzing two complex engineering problems.

In general, CATIA FEA Solver provides reliable comparative tools in reference to the fundamental benchmark problems investigated in this study. Regarding the types of engineering problems CATIA FEA Solver can be employed for, it is shown that within the linear elastic region of the stress-strain graph, CATIA FEA Solver is as accurate as other more advanced commercial solvers such as ABAQUS and ANSYS.

It is recommended to conduct a separate yet detailed study on the role of rosette's implementations applied to complex surface geometries. This is a critical issue, especially in the corners when the rosette's normal is changing direction. All the CAD/FEA computations were carried out using CATIA V5-6R2018 but with some minimal changes are applicable to other software releases.

Some final remarks are in order. Clearly, no comparison with the experimental tests is undertaken since the focus of this study was to explore the functionality of CATIA FEA Solver in modelling and analyzing composite materials. In this context, only employing the existing analytical/numerical solutions has been sufficient. Furthermore, professional CATIA users and students can easily and safely employ the Native Solver for composite materials using the material presented in the thesis.

REFERENCES/BIBLIOGRAPHY

- [1] N. Zamani, "Composites Catia v5 "Native" FEA, video 1, Nader G Zamani," 17 11 2020. [Online]. Available: <https://www.youtube.com/watch?v=EHrks0gGxrM&list=PLN2zL9OVZWP3OQRLPmrdFEodLQNsVWrBG>.
- [2] "COE General Discussion," the community of experts of "Dassault Systèmes" solutions, [Online]. Available: <http://www.coe.org/p/fo/et/topic=107>. [Accessed 6 4 2021].
- [3] J. REDDY, MECHANICS of LAMINATED COMPOSITE PLATES and SHELLS Theory and Analysis, Boca Raton London New York Washington, D.C.: CRC Press, 2004.
- [4] "A history of CATIA by former CEO of Dassault Systèmes Francis Bernard," Dassault Systèmes, 5 2003. [Online]. Available: <http://ridwan.staff.gunadarma.ac.id/Downloads/files/8426/history-catia.pdf>. [Accessed 2 4 2021].
- [5] "DISCOVER CATIA," DASSAULT SYSTEMS, [Online]. Available: <https://www.3ds.com/products-services/catia/>. [Accessed 12 05 2021].
- [6] "HG Insights," HG Insights, [Online]. Available: <https://discovery.hgdata.com/product/catia>. [Accessed 2 4 2021].
- [7] "Is the future of composites up in the air?," PES Media (Production Engineering Solutions), [Online]. Available: <https://www.pesmedia.com/aluminium-matrix-composite-alvant-21072020/>. [Accessed 12 5 2021].
- [8] "Elfini Solver Verification," Dassault systèmes, [Online]. Available: http://catiadoc.free.fr/online/CATIAfr_C2/elfugCATIAfrs.htm. [Accessed 19 05 2021].
- [9] IEEE Standard for System, Software, and Hardware Verification and Validation, IEEE, 2016.
- [10] N. Zamani, "Composite FEA Analysis with CATIA V5," [Online]. Available: <https://www.youtube.com/playlist?list=PLN2zL9OVZWP3OQRLPmrdFEodLQNsVWrBG>. [Accessed 2 10 2021].
- [11] "Solver Computation," Dassault Systèmes, [Online]. Available: http://catiadoc.free.fr/online/estug_C2/estugfq0500.htm. [Accessed 16 05 2021].
- [12] "Design Validation using CATIA Finite Element Analysis," TECHNIA ADDNODE GROUP, [Online]. Available: <https://www.technia.com/blog/design-validation-using-catia-finite-element-analysis/>. [Accessed 16 05 2021].

- [13] "CATIA V5 Training-ELFINI Structural Analysis," Dassault Systems, 2009.
- [14] "An Introduction to CATIA Embedded FEA," TECHNIA UK, 10 2 2016. [Online]. Available: <https://www.youtube.com/watch?v=1bXFcGoUhwk>. [Accessed 12 5 2021].
- [15] "CATIA V5 Training-ELFINI Structural Analysis.PDF," Dassault Systems, 2009.
- [16] ASTM, "Composite Standards," ASME, 03 04 2021. [Online]. Available: <https://www.astm.org/Standards/composite-standards.html>. [Accessed 03 04 2021].
- [17] "Open-Hole Compressive Strength Composite Test Machine for ASTM D6484," tensomax, [Online]. Available: <https://tensomax.com/product/astm-d6484-d6484m-14-standard-test-method-for-open-hole-compressive-strength-of-polymer-matrix-composite-laminates>. [Accessed 05 2021].
- [18] "Boeing 787 Passes Incredible Wing Flex Test," Wired, [Online]. Available: <https://www.wired.com/2010/03/boeing-787-passes-incredible-wing-flex-test/>. [Accessed 13 4 2021].
- [19] ASTM_D3039M, Standard Test Method for Tensile Properties of Polymer Matrix Composite Materials, ASTM Standards, 2017.
- [20] ASTM_D7264, Standard Test Method for Flexural Properties of Polymer Matrix Composite Materials, ASTM standards, 2015.
- [21] v. Goyal, "Mechanics of Composite Materials - Lecture 2E: Stress, Strain, Constitutive Law," 24 2 2021. [Online]. Available: <https://www.youtube.com/watch?v=3IfNlIDWL4s&t=6197s>. [Accessed 12 4 2021].
- [22] ANSYS.com, "Ansys Help," Ansys software, [Online]. Available: <https://ansyshelp.ansys.com/>. [Accessed 01 12 2020].
- [23] D. Alvarez and Feito, "Modelling Composite Materials: ANSYS & ACP," 03 01 2016. [Online]. Available: https://ppd-docdb.fnal.gov/cgi-bin/RetrieveFile?docid=2179&filename=Tuesday%2005%20-%20CompositesWorkshop_ANSYS_DAF.pdf&version=1. [Accessed 02 04 2021].
- [24] "Analysis of Composite Materials with Abaqus (Dassault Systèmes)," [Online]. Available: https://www.3ds.com/fileadmin/PRODUCTS-SERVICES/SIMULIA/Resources-center/PDF/2018-SAoE-Composites_Modeling_Capabilities_of_Abaqus.pdf. [Accessed 4 4 2021].
- [25] H. Farid, "Composites Modeling Capabilities of Abaqus," aventec.com, 3ds.com, Aventec Inc. 327 Renfrew Drive, Suite 301 Markham, ON L3R 9S8 Canada.
- [26] ASTM_D3878, Standard Terminology for Composite Materials, ASTM Standards, 2019.

- [27] A. Tabiei and W. Zhang, "Composite Laminate Delamination Simulation and Experiment: A Review of Recent Development," *NEW YORK: ASME reviews, Applied mechanics*, vol. 70 (3), no. NEW YORK: ASME, 01 05 2018.
- [28] J. Williams, "The science and technology of composite materials," Australian Academy of Science, [Online]. Available: <https://www.science.org.au/curious/technology-future/composite-materials>. [Accessed 08 12 2021].
- [29] I. M. Daniel and O. Ishai, *Engineering mechanics of composite materials*, 2nd ed, New York: Oxford University Press, 2006.
- [30] S. P. Rawal and JOM, "Metal-matrix composites for space applications," *Springer-Verlag*, vol. 53 (4), pp. 14-17, 2001-04.
- [31] Honickman and H. Noah, *Development of hybrid composite co-pultruded structural members*, PhD Dissertation, University of Windsor, 2014.
- [32] R. M. Jones, *MECHANICS OF COMPOSITE MATERIALS*, second edition, Philadelphia,: Taylor & Francis, Inc., 1999.
- [33] T. D. Barry, "STUDY OF A POST STRUCTURE IN COMPOSITE MATERIAL FOR RAIL LINE ELECTRIFICATION ASSEMBLY - Máster en Diseño Avanzado en Ingeniería Mecánica," 2011. [Online]. Available: <http://bibing.us.es/proyectos/abreproy/70301>. [Accessed 06 04 2021].
- [34] A. E. H. Love, *A Treatise on the Mathematical Theory of Elasticity*, Cambridge: University Press, 1906.
- [35] G. Kirchhoff, *Über das Gleichgewicht und die Bewegung einer elastischen Scheibe, für die reine und angewandte Mathematik*, ger, 40, 51-88, 1850.
- [36] M. E. Tuttle, *Structural Analysis of Polymeric Composite Materials*, New York: Taylor & Francis Group, 2003.
- [37] A. A. Baker, S. Dutton and D. Kelly, *Composite materials for aircraft structures*, Virginia: American Institute of Aeronautics and Astronautics, 2004.
- [38] A. Cherniaev, ""Lecture #4 , Laminate Analysis," Windsor University, October, 14, 2020.
- [39] J. M. Whitney, *Structural Analysis of Laminated Anisotropic Plates*, Basel: Technomic Publishing AG, 1987.
- [40] A. K. Kaw, *Mechanics of composite materials*, Boca Raton: Taylor & Francis, 2006.
- [41] A. Cherniaev, "Lecture #5 , Buckling of Composite Structure," Windsor University, November, 04, 2020.
- [42] D. S. Cairns, J. F. Mandell, M. E. Scott and J. Z. Maccagnano, "Design and manufacturing considerations for ply drops in composite structures," *Composites. Part B, Engineering*, vol.

30 (5), no. OXFORD: Elsevier Ltd, pp. 523-534, 1999.

- [43] N. Tiwari, "Introduction to composite, Quasi Laminate Composite: Part-I," Indian Institute of Technology Kanpur, National Programme on Technology Enhanced Learning (NPTEL), 08 April 2018. [Online]. Available: https://www.youtube.com/watch?v=8-B1Nw-RYSc&list=PLSGws_74K01-bdEEUEIQ9-obrujIKGEhg&index=70. [Accessed 30 10 2020].
- [44] "Module 5: Laminate Theory, Lecture 17: Laminate Constitutive Relations," Indian Institute of Technology Kanpur, National Programme on Technology Enhanced Learning (NPTEL), [Online]. Available: https://nptel.ac.in/content/storage2/courses/101104010/lecture17/17_7.htm. [Accessed 02 11 2020].
- [45] M. C. Niu, *Composite Airframe Structures*, Hong Kong: Conmilit Press, 2010.
- [46] A. Cherniaev, "Lecture #6 , Buckling of Composite Structure," Windsor University, November, 11, 2020.
- [47] "Generative Structural Analysis - Failure Criteria," Dassault Systèmes, [Online]. Available: http://catiadoc.free.fr/online/CATIAfr_C2/estugCATIAfrs.htm. [Accessed 17 04 2021].
- [48] L. Jasmine, "Composite Strength and Failure Criteria," O Neal, 2015. [Online]. Available: <https://slideplayer.com/slide/5687695/>. [Accessed 17 11 2020].
- [49] A. Cherniaev, "Lecture #6 , Strength criteria for composites," Windsor University, November, 11, 2020.
- [50] *catia v5 composites*, Wichita, KS: national institution for aviation research Wichita State University, 2012.
- [51] Nader Zamani, *CATIA V5 FEA Tutorials*, release 21, SDC Publications, 2012.
- [52] ASTM_D5448, *Standard Test Method for Inplane Shear Properties of Hoop Wound Polymer Matrix Composite Cylinders*, ASTM Standards, 2016.
- [53] ASTM_D6507, *Standard Practice for Fiber Reinforcement Orientation Codes for Composite Materials*, ASTM international, 2016.
- [54] P. K. Mallick, *Fiber-reinforced composites : materials, manufacturing, and design*, New York: M. Dekker, 1946.
- [55] T. Sofi, S. Neunkirchen and R. Schledjews, "Path calculation, technology and opportunities in dry fiber winding: a review," *Advanced Manufacturing: Polymer & Composites Science*, vol. 4 No.3, no. Taylor & Francis, p. 57–72, 2018.
- [56] O. Hjørungdal, "Carbon fiber subsea sphere, filament winding by Windtec.no," Ola Hjørungdal, 28 10 2009. [Online]. Available:

- <https://www.youtube.com/watch?v=2H3tkaFxHTE>. [Accessed 16 9 2021].
- [57] E. J. Barbero, *Finite Element Analysis of Composite Materials using Abaqus*, NW: CRC Press, 2013.
- [58] E. J. Barbero, "Example 3.6 How to to model a ply drop off using 3D deformable shell and partitions in Abaqus," *wva250*, 14 6 2020. [Online]. Available: <https://www.youtube.com/watch?v=JYYNgfaC2pM&t=412s>. [Accessed 24 9 2021].
- [59] S. Maleki, M. Tahani and A. Andakhshideh, "Transient response of laminated plates with arbitrary laminations and boundary conditions under general dynamic loadings," *Archive of applied mechanics (1991)*, vol. 82 (5), no. Berlin/Heidelberg: Springer-Verlag, pp. 615-630, 2012-05.
- [60] W. Palm III, *Mechanical Vibrations*, Wiley Press, 2006.
- [61] D. Inman, *Engineering Vibrations*, 4th Edition, Pearson Publishing, 2014.
- [62] H. C. Tsai, "Modal superposition method for dynamic analysis of structures excited by prescribed support displacements," *Computers & structures*, vol. 66 (5), no. OXFORD: Elsevier Ltd, pp. 675-683, 1998.
- [63] H. Ramezani and N. G. Zamani, "Linear Dynamics Finite Element Simulation Using Virtual Parts in Catia v5," in *LACCEI International Multi-Conference for Engineering, Education, and Technology "Industry, Innovation, And Infrastructure for Sustainable Cities and Communities"*, Jamaica, 24-26 July 2019.
- [64] B. D. Agarwal, *Analysis and performance of fiber composites*, Sai Printo Pack Pvt. Ltd. Delhi : WILEY, 2015.
- [65] C. S. Babu and T. Kant, "REFINED HIGHER ORDER FINITE ELEMENT MODELS FOR THERMAL BUCKLING OF LAMINATED COMPOSITE AND SANDWICH PLATES," *Journal of thermal stresses*, vol. 23 (2), no. LONDON: Informa UK Ltd, pp. 111-130, 2000-03-01.
- [66] W. Zhao and R. K. Kapania, "Buckling analysis of unitized curvilinearly stiffened composite panels," *Composite structures*, vol. 135, no. OXFORD: Elsevier Ltd, pp. 365-382, 2016-01.
- [67] C. Mittelstedt, "Closed-form buckling analysis of stiffened composite plates and identification of minimum stiffener requirements," *International journal of engineering science*, vol. 46 (10), no. OXFORD: Elsevier Ltd, pp. 1011-1034, 2008.
- [68] V. Goyal and L. Wang, "#ABAQUS TUTORIAL: COMPOSITE WING DESIGN - PART I - THEORY," #ABAQUS Finite Element Tutorial, 09 5 2021. [Online]. Available: <https://www.youtube.com/watch?v=tZJWTL0APKA>. [Accessed 11 12 2021].
- [69] V. Goyal and L. Wang, "#ABAQUS TUTORIALS: COMPOSITE WING DESIGN - PART II - PROBLEM DESCRIPTION," #ABAQUS Finite Element Tutorial, 9 5 2021. [Online]. Available:

- <https://www.youtube.com/watch?v=cIWUruwDlew>. [Accessed 11 12 2021].
- [70] V. Goyal and L. Wang, "#ABAQUS TUTORIALS: COMPOSITE WING DESIGN - PART III - CAD MODEL AND SCRIPTING," #ABAQUS Finite Element Tutorial, 09 05 2021. [Online]. Available: <https://www.youtube.com/watch?v=qjxL4a90Tf4>. [Accessed 11 12 2021].
- [71] V. Goyal and L. Wang, "#ABAQUS TUTORIALS: COMPOSITE WING DESIGN - PART IV - FINITE ELEMENT MODEL," #ABAQUS Finite Element Tutorial, 05 09 2021. [Online]. Available: https://www.youtube.com/watch?v=MTa_uT56YAU. [Accessed 11 12 2021].
- [72] M. V. Bahubalendruni and A. Raju, "Optimization of Composite Laminate Stack-up sequence Using Differential Evolution Algorithm," in *2nd Aircraft Structural Design*, London, United Kingdom, October 2010.
- [73] "Which Licenses to Perform these Scenarios?," dassault systemes, [Online]. Available: http://catiadoc.free.fr/online/CATIAfr_C2/elfugCATIAfrs.htm. [Accessed 14 12 2021].
- [74] "Deformation (physics)," wikipedia, [Online]. Available: [https://en.wikipedia.org/wiki/Deformation_\(physics\)](https://en.wikipedia.org/wiki/Deformation_(physics)). [Accessed 16 10 2021].
- [75] H. Z. J. H. X. Shen, "Dynamic response of shear deformable laminated plates under thermomechanical loading and resting on elastic foundations," no. Compos. Struct. , pp. 60, 57–66 , 2003.

APPENDICES

Appendix A Stacking Sequence Classification:

The properties of general orthotropic materials rely on plies directions and distance from the mid-plane surface. Hence, designers should pay attention to these issues. The number of possibilities to build a laminate consisting of different angles placed in individual distances (Figure 12) is enormously high.

Describing the method employed showing different stacking sequences classification

- I-1) Appendices Table A lists General, Balanced, Symmetric, Cross-Ply, Angle-Ply, Asymmetric, Antisymmetric, Special Orthotropic, Quasi-Isotropic, and Carpet Plot types of laminated stacking sequences. The characteristics of isotropic materials are added for more thorough comparison. Laminate group numbers, 1-16 are assigned, and the characteristics of each group are defined [29], [40], [31].
- I-2) For instance, from Appendices Table A, the name of the “L1” is Balanced Antisymmetric Cross-Ply tetragonal laminate [29], in which the general formulation is presented, and its relative characteristic resulted from investigating ABD matrices and from the literature [29], [40] are summarized. In the end, different types of laminate will be used in Appendices Table B to investigate coupling effects.
- I-3) All the Laminas are unidirectional composite material (AS4), in which the properties are presented in Table 10. For each laminate, one sample layup is presented. Its [ABD] matrices’ components are computed using Classical Laminate Theory (CLT). Most of the samples have zero, or 45°, or 90° since laminate composite structures are usually made of fibres with these orientations [72].
- I-4) The total thickness of each laminate is 2.5 millimetres, which is the thickness of the sample used for the tensile test [19]. Different laminates consist of 15 or 16 laminas, and the thickness of each ply is accordingly calculated and placed in the table. An almost identical number of layers are suggested (15 or 16), and it is especially vital to calculate matrix components (equation 7,8,9). To maintain the total thickness—except in the cases of L7, L9, L11, L14, L16—more than one complete laminate over each other is added to the laminates. This will not affect the results. Orientation codes are based on ASTM D65071, top reference plane method [53].

¹ More detail; Colon (:) is used instead of subscript information like number and symmetry and also, backslash (\) instead of a bar over. For example: [0/45/90\]:s is the same as [0/45/90/45/0] or [0/45/ $\overline{90}$]_s. Note that in all the above examples, the ply with 0° is the first ply.

Appendices Table A: Summary of different laminate characterization

LAM.	L1	L2	L3	L4	L5	L6	L7	L8	L9	L10	L11	L12	L13	L14	L15	L16	L17
Lay-up name	Balanced									Symmetric				Balanced	Specially orthotropic (or Symmetric Cross-Ply)	General Laminate Composite	Isotropic
	Antisymmetric			Asymmetric		Symmetric		Symmetric		Angle-Ply (n):(Odd No)	Angle-Ply (n):(Odd No)	Carpet Plot	Quasi Isotropic				
	Crossply	0<-90	Asymmetric, antisymmetric	Asymmetric	Crossply	Angle-Ply P:(even No)	Modified Quasi Isotropic	Quasi Isotropic									
	Tetragonal	Angle-Ply (P)	Tetragonal	Tetragonal	Tetragonal A11=A22	Tetragonal											
General Form	[90/0/90/0] or [±45]n	[01/02/-02/01]	[±θ]p (P:even No)	[01/02/-01/02]	[0/90]ps (P:even No)	[±θ]ps [±45]s			[0m/90/n]±45:q]s	[±θ/0]:s or [0/-θ/0/-θ/0]	[0]±45]s	[±45]ns or [0/90]ns or [0]±30/90:2]ns	[(0]±60/(90/45/0-45):s/(0/36/72/-36/-72)]	[0/90]:n s	[90/45/-30/(-45):2/0/45/(90)/2/-45/0(45)]	$A_{11}=E/(1-\nu^2)$ $D_{11}=E/(12(1-\nu^2))$	
Sample and its Characteristics	[90/0]:8	[30/60/-60/-30]:4	[±30]:8	[30/60/-30/-60]:4	[90/0]:4s	[±30]:4s	[(90/45/0/45):s/(90/45/0/45):2s	[(0):2(±45):3]s		[±30/30]3s	[0/30/60/90]:2/60/300]s	[±45/45]:3s		[0/90]:5 s	[90/45/-30/(-45):2/0/45/0(45)]	$A_{22}=v A_{11}$ $D_{22}=v D_{11}$	
Type	T5	T6	T6	T7	T1	T2	T1	T2	T2	T4	T4	T3	T3	T7	T1	T8	T0
16	0	30	30	60	90	30	90	90	0							90	
15	90	60	30	30	0	-30	-45	45	0	30	30	-45	45	-36	0	-45	
14	0	60	30	60	0	-30	0	0	45	30	60	45	-45	72	90	0	
13	90	30	30	30	90	30	45	-45	45	30	90	45	45	36	0	45	
12	0	30	30	60	90	30	45	-45	45	30	90	45	-45	0	0	45	
11	90	60	30	30	0	-30	0	0	45	30	60	-45	45	90	90	0	
10	0	60	30	60	0	-30	-45	45	45	30	30	-45	45	45	0	-45	
9	90	30	30	30	90	30	90	90	-45	30	0	45	-45	0	0	90	
8	0	30	30	60	90	30	90	90	45	30	0	-45	45	-45	90	90	
7	90	60	30	30	0	-30	45	45	45	30	30	45	-45	-45	0	45	
6	0	60	30	60	0	-30	0	0	-45	30	60	-45	45	0	0	0	
5	90	30	30	30	90	30	-45	-45	45	30	90	-45	45	45	90	-45	
4	0	30	30	60	90	30	-45	-45	-45	30	90	45	-45	90	0	-45	
3	90	60	30	30	0	-30	0	0	45	30	60	-45	-45	-60	0	-30	
2	0	60	30	60	0	-30	45	45	0	30	30	45	-45	60	90	45	
1	90	30	30	30	90	30	90	90	0	30	0	-45	45	0	0	90	
Ply THK	0.1563	0.1563	0.1563	0.1563	0.1563	0.1563	0.1563	0.1563	0.1563	0.1667	0.1563	0.1667	0.1667	0.1563	0.1667	0.1563	0.1563
T. THK	2.5	2.5	2.5	2.5	2.5	2.5	2.5	2.5	2.5	2.5	2.5	2.5	2.5	2.5	2.5	2.5	2.5
A ₁₁	197635	139267	225143	139267	197635	225143	84727	158723	182205	225143	168451	119811	119811	158723	254885	149708	A11=A22
A ₁₂	6988	65356	65356	65356	6988	65356	27717	45900	65356	65356	36172	84811	84811	45900	6988	49548	v A11
A ₁₆	0	0	0	0	0	0	0	0	0	21614	10168	-17175	17175	0	0	-6754	0
A ₂₂	197635	139267	53391	139267	197635	53391	84727	158723	96329	53391	168451	119811	119811	158723	140384	160442	A11=A22
A ₂₆	0	0	0	0	0	0	0	0	0	8135	27017	-17175	17175	0	0	-2542	0
A ₆₆	17500	75867	75867	75867	17500	75867	28505	36412	75867	75867	46684	95323	95323	36412	17500	60060	(A11-A22)/2
B ₁₁	-13418	0	0	6709	0	0	0	0	0	0	0	0	0	9679	0	-7747	0
B ₁₂	0	0	0	0	0	0	0	0	0	0	0	0	0	-1095	0	3135	0
B ₁₆	0	14253	8443	11620	0	0	0	0	0	0	0	0	0	2702	0	-5805	0
B ₂₂	13418	0	0	-6709	0	0	0	0	0	0	0	0	0	-7489	0	1478	0
B ₂₆	0	8988	3178	11620	0	0	0	0	0	0	0	0	0	3912	0	-2185	0
B ₆₆	0	0	0	0	0	0	0	0	0	0	0	0	0	-1095	0	3135	0
D ₁₁	102935	74632	117262	72535	98741	117262	39522	74085	137551	117262	103123	62402	62402	74050	134873	67409	D11=D22
D ₁₂	3640	34039	34039	34039	3640	34039	13313	22006	20739	34039	18127	44173	44173	22456	3640	24708	v D11
D ₁₆	0	0	0	823	0	2638	0	3145	4717	13659	17743	-10854	10854	-1727	0	-5002	0
D ₂₂	102935	70438	27808	72535	107128	27808	50981	95051	34119	27808	73771	62402	62402	94186	70996	96324	D11=D22
D ₂₆	0	0	0	-823	0	993	0	3145	4717	5141	17058	-10854	10854	-1893	0	-1883	0
D ₆₆	9115	39514	39514	39514	9115	39514	13723	27481	26214	39514	23602	49647	49647	27931	9115	30183	(D11-D22)/2

In order to understand the results from [ABD] matrices, it is important to compare the characteristics of all the 17 types of laminates. In the end, eight different types of stacking sequence, “Type0” representing isotropic material (L17) to “Type8,” are classified to determine the sensitivity of the CATIA software to different stacking sequences. Different effective properties resulted from $[Q(\theta)]$ in equation (7) are

expected. Thus, the coupling effect is presented in equation (11). Units for coefficients for [A], [B], and [D] matrices respectively are [MPa mm], [MPa mm²], [MPa mm³].

The review on the laminate types with similar characteristics

- II -1) A laminate or lamina has a “Tetragonal” characteristic when $A_{11} = A_{22}$ [29], which are underlined in the table. This means that rotating the loads and constraints by 90° in the plane of the laminate will cause no change in the [A] matrix results. Similarly, the transformed compliance matrix for zero and 90° are respectively $(Q_{11})_{\theta=0} = (Q_{22})_{\theta=90}$.
- II -2) When comparing L12 and L13, the components $A_{11}, A_{12}, A_{22}, A_{66}$ and $D_{11}, D_{12}, D_{22}, D_{66}$ are equal despite the different number of $\pm 45^\circ$. Therefore, they are independent of the minus or positive signs of angle. Similarly, when comparing $[Q]_{\pm\theta}$, all following components are the same: $Q_{11}, Q_{12}, Q_{22}, Q_{66}$.
- II -3) Components of [A] matrices of laminates numbers L1 and L5, L2 and L4, or L3 and L6 are the same. The components’ angles are the same despite their varying positions. In other words, only the ply’s orientation is influential when computing [A] matrices. In Appendices Table A, related components are specified with same-coloured ovals.
- II -4) Generally, in balanced laminates, A_{16} and A_{26} are zero (L1 to L9, L14, and L15.) Alternately, D_{16} and D_{26} are more complicated: The orientation and the position of each ply from the mid-plane surface define the sign of D_{16} and D_{26} (L6, L8, L9). When the negative angles are placed precisely at the same distance as the positive ones from the mid-plane surface, the D_{16} and D_{26} are zero (L1, L2, L3, L5, and L7). If they are not balanced, D_{16} and D_{26} are negative based on two factors: For example, in (L12), the negative numbers of the same angles are outnumbered by the positive ones and vice versa for (L10, L13).
- II -5) As it is presented in 3.1.2, the [A] matrix components for quasi-isotropic material have unique structure. With Laminate number 14, three different quasi-isotropic materials are stacked up, and the whole laminate is still quasi-isotropic.

It is noticed that the “Modified Quasi Isotropic” (L7) consists of two symmetric quasi-isotropic materials in which they are formed in a way that the whole laminate has a balanced combination. In regular quasi-isotropic material, [B] matrix and A_{16} and A_{26} are zero; thus, the “Modified¹” name is given to the laminate (L7). Furthermore, here, the values for D_{16} and D_{26} are both zero. When comparing the characteristics of isotropic materials with laminates numbers 1 to 16, only laminates numbers L15, L5, and L7 show similar behaviours. The first two are less likely to be used in real practical problems since

¹ The writer gives the "modified" name since no similar stacking sequence was found in the literature.

their effective Poisson ratio (the equation presented in Table 5) is too small. (Respectively 0.027, 0.035 in compared to 0.327)

Appendices Table B: [ABD] Couplings drawbacks investigation

DIFFERENT STACKING SEQUENCES		Summary of Laminate Characteristics																	
		Type1	Type2	Type2	Type3	Type4	Type5	Type6	Type7	Type8									
		Balanced Modified Quasi Isotropic Tetragonal A11=A22 [B]=0 A16=A26=0 D16=D26=0	Balanced Symmetric Quasi Isotropic Tetragonal A11=A22 [B]=0 A16=A26=0	Balanced Carpet Plot [B]=0 A16=A26=0	symmetric or Asymmetric. n:(Odd No) Tetragonal A11=A22 [B]=0 A16, A26, D16, D26 $\alpha1/n$	Symmetric Tetragonal A11=A22 [B]=0	Antisymmetric Crossply Tetragonal A11=A22 B11=-B22 A16=A26=0 D16=D26=0 Bij=0	Balanced Asymmetric, antisymmetric Angle-Ply (P) B16#0, B26#0 A16=A26=0 D16=D26=0	Balanced Quasi isotropic Tetragonal A11=A22 A16=A26=0	General Laminated Composite [B]#0, A16#0, A26#0, D16#0, D26#0									
LAM.	L7	L8	L9	L12	L10	L1	L3	L14	L16										
peoT pasodup	16	90	90	0	-	0	0	-30	-72	90									
	15	-45	45	0	-45	30	90	-30	-36	-45									
	14	0	0	45	45	60	0	30	72	0									
	13	45	-45	-45	-45	90	90	-30	36	45									
	12	45	-45	45	45	90	0	30	0	45									
	11	0	0	-45	-45	60	90	30	90	0									
	10	-45	45	45	-45	-30	0	-30	45	-45									
	9	90	90	-45	45	0	90	30	0	90									
	8	90	90	-45	-45	0	0	-30	-45	90									
	7	45	45	45	45	-30	90	30	-45	45									
	6	0	-45	-45	-45	60	0	-30	0	0									
	5	-45	-45	45	-45	90	90	30	45	-45									
	4	-45	-45	-45	45	90	0	-30	90	-45									
	3	0	0	45	-45	60	90	30	-60	-30									
	2	45	45	0	45	30	0	-30	60	45									
	1	90	90	0	-45	-45	90	30	0	90									
	Ply THK.	0.1563	0.1563	0.1563	0.1667	0.1563	0.1563	0.1563	0.1563	0.1563									
	T. THK.	2.5	2.5	2.5	2.5	2.5	2.5	2.5	2.5	2.5									
100	N/mm	6.88E-04	100%	6.88E-04	100%	7.25E-04	100%	1.68E-03	102%	6.24E-04	104%	5.11E-04	98%	6.91E-04	102%	6.95E-04	104%	7.63E-04	90%
0	N/mm	-1.99E-04	100%	-1.99E-04	100%	-4.92E-04	100%	-1.18E-03	97%	-1.24E-04	47%	-1.81E-05	100%	-8.42E-04	99%	-2.00E-04	94%	-2.35E-04	94%
0	N/mm	1.65E-20	0%	1.65E-20	0%	1.07E-36	0%	-9.08E-05	-29%	-6.43E-05	-8%	-4.20E-21	0%	1.48E-21	0%	2.87E-06	0%	7.97E-05	11%
0	N	-4.33E-20	0%	-4.36E-20	0%	3.44E-20	0%	2.85E-19	0%	-2.53E-20	0%	6.66E-05	27%	-1.11E-20	0%	-9.94E-05	-57%	1.35E-04	24%
0	N	1.15E-20	0%	1.13E-20	0%	3.31E-21	0%	-2.76E-19	0%	6.69E-21	0%	-2.98E-21	0%	3.99E-20	0%	1.49E-05	-23%	-5.12E-05	38%
0	N	-1.18E-20	0%	8.04E-21	0%	1.84E-20	0%	1.79E-19	0%	1.16E-20	0%	-2.49E-21	0%	-8.01E-05	-20%	-4.42E-05	-7%	1.41E-04	18%
0	N/mm	6.18E-21	0%	6.18E-21	0%	4.03E-37	0%	-3.41E-05	-2%	-2.41E-05	-4%	-1.57E-21	0%	5.55E-22	0%	1.08E-06	0%	2.99E-05	4%
0	N/mm	-2.23E-20	0%	-2.23E-20	0%	-1.86E-37	0%	-3.41E-05	3%	-1.37E-04	53%	-1.09E-19	0%	-1.28E-21	0%	-2.12E-06	1%	-8.12E-07	0%
37.5	N/mm	6.65E-04	100%	6.65E-04	100%	4.94E-04	100%	4.06E-04	129%	8.88E-04	108%	2.14E-03	100%	4.98E-04	103%	6.68E-04	99%	6.36E-04	89%
0	N	-5.26E-21	0%	3.02E-21	0%	2.82E-21	0%	6.70E-20	0%	-1.18E-20	0%	-9.32E-22	0%	-3.00E-05	-1.4%	-1.69E-05	-10%	5.50E-05	10%
0	N	-7.59E-21	0%	-1.69E-21	0%	-8.98E-21	0%	2.65E-20	0%	-2.23E-20	0%	-2.13E-21	0%	-2.02E-05	6%	-2.34E-05	36%	1.88E-06	1%
0	N	-4.40E-20	0%	-4.42E-20	0%	5.26E-20	0%	5.45E-21	0%	9.61E-20	0%	1.06E-35	0%	-2.43E-20	0%	2.37E-05	4%	-5.13E-05	-7%
0	N/mm	-8.14E-21	0%	-8.20E-21	0%	6.47E-21	0%	5.36E-20	0%	-4.75E-21	0%	1.25E-05	2%	-2.08E-21	0%	-1.87E-05	-3%	2.53E-05	3%
0	N/mm	2.34E-21	0%	2.39E-21	0%	-2.50E-21	0%	-5.15E-20	0%	2.58E-21	0%	-4.13E-22	0%	6.82E-21	0%	3.90E-06	-2%	-1.22E-05	5%
0	N/mm	-2.64E-21	0%	1.52E-21	0%	1.41E-21	0%	3.36E-20	0%	-5.94E-21	0%	-4.67E-22	0%	-1.51E-05	-3%	-8.47E-06	-1%	2.76E-05	4%
18.8	N	2.73E-04	100%	2.73E-04	110%	1.51E-04	108%	6.08E-04	107%	2.10E-04	322%	1.85E-04	73%	2.50E-04	114%	2.77E-04	159%	3.18E-04	57%
0	N	-6.31E-05	100%	-6.25E-05	78%	-9.01E-05	49%	-4.23E-04	91%	-1.82E-05	8%	-6.33E-06	100%	-3.04E-04	94%	-6.53E-05	100%	-8.06E-05	60%
0	N	7.29E-21	0%	-2.41E-05	-4%	-1.09E-05	-2%	-4.04E-05	-11%	-1.45E-04	-16%	-1.52E-21	0%	1.21E-20	0%	1.36E-05	2%	4.88E-05	6%
0	N/mm	-2.22E-21	0%	1.51E-21	0%	3.46E-21	0%	3.36E-20	0%	2.18E-21	0%	-4.67E-22	0%	-1.51E-05	-2%	-8.33E-06	-1%	2.64E-05	3%
0	N/mm	-4.79E-21	0%	-1.43E-21	0%	-1.76E-21	0%	1.30E-20	0%	-9.40E-21	0%	-1.07E-21	0%	-1.01E-05	1%	-1.38E-05	7%	-8.33E-07	0%
0	N/mm	-2.21E-20	0%	-2.21E-20	0%	2.63E-20	0%	2.73E-21	0%	4.82E-20	0%	5.30E-36	0%	-1.22E-20	0%	1.19E-05	2%	-2.57E-05	-4%
0	N	7.29E-21	0%	-2.41E-05	-10%	-1.09E-05	-8%	-4.04E-05	-7%	-1.45E-04	-222%	-1.52E-21	0%	1.21E-20	0%	1.36E-05	8%	4.88E-05	9%
0	N	-2.72E-20	0%	-1.72E-05	22%	-9.52E-05	51%	-4.04E-05	9%	-2.09E-04	92%	-1.04E-19	0%	-1.54E-20	0%	8.69E-06	-13%	-1.48E-06	1%
18.8	N	6.84E-04	100%	6.89E-04	104%	7.36E-04	102%	3.96E-04	111%	1.06E-03	116%	2.06E-03	100%	4.80E-04	120%	6.78E-04	101%	6.39E-04	82%
100	N/mm	6.88E-04		6.88E-04		7.25E-04		1.65E-03		6.00E-04		5.24E-04		6.76E-04		6.69E-04		8.44E-04	
0	N/mm	-1.99E-04		-1.99E-04		-4.92E-04		-1.21E-03		-2.61E-04		-1.81E-05		-8.52E-04		-2.12E-04		-2.48E-04	
37.5	N/mm	6.65E-04		6.65E-04		4.94E-04		3.15E-04		8.24E-04		2.14E-03		4.83E-04		6.74E-04		7.17E-04	
18.8	N	2.73E-04		2.49E-04		1.40E-04		5.68E-04		6.54E-05		2.51E-04		2.20E-04		1.74E-04		5.56E-04	
0	N	-6.31E-05		-7.97E-05		-1.85E-04		-4.64E-04		-2.27E-04		-6.33E-06		-3.24E-04		-6.51E-05		-1.35E-04	
18.8	N	6.84E-04		6.65E-04		7.25E-04		3.56E-04		9.11E-04		2.06E-03		4.00E-04		6.71E-04		7.77E-04	

[ABD] Couplings drawbacks

III-1) In equation (11), three different couplings extensions that bend and twist are shown in the [ABD] matrices. The effect of the Extension-Extension coupling ($A_{16}, A_{26} \neq 0$), Bend-Extension coupling ($[B] \neq 0$), and Bend-Twist coupling ($D_{16}, D_{26} \neq 0$) are the reason that different types of stacking sequence respond differently to identical loading conditions. One of the challenges for composite designers is to eliminate, reduce, or control these couplings.

III-2) To compare states' responses (strain and curvature), the same loading conditions are imposed on all the types (from 1 to 8) resulting from Appendices Table A. The strain and curvature are then computed as shown in Appendices Table B.

III-3) The effects of each coupling are investigated in a superposition problem. The strains and curvatures magnitudes show four interesting facts about the true nature of the mentioned couplings:

III-2.1) First, it is noticed that equation (40) for all sample types is computable.

$$\begin{aligned} \sum_{state=1}^4 \varepsilon_{ij} &= \varepsilon_{ij_{state\ 5}} \quad , i, j = 1, 2, 6 \\ \sum_{state=1}^4 \alpha_{ij} &= \alpha_{ij_{state\ 5}} \quad , i, j = 1, 2, 6 \end{aligned} \quad 40$$

III-2.2) Second, the values and relative percentages presented in the table shows the exact contribution for each of the loads' state, 1 to 4. For instance, Type8 "general laminated composite" percentages for curvature in the longitudinal direction are 24%, 10%, 57%, and 9%, in which the total of 100% is equal to state 5. In this context, it is important to note that imposing pure tensile loads, like suggested here, causes 24% of the bending in the transverse direction. Generally, for each type of pure tensile, shear, bending, and twisting load states 1 to 4, the responses are not relative to the imposed load and just a portion of the expected strain or curvature.

III-2.3) Third, Type1 responses for single and superposed loads are the same, and almost 100% of the strain and curvature are resulted from the relative load as illustrated in the table.


III-2.4) Fourth, the highest strain in responses to the same tensile loads and shear loads are respectively Type3 and Type5, in which they have the least resistance about these types of loads. Orientation of the fibres governs the amount of strains in this condition. As expected, Type3 has the least amount of curvature in the "xy" direction (κ_{xy}) in the State4 condition.



Appendix B Licenses needed to perform the indicated scenarios [73].

5/19/2021

Which Licenses to Perform these Scenarios?

Which Licenses to Perform these Scenarios?

 This section provides the list of the tests presented in this guide, with their descriptions, and the necessary licenses needed to perform these scenarios.

Static Analysis	This test studies...	Licenses of Analysis					
							
		GPS	EST	GAS	GDY	FMS	FMD
Space Structure on Elastic Supports	beam elements associated with springs and connections.	▲					
Cylindrical Roof Under its Own Weight	the coupling inflection/extension of a simple curved structure.	▲				▲	
Hemispherical Shell under Concentrated Load	the coupling inflection/extension of a double curved structure.	▲				▲	
Morley's Problem	the in-plane angular distortion (constant Jacobian) of plates elements.	▲				▲	
Pinched Cylinder	the convergence of the results for a coupling inflection/extension and check the non-locking.	▲				▲	
Simply-supported Square Plate	a very thin shell.	▲				▲	
Thick Beam	an in-plane distortion (non-constant Jacobian) of membrane elements.	▲				▲	
Twisted Beam	the twist of plates elements.	▲				▲	
Bending of a Beam	the bending of a 3D beam.	▲					▲
Thick Cylinder	test studies the 3D elements.	▲					▲
Rotation Loading	a beam with an applied rotation at one of its extremity.	▲					
Periodicity	the periodicity of a disc.	▲	▲				
Self-balancing	inertia forces which counter balance external loads.	▲	▲				

castiadc.free.fr/online/elfug_C2/elfugbt0001.htm

1/4

5/19/2021

Which Licenses to Perform these Scenarios?

Articulated Truss Under a Punctual Load	the displacements of an articulated truss in the plane.	▲	▲				
Center of Torsion of a Thin U-Beam	the center of torsion of a 1D thin U-beam.	▲	▲				
Thin Arc Clamped in Plane Bending	a comparison between a static case and a combination of static cases.	▲	▲				
Cylindrical Coil Spring	the rigidity of a cylindrical coil spring.	▲	▲				▲
Comparison between Bolt and Virtual Spring Bolt	a comparison between a bolt tightening connection property and a virtual bolt tightening connection property.	▲		▲			
Frequency/Modal Analysis	This test studies...	GPS	EST	GAS	GDY	FMS	FMD
Simply-supported Thick Beam	the repeated eigen values and the transverse shear effects.	▲					
Plane Vibrations of a Simply-supported Double Cross	the repeated eigen values.	▲					
Modal Analysis of a Beam with Axial Load	the case of a static preload.	▲					
Slender Beam with Variable Cross Section	the variable cross section, the plane bending and the natural frequencies.	▲				▲	
Cantilever Beam with Eccentric Point Masses	the coupling torsion/inflection.	▲					
Free Thin Square Plate	the repeated eigen values and the rigid body mode.	▲	▲			▲	
Free Vibrations of a Simply-supported Thin Square Plate	the convergence of the results.	▲				▲	
Free Vibrations of a Compressor Blade	shell elements.	▲				▲	
Cantilever Thin Square Plate	the in-plane distortion (non-constant Jacobian) of elements.	▲				▲	
Deep Simply-supported Solid Beam	3D elements.	▲					▲
Buckling Analysis	This test studies...	GPS	EST	GAS	GDY	FMS	FMD
Buckling of a Straight Beam (Out-of-Plane Buckling)	the out-of-plane distortion (non-constant Jacobian) of plates elements.	▲				▲	

castiadc.free.fr/online/elfug_C2/elfugbt0001.htm

2/4

5/19/2021

Which Licenses to Perform these Scenarios?

Buckling of a Straight Beam (In-Plane Buckling)	the in-plane distortion (non-constant Jacobian) of membrane elements.	▲					▲	
Lateral Buckling of Narrow Rectangular Beam	other terms of buckling than compression.	▲						
Dynamic Response Analysis	This test studies...	GPS	EST	GAS	GDY	FMS	FMD	
Harmonic Forced Vibration of a Plane Grid	the harmonic dynamic response.	▲	▲	▲	▲			
Harmonic Forced Vibration of a Simply-supported Thin Square Plate	the harmonic dynamic response.	▲	▲		▲	▲		
Transient Forced Vibration of a Simply-supported Thin Square Plate	the transient dynamic response.	▲	▲		▲	▲		
Transient Dynamic Response of a Clamp Beam with Different Inertia	the transient dynamic response.	▲	▲		▲			
Transient Response of a Spring-mass System with Imposed Acceleration	the transient dynamic response.	▲	▲		▲			
Thermo Mechanical Analysis	This test studies...	GPS	EST	GAS	GDY	FMS	FMD	
Thermal Expansion of a Beam	the thermal load.	▲				▲	▲	
Data Mapping	data mapping in thermal loading.	▲	▲					
Analysis of an Assembly	This test studies...	GPS	EST	GAS	GDY	FMS	FMD	
Smooth Connection on a Free Thin Square Plate	an assembly.	▲				▲		
Fastened Connections on Braced Plates	an assembly and an automatic mesh capture.	▲		▲		▲		
Fastened Connection on Beams	an assembly.	▲		▲				

Composites	This test studies...	GPS	EST	GAS	GDY	FMS	FMD	
Bonded Blades in Compression	the coupling bending/extension of a composite made of two isotropic layers.	▲	▲			▲		
Isotropic Biased and Orthotropic Analog Plates	a composite made of an orthotropic layer.	▲	▲			▲		
Simply-supported Sandwich Plate	the transverse shear effect of a sandwich plate.	▲	▲			▲		

catia doc: free_fr/online/elfug_C2/elfugbt0001.htm

3/4

5/19/2021

Which Licenses to Perform these Scenarios?

Thermal Expansion of a Composite Plate	the thermal expansion of a composite plate.	▲	▲				▲	
Laminated Plates with Orientation	laminated plates with orthotropic materials using an angle of orientation.	▲	▲					
Vibration of Simply Supported Laminated Plates	laminated plates with orthotropic materials.	▲	▲					



catia doc: free_fr/online/elfug_C2/elfugbt0001.htm

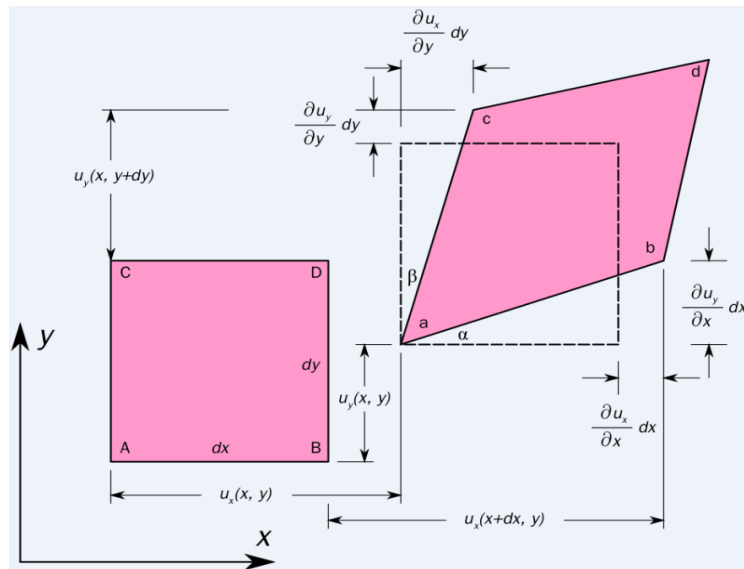
4/4

Appendix C Figures



Figure 1. Mid-fuselage structure of Space Shuttle Orbiter showing boron-aluminum tubes. (Photo courtesy of U.S. Air Force/NASA).

Appendices Figure A: Mid-fuselage structure of Space Shuttle Orbiter showing boron-aluminum tubes (photo courtesy of U.S. Air Force/NASA)



Appendices Figure B: Two-dimensional geometric deformation of an infinitesimal material element [74]

VITA AUCTORIS

NAME: MOHAMAD EDRISY

PLACE OF BIRTH: Arak, Iran

YEAR OF BIRTH: 1982

EDUCATION: Azad University of Arak,
Field of study: Solid Mechanics and Design,
Arak, Iran, 2001-2005, B.Sc.,

University of Applied Science and Technology
(UAST), Damavand Lift Manufacturing
Company,
Field of study: Lift Safety Mechanism Design
and Manufacturing Engineering,
Tehran, Iran, 2014-2018, M.Sc.,

University of Windsor,
Field of study: Mechanical Engineering,
Windsor, CANADA, 2020-2022, M.ASc.,